UNIVERSIDAD DE CHILE
FACULTAD DE CIENCIAS FISICAS Y MATEMATICAS
DEPARTAMENTO DE GEOLOGIA

KINEMATIC AND DYNAMIC INVERSIONS OF SUBDUCTION EARTHQUAKES USING STRONG MOTION AND cGPS DATA

TESIS PARA OPTAR AL GRADO DE DOCTOR EN CIENCIAS MENCION GEOLOGIA

EN COTUTELA CON EL INSTITUTE DU PHYSIQUE DU GLOBE DE PARIS, FRANCE

SERGIO ARTURO RUIZ TAPIA

PROFESOR GUIA:
JAIME CAMPOS MUÑOZ
RAUL MADARIAGA MEZA

MIEMBROS DE LA COMISION:
CESAR ARRIAGADA ORTEGA
CHRISTOPHE VIGNY
JEAN PIERRE VILLOTE
RAFAEL RIDDELL CARVAJAL

SANTIAGO DE CHILE
SEPTIEMBRE 2012

ABSTRACT

We study the inversion of the slip distribution of five earthquakes: 3 that occurred in Chile (Tocopilla 2007, Mw 7.8; Michilla 2007, Mw 6.7; Maule 2010, Mw 8.8) and two from Japan (Iwate 2008, Mw 6.8, Tohoku 2011, Mw 9.0). Kinematic inversions are made for them with the exception of Michilla 2007 and dynamic inversions were made for Michilla 2007 and Iwate 2008. Inversions are made using an elliptical rupture area which is characterized by a Gaussian distribution of slip. The search for the best solution is approached using the neighborhood algorithm. Strong motion and continuous GPS (cGPS) data were used in the inversion. For Tocopilla 2007 we proposed a slip distribution characterized by two ellipses confirming previous work by Peyrat et al. (2010). For the Maule 2010 earthquake two ellipses were proposed, the results showed that the maximum slip is located on the northern part of the rupture. Here also we identified the asperities that controlled the movement in the range of intermediate frequencies (0.02 Hz to 0.1 Hz) in the north of the rupture. The Tohoku 2011 earthquake was characterized by the rupture of one ellipse. Then we searched for the best solution using a Monte Carlo method, we fixed some parameters and released 3 of them: rupture velocity, maximum slip and ellipse size (keeping fixed the aspect ratio between their axes), finding that between these three parameters there are strong links, confirming that the solution is non unique. Also for this earthquake is develops a preliminary inversion using a classical discretization with rectangles, finding similar results to the elliptical inversion. Finally we made the inversion of two intraplate intermediate depth earthquakes of magnitudes around Mw 6.8. For these earthquakes we made the first full dynamic inversions. Here we confirmed, making Monte Carlo inversion, those dynamics inversions are not unique and that are characterized by the parameters of the friction law. These parameters can take different values, but they share common values of seismic moment and kappa values (kappa is a parameter that relates the energy released with the energy available for the earthquake rupture).

RESUMEN

Se invierte la distribución de deslizamiento de cinco terremotos, 3 ocurridos en Chile (Tocopilla 2007, Mw 7.8; Michilla 2007, Mw 6.7; Maule 2010; Mw 8.8) y dos de Japón (Iwate 2008, Mw 6.8 y Tohoku 2011, Mw 9.0). Se realizan inversiones cinemáticas para ellos con la excepción de Michilla 2007 e inversiones dinámicas para Michilla 2007 e Iwate 2008. Las inversiones son hechas proponiendo a priori una distribución geométrica del área de ruptura formada por una o dos elipses y distribución gaussiana de deslizamiento. La búsqueda de la mejor solución se realiza utilizando el algoritmo de vecindad. Acelerogramas y GPS continuos (cGPS) fueron invertidos. Para Tocopilla 2007 se obtiene una distribución de slip caracterizado por 2 elipses. Para el terremoto del Maule dos elipses fueron propuestas encontrándose que el máximo deslizamiento se ubica en la zona norte de una ruptura de casi 500 km; para este terremoto además se identificaron las asperezas que controlaron el movimiento en el rango de frecuencias intermedias (0.02 Hz a 0.1 Hz) en la zona norte de la ruptura. El terremoto de Tohoku 2011 pudo ser caracterizado por la ruptura de una elipses y luego se realizó una búsqueda de la mejor solución utilizando un método de Monte Carlo fijando algunos parámetros y liberando solo 3 de ellos: velocidad de ruptura, deslizamiento máximo y el tamaño de la elipse (manteniendo fija la razón de aspecto entre sus ejes), encontrando que entre estos tres parámetros existen fuertes acoplamientos, confirmando que la solución no es única. También para este terremoto se realiza desarrolla una preliminar inversión utilizando una discretización clásica de rectángulos, encontrándose resultados similares a la inversión por elipse. Finalmente realizamos la inversión de dos terremotos intraplaca de profundidad intermedia de magnitud cercana a Mw 6.8. Para estos terremotos nosotros realizamos las primeras inversiones dinámicas liberando todos los parámetros. Aquí se confirma, realizando inversiones del tipo Monte Carlo, que las inversiones no son únicas y que la ruptura de los terremotos queda controlada por los parámetros de la ley de fricción, pudiendo tomar diferentes valores pero agrupándose en valores específicos de momento sísmico y kappa (kappa es un parámetro que relaciona la energía liberada con la energía disponible para que el terremoto se propague).

RÉSUMÉ

L'objectif principal de cette thèses est d'effectuer des inversions des données sismologiques fin à d'obtenir la distribution de glissement de cinq tremblements de terre qu'ont eu lieux dans des zones de subduction. Ils sont les séismes de: Tocopilla 2007(Mw 7.8) ; Michilla 2007 (Mw 6.7) et Maule 2010 (Mw 8.8) lesquelles ont frappé le Chili, et ceux de Iwate 2008 (Mw 6.8) et Tohoku 2011 (Mw9.0) au Japon. Nous avons calculé des inversions cinématiques pour tous ces événements et avons fait des inversions dynamiques pour Michilla 2007 et Iwate 2008. Ces inversions ont été réalisées proposant une distribution géométrique à priori de forme elliptique pour la zone de rupture avec une distribution gaussienne de glissement. La recherche de la meilleure solution est réalisée en utilisant l'algorithme de voisinage. Accélérogrammes et GPS en continu (cGPS) ont été utilisés dans l'inversion. Pour l'inversion du séisme de Tocopilla 2007 la solution converge vers une distribution de glissement modélisée par deux ellipses. Similaire à celle proposée par Peyrat et la. (2010). Pour le tremblement de terre de Maule 2010 la solution converge vers une distribution de glissement modélisée par deux ellipses, le glissement maximal est situé sur le côté nord de la rupture sismique. De inversion des accelerogrames, deux aspérités était localisées dans le nord de la rupture, ces aspérités contrôlaient le mouvement dans la zone de fréquences intermédiaires (0,02 Hz à 0,1 Hz). Le tremblement de terre de Tohoku 2011 été caractérisé par la rupture d'une seule ellipse. A partir de ces résultats nous avons exploré l'espace de solutions avec une méthode de Monte Carlo ou seulement 3 paramètres sont libérés: la vitesse de rupture, la taille maximale de glissement l'ellipse et la taille de l'ellipse (en gardant le ratio d'aspect fixe entre leurs axes). Entre ces trois paramètres, il existe une forte ambigüité, ce qui confirme que la solution n'est pas unique. Aussi pour ce tremblement de terre est effectuée une inversion préliminaire avec une discrétisation classique en rectangles, et nous avons trouvé des résultats similaires à l'inversion elliptique. Enfin nous avons fait l'inversion de deux tremblements de terre intraplaques de profondeur intermédiaire (Mw 6.8). Nous avons fait les premières inversions dynamiques avec la libération de tous les paramètres. Par les inversions de Monte Carlo, nous confirmons que les inversions dynamiques ne sont pas uniques, et que la rupture des séismes est contrôlé par les paramètres de la loi de frottement. Ces paramètres peuvent prendre des valeurs différentes, mais ils sont regroupés dans une valeur spécifique de moment sismique et du

paramètre kappa (kappa est un paramètre proportionnel au rapport entre ligue l'énergie libérée et l'énergie disponible pour la rupture sismique).

A mis padres

Agradecimientos

Esta tesis ha sido financiada gracias a una Beca Doctorado Nacional de Conicyt, Chile.

Quiero agradecer profundamente a Raúl Madariaga quien durante estos 4 años se ha transformado no solamente en un gran profesor si no que también en un gran amigo y a Jaime Campos por todo el apoyo y amistad de estos años.

Muchas gracias a Cristhope Vigny, Jean Pierre Vilotte, Cesar Arriagada, Rafael Riddell y Gabriel González por sus aportes y comentarios para el mejor termino de este trabajo. Muchas gracias a todas las personas que han hecho un gran esfuerzo por resolver todos los problemas de una tesis en co-tutela: Francoise, Maritza, Prisca, Erica, Lorena. A Rodrigo Sanchez por toda la ayuda prestada para que los procesos computines funcionaran.

A los amigos que he conocido durante este camino, Felipe Leyton , Daniel Carrizo, Eduardo Contreras, Pato Toledo, Sebastian Riquelme, Adriana Perez, Amaya Fuenzalida, Andrei, y obviamente a todos los que olvido.

Y principalmente a Marianela, muchas gracias por tu apoyo, ayuda, paciencia y amor.

INDICE

1. INTRODUCTION

Chilean and Japan are two of the most active subduction zones, both have been very well instrumented in the last years, recording some important interplate subduction earthquakes like Maule 2010 Mw 8.8, Chile (Vigny et al., 2011) and Tohoku 2011 Mw 9.0, Japan (Simmons et al., 2011). Many intraplate earthquakes like Michilla 2007 Mw 6.7, Chile (Ruiz and Madariaga, 2011) and Northern Iwate 2008 Mw 6.8, Japan (Suzuki et al., 2009) have also been very well recorded. The high quality of strong motion (SM) and continuous GPS (cGPS) data obtained during these earthquakes allow us to make detailed studies of the seismic rupture using kinematic and dynamic inversions.

The kinematic and dynamic theories of earthquake rupture were proposed in the late 1960s from the observation of a few near field strong motion records. The first good quality observations were those of the 1966 Parkfield earthquake which was recorded by the Station N°2 located near the southern end of the fault trace at a distance of only 80 m from the mapped surface break. The simplicity of this record was of great interest among seismologists, who computed the first synthetic records with an excellent agreement with observed records (Aki, 1968; Haskell, 1969). Since then two approaches have been used in the representation of an earthquake source. The first approach is known as the kinematic dislocation model, which was introduced by Haskell (1964, 1966) who proposed a simple solution for the far field of a rectangular fault, the main characteristic of this model is that the rupture velocity *Vr* is defined without consideration of the physical constraints that control the earthquake rupture, showing some unacceptable physical features (Madariaga, 1978). The second approach is known as dynamic rupture model, which relates the slip on the fault to stress changes considering physical constrains such as the stress and friction that control the rupture (some early works were Keilis-Borok (1959), Savage (1966), Brune (1970) among them). Until recently the dynamic rupture theory had not been implemented to study earthquakes in the near field; mainly because of the scarcity of well recorded earthquakes and the requirement of large computational resources. Nowadays, thanks to progress in instrumentation several earthquakes have been well recorded in the near source

area by strong motion and cGPS data; most of these events have been studied using kinematic inversion (Festa and Zollo, 2011, to see examples and description of this technique). In spite of this progress, there are few inversions of large subduction earthquakes and there are no full dynamic inversions of subduction earthquakes (see Madariaga and Olsen, 2000, to see details of this technique). Some authors have used the dynamic model to study the earthquake rupture process, most of them based on previous kinematic models (Fukuyama and Mikumo, 1993; Bouchon et al, 1998, among others). Unfortunately, this approach affects the inferred dynamic parameters (Guatteri and Spudich, 2000; Piatanesi et al., 2004). Full dynamic inversions are still very limited. Peyrat and Olsen (2004) were the first to do a full dynamic inversion for the Tottori earthquake of July 2000 using a classical discretisation of the fault into rectangles with constant stress and rupture resistance. DiCarli et al. (2010) improved these results using a stress distribution described by a few elliptical patches. Because of limited resolution and computer resources DiCarli et al. (2010) could not completely invert for all the parameters of the friction law. The present thesis is dedicated to studying both kinematic and dynamic inversion of earthquakes in the subduction zones of Chile and Japan.

SUBDUCTION CONTEXT

Japan and most of Chile are located in two important subduction zones, Figure 1.1 shows that Japan is on the Eurasian plate which is subducted from the East by the Pacific plate; Chile is on the South American plate which is subducted from the West by the Nazca plate. Both subduction zones are characterized by high convergence velocities and by some of the most active seismicity in the Earth. This seismicity is characterized by different types of earthquakes: shallow, outer rise, interplate thrust type and intraplate intermediate depth earthquakes. Figure 1.2 shows two sketches with the zones where these earthquakes occur. During the last five years important interplate thrust and intraplate intermediate depth earthquakes were recorded by local networks, which allow us to make detailed studies of the seismic source, Figure 1.1. The outer-rise earthquakes are not studied because there are not well recorded events by local networks. In Chile there are practically no well recorded shallow crustal events and although in Japan there are several well recorded shallow earthquakes, in this thesis they are not studied.

Interplate thrust earthquakes

During the last 10 years a cluster of larger mega interplate thrust earthquakes have occurred in the world, these include: the Peru earthquake of 8 July 2001, the Sumatra earthquakes of Mw > 8.5 (2004, 2005, 2007 and 2012), Maule 2010 Chile Mw 8.8 and Tohoku Japon Mw 9.0 and the very recent Wharton Sea event of Mw 8.8 last 11 April 2012. Before the current set of large events, previous mega-earthquakes occurred in the fifties and sixties (Kamchatka, 1952 Mw 9.0; Price William Sound, Alaska, 1964 Mw 9.2; Kuril Islands, 1963 Mw 8.5; Valdvia, Chile 1960 Mw 9.5; Rat Islands, Alaska, 1965 Mw 8.7). This apparently seismic "silence" of almost 40 years had severe consequences; the most important is that recent mega-earthquakes (Sumatra 2004, Maule 2010 and Tohoku 2011) generated important unannounced tsunamis. However, it allowed to observe the response of civil structures to the seismic demand of a maximum credible earthquake (Saragoni and Ruiz, 2012), with good performance for most of them in Chile and Japan (Kawase, 2011; Astroza et al., 2012; Saragoni and Ruiz, 2012).

The Maule 2010 and Tohoku 2011 are the first mega-earthquakes that were well recorded by near field instruments. This new seismological information let us study the seismic rupture and details of the source of subduction mega-earthquakes. In contrast with the Sumatra 2004 earthquake which led to an important development of tele-seismic methods to study mega earthquakes (see Ishii et al., 2005; Lay et al., 2005), the Maule 2010 and Tohoku 2011 have led to the development of near field inversion methods to use the continuous GPS records (cGPS). Vigny et al. (2011) proposed that cGPS could be used as seismograms, showing important advantages such as the non saturation during strong shaking and precise displacement measures of the ground. Recently, Yue and Lay (2012) made the first kinematic inversion of a subduction earthquake using only cGPS records. In the present thesis we make the first kinematic inversion of Maule 2010 earthquake using cGPS data, Chapter 3 and the first kinematic inversion of Tohoku 2011 using jointly cGPS data and GPS/acoustic records of ocean bottom instruments, Chapter 4.

In chapter 2 we present a kinematic inversion of the Tocopilla 2007 Mw 7.8 earthquake using both strong motion and cGPS data. This event is the first well recorded Chilean

earthquake of Mw ~ 8.0 and, at this moment, the only well inverted event. The seismological study of the Tocopilla earthquake is of great importance because these M~8.0 earthquakes occur frequently in Chile (see Ruiz and Madariaga, 2012). Ruiz et al. (2011) found that the Tocopilla 2007 earthquake was similar to the Valparaiso 1985 earthquake (Mw 8.0) proposing that all these earthquakes M ~ 8.0 have similar characteristics.

Intraplate intermediate depth earthquakes

The most important challenge for earthquake studies is to make dynamic inversion because it is the only method that captures the physics of the seismic rupture. Unfortunately, for mega-earthquakes and even for smaller M ~ 8.0 earthquakes it is an unrealistic problem because of the huge computational resources required for inversion. For this reason we studied two smaller, but very well recorded intraplate intermediate depth earthquakes. In Chile, this type of earthquake are the most destructive events (Astroza et al., 2002; Saragoni et al., 2004). These earthquakes in contrast with interplate thrust events are located inland and do not produce tsunamis, Figure 1.2 and 1.3. In Chile only the Chillan 1939, Calama 1950 and Tarapaca 2005 intermediate depth events have magnitudes around M ~ 8.0 (Kausel and Campos, 1990, Peyrat et al., 2006). However these earthquakes were not well recorded by near field instruments. In Japan, strong intermediate earthquakes of this kind occur often, for instance the 1987 eastern Chiba event of M_{JMA} 6.7; the 1993 Kushiro-oki of Mw 7.6; the 2001 Geiyo earthquake of Mw 6.7; the 2003 Miyagi-oki earthquake M 7.1 or the 1994 Hokkaido Toho-oki (Shikotan) earthquake Mw 8.2.

The location of the two best recorded intraplate intermediate depth earthquake of Chile and Japan, Michilla 2007 Mw 6.8 and Iwate 2008 Mw 6.8, respectively, is shown in Figure 1.3. These earthquakes have rupture areas smaller than 40 x 40 km. At present, due to limitations in computational resources, this is the largest rupture area for which we can do dynamic inversion. Only few dynamic inversions have been made and there are no dynamic inversions of subduction earthquakes, for this reason we think that the results obtained here could improve our understanding of subduction seismic sources. The Michilla 2007 inversion is presented in Chapter 5 and the Iwate 2008 inversion in Chapter 6.

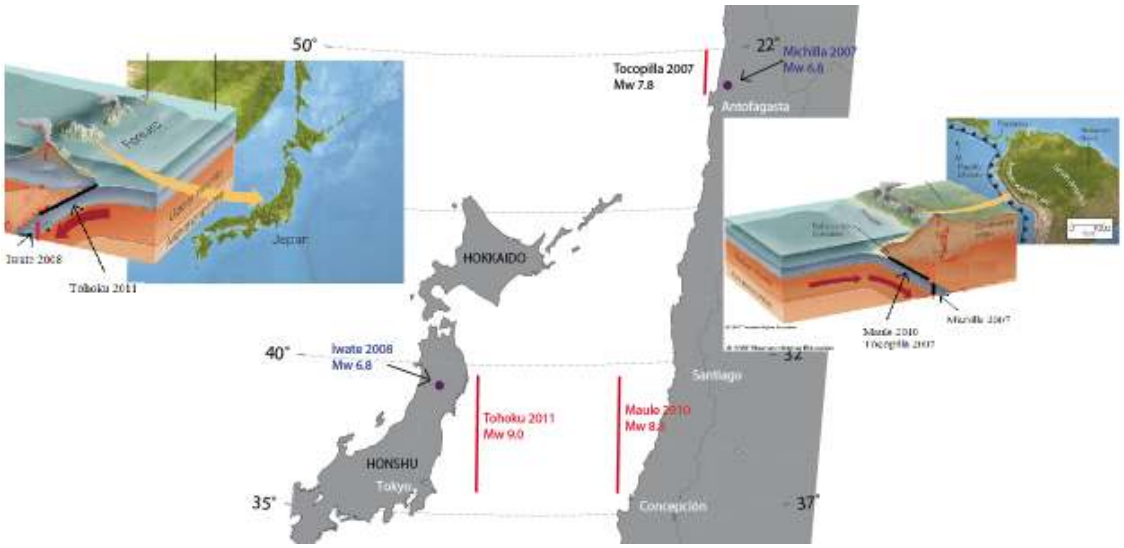

Figure 1.1. Schematic rupture zones of the earthquakes studied in this thesis. The color figures show the Japan and South America subduction zones.

a)

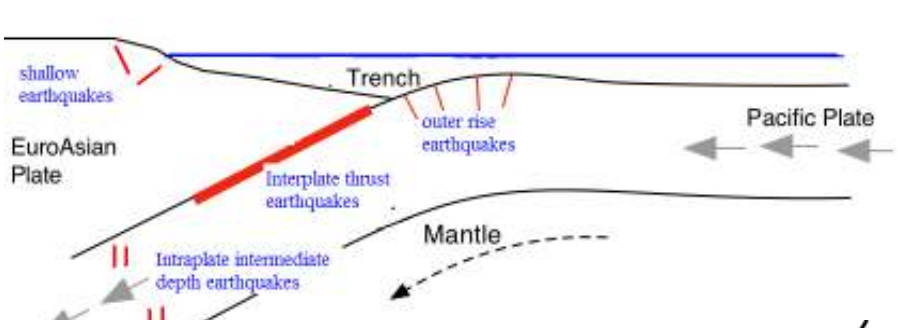

b)

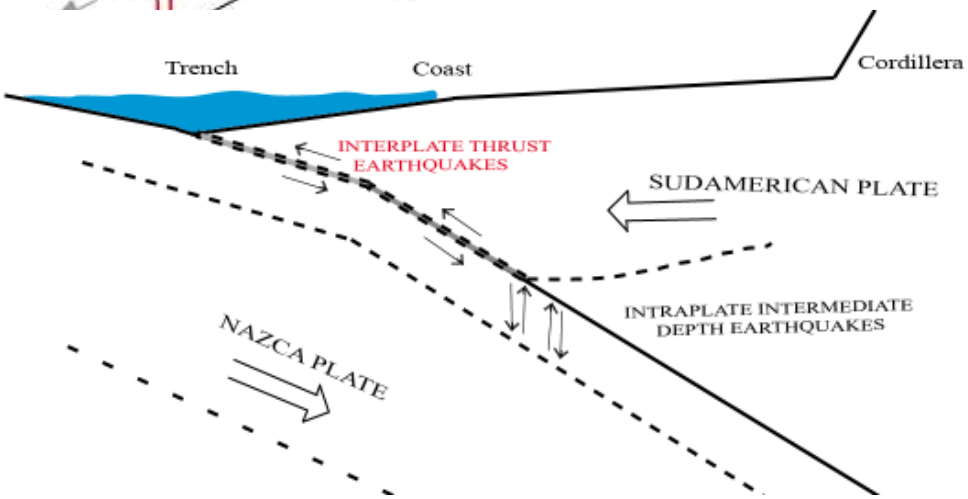

Figure 1.2. Sketch section of subduction zones showing the 4 main earthquakes types: Interplate thrust, intraplate intermediate depth, shallow and outer rise earthquakes. **a)** Japan zone (modified from http://cires.colorado.edu/~bilham) and **b)** Chilean zone (modified from Ruiz and Madariaga, 2012).

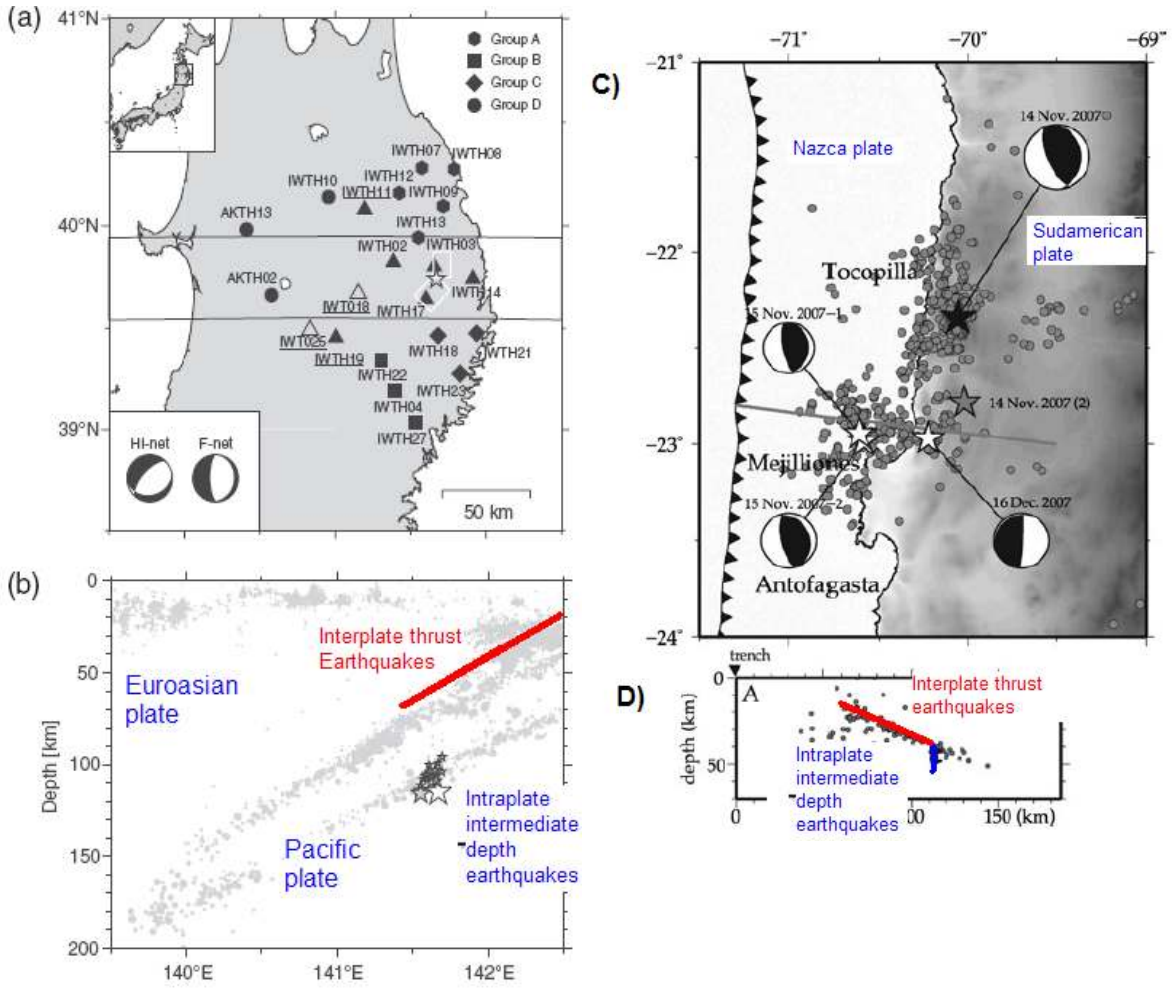

Figure 1.3. (a) and **(b)** Japanese subduction zone (modified from Suzuki et al., 2009), **(c)** and **(d)** Chilean subduction (modified from Peyrat et al., 2010 and Fuenzalida et al., 2012). Only the interplate thrust earthquakes and intermediate depth earthquakes are highlighted in the figures (b) and (d). The red line outlined the rupture zone of interplate thrust earthquakes such as: Tocopilla 2007, Maule 2010 and Tohoku 2011 and the blue line (d) and stars (c) outline the rupture zone of intraplate intermediate depth earthquakes of Michilla 2007 and Iwate 2008, respectively. Figure (a) shows two proposed focal mechanism of Michilla 2007 intraplate intermediate depth earthquakes and Figure (c) shows the aftershocks of Tocopilla 2007 sequences and main focal mechanisms of larger earthquakes.

SEISMIC SOURCE MODEL DESCRIPTIONS

For seismological applications, complete Green functions must be modelled during kinematic or dynamic inversions. It is necessary to provide the shape of the slip function at every point of the fault. Seismologists call this the source time function that is often assumed to be the same everywhere on the fault. The expression in time for each Green function that is propagated from a point source in a homogeneous medium (i.e. Aki and Richards, 2002) is given by:

$$
\begin{aligned}
u(x,t) = {} & \frac{1}{4\pi\rho} A_{ij}^{N} \frac{1}{r^4} \int_{\frac{r}{\alpha}}^{\frac{r}{\beta}} \tau M_0(t-\tau) d\tau + \\
& \frac{1}{4\pi\rho\alpha^2} A_{ij}^{IP} \frac{1}{r^2} M_0\left(t-\frac{r}{\alpha}\right) + \frac{1}{4\pi\rho\beta^2} A_{ij}^{IS} \frac{1}{r^2} M_0\left(t-\frac{r}{\beta}\right) + \\
& \frac{1}{4\pi\rho\alpha^3} A_{ij}^{FP} \frac{1}{r} \dot{M}_0\left(t-\frac{r}{\alpha}\right) + \frac{1}{4\pi\rho\beta^3} A_{ij}^{FS} \frac{1}{r} \dot{M}_0\left(t-\frac{r}{\beta}\right)
\end{aligned}
\tag{1}
$$

Where, A_{ij}^{XY} is the radiation patrons to P and S waves for near (N), intermediate (I) and far field waves (F). α and β are the velocity of P and S waves, respectively. ρ is the medium density and r is the hypocentral distance.

The expression shown in (1) has all the information radiated by an earthquake in a homogeneous medium. $\dot{M}_0\left(t-\frac{r}{\alpha}\right)$ and $\dot{M}_0\left(t-\frac{r}{\beta}\right)$ give the arrival time and shape of P and S far field waves. The term $\int_{\frac{r}{\alpha}}^{\frac{r}{\beta}} \tau M_0(t-\tau) d\tau$ corresponds to the ramp between the P and S far field waves arrivals (near field waves). The sum of the terms $M_0\left(t-\frac{r}{\alpha}\right)$ and $M_0\left(t-\frac{r}{\beta}\right)$ gives the final offset of the slip (static field). Finally, each Green function of the discretized fault plane is summed; and the influence of the propagation path and instrumental response. Figure 1.4 shows the cGPS recorded in San Javier station (SJAV) for Maule 2010 earthquake, where we schematically identified the three waves expressed

in Equation (1). In this thesis the AXITRA code is used to propagate the Green function (Bouchon, 1981; Coutant, 1990).

The study of observed offset during earthquakes could be modeled using static GPS or satellite images (inferograms), however they do not have information about the rupture process which is controlled by the waves produced during the earthquake. For the description of this problem, there are two approaches: a kinematic approach in which the emphasis is put on the distribution of slip on the faults and a dynamic approach where the emphasis is on the state and friction on the fault.

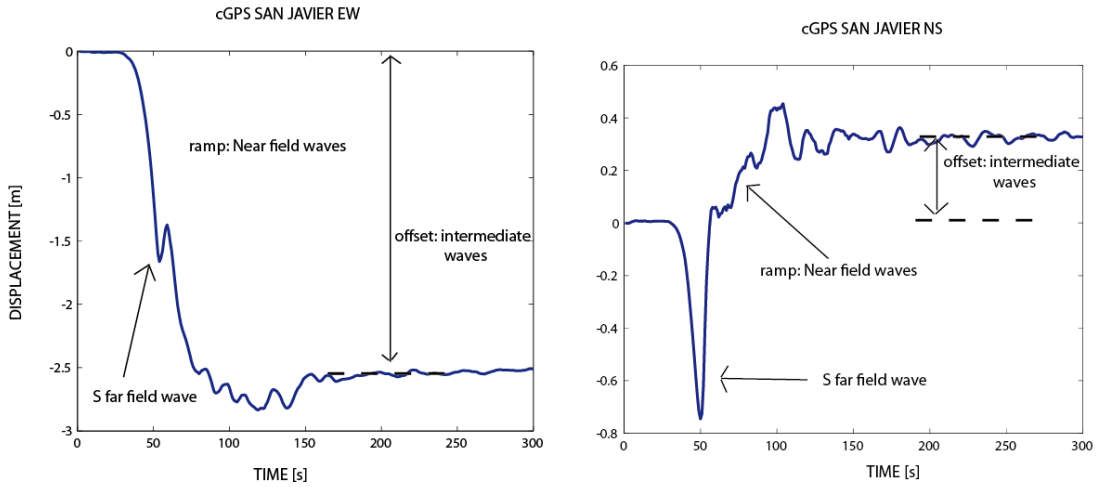

Figure 1.4. San Javier station (SJAV) for Maule 2010 earthquake. We identify schematically the three waves defined in Equation (1).

Kinematic model

These are the most commonly used models of the source. The main emphasis is on the determination of details of the distribution of slip on the fault. This approach is complementary to that used by geodesists and earthquake geologists that are primarily interested in the distribution of slip.

For seismological applications the kinematic model is specified by the description of slip plus the rupture process specified by the propagation of the rupture front. A common example of a kinematic model is a uniform displacement discontinuity that spreads at

constant rupture velocity inside a fault of arbitrary shape. At low frequencies, or wavelengths much longer than the size of the fault, this model is a reasonable approximation to the seismic rupture. For instance, in the rectangular Haskell's model, at time t=0 a line of dislocation of with W appears suddenly and propagates along the fault length at a constant rupture velocity until a region of length L of the fault has been broken. As the dislocation moves, it leaves behind a zone of constant slip D. The fault area L x W times the slip D and the rigidity μ of the medium defines the seismic moment $M_0 = \mu DLW$ of this model. Haskell´s model captures some of the most important features of an earthquake and has been used extensively to invert for seismic source parameters from near-field and far-field seismic and geodetic data. The complete seismic radiation for Haskell's model was computed by Madariaga (1978) who showed that, because of the stress singularities around the edges, the Haskell model fails at high frequencies, as was noted by Haskell (1964) himself.

Figure 1.5 shows the kinematic rupture of Maule 2010 earthquake proposed by Vigny et al. (2011). It shows the isochrones where the rupture starts at the hypocenter and then propagates with constant rupture velocity. From each dot in the figure we have to compute the Green function with fixed source and rise time, because only the slip for each dot is inverted. Finally, all Green functions for each dot are summed in the sites where the Maule earthquake was recorded.

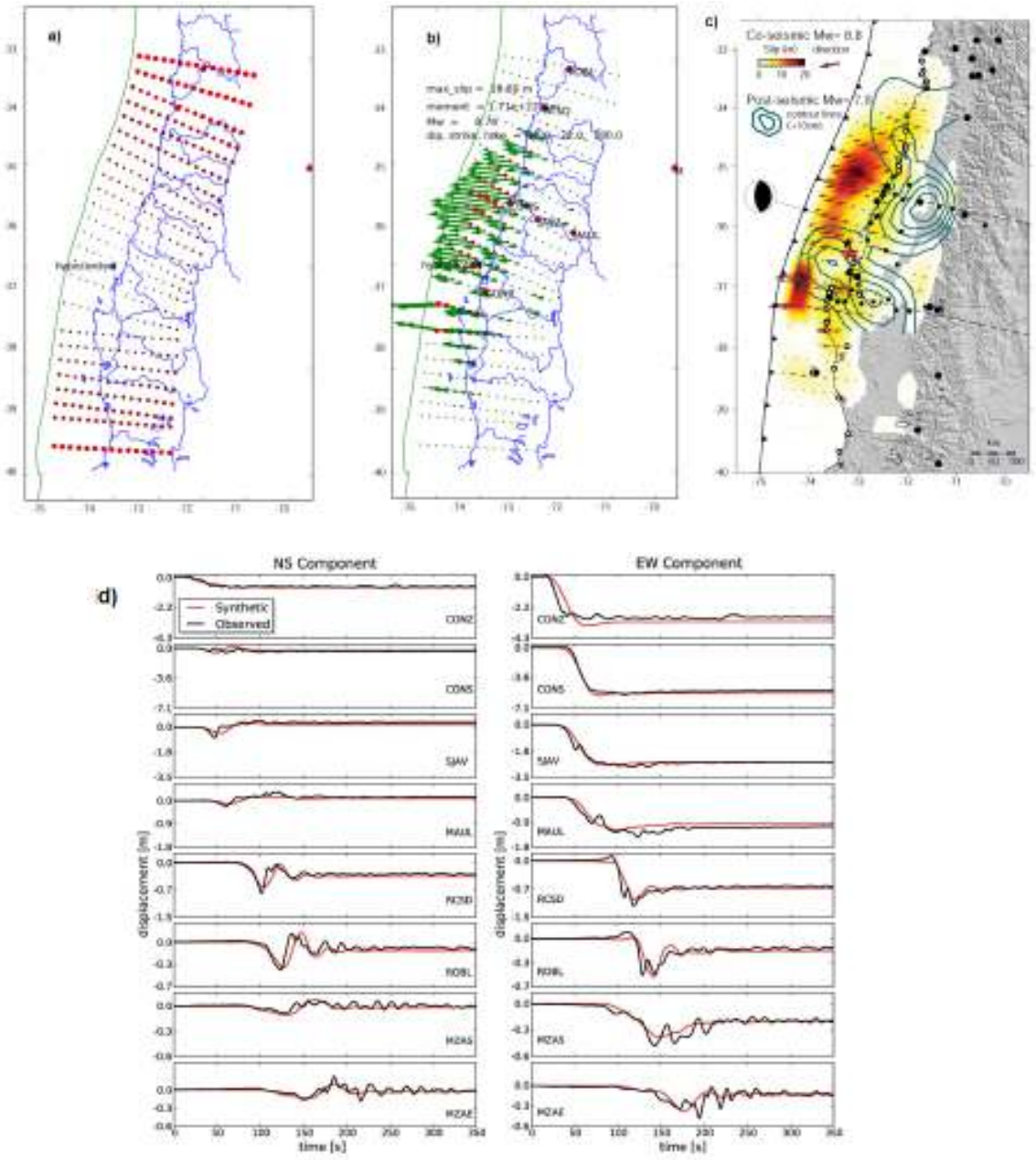

Figure 1.5. Kinematic rupture model proposed by Vigny et al., (2011) for the Maule 2010 earthquake. **(a)** Isochrones of rupture, the dots are larger at longer times. The rupture starts at the hypocenter and is propagated with constant rupture velocity. **(b)** From each dot we compute the Green function with a specific source time and rise time, only the slip for each dot is inverted. **(c)** Shows the slip distribution using a smoothed version of (b). **(d)** The synthetic records show a good misfit with the cGPS that recorded this earthquake.

Dynamic model

Rupture propagation on a major earthquake fault is controlled by the properties of the friction law on the fault. Friction controls the initiation, development of rupture and the healing of faults. Laboratory experiments at low slip rates were analyzed by Dieterich (1978), who proposed models of rate and state-dependent friction, and by Ohnaka and Shen (1999) who concluded that their experiments could be explained with a simpler slip-weakening friction law. Actually, from the point of view of earthquake observations, these two models of friction are essentially indistinguishable as shown by Okubo (1989). Basically, both slip-weakening and rate- and state-dependent friction contain finite length scales that control the behavior of the rupture front. Although, these intrinsic length scales are of very different origin, we can hypothesize that their effects on rupture is similar. This is the friction length scale, which we will generically refer to as *Dc*. Without this length scale earthquake faulting makes little sense due to lack of energy conservation in the fault system. Because of the equivalence of friction laws at high slip rates, in this thesis a simple slip-weakening friction law by Ida (1972), in which slip is zero until the total stress reaches a peak value (yield stress) that we denote with *Tu*. Once this stress has been reached, slip D increases and $T_f(D)$ decreases:

$$T_f(D) = (T_u - T_r)\left(1 - \frac{D}{Dc}\right) + T_r \qquad (1)$$

where T_f is friction as a function of slip D. T_u is the peak frictional stress or strength and D_c is the slip weakening distance. For simplicity, in this theses we assume that the residual friction $T_r = 0$.

Figure 1.6 presents the geometry of the fault model we study. The most important feature of the friction law is slip-weakening that occurs near the rupture zone on a so-called breakdown or slip-weakening zone just behind the rupture front. The propagation of the rupture front is completely controlled by the friction law and the distribution of initial stress on the fault. The non linear rupture propagation velocity is may be the most important difference with kinematic models. Figure 1.7 shows the snapshots of slip rate of Iwate

2008 earthquake, where it is possible to observe that the rupture velocity is not constant with time.

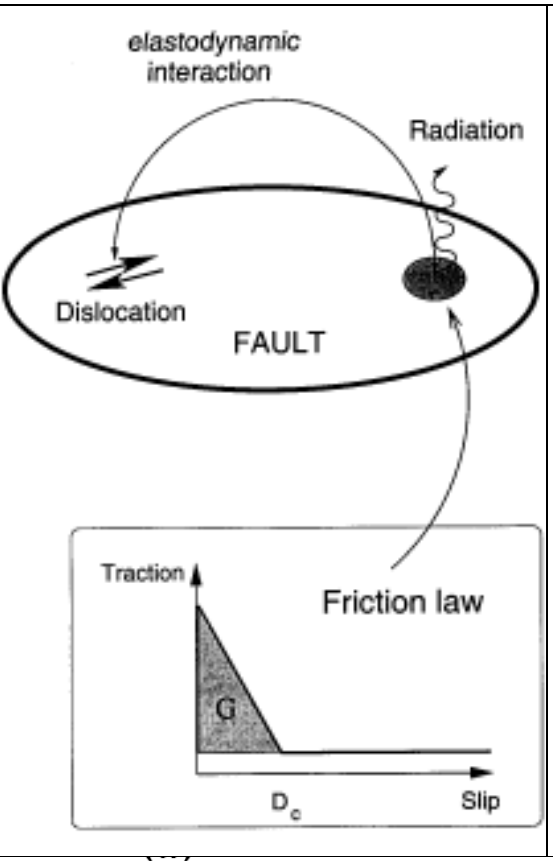

Figure 1.6. Geometry of a simple rupture propagating along a flat fault embedded in a 3-D elastic medium. Rupture propagation is controlled by elastodynamic interactions and is damped by seismic radiation. The boundary conditions on the fault are dominated by friction. We use a simple slip-weakening friction of peak stress *Tu*, slip-weakening *Dc* and energy release rate *G*. Modified from Madariaga and Olsen (2000)

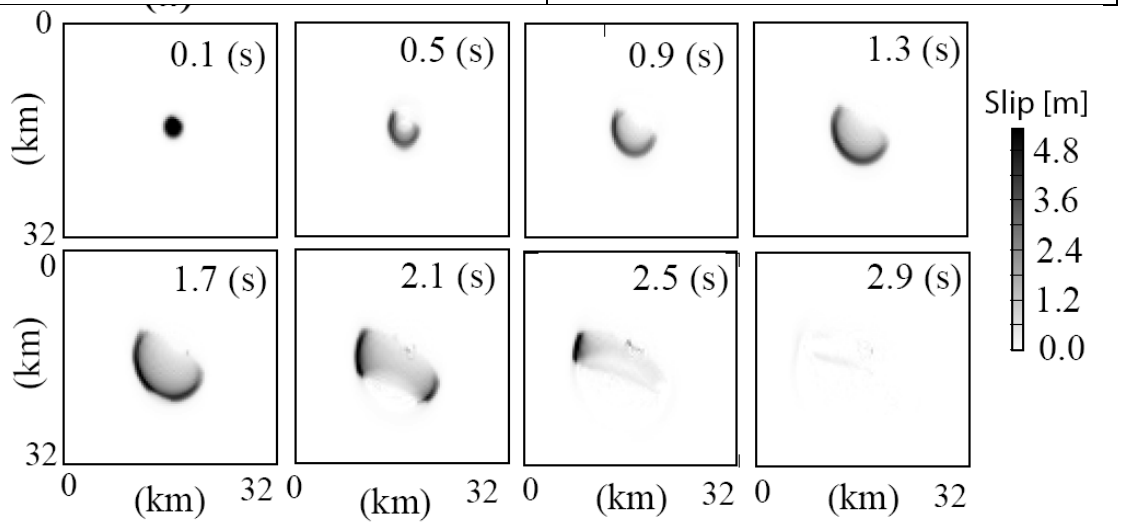

Figure 1.7. Dynamic inversion of the Northern Iwate intermediate depth earthquake. Snapshots of slip rate for the best model obtained by dynamic inversion. The rupture has a faster nucleation and is stopped in the bounders of the rupture by the stopping phase waves.

Finally the dynamic rupture is controlled by the ratio of available strain energy to energy release rate; it controls the overall characteristics of the rupture process as discussed by Madariaga and Olsen (2000). Madariaga and Olsen (2000) defined the parameter κ (Equation 2) which represents this physical characteristic of the rupture of earthquakes.

$$\kappa = \frac{T_e^2}{\mu T_u} \frac{L}{D_c} \tag{2}$$

where L, the characteristic size of the event, is taken as the shorter semi axis of the source ellipse, μ is the shear modulus, T_e, T_u and D_c were already defined.

To include different aspects of the rupture process, such as the nucleation process, the dependence of friction on the propagation and the physical phenomena that stop the rupture, we generated a simple but powerful model of the earthquake rupture shown in Figure 1.8. The nucleation is modelled as a small asperity with a state of stress that exceeds the peak stress Tu, so that rupture is ready to start (here two parameters are inverted, the radius of the asperity and the critical stress). Then the rupture grows unstably accompanied by a rapid slip, slip-rate and stress drop. The rupture process is controlled by the friction, which is the resistance to motion that occurs when a body slides tangentially to a surface on which it contacts another body. Using this model, in this thesis for first time all the parameters included in the parameter κ are inverted. Then Monte Carlo inversions are made to demonstrate that this parameter controlled the dynamic rupture process, Figure 1.9. The best families of solution are clustered in a small zone that satisfied the physical requirement that can only be considered in dynamic inversions (see Chapters 5 and 6).

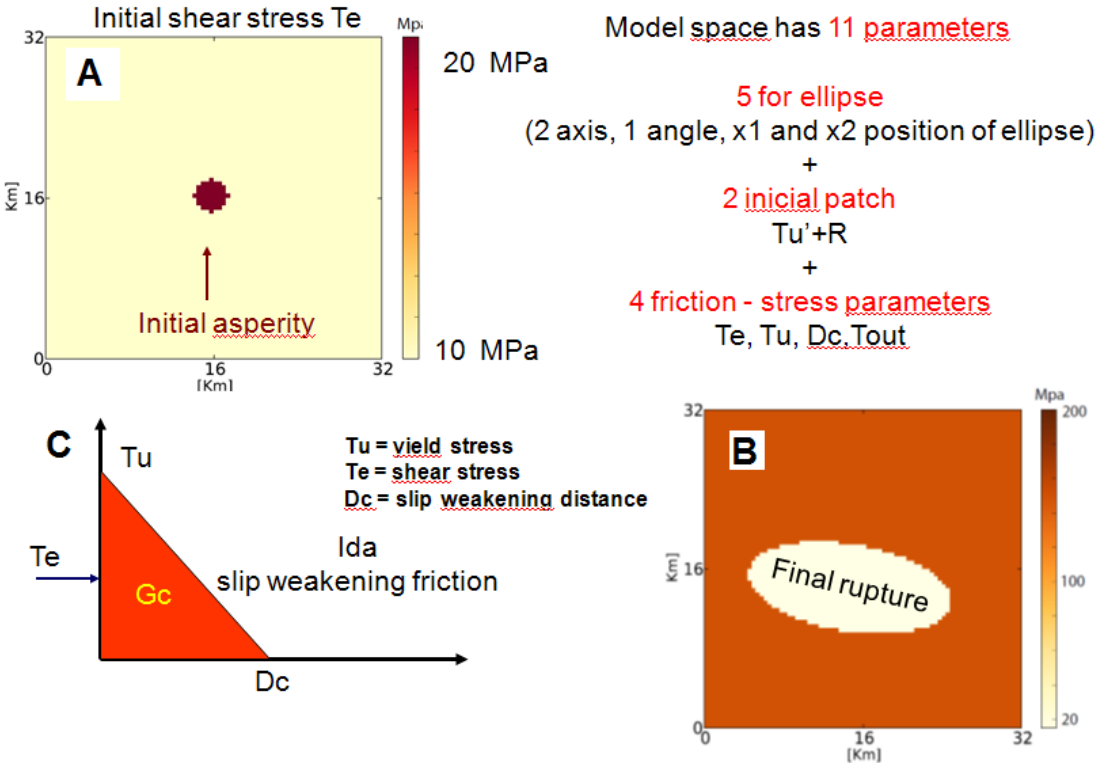

Figure 1.8. Sketch showing the initial state of the rupture **(A)** where the initial stress is constant except in a small asperity shown in deep brown colour. Once the rupture leaves the asperity it is controlled by the slip weakening friction law shown in **(C)** . The final rupture is show in **(B). T**his model can be fully described by only 11 parameters.

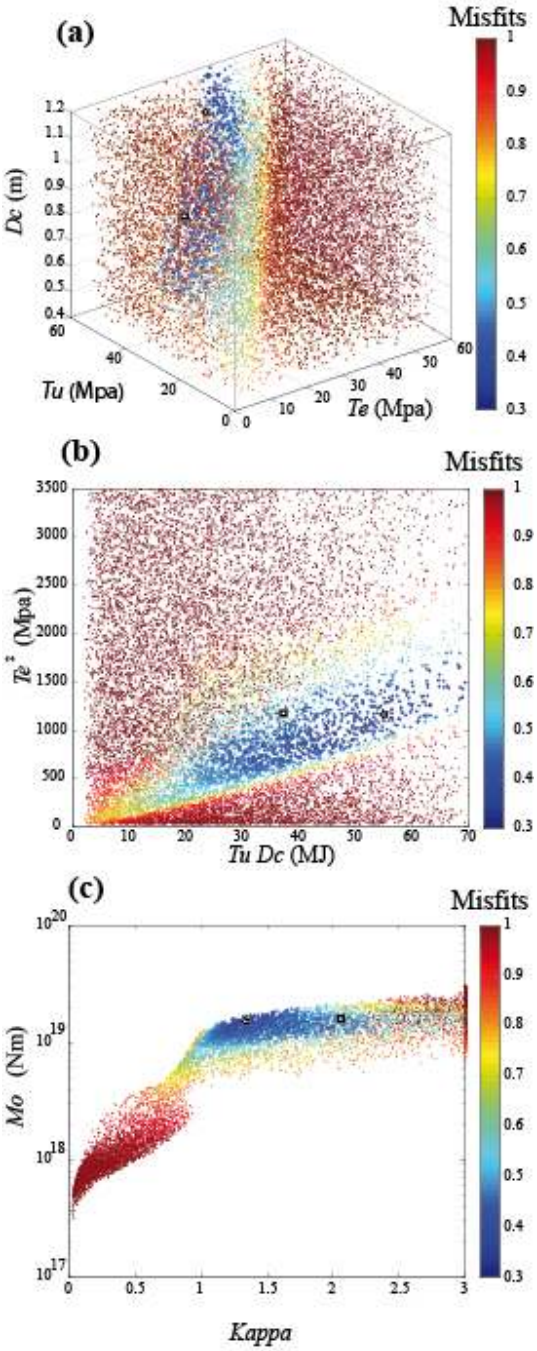

Figure 1.9. Dynamic inversion of the 2008 Northern Iwate intermediate depth earthquake. Each dot represents a model, the dots are colored by the misfit value following the color scale shown on the right. The scale is saturated for misfits ≥ 0.5. **(a)** Plot of misfits for each model projected onto the space of dynamic parameters T_e, T_u and D_c **(b)** Projection of model space onto the plane T_e^2 and T_uD_c The misfits lower than 0.5 converge to narrow band which ratio tends to Kappa (κ) value. **(c)** Projection of model space onto the plane Mo and κ. The misfits lower than 0.5 are controlled by the seismic moment (~Mw 6.7) and a narrow band of κ value ($1 \leq \kappa \leq 1.6$). The black star corresponds to the optimal solution determinate by NA, and the black square is the supershear solution (see Chapter 6).

SEISMIC SOURCE INVERSION APPROACH

Elliptical and Rectangular shaped inversion approaches

To model the geometry of seismic source rupture there are many different approaches that include simple plane faults to several plane faults or other even more complex geometrical distributions. As the inversion problem is largely under determined the main strategy of this thesis is to reduce the number of free parameter in our inversions. For this reason, a simple fault plane is chosen to make the inversions; this approach is in general a good simplification for subduction earthquakes. The slip distribution was characterized by an elliptical approach, which reduces the number of free parameters (Vallé and Bouchon, 2004), but we also used the approach of subdividing the fault into a set of rectangles. Figure 1.10 shows the two discretizations for the kinematic inversion of Tohoku 2011 earthquake discussed in Chapter 4. In this example it was necessary to use to use 41 parameters in the traditional rectangular parametrisation, while only seven parameters were required by the elliptical approach. Both models converge to good and similar result.

For kinematic inversion where generally only the slip and rupture velocity are inverted the approach of using rectangular patches is a good strategy. However when the number the records is limited as happened for the Tocopilla 2007 and Maule 2010 earthquakes where only a few cGPS and strong motion records recorded this large event, the elliptical approach is the better strategy because of the reduced number of parameters that are required to invert, see chapters 2 and 3.

For dynamic inversion the use of a grid of rectangular stress patches to describe the initial stress and the distribution of friction on the fault surface poses several problems that need to be carefully considered. (1) The rectangular patches produce strong stress singularities at the edge of the patches. These singularities appear in the stress components that are not directly inverted for. Their effect on rupture propagation is not clear. (2) In order to reduce the effect of these spurious stresses some scheme must be devised in order to smooth numerical solutions. (3) A large number of rectangular patches are needed to properly simulate the variability of stress and friction on the fault plane. As a consequence, the

inversion contains a large number of degrees of freedom making it very expensive even for simple source models. (4) The implementation of rectangular patches does not have a simple mechanism to stop rupture propagation, so that many of the models generated by the inversion algorithm do not stop and therefore
do not satisfy the data. Most of these difficulties can be avoided using the elliptical approaches used in this thesis, see Chapter, 5 and 6.

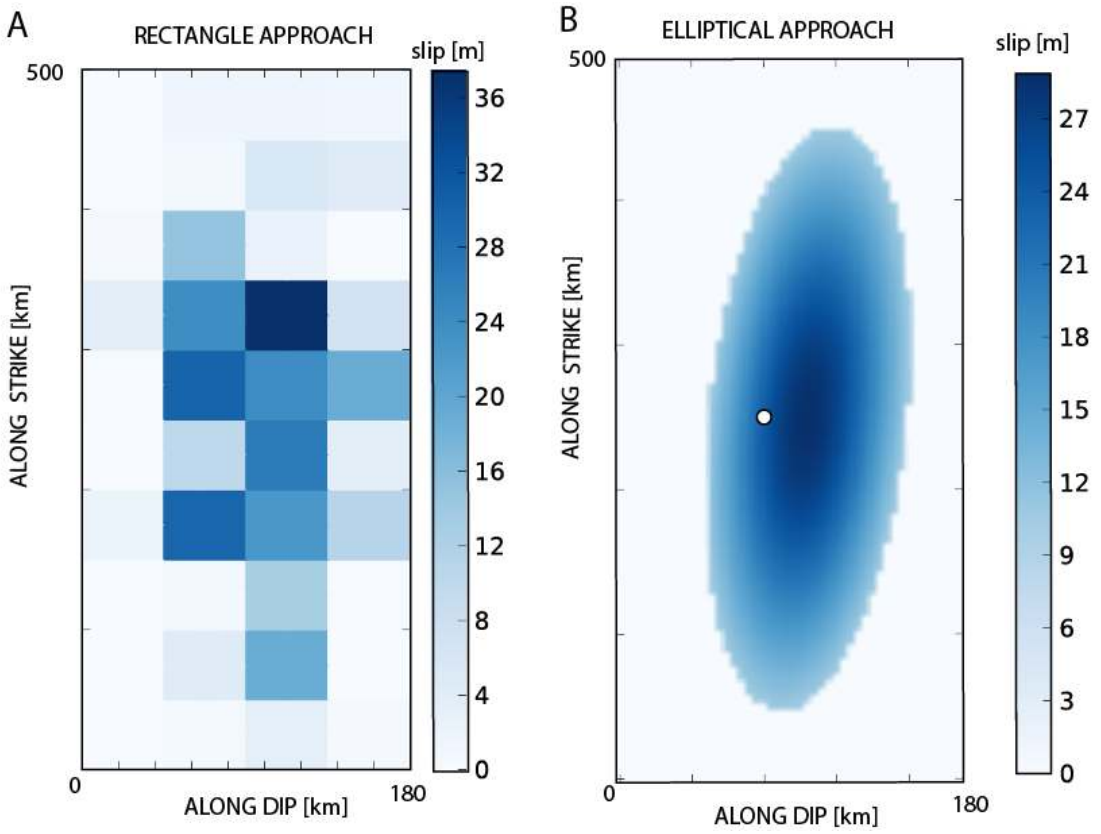

Figure 1.10. A rectangle and **B** elliptical approaches to make the kinematic inversions of Tohoku 2011 earthquake. During the inversion in **A** each rectangle can take a different slip value, in **B** the slip distribution is defined a priori and only the maximum slip and geometrical aspect of the ellipse are inverted.

Non linear inversion

In this thesis the strategy for making the inversion is inspired in Tarantola's work on non-linear inversion (i.e. Taratola, 2005). The inversion problem is over indeterminate and the

solutions are not unique, then the best solution should be characterized by a family of solutions. In a first step, we look for the minimum residual solution using the neighbourhood algorithm (NA) (Sambridge, 1999) with an error function measured by the L2 norm. The NA is a nonlinear derivative-free method employing geometrical concepts to guide a direct search in the parameter space. This parameter space is partitioned into a set of Voronoi cells, each cell being associated with one model. At every iteration, a set of models is recalculated in the Voronoi cells of the previous set with the smallest misfit. The neighborhood algorithm requires only two control parameters: the sample size of each iteration Ns and the number of cells Nr in which a new sample is searched. Once the minimum is identified we used Monte Carlo inversion around the best solution found by NA with a reduced number the parameters (Chapters, 4, 5 and 6).

Signal processing

We use continuous GPS (cGPS) and strong motion records to make our kinematic and dynamic inversions. The inversions were focused on long periods from static displacement (infinite period) to 50 or 10 seconds. The high cut off frequency is chosen in order to avoid large site-effects or complex soil structures that our simple 1D velocity models cannot to reproduce. The low cut off frequency is chosen in order to reduce the problems with the integration of accelerograms which have inherent problems to record adequately the long periods.

Figure 1.11 shows an example of the signal processing for accelerogram data. IWTH03 EW is a record obtained for the Iwate 2008 Japan earthquake in a down-hole station whereas IWT003 is a record for the same event but recorded on the free surface. In this case the low pass filter chosen was 0.02 Hz and 0.04 Hz for the down-hole and surface records, respectively. The high pass corner frequency was controlled by the basin waves, rotation waves and instrumental noise, among other problems that do not allow a proper integration of strong motion records especially for medium magnitude earthquakes (Boore and Bommer, 2005). For this reason for the Michilla Mw 6.8 Chile earthquakes and Iwate 2008 Mw 6.8 Japan, chapters 5 and 6 respectively, the strong motion records are filtered and then twice integrated. For largest earthquakes a better solution is to use the continuous GPS

signal (cGPS) where the long period are very well constrained, however in this cases the problem is the need of low pass filter to remove the high frequency noise.

Figure 1.12 shows a cGPS record of the Tohoku 2011 earthquake, this record was filtered using a low pass filter of 0.02 Hz to delete the basin waves, atmospheric noise, etc. The influence of spurious signal is not important in records with large displacement like T944 EW (Figure 1.12A), but for smaller displacement the noise could be important (Figure 1.12B). In Chapter 4 the cGPS data are filtered using the filter shown in Figure 1.12.

Finally there is a frequency band where the strong motion and cGPS have similar response. Figures 1.13A and 1.13B shows the El Roble records for the Maule 2010 earthquake where in the same place a cGPS antenna and an accelerograph are installed. The strong motion record is integrated twice and compared with cGPS record, Figure 1.13C shows a very good match. The double integration of the El Roble accelerogram is made using the technique proposed by Boore and Bommer (2005), as this integration is not-unique, several test were made and by trial and error the same static displacement for both records was found. Figures 1.13D and 1.13E show the Fourier spectra of both displacement records, where it is possible to appreciate that the two records match very well in the 100 and 10 seconds perio range. For higher frequencies the cGPS record shows an erratic behaviour with respect to the accelerogram signal. In Chapter 2 we propose a kinematic inversion of the 2007 Tocopilla, Mw 7.8 earthquake using jointly strong motion and cGPS data. The inversion was made in velocity in the frequency range where both records work adequately. In Chapter 3 we inverted the Maule 2010 earthquale using cGPS records derived to find ground velocity and filtered with a low corner frequency of 0.05 Hz .

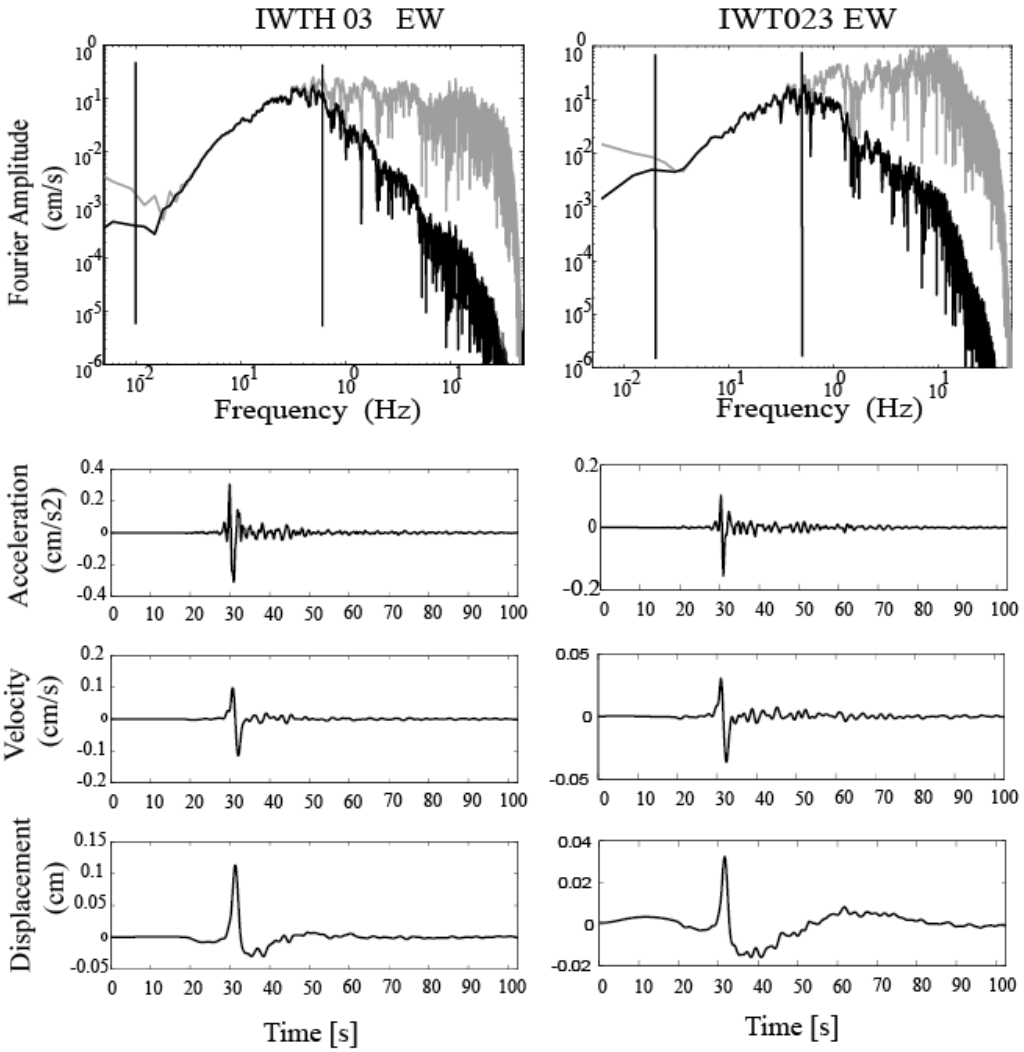

Figure 1.11. Northern Iwate intermediate depth earthquake of 2008. Fourier spectra of the EW accelerograms recorded at stations IWTH03 (a) and IWT023 (b). The unfiltered spectra are shown in gray; the filtered spectra in black. The band-pass filter had corners of 0.02 – 0.5 Hz and 0.04 – 0.5 Hz, respectively. (c) and (d) filtered acceleration, velocity and displacement EW records at IWTH03 and IWT023.

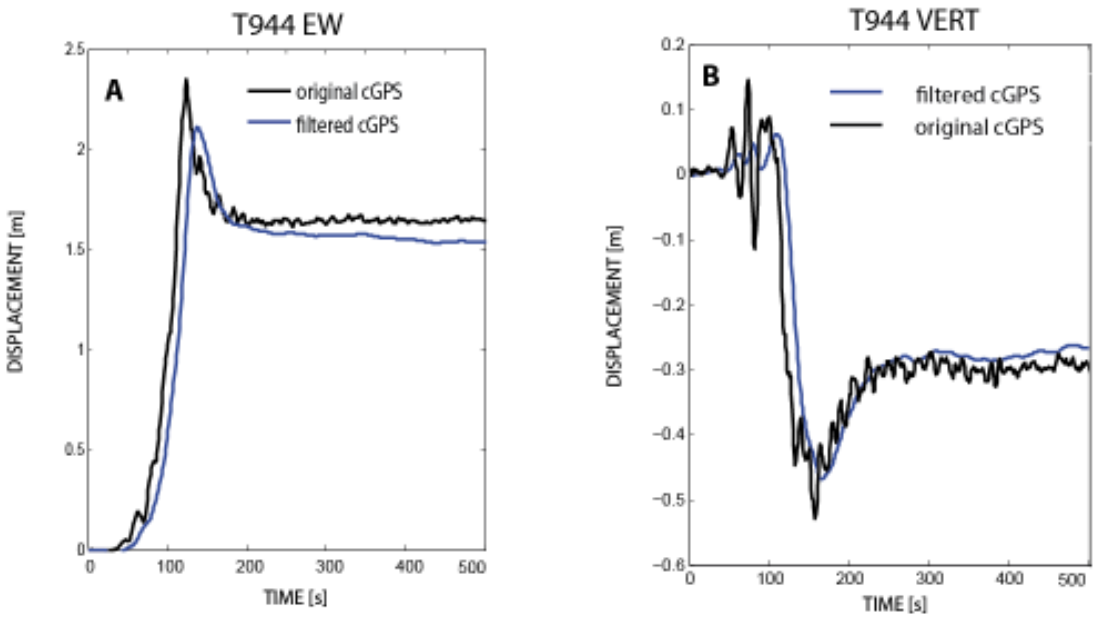

Figure 1.12. A. T944 EW and **B.** T944 VERT cGPS record of Tohoku 2011 earthquake. The records were filter using a high pass corner frequency of 0.02 Hz. The filtered signal reduces the noise signal however introduce a change of phase.

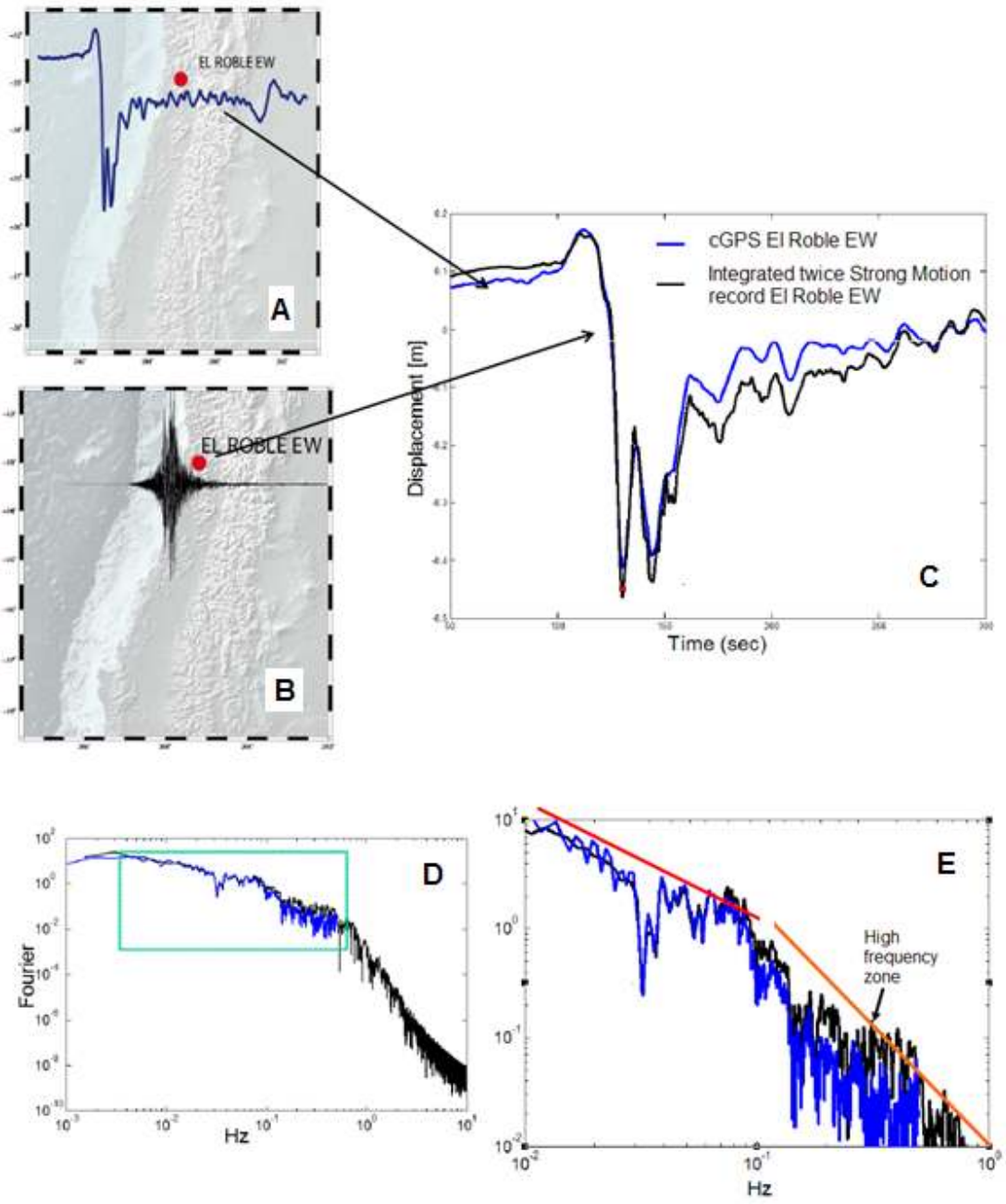

Figure 1.13. A cGPS and **B** accelerogram records obtained in the El Roble station for the Maule 2010 earthquake. **C** twice integrated accelerogram and comparison with cGPS. D **D** Fourier spectra of both records in displacement and **E** a zoom of figure D.

Finally, this thesis is divided in the following chapters and annexes:

Chapter 2. *Simultaneous kinematic inversion of 2007 Tocopilla 2007, Chile earthquake using Strong Motion and cGPS data*. In this chapter a kinematic simultaneous inversion of SM and cGPS records is made using an elliptical patch approach (Vallé and Bouchon, 2004) using Neighborhood algorithm (Sambridge, 1999) for find the best solution.

Chapter 3. *Short Period Rupture Process of the 2010 Mw 8.8 Maule Earthquake in Chile.* This chapter corresponds to the paper accepted in *Earthquake Spectra* by S. Ruiz, R. Madariaga, M. Astroza, R. Saragoni, M. Lancieri, C. Vigny and J. Campos. Kinematic inversion using of cGPS data is made. The study focuses on the high frequency behavior of the Maule 2010 earthquake, for this reason the cGPS inversion is complemented with a detailed study of strong motion data.

Chapter 4. *Kinematic inversion of Tohoku 2011 Mw 9.0 earthquake using cGPS data.* In this chapter we made a preliminary cGPS kinematic inversion using an elliptical approach which is compared with a traditional inversion using a discretization based on fixed rectangles.

Chapter 5. Determination of the friction law parameters of the Mw 6.7 Michilla earthquake in northern Chile by dynamic inversion. This chapter corresponds to the paper published in Geophysical Research Letter by S. Ruiz and R. Madariaga. A dynamic inversion was made using five near field strong motion record, the excellent quality of these records almost without site effect and good azimuthal distribution allowed us to study a family of solutions using the asperity models (Kanamori and Stewart, 1978) and barrier models (Das and Aki, 1977). The Neighborhood algorithm (Sambridge, 1999) and Monte Carlo technique were used to find the best solutions.

Chapter 6. *Kinematic and Dynamic inversion of the 2008 Northern Iwate Earthquake.* This chapter corresponds to the paper submitted to *Bulletin of the Seismological Society of America* by S. Ruiz and R. Madariaga. Kinematic and dynamic inversions were made using

different dataset of the K-net and KIK-net networks. More than 15 SM records were inverted to obtained the seismic source characteristics. Also, the Neighborhood algorithm and Monte Carlo technique were used.

Chapter 7. *Conclusions and Perspectives.*

Chapter 8. *Extended Abstracts.* Extended abstract in French and in Spanish are presented.

The annexes are composed by some papers published and submitted which are not related directly with the inversion of seismic rupture of earthquakes, but all of them were necessary to understand the seismic source process of the subduction earthquakes.

Annex A. Lancieri, M., Fuenzalida, A., Ruiz, S**.** and Madariaga, R (2011) Magnitude Scaling of early-warning parameters for the Mw 7.8 Tocopilla, Chile, earthquake and its aftershocks. *Bulletin of the Seismological Society of America (BSSA); 101 (2); 447-463.*

Annex B. Contreras-Reyes, E., Jara, J., Grevemeyer, I., Ruiz, S. and Carrizo, D., (2012). Abrupt change in the dip of the subducting plate beneath north Chile. *Nature Geoscience*. DOI 10.1038/NGEO1447.

Annex C. Ruiz, S**.**, Kausel, E., Campos, J., Saragoni, G. R. y Madariaga, R. (2011). Identification of High Frequency Pulses from Earthquake Asperities Along Chilean Subduction Zone Using Strong Motion. *Pure and Applied Geophysics, 168, (1-2), 125-139.*

Annex D. Astroza, M., Ruiz, S. and Astroza, R. (2012). Damage assessment and seismic intensity analysis of the 2010 (Mw 8.8) Maule Earthquake. Accepted in *Earthquake Spectra*

Annex E. Ruiz, S. and Madariaga R. (2012). Sismogénesis, proceso de ruptura y réplicas del mega terremoto del Maule 2010, Chile. Chapter XX in press “Mw= 8.8, Terremoto en

Chile, 27 de Febrero 2010" Departamento de Ingeniería Civil, Universidad de Chile. (In Spanish)

Annex F. Saragoni, G. R. and Ruiz, S. (2012). Implicaciones y nuevos desafíos de diseño sísmico de los acelerogramas del terremoto del 2010. Chapter XX in press. "Mw= 8.8, Terremoto en Chile, 27 de Febrero 2010" Departamento de Ingeniería Civil, Universidad de Chile. (In Spanish)

Annex G. Astroza, M., Ruiz, S., Astroza, R. and Molina, J. (2012). Intensidades Sísmicas del Terremoto del 27F. Chapter XX in press. "Mw= 8.8, Terremoto en Chile, 27 de Febrero 2010" Departamento de Ingeniería Civil, Universidad de Chile. (In Spanish)

REFERENCES

Aki, K., (1968). Seismic displacement near a fault. J. Geophys. Res. 73, 5359-5376.

Aki, K., and P. G. Richards, 2002. Quantitative Seismology, Second Edition, University Science. Books, Sausalito, CA

Bouchon, M. (1981), A simple method to calculate Green's functions for elastic layered media, *Bull. Seismol. Soc. Am*., **71**, 959–971.

Astroza M, Moya A, Sanhueza S, (2002) "Comparative study of the effects of Chillán 1939 and Talca 1928 earthquakes." VIII Congreso Chileano de Sismologia e Ingenieria Antisísmica, Valparaiso, Chile.

Astroza, M., Ruiz, S. and Astroza, R. (2012). Damage assessment and seismic intensity analysis of the 2010 (Mw 8.8) Maule Earthquake. In press. Earthquake Spectra

Bouchon, M., Campillo, M. and Cotton, F., (1998). Stress field associated with the rupture of the 1992 Landers, California, earthquake and its implications concerning the fault strength at the onset of the earthquake. J. Geophys. Res., 103, 32091-21097.

Boore, D. M. and J. J. Bommer (2005). Processing of strong-motion accelerograms: Needs, options and consequences, *Soil Dynamics and Earthquake Engineering* 25, 93--115

Brune, J., (1970). Tectonic stress and the spectra of seismic shear waves from earthquakes. J. Geophys. Res. 75, 745-759

Campos, J., Hatzfeld, D., Madariaga, R., Lopez, G., Kausel, E., Zollo, A., Barrientos, S., and Lyon-Caen, H., 2002. The 1835 seismic gap in South Central Chile, *Phys. Earth Planet. Int.*, **132**, 177-195.

Coutant, O. (1990), Programme de simulation numerique AXITRA, Rapport LGIT, Univ Joseph Fourier, Grenoble, France

Das, S. and K. Aki (1977), Fault plane with barriers-versatile earthquake model, *J. Geophys. Res*., 82 (B36), 5658-5670.

Di Carli, S., C. Francois-Holden, S. Peyrat and R. Madariaga (2011). Dynamic inversion of the 2000 Tottori earthquake based on elliptical subfault approximations. J. Geophys. Res.,115,B12328, doi:10.1029/20095B006358

Dieterich, J. (1978), *Time-dependent Friction and the Mechanics of Stick-slip*, Pure appl. geophys. 116, 792–806.
Festa, G. and Zollo, A., (2011) From data to source parameters: kinematic modeling. Chapter of the book entitled " The mechanics of faulting: From laboratory to real earthquakes " edited by A Bizzarri and H Bath.
Fukuyama, E. and Mikumo, T., (1993). Dynamic rupture analysis: Inversion for the source process of the 1990 Izu Oshima, Japan earthquake (M6.5), J. Geophys. Res., 115, B12328.
Fuenzalida, A., Schurr, B., Lancieri,M. and Madariaga, R. (2012). High-resolution relocalitions and mechanisms of aftershocks of the 2007 Tocopilla (Chile) earthquake. In preparation.
Geller, R., 2011. Shake-up time for Japanese seismology (2011). Nature, 472, 407–409.
Guatteri, M. and P. Spudich (2000), What can strong-motion data tell us about slip-weakening fault friction laws?, Bull. Seismol. Soc. Am., 90, 98-116.
Haskell, N.A., (1964). Total energy spectral density of elastic wave radiation from propagation faults. Bull. Seis. Soc. Am. 54, 1811-1841.
Haskell, N.A., (1966). Total energy spectral density of elastic wave radiation from propagation faults, Part II. A statistical source model. Bull. Seis. Soc. Am. 56, 125-140.
Haskell, N.A., (1969). Elastic displacement in the near-field of a propagating fault. Bull. Seis. Soc. Am. 72, 1867-1879.
Kanamori H. and G. S. Stewart (1978), Seismological aspects of the Guatemala earthquake of February 4, 1976. *J. Geophys. Res*., **83**, 3427-3434.
Kausel, E., and J. Campos (1992), The Ms = 8 tensional earthquake of 9 December 1950 northern Chile and its relation to the seismic potential of the region, Phys. Earth Planet. Inter., 72, 220– 235.
Kawase, H. (2011). Strong motion characteristics and their damage impact to structures during the off pacific coast of Tohoku earthquake of March 11, 2011; How extraordinary was this M9.0 earthquake?. In proceeding, *4th IASPEI / IAEE International Symposium,* Santa Barbara, EEUU.
Keilis-Borok, V.I., (1959). On the estimation of the displacement in an earthquake source and of source dimensions. Annales de Geophysique, 12, 205-214.
Ida, Y (1972), Cohesive force across tip of a longitudinal-shear crack and Griffith specific surface-energy, *J. Geophys. Res*., **77**, 3796-3805.
Ishii**,** M., Shearer, P.M., Houston, H., & Vidale, J.E., 2005. Extent, duration and speed of the 2004 Sumatra-Andaman earthquake imaged by the Hi-Net-array. Nature 435 (7044), 933-936, doi10.1038/nature03675.
Lay, T., H. Kanamori, C. J. Ammon, M. Nettles, S. N. Ward, R. Aster, S. L. Beck, S. L. Bilek, M. R. Brudzinski, R. Butler, H. R. DeShon, G. Ekstrom, K. Satake, and S. Sipkin (2005). The great Sumatra-Andaman earthquake of 26 December 2004, *Science*, 308, 1127-1133
Madariaga, R., (1978). The dynamic field of Haskell's rectangular dislocation fault model. Bull. Seis. Soc. Am. 68, 869-887.
Madariaga, R. and K.B Olsen (2000), Criticality of Rupture Dynamics in 3-D, Pageoph, 157, 1981-2001.
Ohnaka, M., and Shen, L.F. (1999), Scaling of Rupture Process from Nucleation to Dynamic Propagation: Implications of Geometric Irregularity of the Rupturing Surfaces, J. Geophys. Res. 104, 817–844.
Okubo, P. (1989), Dynamic Rupture Modeling with Laboratory-deri6ed Constituti6e Relations, J. Geophys. Res. 94, 12,321–12,335
Peyrat, S. and K. B. Olsen (2004), Nonlinear dynamic rupture inversion of the 2000 Western Tottori, Japan, earthquake, Geophys. Res. Lett., 31, L05604, doi:10.1029/2003GL019058.
Peyrat S., J. Campos, J.B. de Chabalier, A. Perez, S. Bonvalot, M.-P. Bouin, D. Legrand, A. Nercessian, O. Charade, G. Patau, E. Clévédé, E. Kausel, P. Bernard, J.-P. Vilotte, (2006). The Tarapaca intermediate-depth earthquake (Mw 7.7, 2005, Northern Chile): A slab-pull event with

horizontal fault plane constrained from seismologic and geodetic observations, Geophysical Research Letters, 33, 2006GL027710.
Peyrat, S., R. Madariaga, E. Buforn, J. Campos, G. Asch, and J.P. Vilotte, 2010. Kinematic rupture process of the 2007 Tocopilla earthquake and its main aftershocks from teleseismic and strong motion data. Geophys. J. Int., 182, 1411-1430.
Piatanesi A., E. Tinti, M. Cocco and E. Fukuyama (2004), The dependence of traction evolution on the earthquake source time function adopted in kinematic rupture models, Geophys. Res. Lett., 31, L04609, doi:10.1029/2003GL019225
Ruiz, S and Madariaga, R. (2011). Determination of the friction law parameters of the Mw 6.7 Michilla earthquake in northern Chile by dynamic inversion. Geophys. Res. Lett., 38, L09317, doi:10.1029/2011GL047147
Ruiz, S. and Madariaga, R., (2012). Sismogénesis, proceso de ruptura y réplicas del mega terremoto del Maule 2010, Chile. Chapter 1 in book "Mw= 8.8, Terremoto en Chile, 27 de Febrero 2010" Departamento de Ingeniería Civil, Universidad de Chile. (In Spanish)
Ruiz, S and Saragoni, G.R., (2012). Implicaciones y nuevos desafíos de diseño sísmico de los acelerogramas del terremoto del 2010. Chapter 6 in book. "Mw =8.8, Terremoto en Chile, 27 de Febrero 2010". Universidad de Chile.
Tarantola, A., (2005). Inverse Problem Theory and Methods for Model Parameter Estimation. SIAM. ISBN 978-0-89871-572-9
Sambridge, M. (1999), Geophysical Inversion with a Neighbourhood Algorithm -I. Searching a parameter space, Geophys. J. Int., 138, 479-494.
Savage, J.C., 1966. Radiation from a realistic model of faulting. Bull. Seis. Soc. Am., 56, 577-592.
Saragoni, G. R., Astroza, M., and Ruiz, S. (2004) Comparative study of subduction earthquake ground motion of north, central and south America. 13th World Conference on Earthquake Engineering. Canada.
Simons, M., S. E. Minson, A. Sladen, F. Ortega, J. Jiang, S. E. Owen, L. Meng, J-P. Ampuero, S. Wei, R. Chu, D. V. Helmberger, H. Kanamori, E. Hetland, A. W. Moore, and F. H. Webb, (2011) The 2011 Magnitude 9.0 Tohoku-Oki Earthquake: Mosaicking The Megathrust From Seconds To Centuries, Science, 322, 1421.
Suzuki, W., Aoi, S., and Sekiguchi, H. (2009): Rupture Process of the 2008 Northern Iwate Intraslab Earthquake Derived from Strong-Motion Records, BSSA, 99-5, 2825–2835.
Vallée, M., and M. Bouchon (2004), Imaging coseismic rupture in far field by slip patches, Geophys. J. Int., 156, 615–630.
Vigny, Ch., A. Socquet, S. Peyrat, J.-C. Ruegg, M. Métois, R. Madariaga, S. Morvan, M. Lancieri, R. Lacassin, J. Campos, D. Carrizo, M. Bejar-Pizarro, S. Barrientos, R. Armijo, C. Aranda, M.-C. Valderas, I. Ortega, F. Bondoux, S. Baize, H. Lyon-Caen, A. Pavez, J. P. Vilotte, M. Bevis, B. Brooks, R. Smalley, H. Parra, J.-C. Baez, M. Blanco, S. Cimbaro, E. Kendrick, (2011) The 2010 Mw 8.8 Maule Mega-Thrust Earthquake of Central Chile, Monitored by GPS Science 331 1417-1421.

2. SIMULTANEOUS KINEMATIC INVERSION OF 2007 TOCOPILLA 2007, CHILE EARTHQUAKE USING STRONG MOTION AND cGPS

INTRODUCTION

On November 14, 2007 a Mw 7.8 earthquake occurred near the northern Chile city of Tocopilla; this earthquake broke the southern part of the tsunamigenic 1877 mega earthquake of 1877 of Mw ~ 8.5 (see Peyrat et al. (2010) and references herein). The Tocopilla 2007 earthquake ruptured the deepest part of the seismogenic zone of the plate contact between the Nazca and South American plates in Northern Chile (Delouis et al., 2009; Peyrat et al., 2010; Bejar-Pizarro et al., 2010; Motagh et al., 2010), Figure 2.1. In the last 100 years only two events of Mw>7 in 1967 and 2007 have occurred in the Tocopilla zone, both earthquakes had hypocenters at depths around ~ 40 km (Delouise et al., 2009; Peyrat et al., 2010; Malgrange and Madariaga, 1983). However only for the 2007 earthquake the seismic rupture can be studied in detail using seismic and geodetic data.

In the last 6-8 years seismic and geodetic data in northern Chile has significantly improved thanks to the IPOC (Integrated Plate boundary Observatory in Chile) and to CAnTO (Central Andean Tectonic Observatory) networks, Figure 2.3. The IPOC network produces continuous broad band and strong motion seismic data that was used to do an in-depth study of the Tocopilla earthquake and aftershocks (Lancieri et al., 2011, see Annex A; Lancieri et al., 2012 and Fuenzalida et al., 2012), specifically in Lancieri et al. (2011) a robust data base was made to study an early warning system for the subduction earthquakes of Northern Chile. Continuous GPS data from the CAnTO network can be used to make kinematic inversions of main-shock (Minson, 2010). Finally, after the main Tocopilla shock, short period instruments were installed by the GFZ German Task Force (Sobiesiak et al., 2008), that provided precise re-localization of the aftershocks of this event (Fuenzalida et al., 2012), Figure 2.4.

Several slip distributions for the Tocopilla earthquake have been proposed from the inversion of different data sets: Delouis et al. (2009) used teleseismic waveforms and low-pass filtered strong motion data; Peyrat et al. (2010) used teleseismic data and strong motion data; Bejar-Pizarro et al. (2010) used GPS and InSar data, Motagh et al. (2010) only InSar data and Minson (2010) only cGPS data. In this chapter we make a kinematic inversion jointly using strong motion data and cGPS using the elliptical patch approach of Vallée and Bouchon (2004) and the Neighborhood algorithm (Sambridge, 1999) to find the best solution. We will use non-linear dynamic inversion of strong motion and geodetic data to validate previous works on the Tocopilla earthquake and to test the joint use of different type of data (cGPS and strong motion).

AVAILABLE DATA AND THIER PROCESSING

The Tocopilla earthquake and its aftershocks were well recorded on seismological global networks as well as by several recently installed digital accelerometric networks. IPOC is a permanent seismological network of 12 stations (Fig. 2.3) installed in Northern Chile starting in 2006. Most of the seismological stations are composed of STS-2 broadband seismometers, GMG-5 accelerometers for the French stations and Episensor FBA ES-T for the German stations, continuously recording at 100 Hz with 24 bit Q330 digitizers and SeiscomPC (http://geofon.gfz-potsdam.de/geofon/seiscomp). We also used the strong-motion data recorded by a permanent digital strong motion network operated jointly by the University of Chile, Swiss and German institutions (Boroschek *et al.* 2008). These instruments are triggered so that only the main-shock was recorded by all the stations, and only the strongest aftershocks were recorded at some of them. At the end of November 2007 a temporary seismic network was deployed in the focal area by the German Task Force of GFZ (Sobiesiak *et al.* 2008), in collaboration with IPGP and ENS in France, and DGF in Chile. The network was composed of 20 short period, 4 broadband and 10 strong motion stations and has been used mainly to do precise relocalization of aftershocks (Fuenzalida et al., 2012).

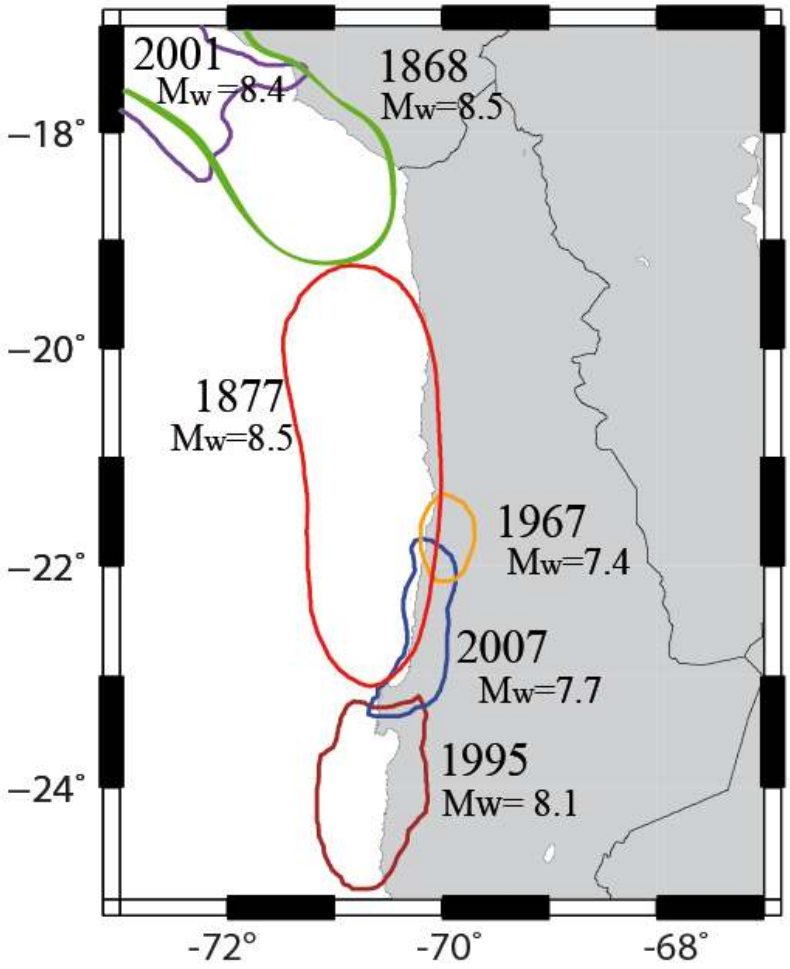

Figure 2.1. Schematic rupture areas of Northern Chile and Southern Peru earthquakes.

Together with these seismic data we used continuous GPS data sampled at 5 Hz from the CAnTO (Central Andean Tectonic Observatory) network deployed by CALTECH. Figure 2.5 shows the records used to make the kinematic inversion. The strong motion data are baseline corrected and filtered using a band-pass causal Butterworth filter of order 2 between 0.02 to 0.1 Hz, and then integrated once. The cGPS data were filtered using the same filter as strong motion records and derived numerically once to compute ground velocity. The synthetic records were filtered using same kind of filter.

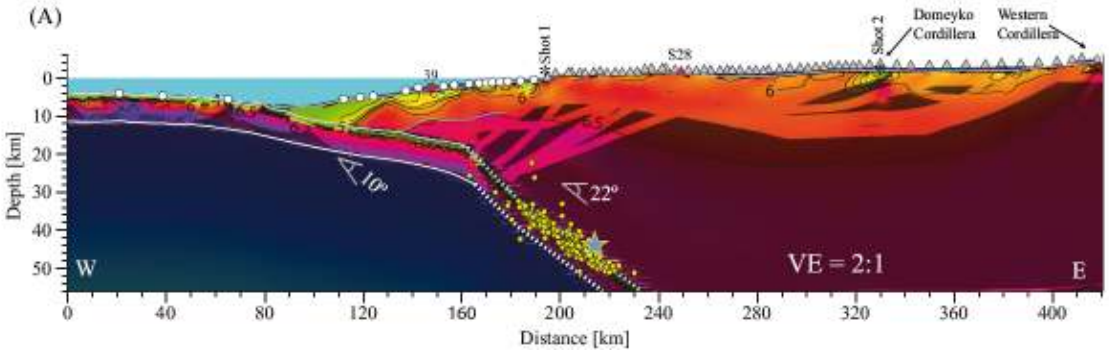

Figure 2.2. Seismic velocity structure and Tocopilla aftershock relocalization (Fuenzalida et al., 2012) at 22°S. (Contreras-Reyes et al., 2012).

(a) **(b)**

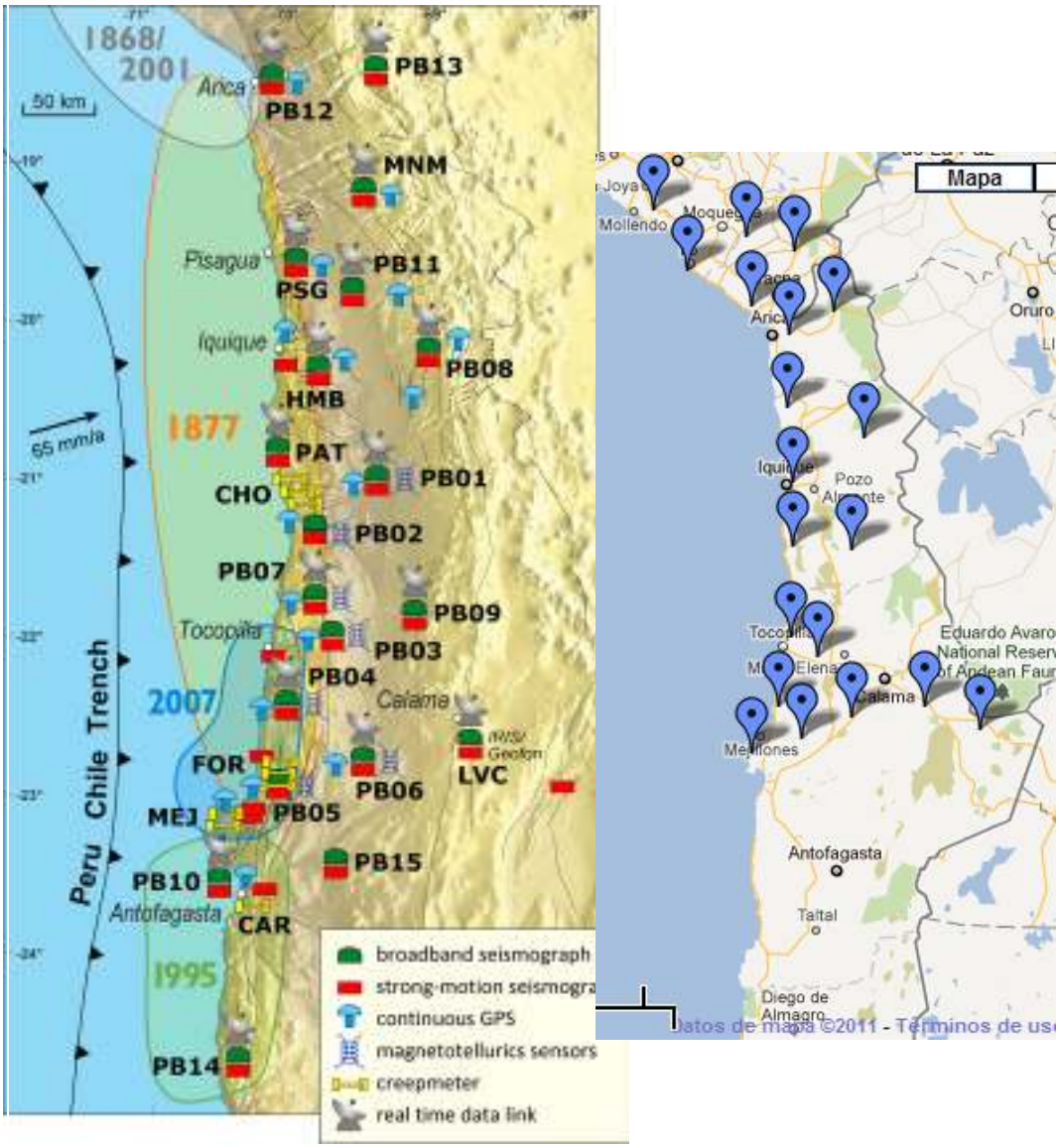

Figure 2.3. (a) Distribution of monitoring equipment in northern Chile IPOC project (www.ipoc-network.org) (b) Distribution cGPS stations CAnTO project (http://www.tectonics.caltech.edu/resources/kmlandes.html).

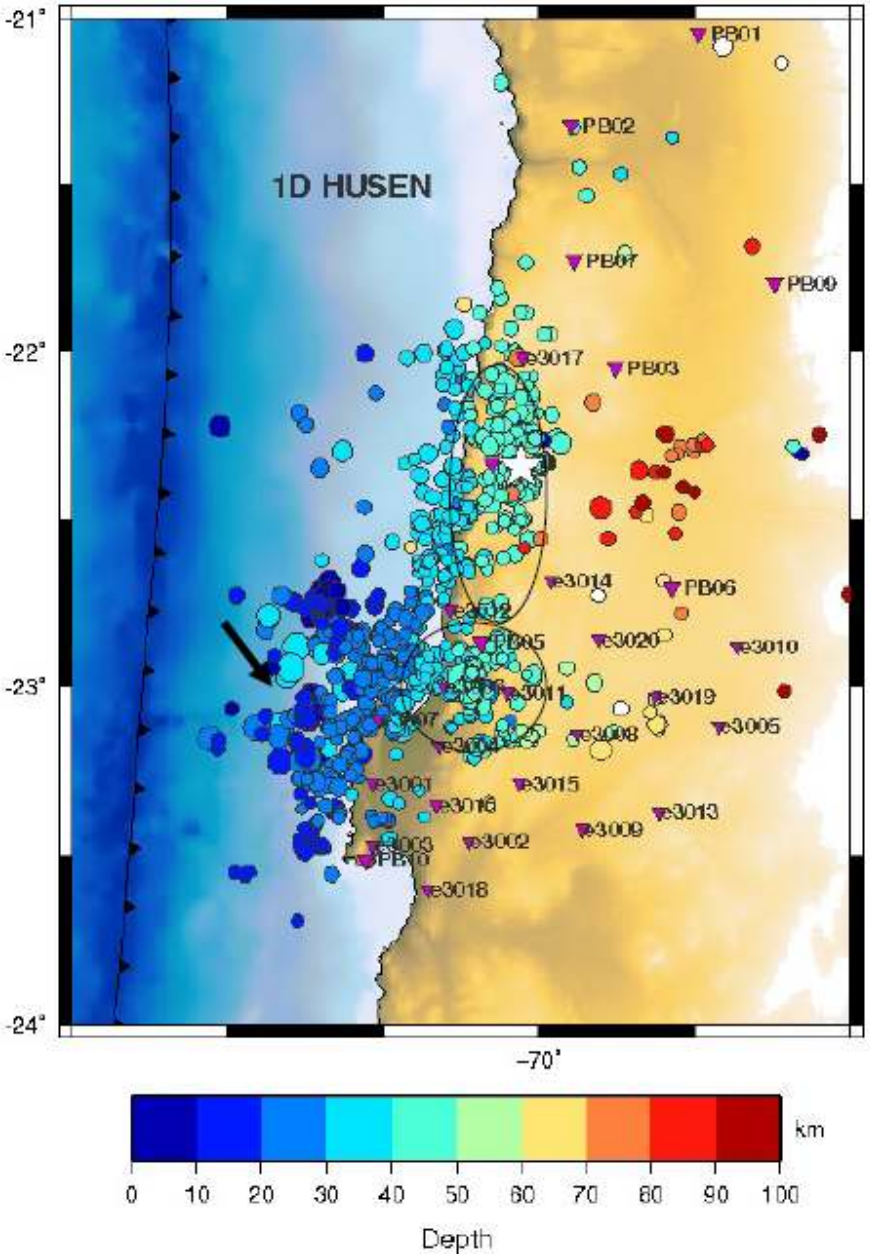

Figure 2.4. Aftershock of Tocopilla 2007 earthquake, relocalization of 14 November to 17 December by Fuenzalida et al. (2012).

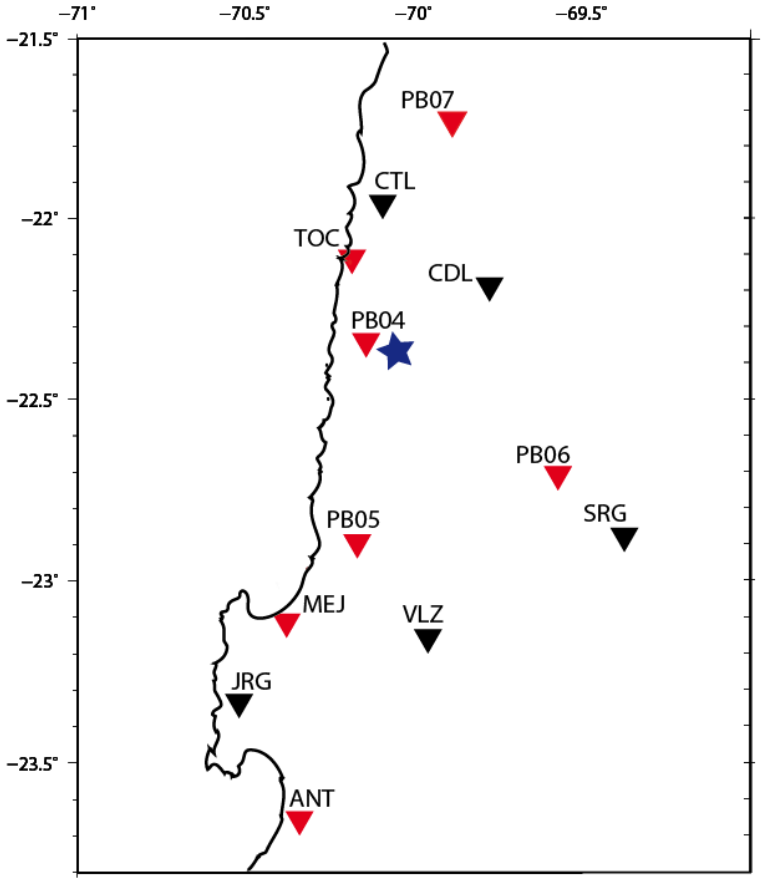

Figure 2.5. Inverted triangles location of SM and cGPS stations used in this thesis. Red are SM and Black are cGPS. The star indicates the Tocopilla 2007 epicenter.

KINEMATIC INVERSION OF THE 2007 TOCOPILLA EARTHQUAKE

We inverted the band-pass filtered ground velocity records using an elliptical patch approximation, because we think that this approximation is adequate for situations like that of the Tocopilla 2007 earthquake, where the seismic stations are located roughly 50 km apart and the velocity structure is not known in enough detail. Elliptical patch parameterization was introduced by Vallé and Bouchon (2004) to model far-field waveforms for teleseismic events. The application of the method to near-field strong-motion kinematic inversion and its resolution was discussed in additional detail by Di Carli et al. (2010). This parameterization has the advantage that it produces an image of the source made of asperity-like patches. We inverted the cGPS and SM data using two

elliptical patches assuming that the slip distribution D measured from the center of the ellipse has the Gaussian distribution:

$$D(x,y) = D_m e^{-\left(\frac{x^2}{a^2}+\frac{y^2}{b^2}\right)} \quad (1)$$

where D_m is the maximum amplitude in the elliptical patch of semiaxes a and b. The slip distribution is continuous but concentrated inside the ellipse. In every patch, rupture speed was assumed to be constant and the time of rupture tr was computed with respect to distance from the hypocenter in order to insure causality in the forward models. Slip rate on every patch was also very simple. The source time function at any point on the fault was a triangular function of total duration t = 4 s around the rupture time tr. In the forward model, each elliptical patch is described by 7 parameters: two coordinates of the center, two semiaxes a and b, an angle of orientation α, slip amplitude D_m and rupture speed v_r, Figure 2.6. The AXITRA code (Coutant, 1990; Bouchon,1981) was used to simulate wave propagation from the source to the receivers. The fit between observed (*obs*) and synthetic (*synth*) records was measured with the L2 norm:

$$\chi^2 = \frac{\sum_i (obs_i - synth_i)^2}{\sum_i (obs_i)^2} \quad (2)$$

where the index i runs over all samples in every seismogram considered in the inversion. The neighborhood algorithm (NA) of Sambridge (1999) was chosen to search for the minimum value of the L2 norm.

SLIP DISTRIBUTION OF TOCOPILLA 2007 EARTHQUAKE

Figure 2.7 shows the slip distribution results and Figure 2.8 the rupture time isochrones for the best solution found by the NA algorithm. This solution has a misfit χ^2 = 0.52. We modeled the earthquake with two elliptical patches which confirm the deep rupture earthquake, the northern patch had a maximum slip of 1.52 m and 1.38 m for the southern one. Rupture velocity was assumed to be sub-shear for both patches, we found a rupture velocity of 2.63 km/s in the northern patch and 2.82 km/s in the southern one. Figure 2.9 shows the fit between observed and synthetic ground velocity derived from high-rate cGPS and strong motion data.

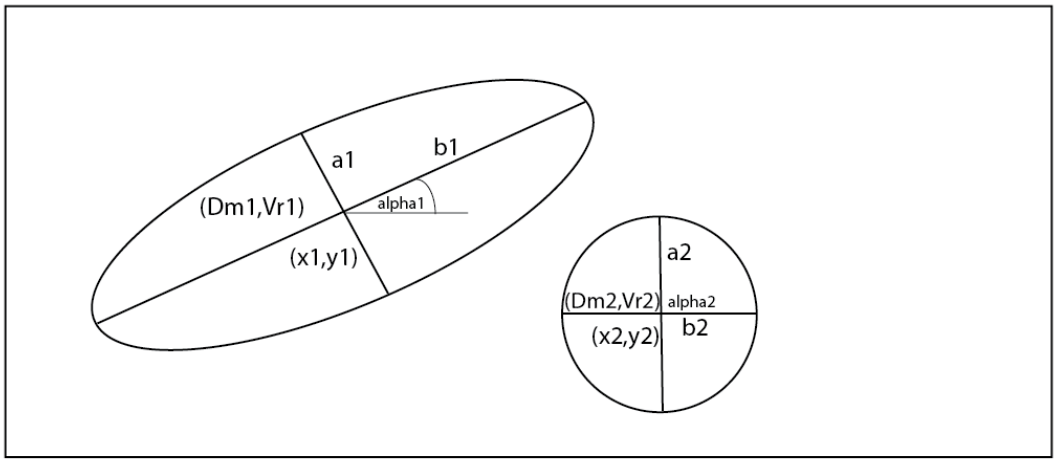

Figure 2.6. Schematic interpretation of two elliptical patches and the 14 inverted parameters.

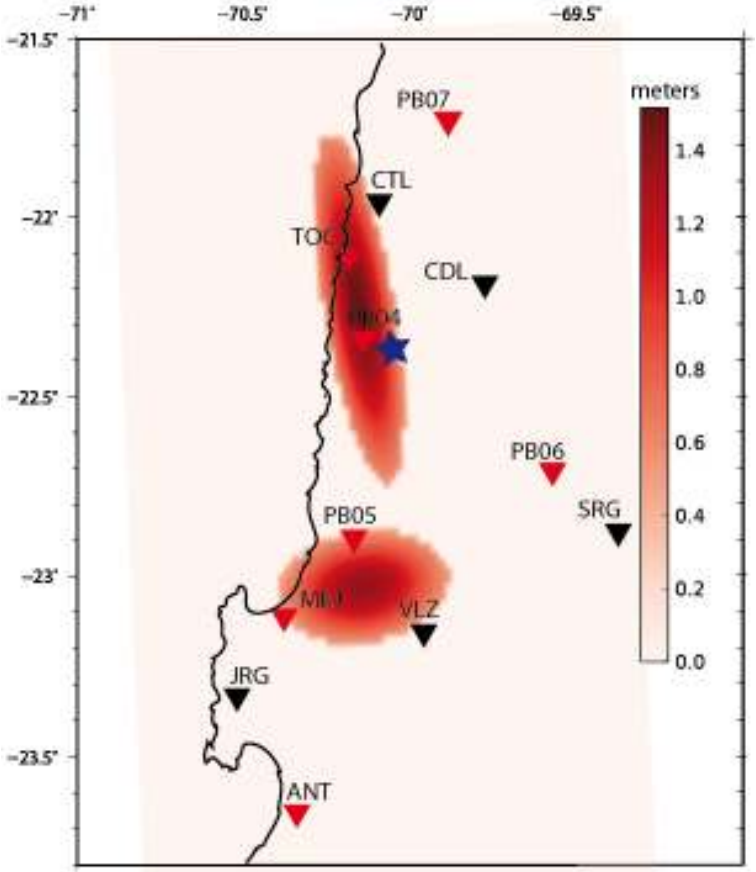

Figure 2.7. Slip distribution of Tocopilla 2007 earthquake. The star is the epicenter of Tocopilla. Inverted triangles location of SM and cGPS, red are SM and Black are cGPS.

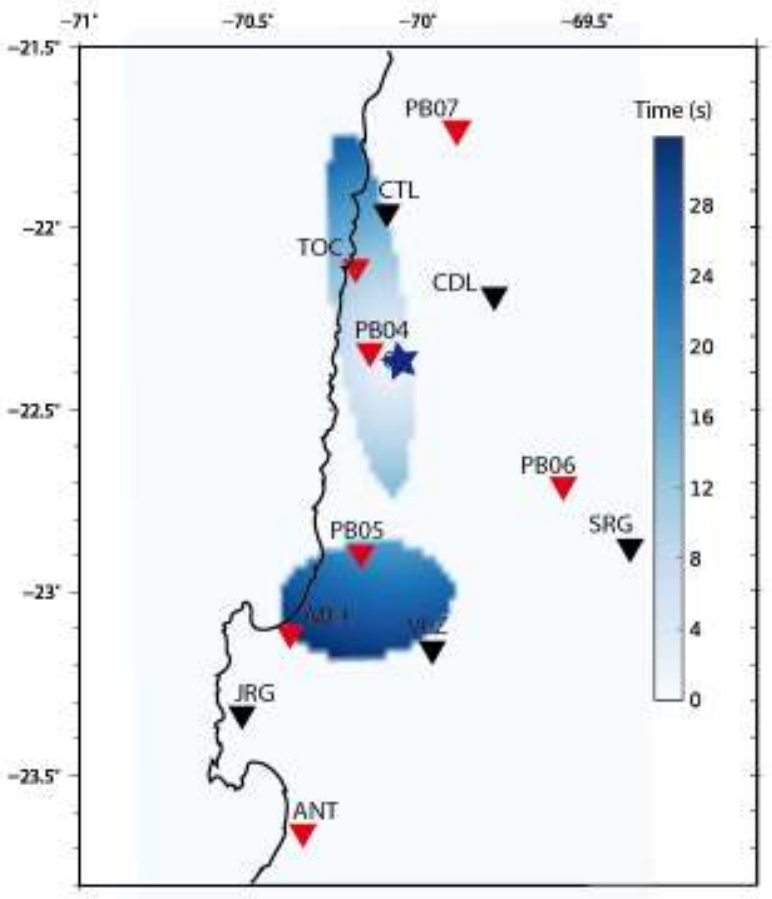

Figure 2.8. Rupture time of Tocopilla 2007 earthquake. The star is the epicenter of Tocopilla. Inverted triangles location of SM and cGPS, red are SM and Black are cGPS.

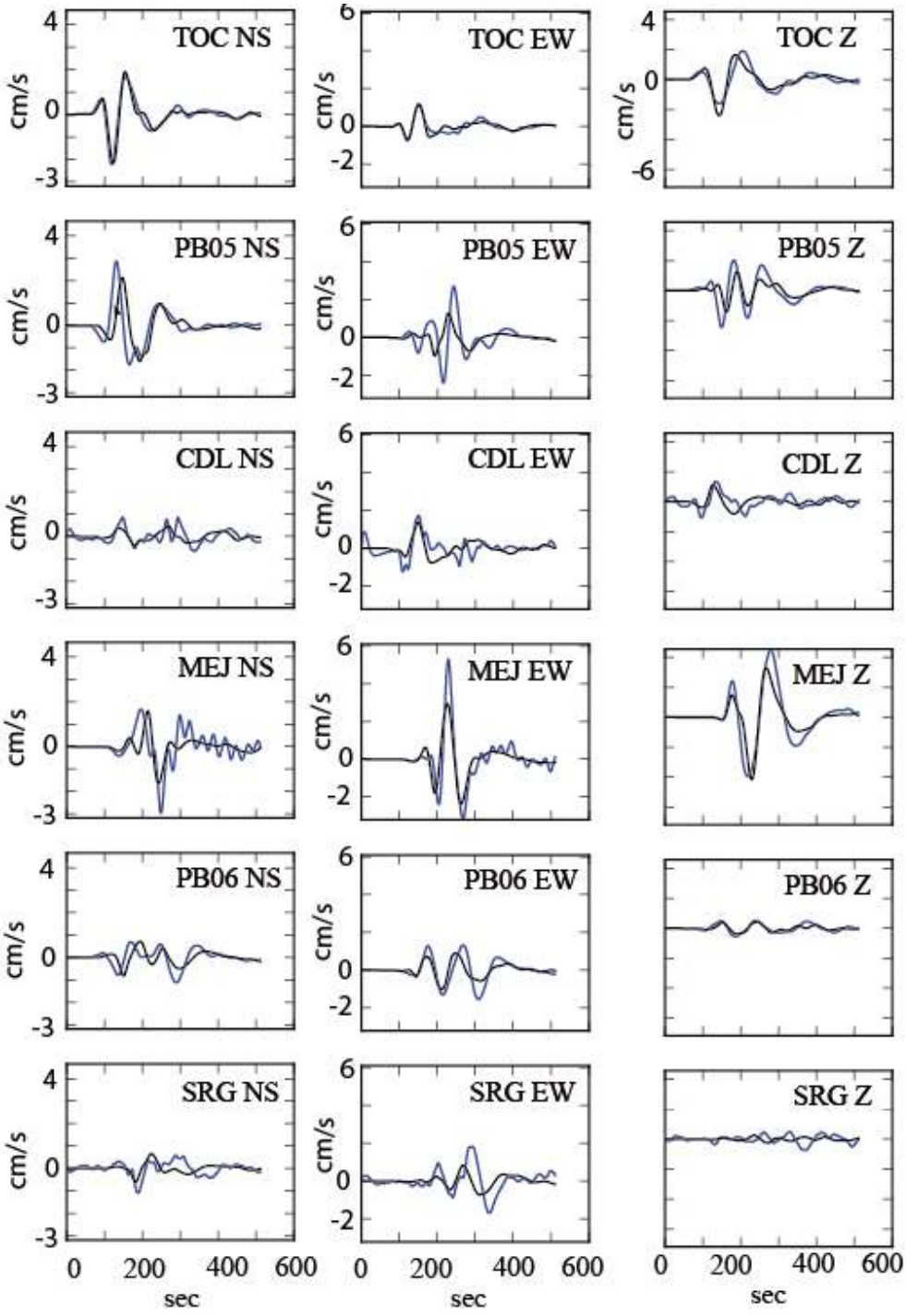

Figure 2.9. (continue)

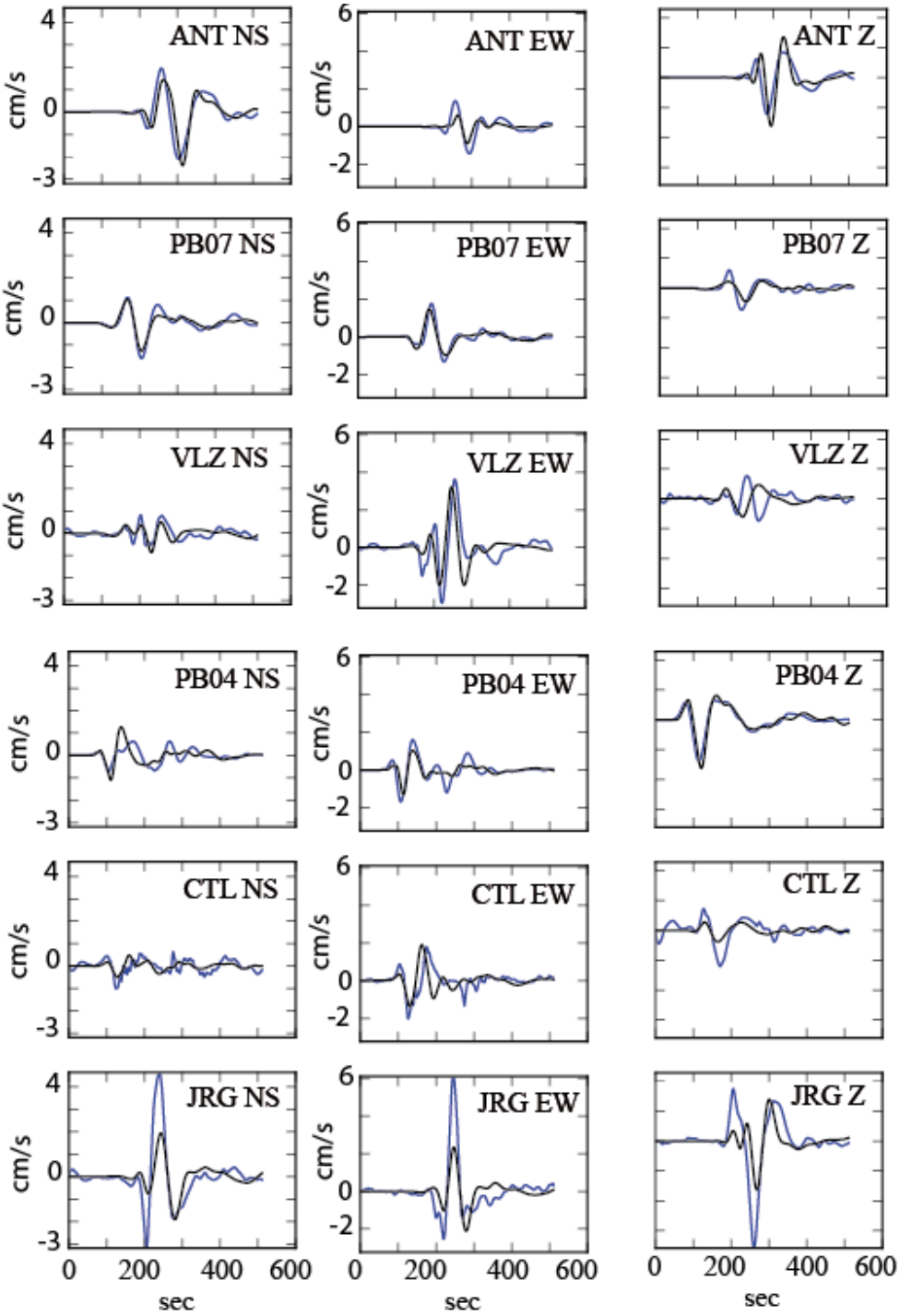

Figure 2.9. Comparison of real data (blue) and synthetic data (black). For the best NA result.

DISCUSSION

The Tocopilla 2007 earthquake ruptured two patches of ~ 25 to 50 km depth (Figure 2.10) confirming that this event broke the bottom of the seismogenic zone in Northern Chile. The Tocopilla 2007 earthquake released only a fraction of elastic strain accumulated in this area since the great 1877 earthquake, assuming that this large earthquake broke both the shallow and deeper contact zones. It is clear that the 1877 earthquake broke the shallow part because of the large tsunami that it generated. It is however not clear whether the deeper part of the seismogenic zone was broken. Riquelme et al. (2012) claimed that is possible that the deeper part of the contact zone only breaks during smaller earthquakes like the earthquakes of 2007 and 1967 with magnitudes less than Mw ~ 8.0.

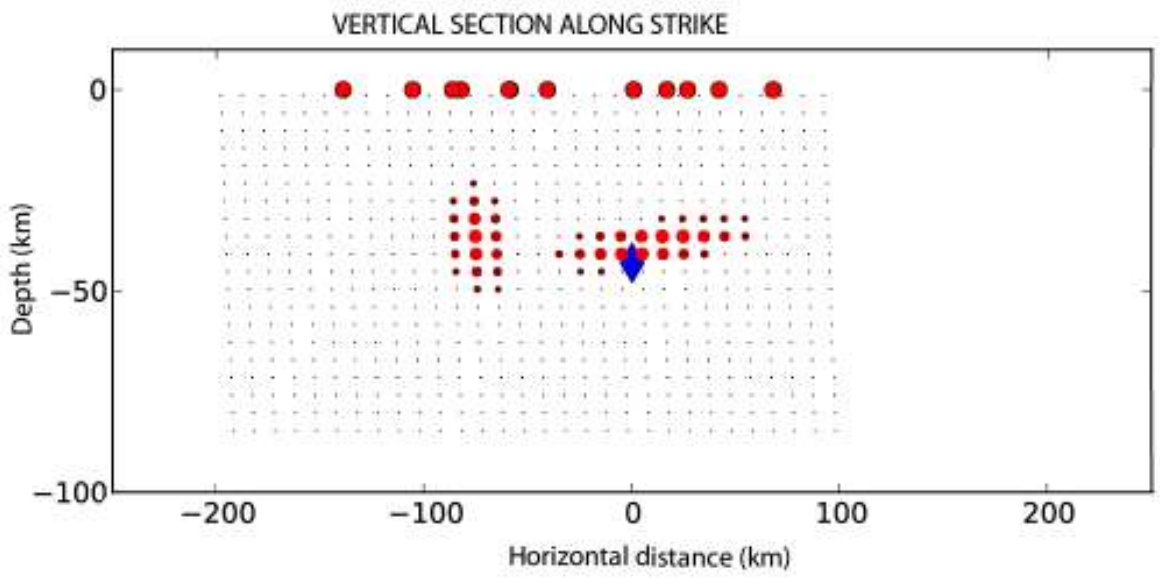

Figure 2.10. Vertical section along strike, the slip distribution is located around 25 to 50 km.

The Tocopilla earthquake is the first Chilean event that is clearly shown to have broken the deep seismogenic zone. The occurrence of earthquakes with magnitude M ~ 8.0 in the deeper part of the subduction zone is an important issue for the study of future seismic hazard. Similar observations have been reported for the bending subducting plate in Japan (Ito et al.,2005) with similar distribution of earthquakes (Lay et al., 2012).

The slip distribution of the Tocopilla earthquake is similar to that of other magnitude M ~ 8.0 Chilean earthquakes, like Valparaiso 1985 Mw 8.0 (Ruiz et al., 2011 see Annex C). However, due the lack of good quality near field instruments that recorded Valparaiso 1985, it is not possible to confirm whether the 1985 earthquake broke only the deeper part of seismogenic contact. The precise location of all M ~ 8.0 Chilean subduction earthquakes is necessary to understand its role in the accumulation of slip inside the seismic gaps.

CONCLUSIONS

The joint inversion of Tocopilla 2007 earthquake using strong motion and cGPS data is possible in the frequency range between 0.01 to 0.1 Hz. The kinematic inversion confirms that this earthquake is characterized by a sub-shear rupture with two main zone of larger slip. The slip distribution is confined at 35 to 50 km depth. This result confirms the previous works by Delouis et al. (2009); Peyrat et al. (2010) and Bejar et al (2010).

REFERENCE

Bejar-Pizzaro M., Carrizo D., Socquet A., Armijo R., S. Barrientos, F. Bondoux, S. Bonvalot, J. Campos, D. Comte, J. B. de Chabalier, O. Charade, A. Delorme, G. Gabalda, J. Galetzka, J. Genrich, A. Nercessian, M. Olcay, F. Ortega, I. Ortega, D. Remy, J. C.Ruegg, M. Simons, C. Valderas and C. Vigny (2010). Asperities, barriers and transition zone in the North Chile seismic gap: State of the art after the 2007 Mw 7.7 Tocopilla earthquake inferred by GPS and InSAR data, Geoph. Journ. Int., GJI-S-09-0648.

Boroschek, R., Comte, D., Soto, P. and Leon, R., (2008). Terremoto Norte Chile 14 de Noviembre de 2007 M =7.7, Informe preliminar N°4. Departamento Ingenieria Civil, Universidad de Chile. http://www.renadic.cl/red_archivos/Informe_20071114Ing_Civil_UCh_Inf_4_v1.pdf

Bouchon, M. (1981), A simple method to calculate Green's functions for elastic layered media, Bull. Seismol. Soc. Am., 71, 959–971.

Chlieh, M., H. Perfettini, H. Tavera, J.-P. Avouac, D. Remy, J.-M. Nocquet, F. Rolandone, F. Bondoux, G. Gabalda, and S. Bonvalot (2011), Interseismic coupling and seismic potential along the Central Andes subduction zone, *J. Geophys. Res.*, 116, B12405, doi:10.1029/2010JB008166.

Contreras-Reyes, E., Jara, J., Grevemeyer, I., Ruiz, S. and Carrizo, D., (2012) Abrupt subducting plate dip change governs megathurst and upper plate seismicity in North Chile. Submitted to *Nature Geoscience*.

Coutant, O. (1990), Programme de simulation numerique AXITRA, Rapport LGIT, Univ. Joseph Fourier, Grenoble, France.

Delouis, B., Pardo, M., Legrand, D., & Monfret, T. (2009). The M-w 7.7 Tocopilla Earthquake of 14 November 2007 at the southern edge of the northern Chile seismic gap: Rupture in the deep part of the coupled plate interface. Bulletin of the Seismological Society of America, 99(1), 87-94.

Fuenzalida, A., Schurr, B., Lancieri,M. and Madariaga, R. (2012). High-resolution relocalitions and mechanisms of aftershocks of the 2007 Tocopilla (Chile) earthquake. In preparation.
Ito, A., G. Fujie, S. Miura, S. Kodaira, Y. Kaneda, and R. Hino (2005), Bending of the subducting oceanic plate and its implication for rupture propagation of large interplate earthquakes off Miyagi, Japan, in the Japan Trench subduction zone, *Geophys. Res. Lett.*, 32, L05310, doi:10.1029/2004GL022307.
Malgrange, M. and R. Madariaga, Complex distribution of large thrust and normal fault earthquakes in the Chilean subduction zone. Geophys. J. R. Astr. Soc., **73**, 489-506, 1983.
Peyrat, S., R. Madariaga, E. Buforn, J. Campos, G. Asch, and J.P. Vilotte, 2010. Kinematic rupture process of the 2007 Tocopilla earthquake and its main aftershocks from teleseismic and strong motion data. Geophys. J. Int., 182, 1411-1430.
Lancieri, M., A. Fuenzalida, S. Ruiz and R. Madariaga, Magnitude scaling of early-warning parameters for the Mw 7.8 Tocopilla, Chile, earthquake and its aftershocks *Bull. Seismol. Soc. Am,* 101, 447 - 463, 2011
Lay, T., H. Kanamori, C. J. Ammon, K. D. Koper, A. R. Hutko, L. Ye, H. Yue, and T. M. Rushing (2012), Depth-varying rupture properties of subduction zone megathrust faults, J. Geophys. Res., doi:10.1029/2011JB009133, in press.
Minson, S., (2010). A Bayesian Approach to Earthquake Source Studies. Thesis for the Degree of Doctor of Philosophy, California Institute of Technology Pasadena, California, EEUU.
Motagh, M.; Schurr, B.; Anderssohn, J.; Cailleau, B.; Walter, T. R.; Wang, R.; Villotte, J. P. (2010): Subduction earthquake deformation associated with 14 November 2007, Mw 7.8 Tocopilla earthquake in Chile: Results from InSAR and aftershocks. Tectonophysics, 490, 1-2, 66-68.
Riquelme, S., Ruiz, S., Yamazaki, Y. and Campos, J. (2012). Fault Parameters of the 1868 and 1877 earthquakes, inferred from historical records: Run-up measurements, Isoseismals and coseismic deformation. EGU, Vienna.
Sambridge, M. (1999), Geophysical Inversion with a Neighbourhood Algorithm -I. Searching a parameter space, Geophys. J. Int., 138, 479-494.
Sobiesiak and the Task Force Team (2008). Post seismic Task Force operation after the Mw 7.8 Tocopilla earthquake in Northern Chile. EGU meeting. Vol. 10, EGU2008-A-09928.
Vallée, M., and M. Bouchon (2004), Imaging coseismic rupture in far field by slip patches, Geophys. J. Int., 156, 615–630.

3 SHORT PERIOD RUPTURE PROCESS OF THE 2010 MW 8.8 MAULE EARTHQUAKE IN CHILE

Paper accepted in Earthquake Spectra

Authors:

Sergio Ruiz, Raúl Madariaga, Maximiliano Astroza, G. Rodolfo Saragoni, María Lancieri , Christophe Vigny and Jaime Campos

ABSTRACT

The 2010 Maule earthquake is one of the largest events ever recorded with modern instruments. We used the cGPS records to invert for the kinematic rupture process using an elliptical sub patch approximation. The largest slip is found in the Northern part of the rupture zone in agreement with previous inversions. By cross-correlating signals from cGPS and strong motion records (SM) located in the northern part of the rupture zone we identified two distinct seismic pulses. Using the arrival time of these pulses we propose a short period (<20s) rupture process, the zone where pulses are generated agree with the areas with highest seismic slip and maximum observed intensity. The comparison with SM of the 1985 Mw=8 Valparaiso earthquake show that spectral contents and duration of the records is very similar. Thus, at least in the northern part, the Maule earthquake radiated high frequency waves like a Mw=8 earthquake.

INTRODUCTION

The Mw 8.8 Maule earthquake occurred in central Chile on 27 February 2010. With a rupture zone of about 500 km by 140 km this is the largest event ever recorded instrumentally in Chile (no strong motion instruments recorded the May 23, 1960 event). The Maule earthquake has been studied by many authors (e. g. Madariaga et al, 2010; Delouis et al., 2010; Lay et al., 2010; Moreno et al, 2011; Tong et al., 2011; Lorito et al., 2011; Vigny et al., 2011, Pollitz et al., 2011, Pulido et al., 2011; among others) using a combination of low frequency data like interferometry (> days), static GPS (>1000 sec), tsunami waveforms; and far field broad-band seismograms (>100

sec). These studies provide a coherent picture of the long period features, although these data can not resolve whether rupture extended all the way to the trench or was limited to the part of the plate interface.

The Maule mega earthquake ruptured a large segment of Central Chile that covers not only the gap left by the 1835 Darwin earthquake estimated as Mw 8.3 (see Campos et al, 2002), but also the rupture zones of at least two large events of last century: the 1928 Talca earthquake of Mw 7.7, and the 21 May 1960 Concepcion earthquake of Mw 8.2. Although we lack data constraining the Southern end of the rupture zone, the Maule earthquake definitely ruptured the source area of the Arauco 1975 earthquake of Mw 7.8 and may have partly ruptured the rupture zone of the Valdivia earthquake of 22 May 1960 of Mw 9.5. In the north, rupture stopped near the southern end of the Valparaiso earthquakes of 3 March 1985, Mw 8.0, and the Valparaiso mega earthquake of 17 August 1906, Mw 8.5. These events are depicted in Figure 3.1 where the rupture zones are those proposed by Campos et al, (2002). Magnitudes of the 20th century events are those estimated by Engdahl and Villaseñor (2002).

In spite of the large magnitude of the Maule earthquake, its maximum seismic intensity of IX was observed on low-rise rigid building of the city of Constitucion (Ruiz and Astroza, 2012; Astroza et al., 2012). Low intensity in rigid structures seem to be a characteristic of other large Chilean earthquakes such as those of Valparaíso 1985 (EERI, 1986) and Valdivia 1960 (Housner, 1963). Before the 2010 Maule earthquake the only good quality strong motion data available in south-central Chile were those recorded during the 1985 Valparaiso earthquake (Comte et al, 1986, EERI, 1986). The Valparaiso earthquake produced three main short period waves or pulses that were identified in the strong motion data by Ruiz et al. (2011). These pulses were characterized by low displacement amplitudes; for this reason Ruiz et al. (2011) proposed that the good behavior of short period structures during the Valparaiso earthquake. These singular aspects are not well resolved by seismological studied for the limited seismological works at short period waves.

Kiser and Ishii (2011) and Wang and Mori (2011) studied short period waves observed in dense seismograph arrays of Japan and the United States using a back projection technique. They proposed a different high frequency behavior between the regions north and south of 35.5°S. A more detailed study of short period waves in the near field is necessary to understand the generation of high frequency waves by the Maule earthquake. In the present paper, we invert cGPS recordings of intermediate frequency waves using a kinematic inversion method based on elliptical sub-source approximation (Vallé and Bouchon, 2004; DiCarli et al., 2010). Then we compare these results with the short period waves observed in strong motion data (SM). We will use these observations in an attempt to propose a model for the origin of short period rupture radiated by the Maule earthquake, which could be useful to understand the moderate observed damage in rigid structures like adobe and masonry houses. Interestingly, some strong motion instruments recorded both the Maule 2010 and Central Chile 1985 at the same place. We can thus compare the recordings of a mega thrust event like Maule 2010 with those of a regular Mw ~8 earthquake like that of Valparaiso 1985. The comparison of these strong motion data allows us to understand the differences, and similarities, between M~8.0 and M~9.0 subduction events.

LONG PERIOD AND SHORT PERIOD HYPOCENTERS

Several different hypocenters have been proposed for the Maule 2010 earthquake by different agencies and authors, some of which are listed in Table 3.1. It is crucial for the successful modeling of near field data to determine the hypocenter accurately. The main reason for the discrepancies in location is that near source data were not available for several months after the event. In the following we will use as high frequency hypocenter the location determined by the National Seismological Service of University of Chile (SSN) since they used all the short period seismological stations that recorded the earthquake in Chile. Independently, Vigny et al (2011) relocated the earthquake using arrival times at the high-rate GPS sites located near the earthquake. They located epicenter is located about 10 km south-east of that of SSN in a region where several foreshocks occurred in December 2009 and January 2010

(Madariaga et al., 2010). In our study we will use the low frequency hypocenter of Vigny et al. (2011) to invert cGPS data and the SSN hypocenter for the modeling the short period seismic waves. Figure 3.2 shows an example of S waves in Constitucion by the CONS high-rate GPS receiver and the CONS strong motion instrument. Since the strong motion instrument did not record the real time, we cross-correlated the records and shifted the strong motion. The S waves in the strong motion record appear from 8-10 before the large S-wave in the high-rate GPS record. We did not use the hypocenters proposed by USGS because of the possible bias introduced by the use of far field stations situated mostly to the north-east of the hypocenter.

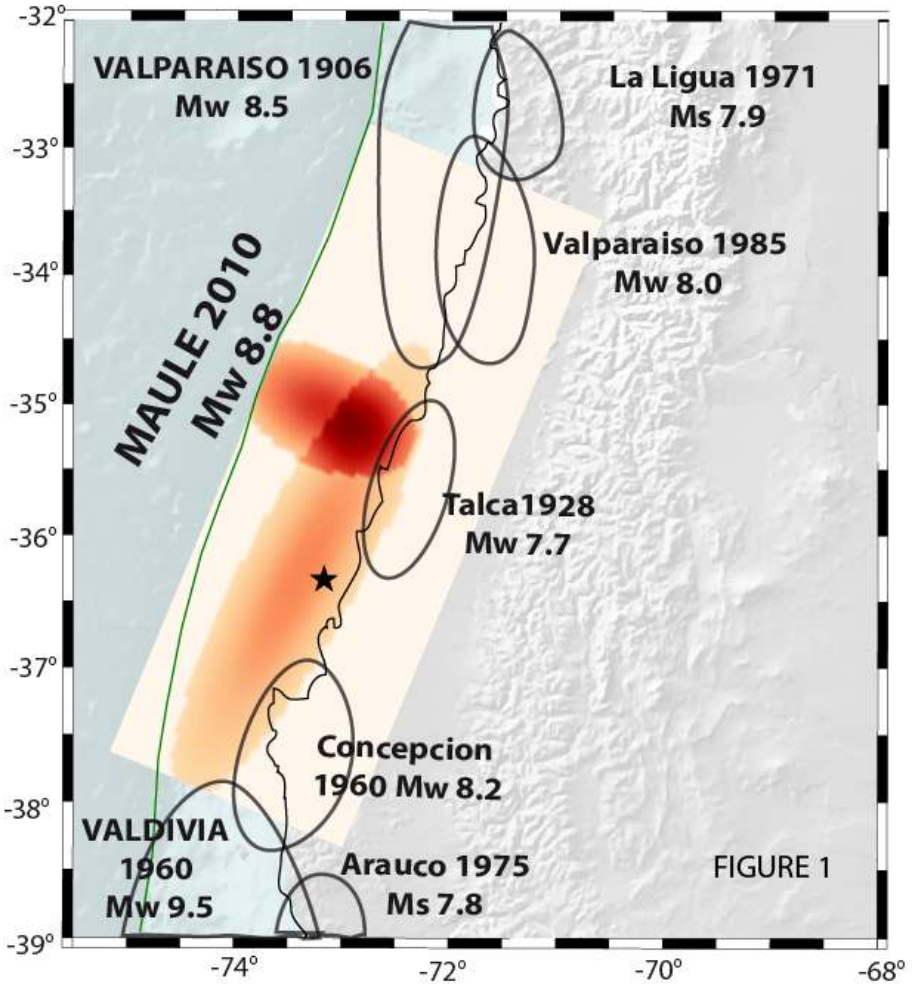

Figure 3.1. Rupture zone of the 2010 Maule earthquake and previous 20th century events of magnitude close to 8. The star shows the low frequency epicenter of the Maule 2010 earthquake, the orange elliptical zones are the results of intermediate frequency inversion of the Maule 2010

earthquake. Rupture zones of 20th century earthquakes proposed by Campos et al (2002) are shown in black. The magnitudes of these events are from Engdahl and Villaseñor (2002). The Concepcion earthquake of 21 May 1960 Mw 8.2 is a separate event from the 22 May 1960 mega earthquake.

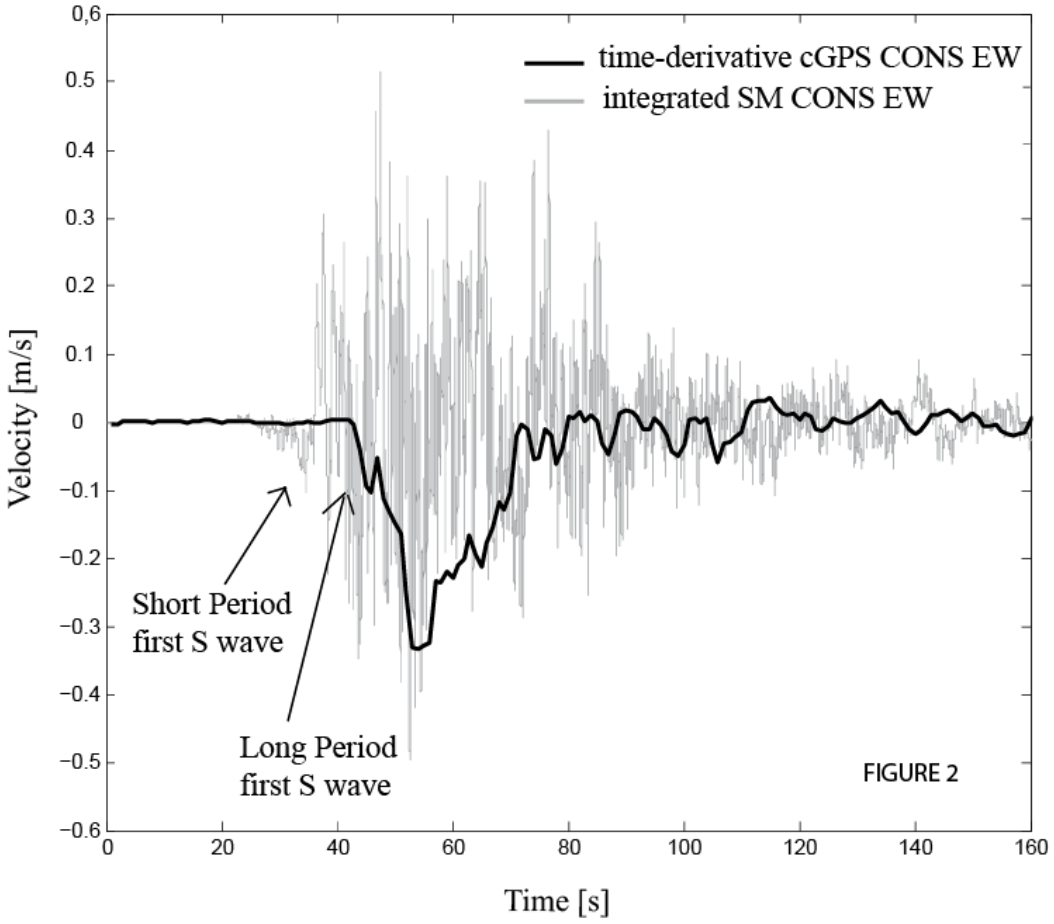

Figure 3.2. Ground velocity record at station CONS (Constitucion) obtained from the time-derivative of the high rate GPS record shown in black compared to the ground velocity integrated from the strong motion record at CONS. We observe a clear difference of 8-10 seconds between the high and low frequency first S wave arrivals. The cGPS time was corrected by UT + 14 leap seconds.

KINEMATIC INVERSION USING HIGH RATE CGPS DATA

The Maule 2010 earthquake was the first mega-earthquake recorded at short epicentral distances by high-rate GPS instruments at 1 Hz sampling rate (Vigny et al., 2011) (see Table 3.2) . A band passed-version of the ground displacement records obtained

for the central Chile cGPS stations were used by Delouis et al (2010) in a first inversion of the Maule event. Vigny et al (2011) modeled the displacement records for stations in Central Chile and Western Argentina using the slip distribution they determined from static GPS and inSAR interferometric data. They found excellent fit to the observed records, but high rate GPS records were dominated by near field static displacements so that they could not be used to determine higher frequency details of the rupture process. In order to get intermediate frequency information from the high-rate GPS records we computed ground velocity by time derivation and filtering. In Figure 3.3 we show the processing of the Constitucion (CONS) and Concepcion (CONZ) GPS records. The original displacement record is shown on top, the raw velocity in the central panel and the filtered trace from 0.005 to 0.05 Hz at the bottom. The raw ground velocity record observed at CONS is very similar to a Yoffe rupture pulse (Yoffe, 1951) with a total duration of only 25 s. The peak observed near 50 s (Figure 3.3b) is associated with the passage of the rupture front about 35 km below the station at Constitucion; and the healing at 75 s is probably due to stopping phases emitted from the sides of the crack, although we can not exclude a self-healing rupture. In any case, the duration of slip rate is about 30 s which is significantly shorter than the total duration of the earthquake (about 90 s). The record at CONZ also has duration of 30 s but it does not resemble a Yoffe pulse; a possible explanation is that rupture did not propagate right below the station. It must be remarked however that the CONZ record has a glitch a few seconds after the arrival of strong S-waves (Vigny et al, 2011). At lower frequencies (fig 3.4c) the two records are very similar, although CONS is 30 % larger than CONZ. Since we are interested in higher frequencies we decided to use ground velocity records obtained by band pass limited time-derivatives of the high-rate GPS records. The records were filtered using a bandpass Butterworth causal filter between 200 and 20 s (0.005 and 0.05 Hz) see Figure 3.3c.

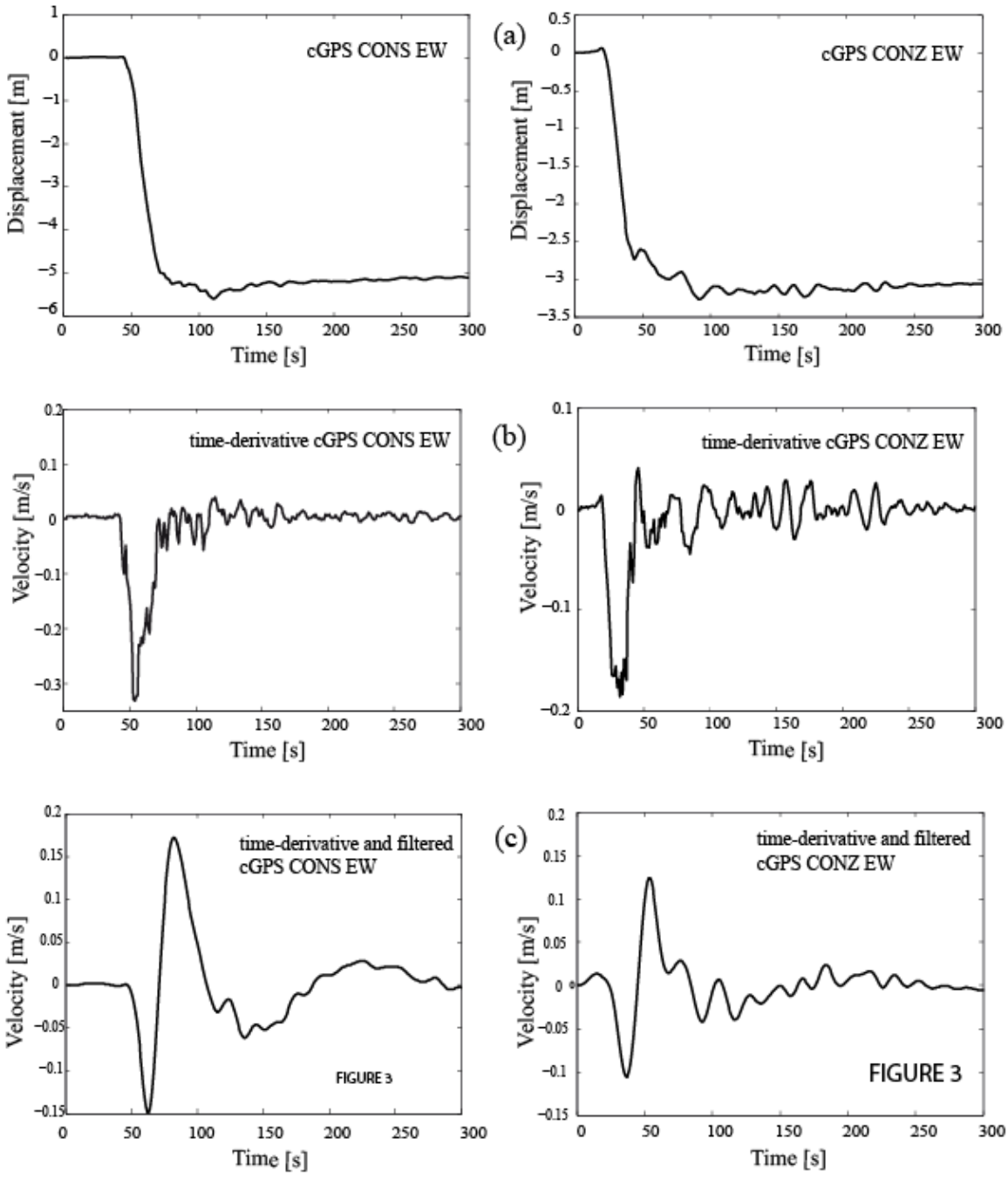

Figure 3.3 (a) high-rate GPS EW displacement records at CONS EW and CONZ EW, see Fig. 3.3 and Table 3.3 for the location of the GPS antennas. (b) Time-derivative of the CONS and CONZ EW records. (c) Ground velocity records at CONS EW and CONZ EW filtered between 0.005 and 0.05 Hz (200 s to 20 s period).

We inverted the band-pass filtered ground velocity records using an elliptical patch approximation, because we think that this approximation is adequate for situations like that of the Maule 2010 earthquake, where the cGPS station locations are roughly 100 km apart and the velocity structure is not known in enough detail. Elliptical patch parameterization was introduced by Vallé and Bouchon (2004) to model far-field waveforms for teleseismic events. The application of the method to near-field strong-motion kinematic inversion and its resolution was discussed in additional detail by Di Carli et al. (2010). This parameterization has the advantage that it produces an image of the source made of asperity-like patches. We inverted the high rate cGPS data using two elliptical patches assuming that the slip distribution D measured from the center of the ellipse has the Gaussian distribution:

$$D(x, y) = D_m e^{-\left(\frac{x^2}{a^2} + \frac{y^2}{b^2}\right)} \quad (1)$$

where D_m is the maximum amplitude in the elliptical patch of semiaxes a and b. The slip distribution is continuous but concentrated inside the ellipse. In every patch, rupture speed was assumed to be constant and the time of rupture tr was computed with respect to distance from the hypocenter in order to insure causality in the forward models. Slip rate on every patch was also very simple. The source time function at any point on the fault was a triangular function of total duration t = 10 s around the rupture time tr. This duration is shorter than that of the ground velocity records at CONZ and CONS shown in Figure 3.3b. In the forward model, each elliptical patch is described by 7 parameters: two coordinates of the center, two semiaxes a and b, an angle of orientation α, slip amplitude D_m and rupture speed v_r. The AXITRA code (Coutant, 1990; Bouchon,1981) was used to simulate wave propagation from the source to the receivers. The fit between observed (*obs*) and synthetic (*synth*) records was measured with the L2 norm:

$$\chi^2 = \frac{\sum_i (obs_i - synth_i)^2}{\sum_i (obs_i)^2} \quad (2)$$

where the index i runs over all samples in every seismogram considered in the inversion. The neighborhood algorithm (NA) of Sambridge (1999) was chosen to search for the minimum value of the L2 norm.

Figure 3.4 shows the slip distribution results and the rupture time isochrones for the best solution found by the NA algorithm. This solution has a misfit $\chi^2 = 0.43$. We modeled the earthquake with two elliptical patches, the maximum slip is larger than 10 m in the Northern zone and the rupture velocity in each ellipse is close to 2.5 km/s. There is not enough resolution in our data to increase the number of ellipses. Figure 3.5 shows the fit between observed and synthetic ground velocity derived from high-rate GPS data. The inital time of observed and modeled records is the same, confirming the proposed long period hypocenter of Vigny et al (2011) and the position of two elliptical patches of slip. On the other hand, not only the long period waves are fitted as observed in EW CONS record but also intermediate frequency period waves as observed in the SJAV EW record. The fit could certainly be improved but the records are sparse and we lack instruments in the southern end of the rupture zone. For this reason we believe that the solution of Figure 3.4 models well only the Northern part of the rupture. Unfortunately there is no seismic data that can be used to study the southern part of the rupture process.

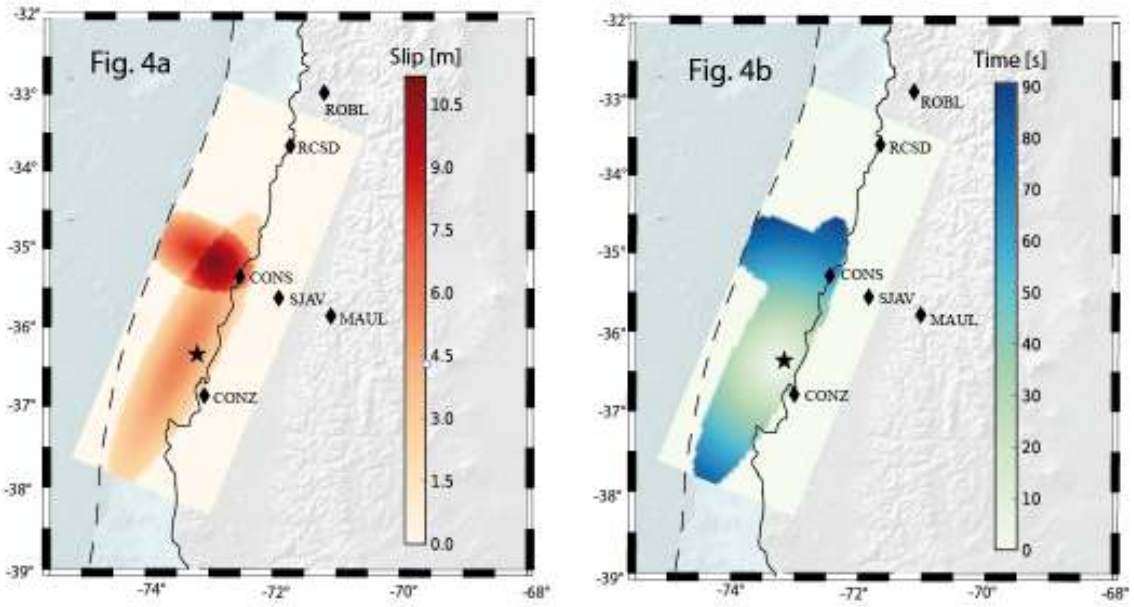

Figure 3.4. Result of kinematic inversion of ground velocity records time-derivative from high-rate cGPS data. On the left (a) slip distribution; and on the right (b) rupture time. Diamonds are locations of cGPS stations used in our inversions, dashed line is ocean trench (plate boundary between Nazca and South American plates), star is long period epicenter.

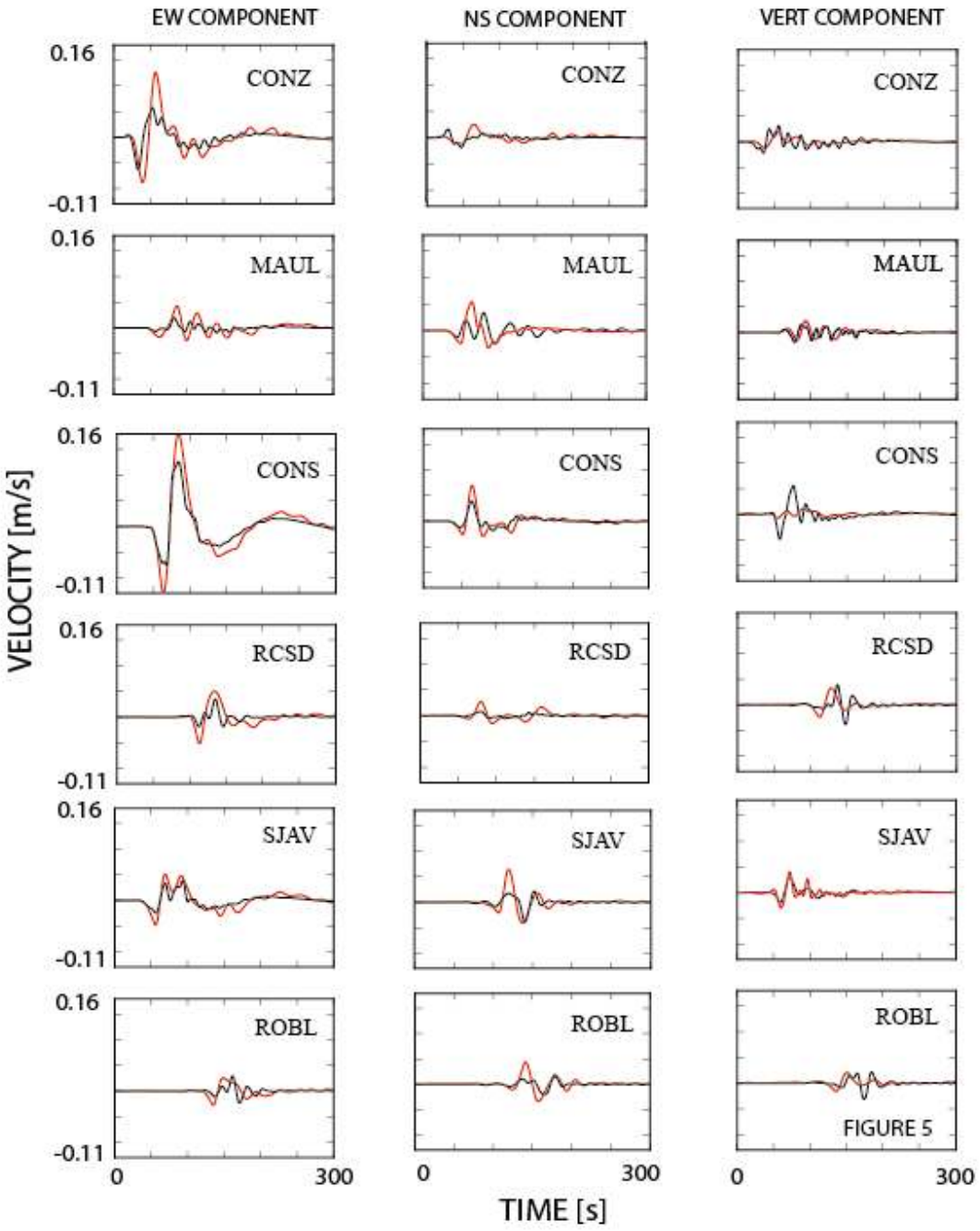

Figure 3.5. Comparison of observed (red) and synthetic (black) ground velocity derived from cGPS records. Both synthetic and observed records were causally filtered between 0.005 and 0.05 Hz (200 to 20 s period).

SHORT PERIOD RUPTURE PROCESS OF THE 2010 MAULE EARTHQUAKE

The Maule 2010 earthquake was recorded by the high rate GPS instruments sampled at 1 Hz that we inverted in last section. It was also recorded by more than 30 strong motion instruments; unfortunately few of them recorded the absolute time and most had a very short pre-event buffer memory (Boroschek et al., 2012). As with high-rate GPS, the northern zone of the rupture is more densely instrumented (Boroschek et al., 2012; Vigny et al., 2011), for this reason we studied in more detail the short period characteristics of this zone. This region is very interesting because of the high seismic intensities recorded in this area when compared to the Southern part of the rupture (see Ruiz and Astroza, 2012; Astroza et al., 2012).

The strong motion data recorded in the higher slip zone show two important zone of energy arrival for periods lower than 20 sec, Figure 3.6. This figure shows the ground displacement computed from strong motion data between 34°S and 36°S. The accelerograms were filtered using a Butterworth non-causal filter between 20 and 0.05 sec (0.05 and 20 Hz), the baseline was removed and then the records were integrated twice to compute displacements. In these records it is possible to clearly identify two main pulses. The components where the pulses were better observed are plotted in Figure 3.6. Since these pulses arrive at different times at the stations of the network, it was possible to identify the area on the fault where they were generated; these zones will be called "asperities" following the original idea of Kanamori and Stewart (1976). The overall duration of the records shown in Figure 3.6 is about 60 s, but the individual pulses observed in the different stations is of the order of 10 to 15 s. This is significantly less than the overall duration of the earthquake which was about 90 s. For this reason we propose that the pulses were emitted by localized asperities that break on top of the large scale rupture process. From the cross correlation of the records we concluded that these asperities were located in the northern zone of the rupture separated at most by a few tens of kilometers.

The asperities are identified using the displacement records shown in Figure 3.6. Of these records only station Convento Viejo (CONV) had absolute time. Fortunately, as we showed in Figure 3.2, the strong motion instrument in Constitucion was located very close to the cGPS antenna CONS. Cross-correlating these two records we could assign absolute time to the CONS strong motion record. For the other four records the time was determined

by comparing the theoretical S arrival time from the high frequency hypocenter and the observed first S arrival in the strong motion record, Figure 3.7a.

Figure 3.7 shows the normalized strong motion displacement records at the same stations shown in Figure 3.6. The seismic traces are located along the ordinate of the plot as a function of the distance in km from the SSN epicenter or proposed asperity hypocenter (Table 3.3) and the abscissa is the time in sec. The curves plotted on top of the seismic section are the travel-times computed using the layered velocity model derived from local data by Campos et al. (2002).

We tested different locations of the asperities ~~were tested~~ until we found the best fit between computed arrival times of pulses emitted by possible asperities and the observed pulses in the strong motion displacement records. The rupture velocity found from the inversion of the cGPS records (~2.5 km/s) was used. The best locations of the two asperities are shown in Table 3.3. The fit between theoretical arrival of S waves from asperities and observed pulses are presented in Figure 3.7b and 3.7c. We obtained a good fit between the theoretical arrival of S waves and observed pulses, the small difference between theoretical and observed arrival time, can be explained by the simplicity of the 1D velocity model considered or assume a constant velocity rupture, or because the travel times were computed assuming that the asperities were located at a single point. Clearly more detailed numerical modeling taking into account a better structural model will be needed to improve this initial schematic model. However the good fit allow assuming that displacement pulses observed in strong ground motion are directly associated to S waves from the proposed location of the asperities.

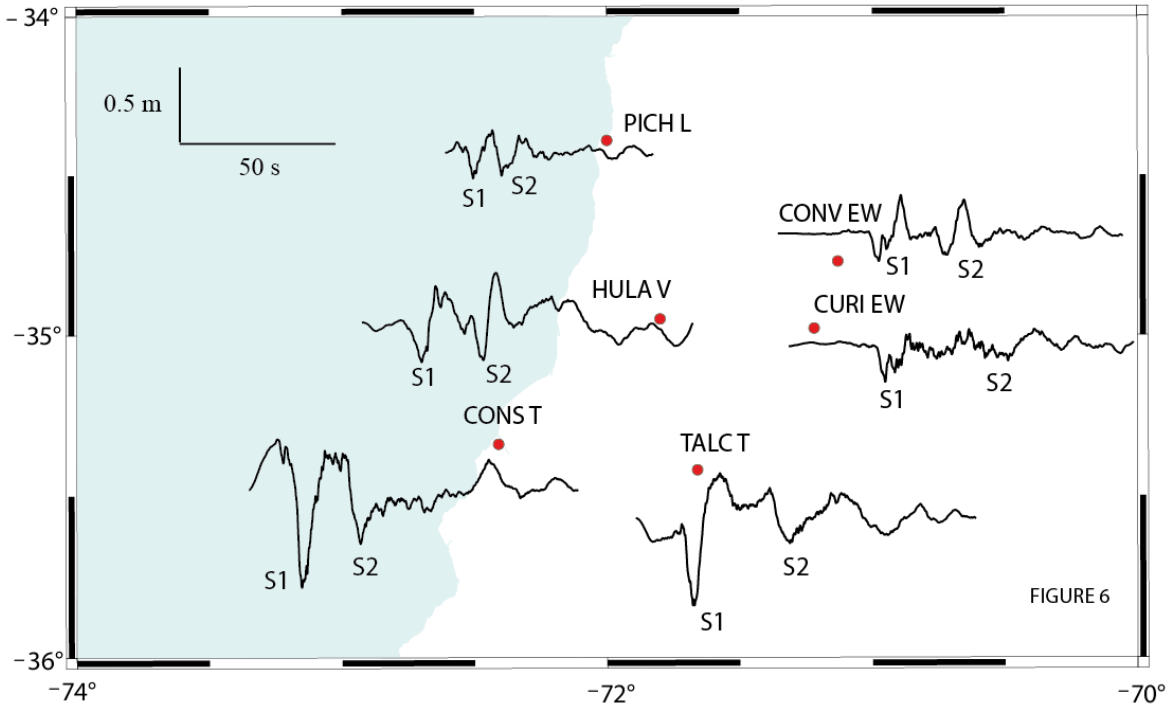

Figure 3.6. The strong motion displacement records located between -34° to -36°, location is listed in Table 3.2. Not all instrument are oriented along geographical coordinate L, T and V refer to Longitudinal, Transversal and Vertical, that unfortunately not always have the same orientation. S1 and S2 correspond to named pulse 1 and pulse 2 inside of the text.

The proposed locations of the two asperities were checked using the cGPS data at the stations listed in Table 3.2. Figure 3.8 shows the cGPS records. The travel times computed using the layered velocity model proposed by Campos et al. (2002) do not fit well the observed arrivals of S waves from asperities in the cGPS station. For this reason new travel-time curves were computed using a simple homogeneous crustal shear speed of 3.3 km/s, these travel times fit very well the first arrival of the S wave at the different cGPS stations, as well as the arrivals of the two observed pulses in ROBL and RCSD, which in this case are associated with surface waves that propagate in the crustal wave guide. These pulses are easily identified in the North components of the cGPS stations, although the second pulse is difficult to identify in the SJAV record. This is probably an effect of the north rupture propagation because SJAV is located south of the second asperity so that the directivity at this station was weak. At the CONZ and CONS stations the pulses are very

difficult to identify because they are hidden by the strong near field displacement due to the passage of the seismic rupture.

In conclusion, the short period rupture process is schematically shown in Figure 3.9 where we plot the location of the hypocenter, the asperities and the direction of rupture propagation. The short period rupture propagates northwards from the hypocenter and has shorter duration than the overall duration of the Maule 2010 earthquake and its source area is smaller than that of the low frequency rupture of the earthquake. This short period rupture has a rupture area and duration similar to that of an Mw ~ 8.0 earthquake, because the two asperities we identified in Figure 3.9 have similar size to the rupture area of a magnitude 8 event in central Chile (Ruiz et al., 2011). The zone where these strong motion short period waves were emitted agrees the zone of higher seismic intensity (MSK > VIII) (Astroza et al., 2012)

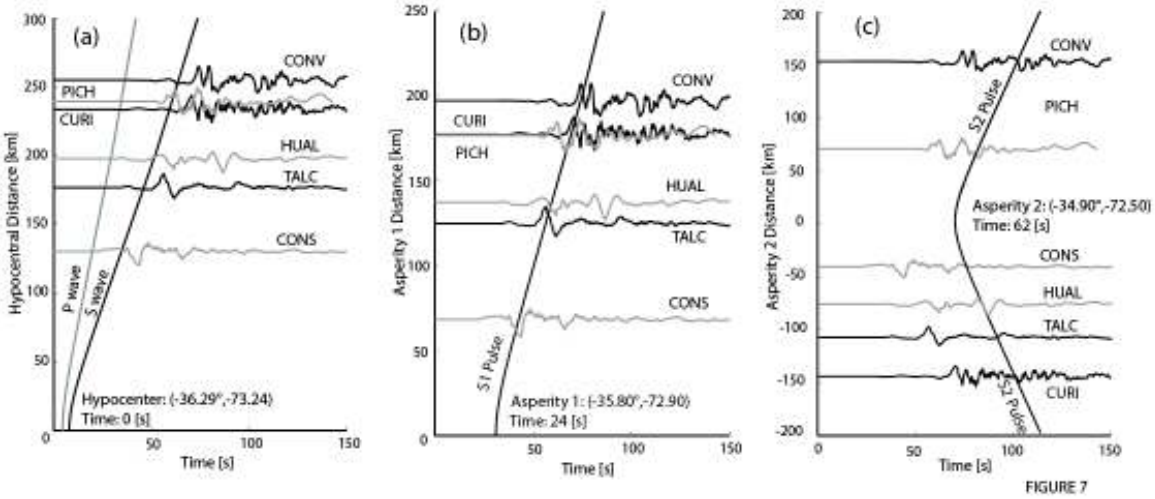

Figure 3.7(a) Strong motion displacement record as a function of distance to hypocenter. (b) and (c) Strong motion displacement record as a function of distance to asperities 1 and 2, respectively. The gray curves are the time-distance calculated for (a) P waves (gray curve) and S waves (black curve), (b) and (c) for S1 and S2 pulses. The hypocenter a location of asperities is shown. Time axis in each figure is the time of start of wave propagation from the hypocenter (a) and asperities (b and c).

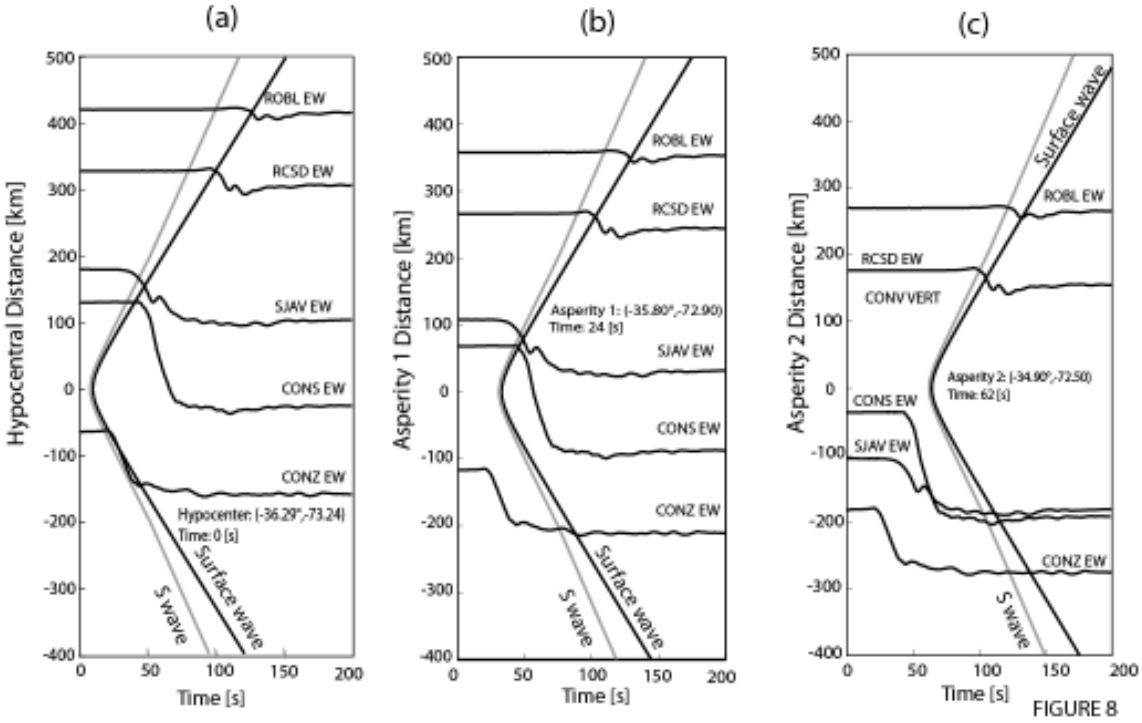

Figure 3.8(a) cGPS as a function of distance to hypocenter. (b) and (c) cGPS as a function of distance to asperities 1 and 2, respectively. The gray curves are the curves time-distance calculated using Campos et al. (2002) velocity model and the black curve are the curves time-distance calculated using a crustal shear velocity. The Time in each figure is the time of start of wave propagation from the hypocenter (a) and asperities (b and c).

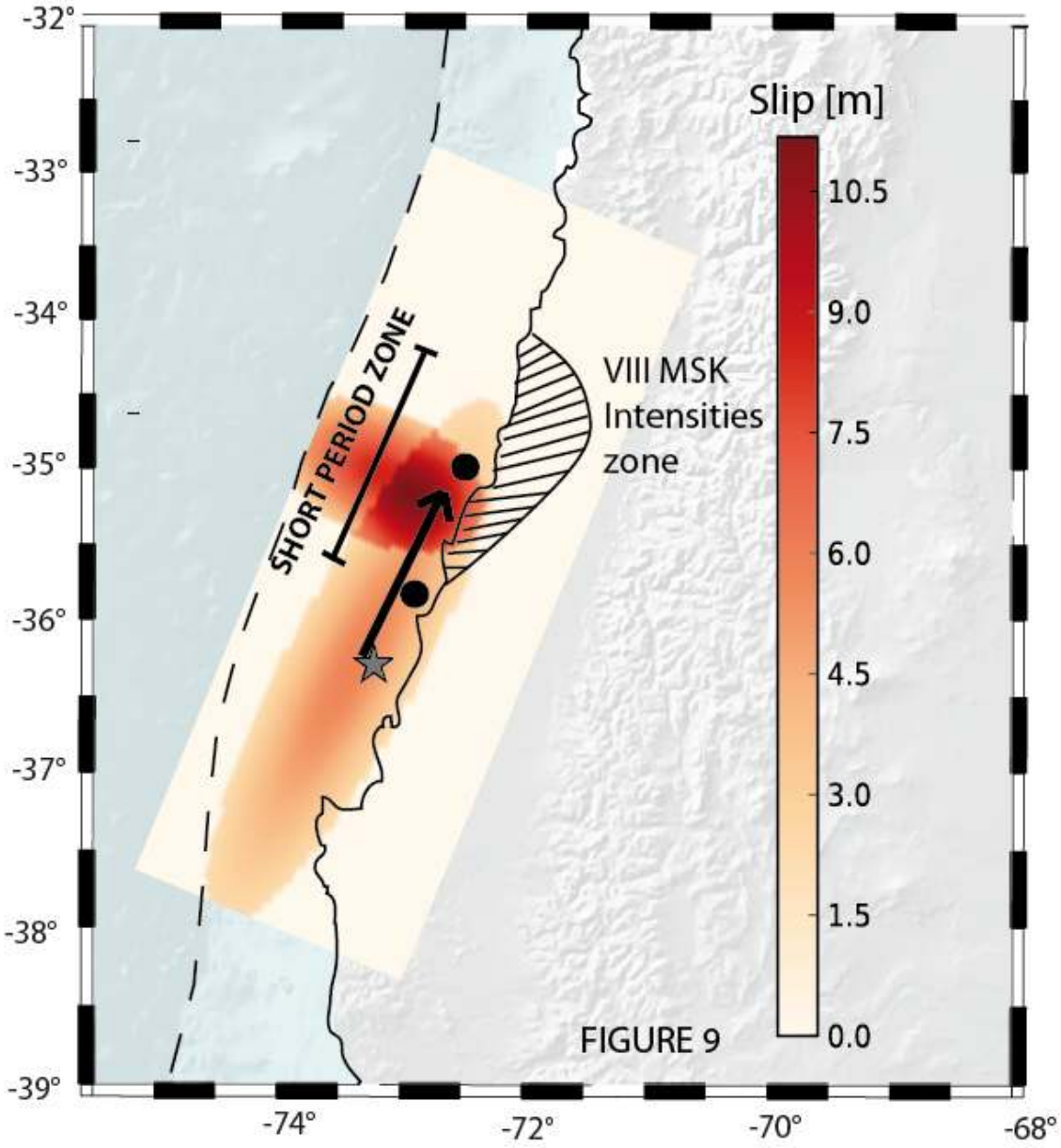

Figure 3.9. Representations of short period rupture process. The rupture start from the hypocenter (star) propagating towards two asperities (black large dots) located to the north. The color zone is the rupture area of Maule 2010 earthquake. The dashed area is the zone of strong seismic intensity (MSK> VIII) of the Maule 2010 identified by Astroza et al (2012).

COMPARISON WITH THE VALPARAISO 1985 STRONG MOTION RECORDS

The Valparaiso 1985, Mw 8.0, earthquake broke a rupture zone situated to the North of the Maule 2010 earthquake. Fortunately a few strong motion instruments located in Central Chile recorded both events as shown in Figures 3.10a and 3.10b. We can use these records to compare the characteristics of these two events. As observed in Figures 3.10a and 3.10b, records from the 1985 and 2010 events had a similar amplitude and duration at the PICH, LLOL and MELP. These stations are located north of the rupture zone of the Maule 2010 earthquake and in the South-Central part of that of Valparaiso 1985. The PAPU, ZAPA, UTFS and VINA have similar amplitude but shorter duration for the Maule records and TALC has a shorter duration for Valparaiso 1985. The different duration of these records could be explained by the different direction of the rupture propagation of both earthquakes South to North by the Maule 2010 and North to South for the 1985 Valparaiso earthquake, Figure 3.10c. Finally in Figure 3.10d the response spectra of acceleration with 5% damping are compared for the two earthquakes, showing similar spectra.

On the other hand, similar pulses to those observed in the Maule 2010 were identified in the SM records of Valparaiso 1985 earthquake and also in Tocopilla 2007 Mw 7.7 Chile earthquake (Ruiz et al., 2011), confirming that the short period waves generated by the Maule 2010 earthquake are similar to those observed in Mw~8.0 Chilean subduction earthquakes.

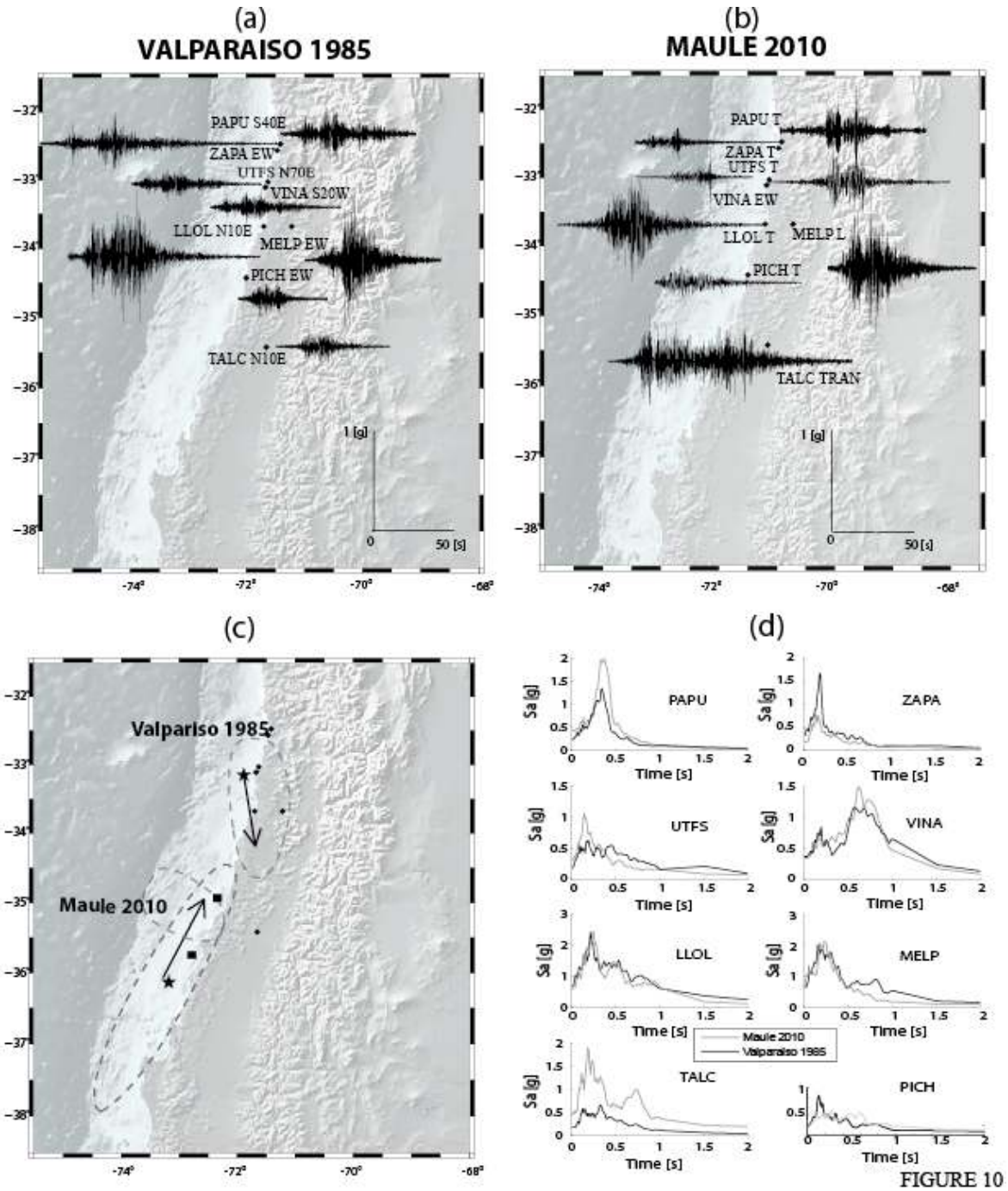

FIGURE 10

Figure 3.10 **(a)** Strong motion records recorded during the Valparaiso 1985 and Maule 2010. Black stars are the epicenters and black square are the asperities **(b)** Strong motion records recorded during the Maule 2010 **(c)** Scheme of rupture propagation by the two earthquakes. **(d)** Comparison of response spectra at 5% damping for the Strong motion records show in the **(a)** and **(b)** figures.

DISCUSSION

The Maule megathrust earthquake was a very large event (Mw 8.8) in the long period domain (> 100 sec) with far field ground motion dominated by the overall rupture process. We recomputed the slip distribution using band limited ground velocities derived from high-rate GPS records. The slip distribution we propose (see Fig. 3.4) is very similar to results proposed by others authors in terms of the spatial pattern, especially for the locations of largest slip in the northern part of the rupture zone (e.g. Delouis et al, 2011, Vigny et al, 2011, etc). However, at short period a different picture emerges where radiation in the North as observed in strong motion records appears to be mostly controlled by two asperities. These asperities produced pulses of similar duration and amplitude as those observed in previous Chilean subduction earthquakes with Mw close to 8.0. The short period rupture process of this mega thrust earthquake may explain why some strong motion records of the Valparaiso earthquake of 1985 are similar to those of the Maule 2010 earthquake. Although the southern part of the Maule earthquake rupture is not well instrumented our rupture process agrees with the back propagation results of Kiser and Ishii (2011) and Wang and Mori (2011). These authors found that more short period energy was emitted in northern zone of the rupture compared to the southern one. Both groups detected an important velocity change in the rupture propagation around near 35.5°S. It is important to emphasize here that these authors located the strong sources of high frequencies with respect to the USGS hypocenter. This may produce an artificial shift of their source to the east and perhaps to the North because the USGS hypocenter does not agree with neither short nor long period near field data. The location of the low frequency hypocenter (Vigny et al., 2011) further to the west and south with respect to the USGS hypocenter is required by the arrival times of long period waves at high rate GPS records in central Chile. The actual location of the hypocenter may have important consequences for the excitation of tsunami waves by the Maule event (Fritz et al., 2011; Wu and Ho. 2011). Further work on this particular point seems necessary.

The cGPS data are dominated by near field surface and body waves that propagate in the crustal wave guide, while the short period strong motion signals propagate like multiply scattered body waves. They show different sensitivity to the velocity model that is

used to locate the asperities. We have to wait for the tomographic studies currently in preparation in order to improve the local velocity model.

The locations of asperities in the northern part of the Maule rupture may explain why the damage to rigid structures was concentrated in this zone, in contrast with the low damage observed south of the epicenter (Astroza et al., 2012).

The short period rupture process observed during the Maule 2010 earthquake may not be only an attribute of the Maule mega-thrust earthquake. Frequency dependent rupture behavior also was observed during the Tohoku 2011 Mw 9.0, Japan earthquake by Koper et al. (2011), Meng et al. (2011) and Wang and Mori (2011) using back-propagation of high frequency waves observed in far field seismic arrays. Furthermore, moderate damage was observed during Tohoku 2011 Mw 9.0 Japan in comparison with shallow earthquakes (Kawase, 2011) and recorded strong motion data were similar to that of previous M~8.0 Japanese earthquakes like the 2003 Tokachi-oki earthquake (Si et al, 2011).

CONCLUSIONS

We studied the intermediate and high frequency radiation generated by the 2010 Maule earthquake using near field high rate GPS and strong motion records. Unfortunately these data are only available for the Northern part of the rupture of the event, from Concepcion (37.5 ° S) the North. There seems to be no high-rate GPS instruments or usable strong motion data from the southern end of the rupture.

We inverted the ground velocities obtained by band limited differentiation of the cGPS records in central Chile. Although the data are heavily dominated by the propagation of the rupture front, we could determine that a local asperity located roughly westward of the city of Constitucion produced a significant part of the high frequency waves observed in local accelerograms. In all the stations situated North of Constitucion two big strong motion pulses are observed that we associated with the two asperities situated north of the city of Constitucion. Finally a comparison of records from the 1985 Valparaiso earthquake shows that high frequency emission from that earthquake and from Maule were very similar in the Northern stations. This similarity is striking in the envelopes of strong motion data and in the acceleration response spectra of accelerograms. Thus it seems that the 2010 mega-

earthquake was huge at low frequencies but the strong motion was very similar to that of a smaller event of magnitude 8. Similar observations have been reported for the recent 2011 Tohoku earthquake.

ACKNOWLEDGEMENTS

The authors would like to SSN (Seismological National Service) and RENADIC (National Network of Civil Department) of the University of Chile for making records of the 2010 Maule earthquake available to us. S.R. and J.C. have been partially funded by Millennium Nucleus Program ''Montessus de Ballore—IERC'', Mideplan, Chile. This work was supported by FONDECIT contract No. 1100429 in Chile and by ANR Risk, contract DEBATE ANR-08-RISK-001, in France.

REFERENCES

Astroza, M., Ruiz, S. and Astroza, R., 2012. Damage assessment and seismic intensity analysis of the 2010 (Mw 8.8) Maule earthquake. Submitted to *Earthquake Spectra*.

Boroschek, R. et al. This issue Earthquake Spectra

Bouchon, M. (1981), A simple method to calculate Green's functions for elastic layered media, Bull. Seismol. Soc. Am., 71, 959–971.

Campos, J., Hatzfeld, D., Madariaga, R., Lopez, G., Kausel, E., Zollo, A., Barrientos, S., and Lyon-Caen, H., 2002. The 1835 seismic gap in South Central Chile, *Phys. Earth Planet. Int.*, **132**, 177-195.

Comte, D., A. Eisenberg, E. Lorca, M. Pardo, L. Ponce, R. Saragoni, S. K. Singh, G. Suarez, 1986. The 1985 central Chile earthquake: a repeat of previous great earthquakes in the region? *Science,* 233**,** 449-453.

Coutant, O. (1990), Programme de simulation numerique AXITRA, Rapport LGIT, Univ. Joseph Fourier, Grenoble, France.

Delouis, B., Nocquet, J.M. and Vallée, M., 2010. Slip distribution of the February 27, 2010 Mw = 8.8 Maule Earthquake, central Chile, from static and high-rate GPS, InSAR and Broadband teleseismic data. Geophysical Research Letters, Vol 37, L17305, doi:10.1029/2010GL043899.

Di Carli, S., C. François-Holden, S. Peyrat and R. Madariaga (2010), Dynamic inversion of the 2000 Tottori earthquake based on elliptical subfault approximations, *J. Geophys. Res.,* 115, B12328, doi:10.1029/ 2009JB006358.

EERI, 1986. The Chile Earthquake of March 3, 1985 – Introduction. *Earthquake Spectra* Vol. 2, N°2. pp. 249-252.

Engdahl, E.R., and A. Villaseñor, Global Seismicity: 1900–1999, in W.H.K. Lee, H. Kanamori, P.C. Jennings, and C. Kisslinger (editors), International Handbook of Earthquake and Engineering Seismology, Part A, 665–690, Academic Press, 2002.

Fritz, H. M., Petroff, C. M., Catal´an, P. A., Cienfuegos, R., Winckler, P., Kalligeris, N., Weiss, R., Barrientos, S. E., Meneses, G., Valderas-Bermejo, C., Ebeling, C., Papadopoulus, A., Contreras, M., Almar, R., Dominguez, J. C., and Synolakis, C. E., (2011), Field survey of the 27 February 2010 Chile tsunami, *Pure Appl. Geophys*., 168, 1989–2010, doi:10.1007/s00024-011-0283-5.

Heaton, T. H. (1990) Evidence for and implication of self-healing pulses of slip in earthquake rupture, *Phys. Earth Planet. Int.*, 64, 1-20.

Housner, G. W. 1963. An Engineering Report on the Chilean Earthquakes of May 1960 Preface. *Bull. Seismol. Soc. Am*., 53, 219-223.

Kanamori, H. and Stewart, G. S., 1976. Seismological aspects of the Guatemala earthquake of February 4, 1976, *J Geophys Res* 83, 3427–3434.

Kawase, H. (2011). Strong motion characteristics and their damage impact to structures during the off pacific coast of Tohoku earthquake of March 11, 2011; How extraordinary was this M9.0 earthquake?. In proceeding, *4th IASPEI / IAEE International Symposium,* Santa Barbara, EEUU.

Kiser, E. and Ishii, M. (2011). The 2010 Mw 8.8 Chile earthquake: Triggering on multiple segments and frequency dependent rupture behavior. *Geophys. Res. Lett* doi:10.1029/2011GL047140.

Koper, K., Hutko, A., Lay, T., Ammon, C. and Kanamori, H. (2011). Frequency-dependent rupture process of the 2011 *M*w 9.0 Tohoku Earthquake: Comparison of short-period *P* wave back projection images and broadband seismic rupture models. *Earth Planets Space*, 63, 599–602.

Lay, T., C. J. Ammon, H. Kanamori, K. D. Koper, O. Sufri, and A. R. Hutko, Teleseismic inversion for rupture process of the 27 February 2010 Chile (Mw 8.8) earthquake, 2010. *Geophys. Res. Lett*., 37, L13301, doi:10.1029/2010GL043379.

Lorito, S., Romano, F., Atzori, F., Tong, X., Avallone, A., McCloskey, J., Cocco, M., Boshi, E. and Piatanesi A., 2011. Limited overlap between the seismic gap and coseismic slip of the great 2010 Chilean earthquake, *Nature Geoscience Letters*, doi:10.1038/NGEO1073.

Madariaga, R., Vigny, Ch., Métois, M., and Campos, J., Central Chile finally breaks *Science* **238**, 181-182, 2010

Meng, L., Inbal, A. and Ampuero, J.P (2011). A window into the complexity of the dynamic rupture of the 2011 Mw 9 Tohoku-Oki earthquake. *Geophys. Res. Let.,* 38, L00G07, doi:10.1029/2011GL048118.

Moreno, M. , D. Melnick, M. Rosenau, J. Bolte, J. Klotz, H. Echtler, J. Baez, K. Bataille, J. Chen, M. Bevis, H. Hase, and O. Oncken, 2011, Heterogeneous plate locking in the South–Central Chile subduction zone: Building up the next great earthquake, Earth Planet Sci. Lett., 305, 413-424

Pollitz, F. F., B. Brooks, X. Tong, M. G. Bevis, J. H. Foster, R. Bürgmann, R. Smalley Jr., C. Vigny, A. Socquet, J.-C. Ruegg, J. Campos, S. Barrientos, H. Parra, J. C. B. Soto, S. Cimbaro, and M. Blanco., 2011. Coseismic slip distribution of the February 27, 2010 Mw 8.8 Maule, Chile earthquake. *Geophys. Res. Lett.*, 38, L09309, doi:10.1029/2011GL047065.

Pulido, N., Yagi., Y., Kumagai, H. and Nishimura, N., 2011. Rupture Process and coseismic deformations of the 27 February 2010 Maule earthquake, Chile. *Earth Planets Space,* 63, 1-4.

Ruiz, S., Kausel, E., Campos, J., Saragoni, G. R. and Madariaga, R. (2011). Identification of High Frequency Pulses from Earthquake Asperities Along Chilean Subduction Zone Using Strong Motion. *Pure and Applied Geophysics*, 168: 125-139

Ruiz, S. and Astroza, M. 2012. Destructiveness of the Maule 2010 Chilean earthquake considering low-rise rigid buildings. Submitted to: *Andean Geology.*

Sambridge, M. (1999), Geophysical inversion with a neighbourhood algorithm—I. Searching a parameter space, Geophys. J. Int., 138, 479–494.

Si, H., H. S. Kuyuk, K. Koketsu, and H. Miyake (2011). Attenuation characteristic of peak ground motion during the 2011 Tohoku, Japan, earthquake, Seismol. Res. Lett., 82, 460.

SSN (2010) Servicio Sismologico. Universidad de Chile – Departamento de Geofisica. (http://www.sismologia.cl/seismo.html).

USGS (2010) U.S. Geological Survey. Preliminary determination of epicenter.

Tong, X., Sandwell, D., Luttrell, K., Brooks, B., Bevis, M., Shimada, M., Foster, J., Smalley Jr., R., Parra, H., Báez Soto, J. C., Blanco, M., Kendrick, E., Genrich, J. and Caccamise, D. J., 2011. The

2010 Maule, Chile earthquake: Downdip rupture limit revealed by space geodesy, *Geophys. Res. Lett.*, doi:10.1029/2010GL045805.

Vallée, M. and Bouchon, M., 2004. Imaging coseismic rupture in far field by slip patches. *Geophys. J. Int. 156, 615-630.*

Vigny, C., Socquet, A., Peyrat, S., Ruegg, J.C., Métois, M., Madariaga, R., Morvan, S., Lancieri, M., Lacassin, R., Campos, J., Carrizo, D., Bejar-Pizarro, M., Barrientos, S., Armijo R., SSN team, LIA-MdB team and CAP team., 2011. The 2010 (Mw 8.8) Maule Mega-Thrust Earthquake of Central Chile, monitored by GPS. *Science,* 331, 1417-1421.

Wang, D. and Mori, J. (2011). Frequency dependent energy radiation and fault coupling for the 2010 Mw 8.8 Maule, Chile, and 2011 Mw9.0 Tohoku, Japan, earthquakes. *Geophys. Res. Lett*. doi:10.1029/2011GL049652.

Wu, T.R. and Ho., T.C. (2011). High resolution tsunami inversion for 2010 Chile earthquake. *Nat. Hazards. Earth. Sci*, 11, 3251-3261

Yoffe, E. (1951) The moving Griffith crack, *Phil. Mag.*, 42, 739-750.

.

Table 3.1. Different epicenters proposed for the Maule 2010 earthquake.

LATITUD	lONGITUD	dEPTH	REF
-36.25	-72.96	47.4	SSN (early determination)
-36.29	-73.24	30.1	SSN (last determination)
-35.83	-72.66	35	USGS (early determination)
-36.12	-72.90	22.9	USGS (last determination)
-36.41	-73.18	26.0	Vigny et al. (2011)

Table 3.2. Location of cGPS instruments.

Station Name	**Station Code**	**Long.**	**Lat**
CONCEPCION	CONZ	-36.830	-73.050
MAULE	MAUL	-35.809	-70.821
CONSTITUCION	CONS	-35.330	-72.412
SAN JAVIER	SJAV	-35.595	-71.733
ROCA STO DOMINGO	RCSD	-33.653	-71.614
EL ROBLE	ROBL	-32.976	-71.015

Table 3.3. Location of the hypocenter and asperities of the Maule 2010 earthquake.

	LATITUDE	LONGITUDE	DEPTH [KM]
SSN Hypocenter	-36.29	-73.24	30.1
Asperity 1	-35.80	-72.90	25
Asperity 2	-34.90	-72.50	25

4. PRELIMINARY INVERSION OF SLIP DISTRIBUTION OF TOHOKU 2011 EARTHQUAKE

INTRODUCTION

On 11 March 2011 occurred the Tohoku mega-earthquake of Mw 9.0, the best instrumented earthquake ever recorded. More than 500 GPS recording sampled at 1 Hz, 7 GPS/acoustic ocean bottom instruments (Sato et al., 2011, Kido et al., 2011) and more than 500 accelerographs recorded this earthquake. All this information gives a unique opportunity to understand the physics of the seismic rupture of this mega-earthquake.

The slip distribution and spatial-temporal evolution of the rupture of the Tohoku earthquake has been studied using kinematic inversion and back-projection techniques. Most of kinematic inversions have used only static displacements (Simmons et al., 2011; Pollitz et al., 2011; Ozawa et al., 2011; Ohzono et al., 2011; among others), some inversions only used continuous GPS (Yue and Lay, 2011), others only strong motion (Suzuki et al., 2011) and finally some inversions used jointly different seismic data (Koketsu et al., 2011; Yokota et al., 2011, many more references in Romano et al., 2012). High-frequency image of the rupture process has been studied using back-project in of teleseismic waveforms (Kiser et al., 2012; Koper et al. 2011, Meng et al. 2011, Wang and Mori, 2011). All these works show similar results for the slip distribution and spatio-temporal evolution of the rupture: the largest slip was located near of hypocenter with an important slip near of the trench and several velocity rupture changes. Here we use continuous GPS (cGPS) and the cGPS and ocean bottom GPS/acoustic records to make our inversions. Two different approaches to obtain the slip distributions are used: the elliptical patches (Vallé and Bouchon, 2004; Ruiz and Madariaga, 2011) and rectangular grid discretization approaches, for both cases we used a non-linear algorithm to search for the best solution. After, finding the best solution, we made Monte Carlo style inversion (MC) in order to obtain a family of solutions with good misfit. With MC we can observe the trade-off among the variables and give the general overall characteristics of slip distributions proposed so far. Finally, to understand the spatial-temporal evolution we made a simple, classic kinematic crack rupture showing the importance of the nucleation process and the generation of important

stopping phases in the border of the rupture. This last observation is complementary to back projection observations and the observed high frequencies characteristics of strong motions records.

METHODOLOGY

Elliptical Patch Approach

To understand the overall aspects of Tohoku 2011 earthquake we first made a very simple inversion using the elliptical patch approach to estimate the slip distribution of the Tohoku 2011 earthquake. We considered that the rupture is located inside a fault plane of 500 km x 250 km. The geometry of each ellipse is defined by the following parameters: the location of the center of the ellipse with respect to the hypocenter of the earthquake, the principal semi-axes (noted *a* and *b*) and the angle of the principal axis with respect to the horizontal. We assumed that the slip distribution was Gaussian:

$$D(x,y) = D_m \exp\left[-\left(\frac{x^2}{a^2}+\frac{y^2}{b^2}\right)\right] \quad (1)$$

Where D_m is the maximum amplitude of slip inside the elliptical patch of semi-axes *a* and *b*. During the inversion a constant rupture velocity *Vr* was assumed. See Table 1 for a list of the parameters that we used. 7 parameters were inverted of which 5 were geometrical: 2 axes (a, b) and 1 angle (α), plus 2 parameters for the position of the center of the ellipse. Two additional parameters define the kinematics: the maximum slip D_m and the rupture velocity *Vr*. The source time function was the same for every point on the fault. By trial and error we chose a triangular function of duration 25 s around the rupture time. The same idea was used to study inversions consisting of two ellipses; in this case the number of inverted parameters was 14.

The AXITRA code (Bouchon, 1981; Coutant, 1990) was used to simulate wave propagation from the source to the receivers. For the propagation of seismic waves we used the same model of the structure and hypocenter used by Lay et al. (2011).

The inversion was made using the Neighborhood Algorithm (NA) (Sambridge, 1999) to search for the rupture model with minimum misfit and the Monte Carlo (MC) technique to study the resolution in the vicinity of the best model. Synthetic records were compared with real records, using the normalized L^2 norm:

$$\chi^2 = \frac{\sum_i w_i \left(obs_i - calc_i\right)^2}{\sum_i w_i obs_i^2} \tag{2}$$

where obs are the observed displacement and calc, the simulated displacement, w_i is the weight. The sum runs over all samples in every seismogram considered in the inversion. The static ocean bottom GPS/acoustic records were attributed a larger weight in the inversions, ten times higher than the inland records.

Rectangular grid approach

We also inverted cGPS records using a fault modeled by a set of 40 rectangles of 50 x 50 km, which covered a rupture area of 500 x 200 km. The rupture velocity was assumed to be constant for all the rupture, and the slip variable for each rectangle. We made NA inversions using the same cost function shown in Eq (2) to which we added two penelatization terms related to the smoothing of the slip distribution:

$$\chi^2 = \frac{\sum_i w_i \left(obs_i - calc_i\right)^2}{\sum_i w_i obs_i^2} + \theta \frac{\sum_i w_i D_i^2}{N \max(w_i D_i)} + \psi \frac{\sum_i w_i (\nabla D_i)^2}{N \max(w_i D_i)^2} \tag{3}$$

The first term is the normalized fit of observed and synthetic data; w_i is the weight. The other terms are covariance terms that penalize models with large displacements and large gradients. We used this penalization in order to obtain smooth models that fit the total moment. By trial and error we found that good results were found for Lagrange multipliers, $\theta = 1$; $\psi = 3$. Also, the static ocean bottom GPS/acoustic records had a larger weight in the inversions, ten times higher than inland records.

THE LONG PERIOD SOLUTIONS

Elliptical approach using the neighborhood algorithm

For our inversions we used 56 records that we think have the best azimuthal distribution, filtered using a high-pass corner frequency of 0.02 Hz, and the 7 static records of GPS/acoustic located at the bottom of the ocean, Figure 1. First we made an inversion using one ellipse and then a new inversion considering two ellipses. Figure 2 shows the slip distribution and the spatio-temporal evolution of the rupture process for the solutions with the lowest misfits. Then, we made an inversion considering 2 ellipses. The misfit is reduced slightly from 0.065 for 1 ellipse patch to 0.059 when searching for 2, Figure 3. The observed and predicted records are shown in Figure 4. In general our elliptical solutions have all the characteristics of static GPS solutions such as those of Simmons et al. (2011); Ozawa et al. (2011), Pollitz et al., (2011) among many others. The main difference among the different published works is the proposed maximum slip and the size of rupture area, however we think that these belong to a family of solutions that fit very well the observed records.

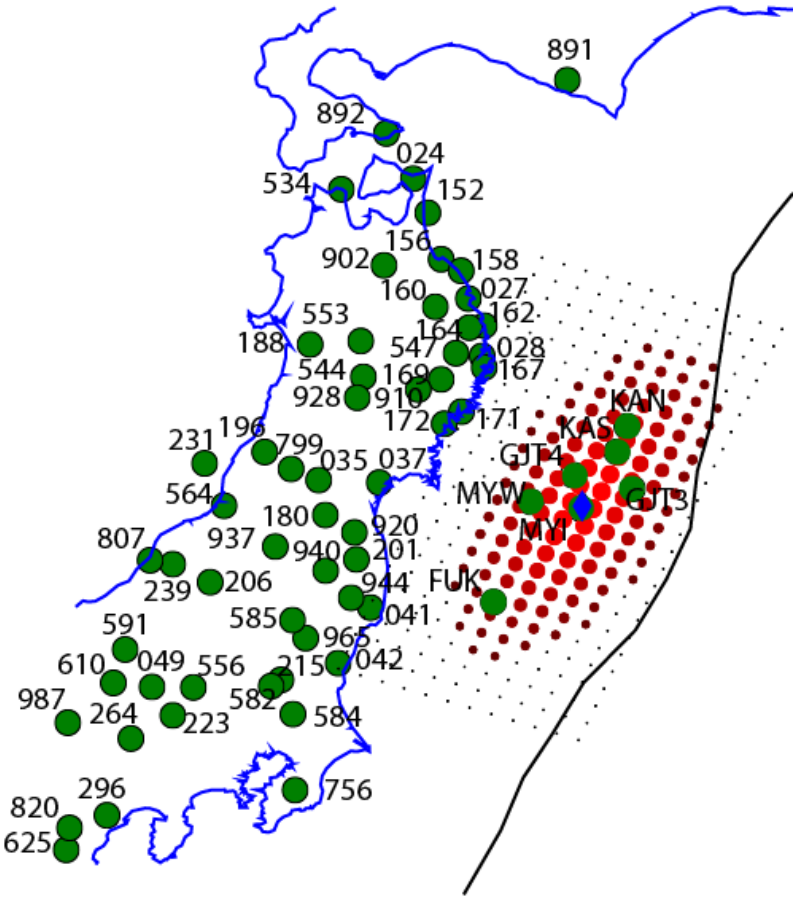

Figure 1. Location of GPS records used in our inversions. The numbers correspond to inland stations and the letters and number to ocean bottom records. The red dots is the slip distribution for the one ellipse approach. The size of the dot is scaled with the proposed slip amplitude.

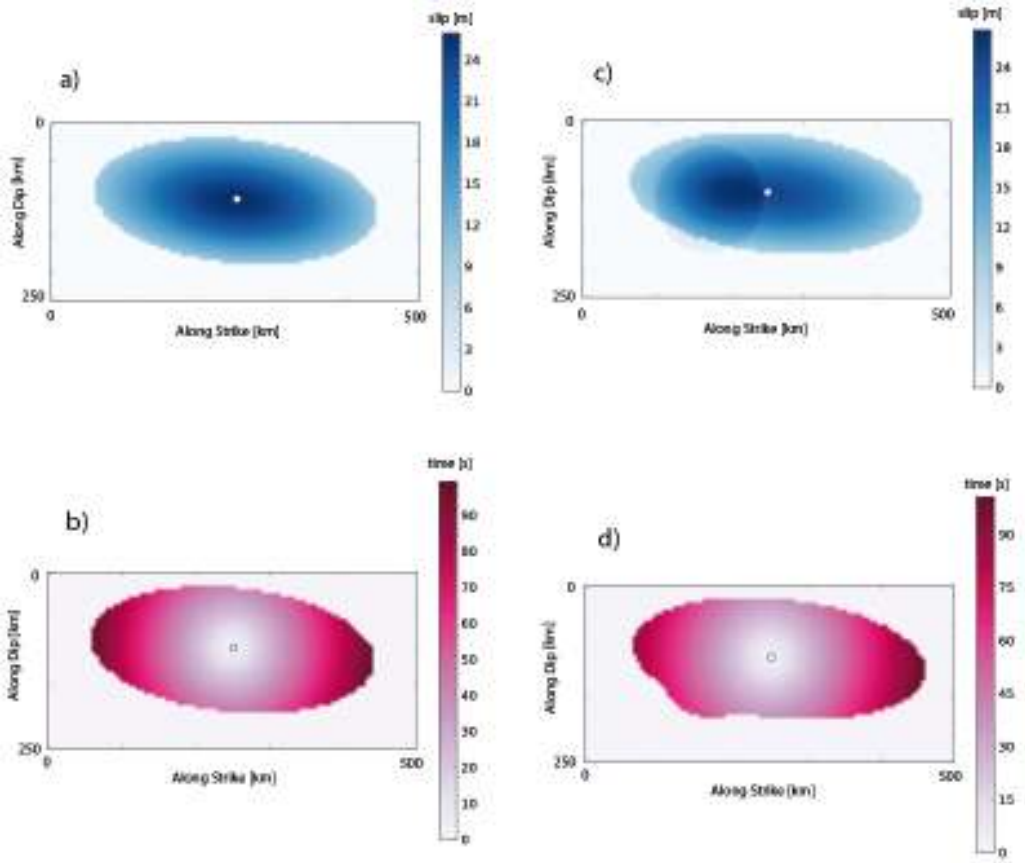

Figure 2. (a) and **(b)** slip distribution (upper) and rupture process (down) for the one ellipse approach, **(c)** and **(d)** slip distribution (upper) and rupture process (down) for the two ellipses approach.

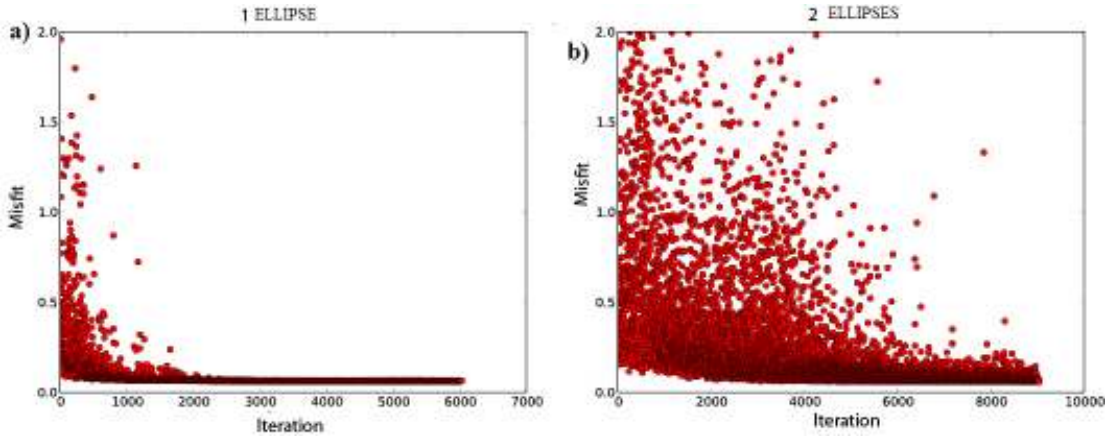

Figure 3. Convergence of inversion. Each dot is one visited model. **a)** 1 ellipse inversion. **b)** two ellipses model

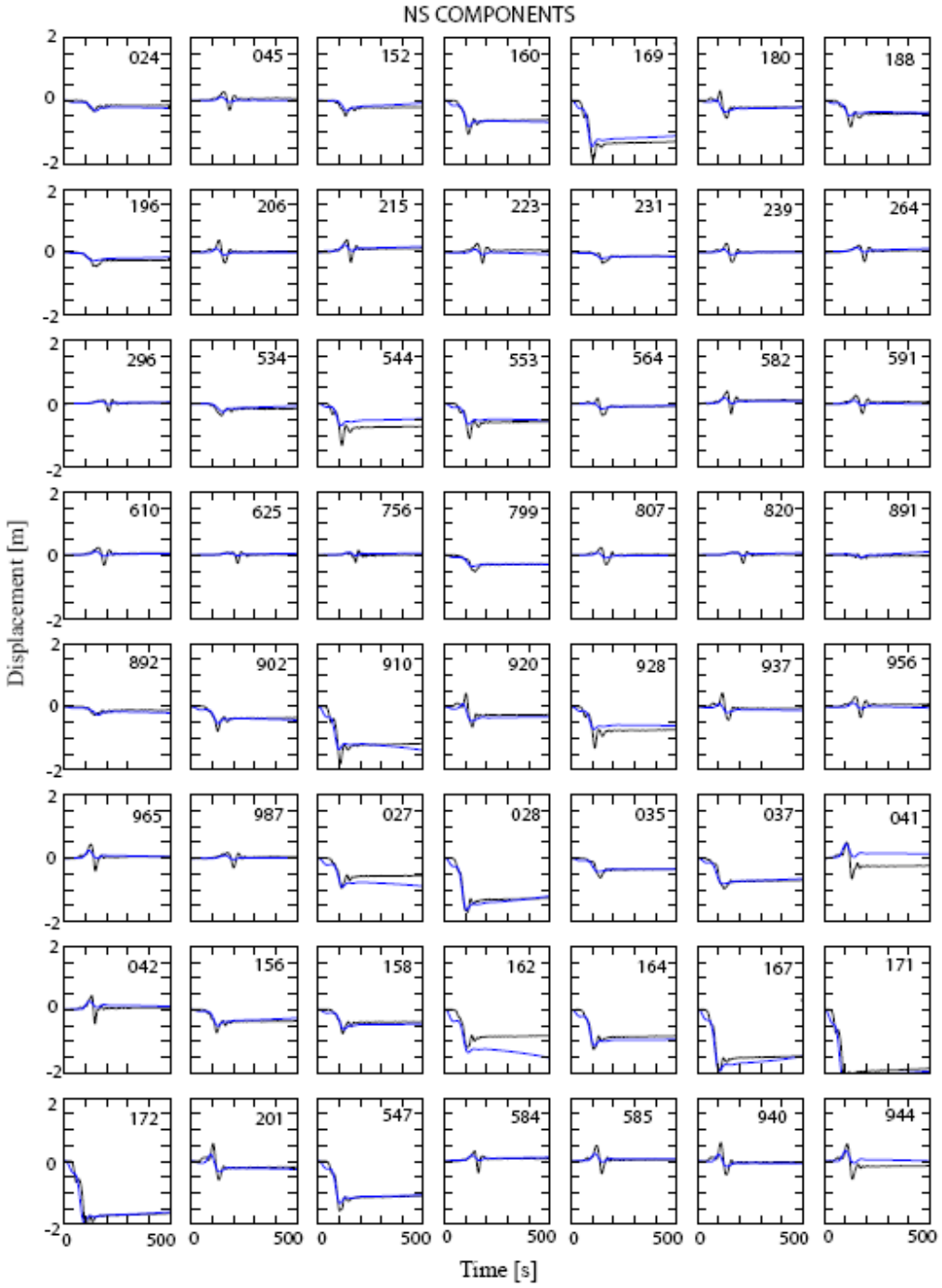

Figure 3a. NS components of one ellipse approach inversion. (black: real data; blue: simulated data)

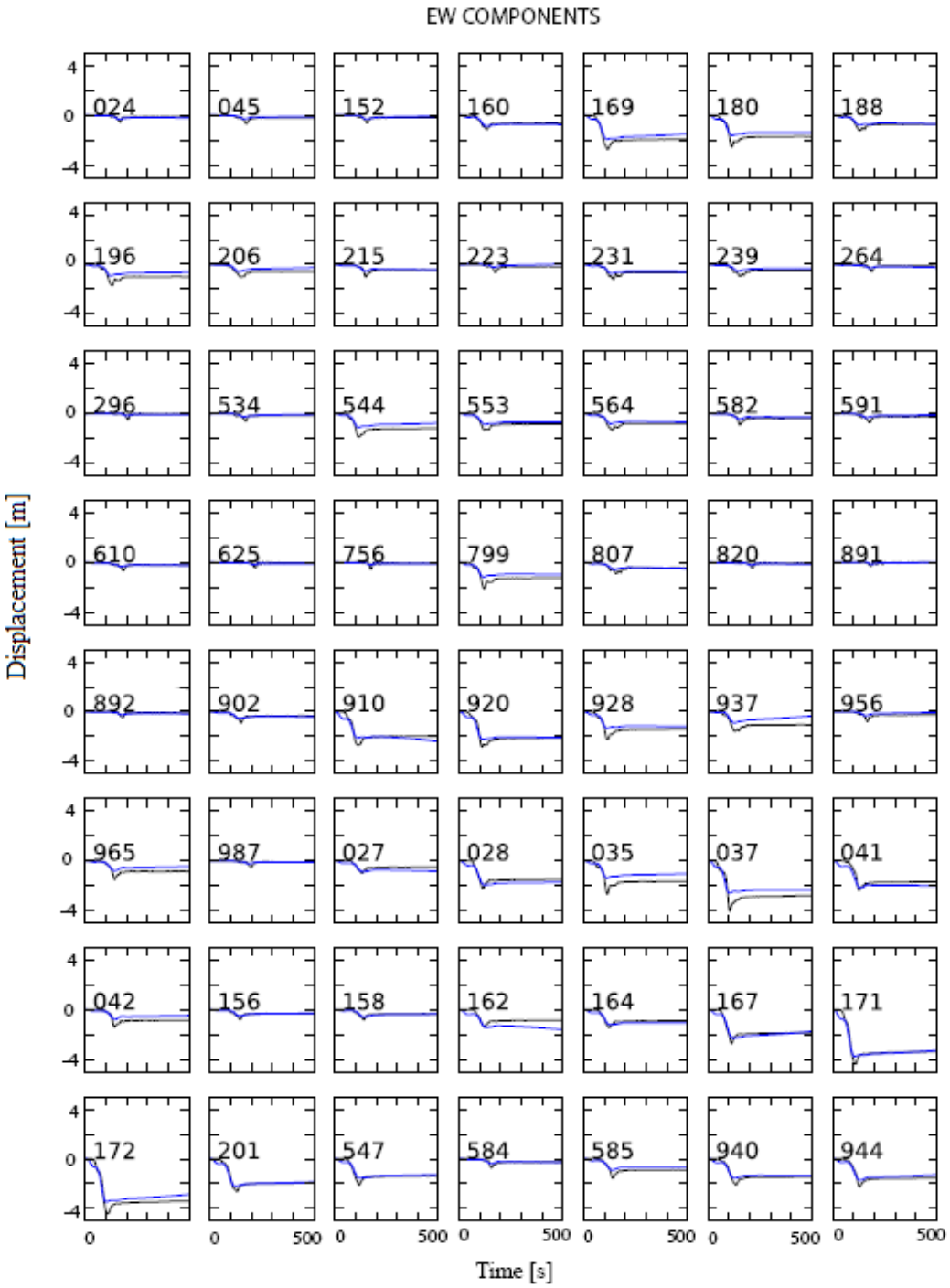

Figure 3b. EW components of one ellipse approach inversion. (black: real data; blue: simulated data)

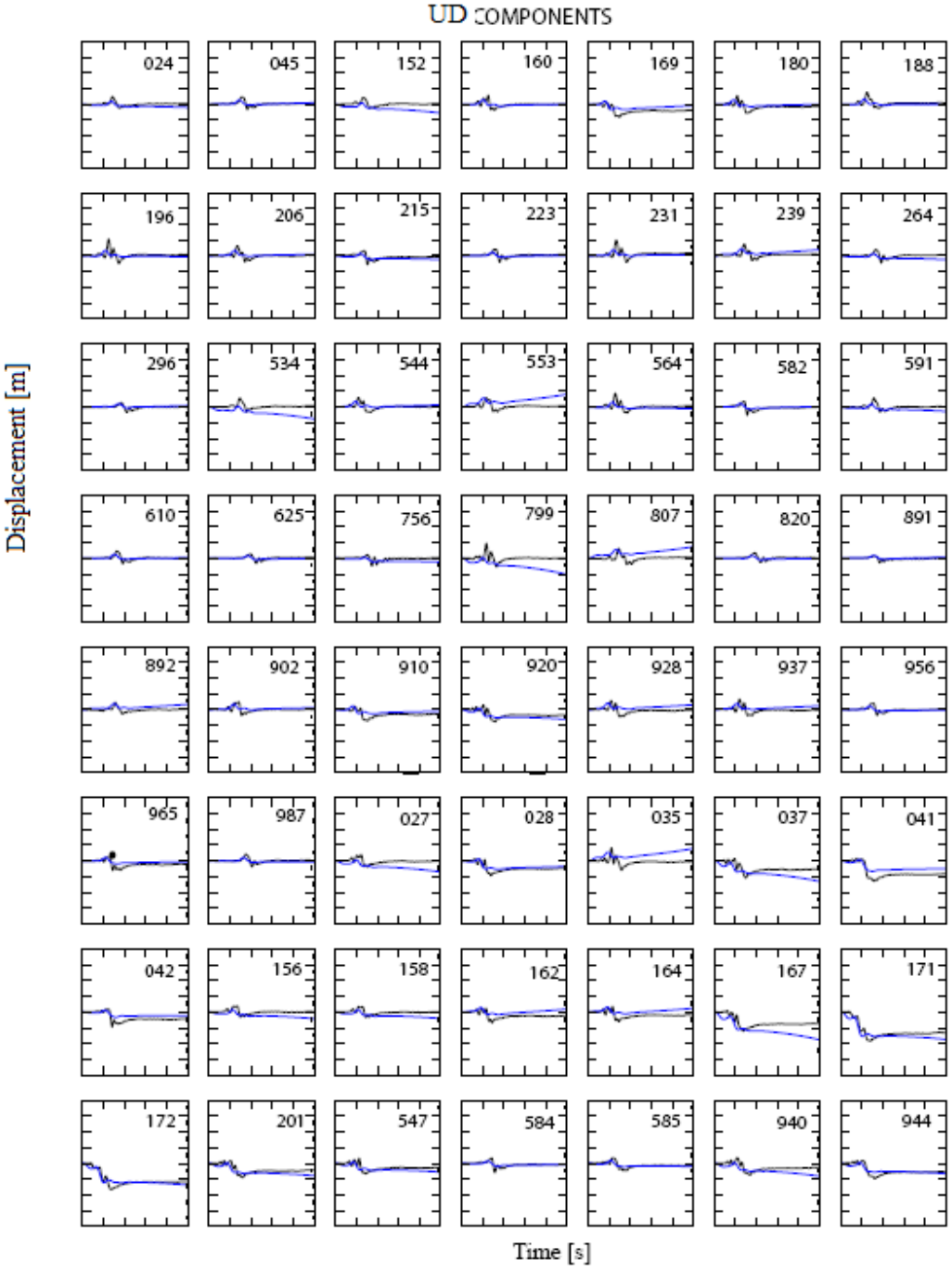

Figure 3c. UD components of one ellipse approach inversion. (black: real data; blue: simulated data)

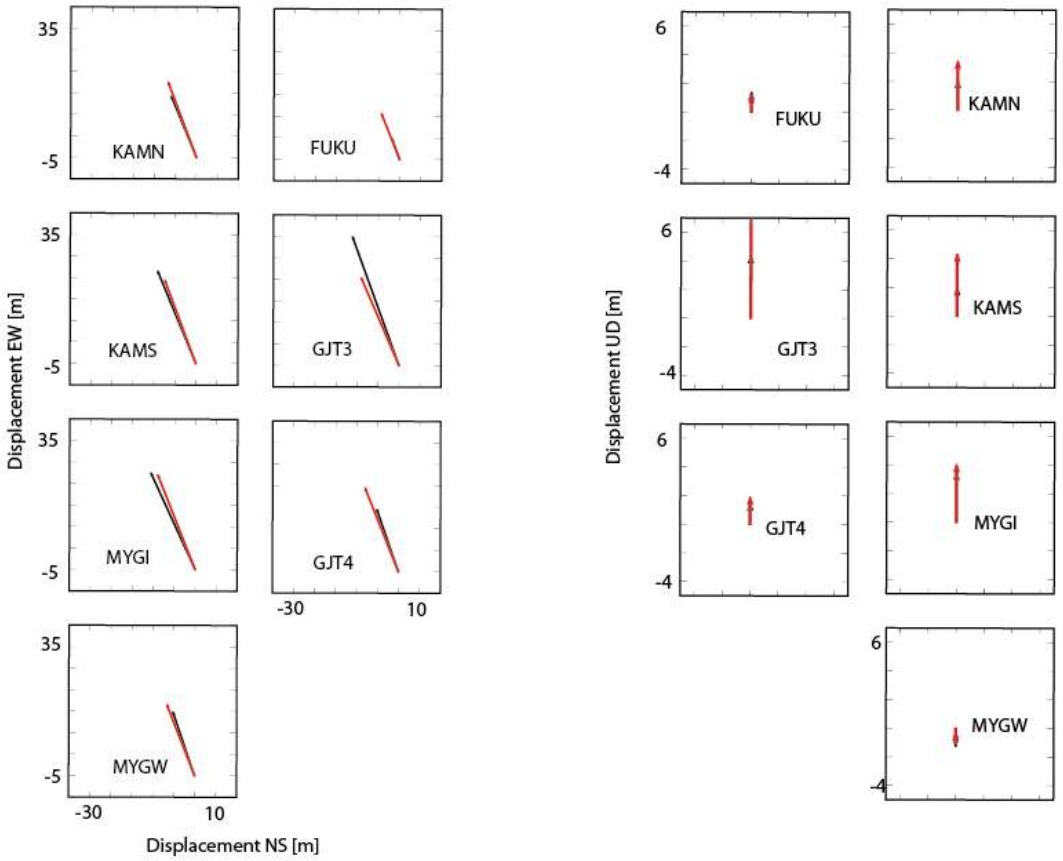

Figure 3d. GPS static components of one ellipse approach inversion. (black: real data; red: simulated data)

Elliptical patch approach using the MC technique

We did a Monte Carlo (MC) inversion in which only V_r, D_m and the semi-axis a were allowed to change. In the MC inversion the semi-axes b and a are forced to have the same aspect ratio (b/a= 0.43). This is the aspect ratio for the best NA one ellipse model. The other parameters were fixed to those of the best NA solution. Figure 4 shows the residuals of the models visited by the MC algorithm; those with misfits lower than 0.08 are plotted with larger dots (8 % of the variance is explained by the data). The models with lowest misfits (<0.08) fill preferably a zone of the V_r space between 1.3 and 2.7 km/sec, D_m from 26 to 32 m and semi-axis a between 170 and 190 km (Figures 5a, 5b and 5c). The seismic moment Mo of these models is almost constant, equal to 4 10^{22} Nm. This family of solutions provides the overall characteristics of the Tohoku earthquake using double-couple mechanism and a single fault plane. These characteristics are in general agreement with all previous long period kinematic studies.

In general, the simulated elliptical slip distribution reproduce well the cGPS records at inland stations, however the GJ3 ocean bottom horizontal component record with the largest displacement of 31.5 meters is not well resolved by our smoothed elliptical solutions. Our solutions give a maximum slip of around 26 to 32 meters. These results agree with the best maximum slip to fit all the data, probably it is necessary to do a more detailed slip distribution to improve these results.

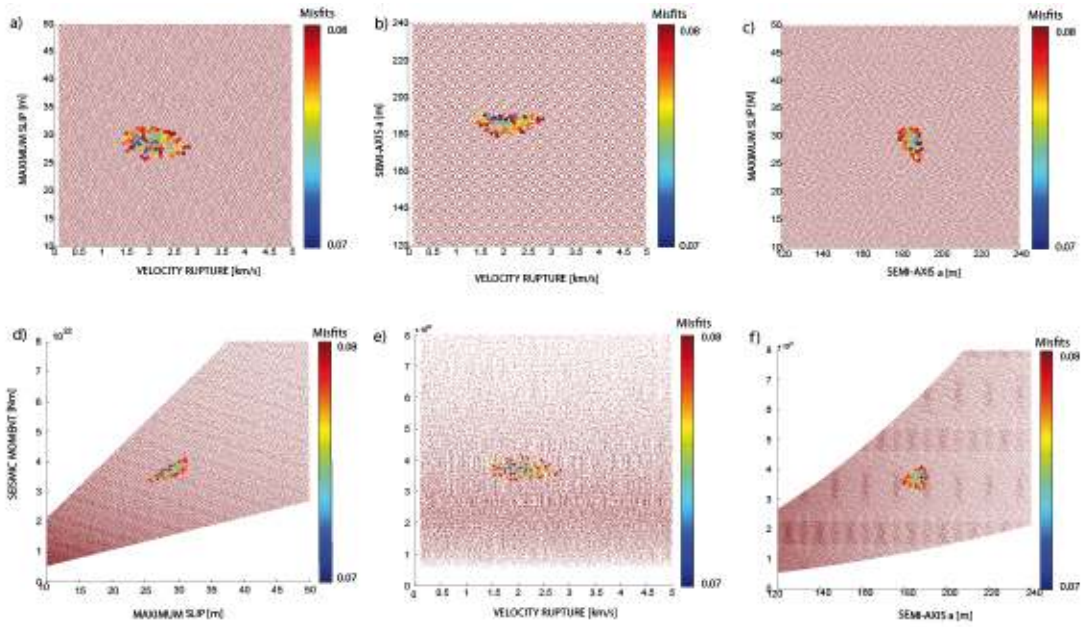

Figure 4. MC inversion by the single ellipse approach. Each dot is a simulation. The color scale was saturated for misfits larger than 0.1 and larger dot are inversions with lower misfits than 0.1. Dm, Vr and the semi axis were inverted. Figures a1, a2 and a3 show the trade-off among them. These three parameters are grouped as function of seismic moment Figures a4, a5 and a6.

Rectangular grid approach using the Neigborhood algorithm

Two rectangular grid inversions were made. First, we did an inversion using the cost function (2) where the smoothing was not considered and, second, an inversion considering the cost function (3) where smoother slip distribution were searched. Figure 5 shows the slip distribution for both approaches and its convergence after several thousand iterations.

The distribution using a smoothing cost function (3) produced smother slip distributions (Figure 5b) in comparison with the result obtained using function cost (2) (Figure 5a). However both distributions are similar to that obtained using the elliptical approach. The misfits are 0.59 and 0.62, for function cost 2 and 3, respectively. Our inversions have problems with the largest coseismic displacement of the GJ3 record, see Figure 6, we think

that our 50 x 50 km rectangle discretization is too coarse to represent adequately the heterogeneous slip distribution of the Tohoku 2011 earthquake.

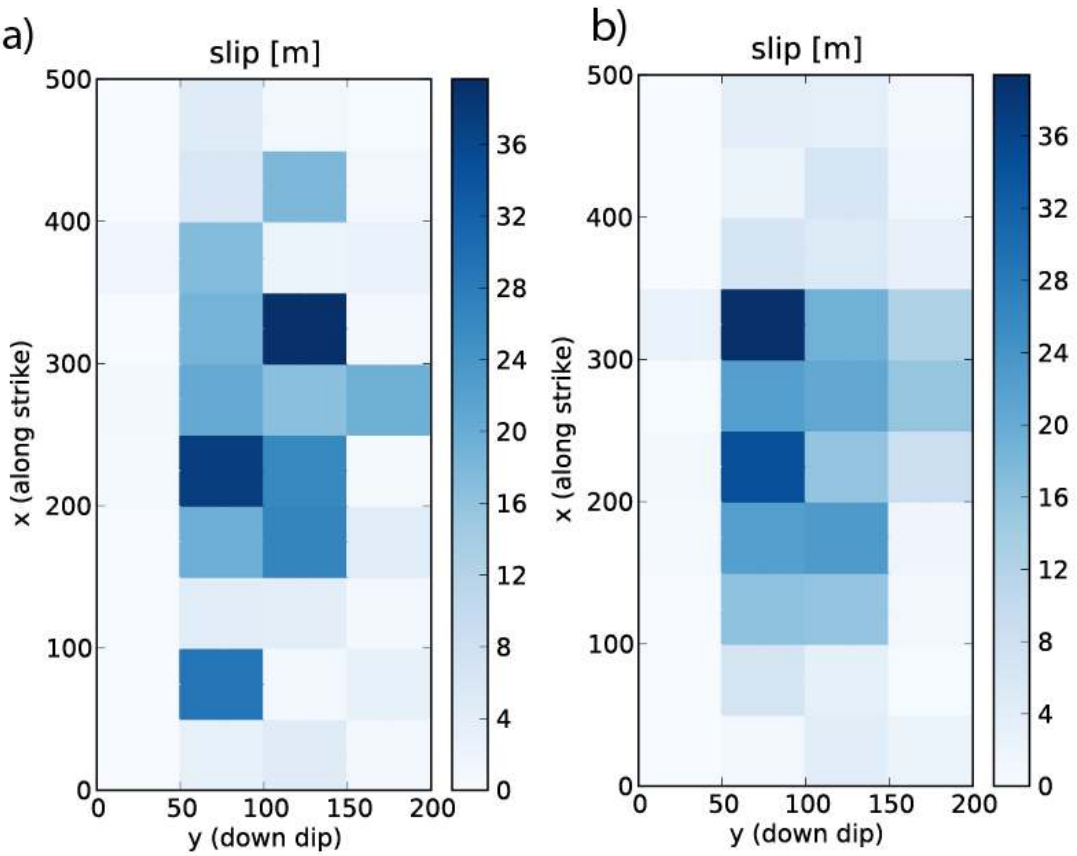

Figure 5. (a) Slip distribution considering the cost function (2) and **(b)** Slip distribution considering the cost function (3).

a)

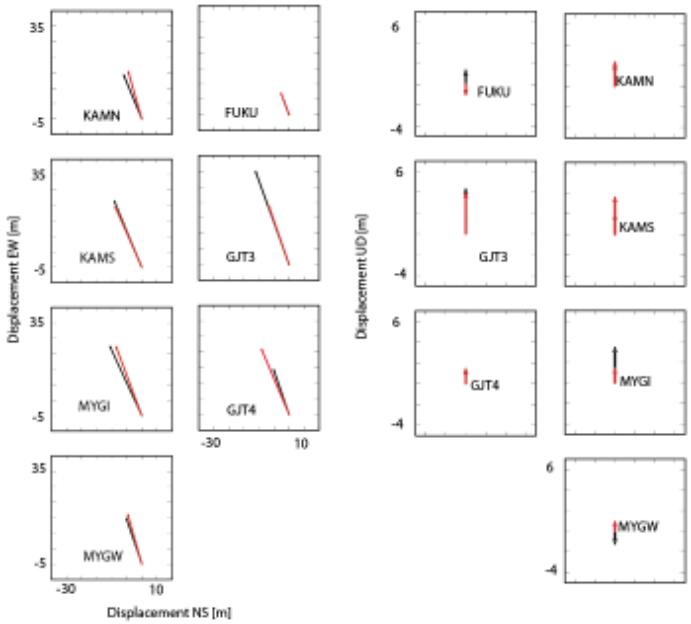

b)

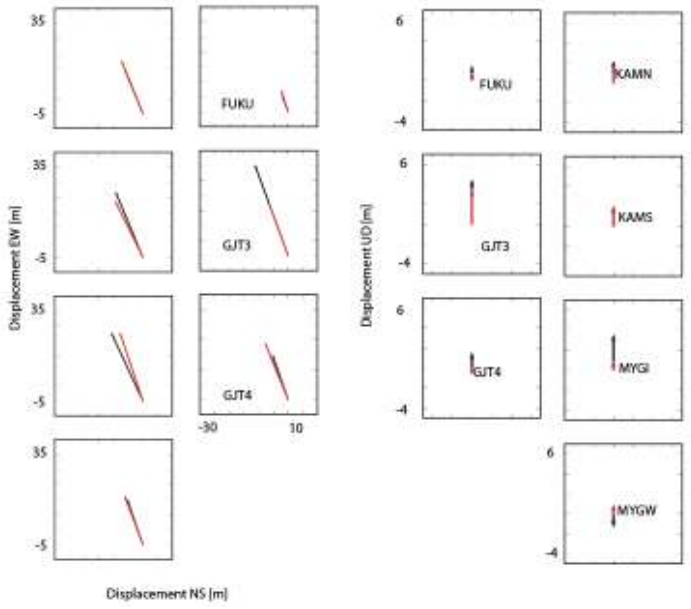

Figure 6. Static observed (black) and simulated (red) ocean bottom GPS **a)** rectangular grid approach considering the cost function (2) **b)** rectangular grid approach considering the cost function (3).

SHORT PERIOD RUPTURE PROCESS

In our previous inversions, we inverted mainly for the long period waves and static displacements. Here we explore the spatio-temporal evolution of the rupture at higher frequencies. For this purpose we used the cGPS records filtered using a high-pass corner frequency of 0.04 Hz; the records were derived once to obtain the ground velocity motions. We chose this signal processing to observe the main high frequency waves generated by the rupture process. We expect to identify and explain the nucleation and stopping phases generated during the Tohoku mega-earthquake.

Figure 7 shows the reduced set of data that we used in this section. The cGPS record number 550 shows two pulses (encircled in red), in the other stations both pulses arrive at different instants as is observed in the records of stations 928 and 033, but in other records, such as 028, both pulses arrive together or in others the first pulse has a very small amplitude (stations 041 and 042). These two pulses are identified as the nucleation wave (first pulse) and the stopping phase wave (second pulse).

First we made a kinematic inversion considering an elliptical crack, with slip distribution defined in Eq (4) and the rupture velocity is considered to be constant in all the rupture area.

$$D(x,y) = D_m \left[1 - \left(\frac{x^2}{a^2} + \frac{y^2}{b^2} \right) \right]^{\frac{1}{2}} \tag{4}$$

Where D_m is the maximum amplitude of slip inside the elliptical patch of semi-axes a and b. With this we obtained a simple solution with a maximum slip of 30 meters and rupture velocity of 1.35 km/s, see Figure 8. This solution fits well the observed records. Figure 9 shows the EW and NS records. This simple model simulated well the largest amplitude and abrupt stopping of the observed waves, because crack slip model produce large stopping phases. However our model does not reproduce the nucleation process. In order to identify the nucleation process, by trial and error we superposed a small circle to the previous elliptical crack solution. We found that superposing a circle of around 30 km of radius, 27

meters of slip and a faster rupture velocity rupture of 3.5 km/s the nucleation wave could be simulated, as shown in Figures 10 and 11.

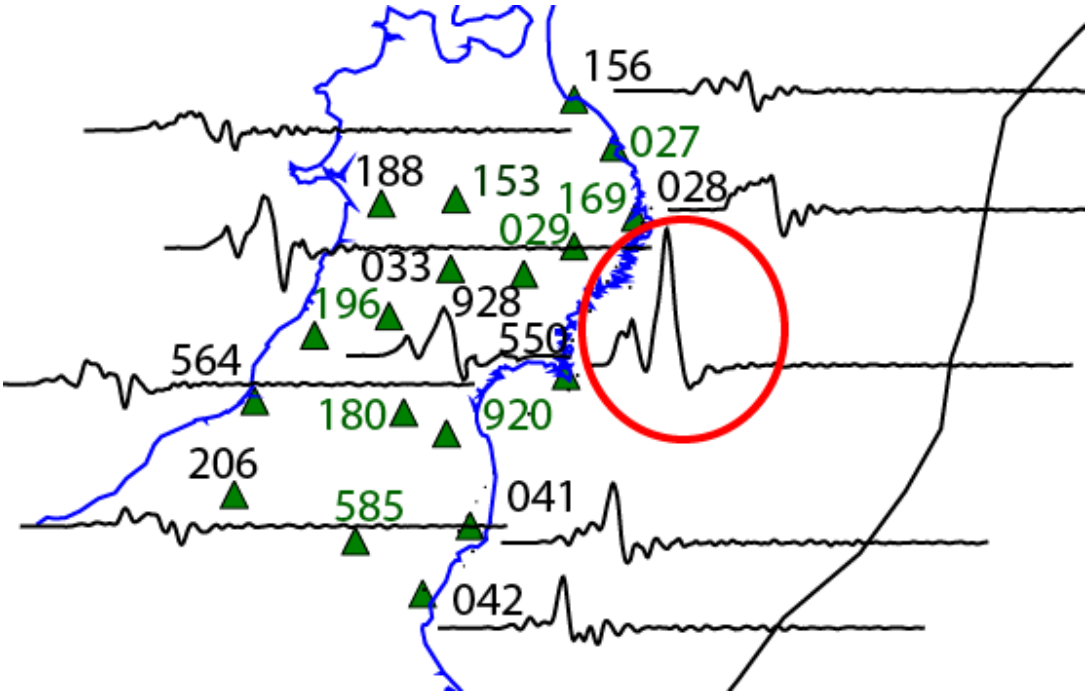

Figure 7. Green triangles are the location of the cGPS records used in the inversion. The number corresponds to the name of the cGPS record. The black numbers correspond to the velocity records shown in this figure.

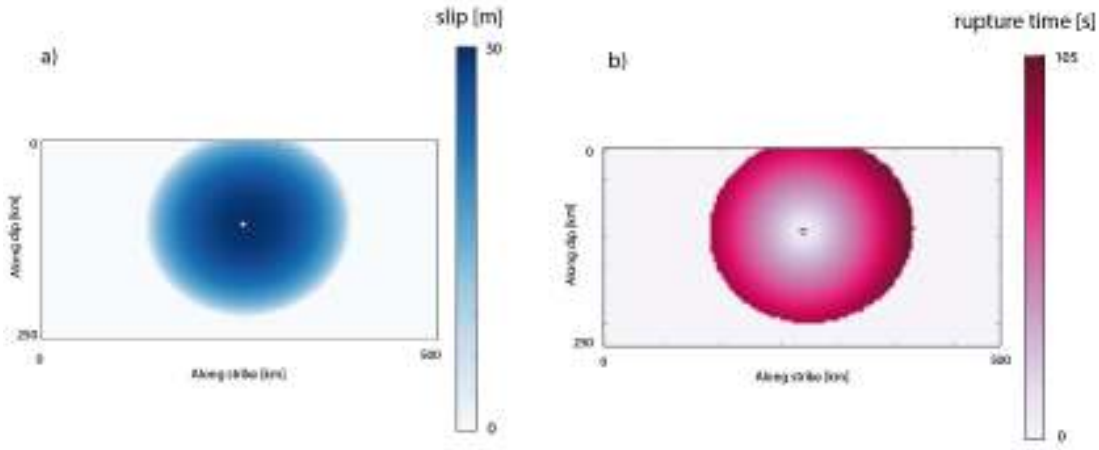

Figure 8. (a) Constant slip distribution and **(b)** constant rupture velocity for 1 ellipse crack simulation.

a)

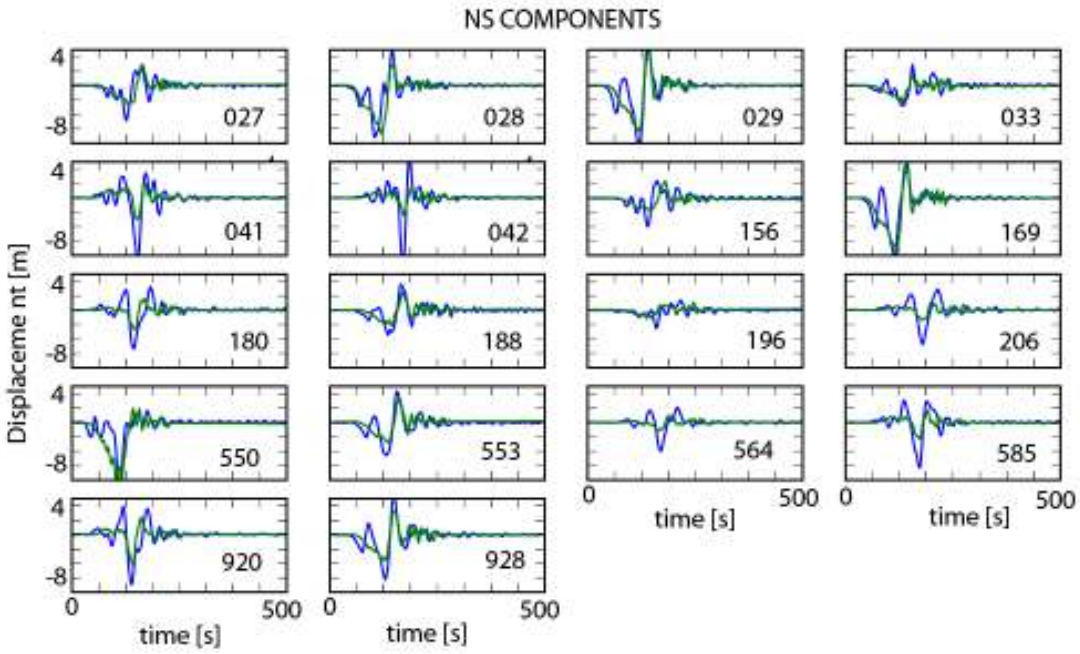

b)

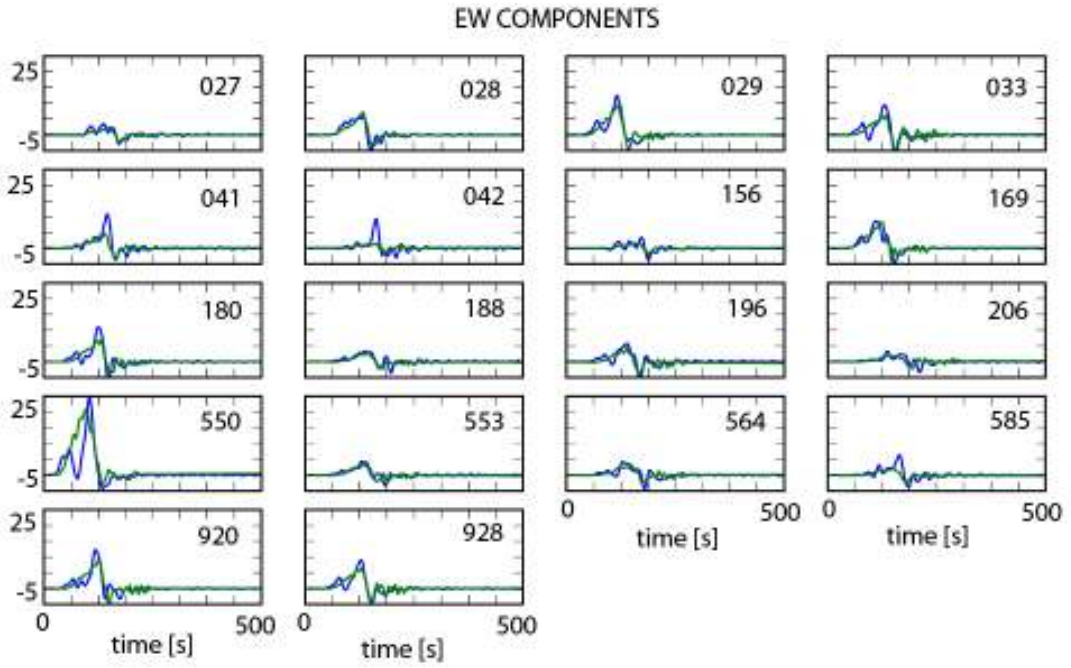

Figure 9. (a) NS and **(b)** EW components of real (blue) and simulated (green) velocity records for 1 elliptical crack simulation (see Eq. 4).

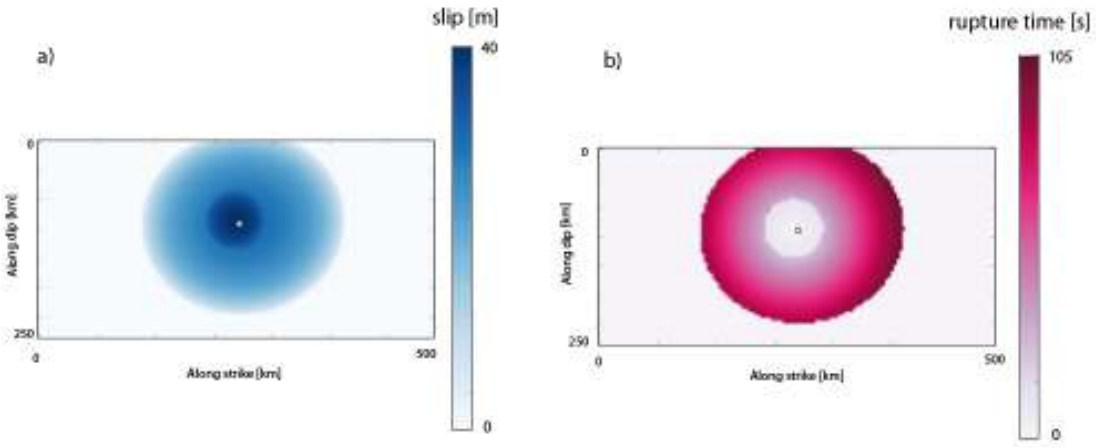

Figure 10. (a) Constant slip distribution and **(b)** constant rupture velocity for 2 ellipse crack simulation.

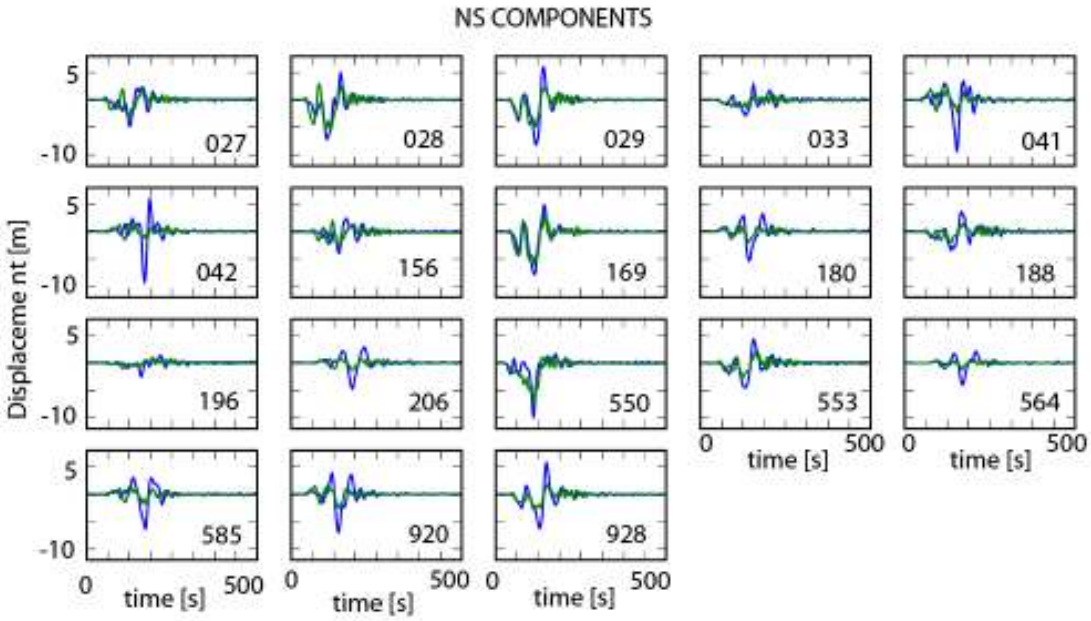

a)

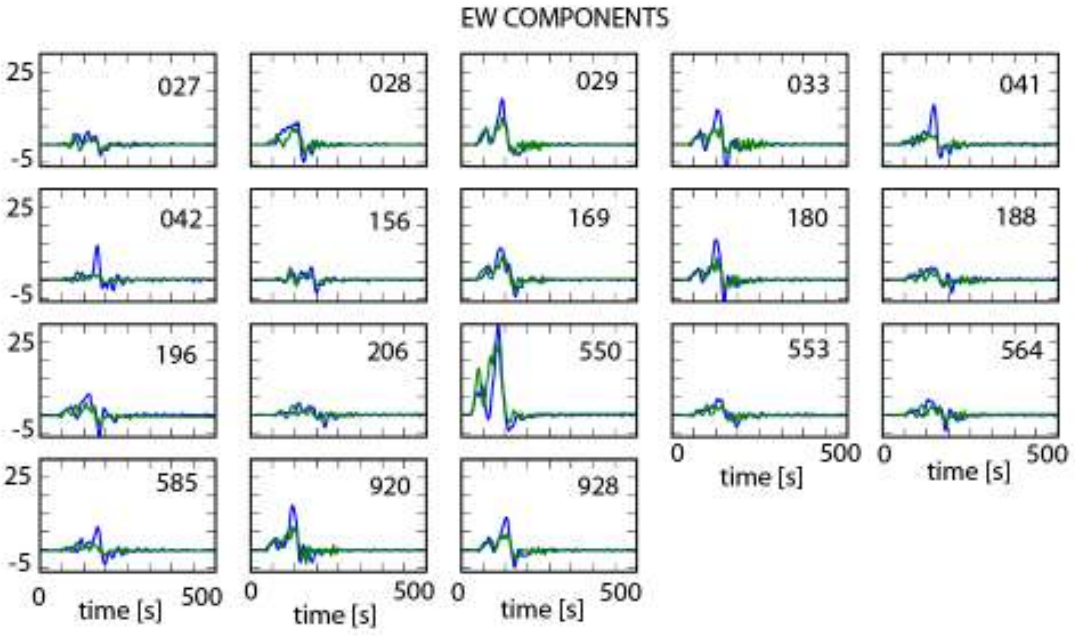

b)

Figure 11. **(a)** NS and **(b)** EW components of real (blue) and simulated (green) velocity records for 1 ellipse crack simulation.

DISCUSSION

The solutions that we obtained are characterized by large slip near of the hypocenter. The overall slip distribution is well described by a single ellipse. This most simple solution fits well the inland cGPS records. However to improve of the results, especially GPS/acoustic ocean bottom records, more heterogeneous slip distribution is necessary. We used two ellipses and a square grid discretization of 50 x 50, however a finer mesh is probably needed to improve the fit between observed and synthetic records.

The nucleation and stopping phase waves were identified and characterized by a simple crack model. We think that velocity changes observed by the back projection technique are the results of the nucleation and stopping of the rupture process proposed here. The nucleation and stopping phase waves probably may be observed directly in the strong motion records. Figure 12 derived from Suzuki et al. (2012) identified two energy arrival in the strong motion, which we proposed are related with the nucleation and stopping phase of the rupture process.

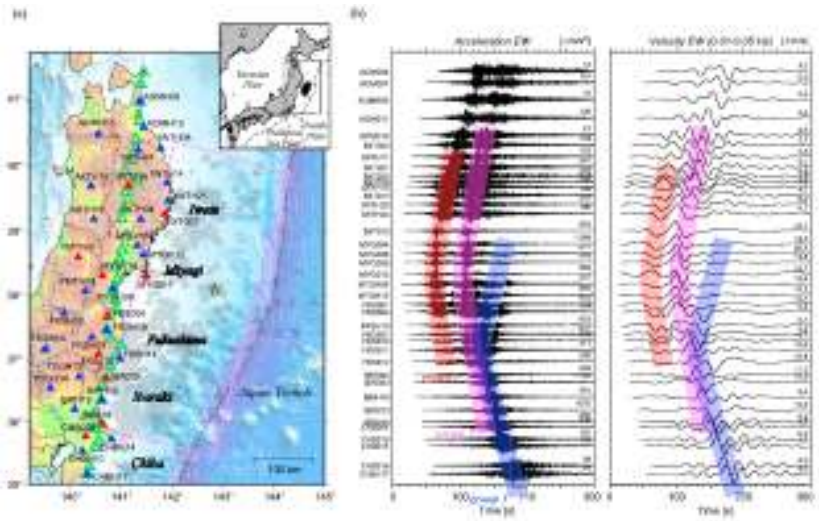

Figure 12. Strong motion records (a) location and (b) acceleration and velocity records. The color in the records identified two energy arrivals. (from Suzuki et al., 2011)

CONCLUSION

We made different preliminary inversions using elliptical patch and rectangular grid discretization of the slip distribution. We jointly continuous GPS and ocean bottom GPS/acoustic records. The optimal solutions are found comparing observed and synthetic records using the neighborhood algorithm to search for the best solution. Then we followed by an exploration of solution space with a Monte Carlo technique and we give the ranges the overall seismological characteristics of the Tohoku 2011 earthquake, which show larger displacement near of the hypocenter with a range of maximum displacement between 26 to 32 m, sub-shear velocity rupture (1.3 km/s to 2.7 km/s). The simple elliptical distribution gives similar results as those obtained with a rectangular grid approach, observing very good misfits for inland records. However, in order to improve these results we will have to work with finer grids.

The nucleation and stopping phase waves were identified and characterized with a simple crack model which could explain well the results obtained using the back projection technique and the energy arrivals in the strong motion records.

REFERENCES

Kido, M., Y. Osada, H. Fujimoto, R. Hino, and Y. Ito (2011), Trench-normal variation in observed seafloor displacements associated with the 2011 Tohoku-Oki earthquake, Geophys. Res. Lett., 38, L24303, doi:10.1029/2011GL050057.

Kiser, E. and M. Ishii (2012), The March 11, 2011 Tohoku-oki earthquake and cascading failure of the plate interface, Geophys. Res. Lett., 39, L00G25, doi:10.1029/2012GL051170.

Koketsu, K., Y. Yokota, N. Nishimura, Y. Yagi, S. Miyazaki, K. Satake, Y. Fujii, H. Miyake, Y. Yamanaka, S. Sakai, and T. Okada (2011). A unified source model for the 2011 Tohoku earthquake, Earth Planet. Sci. Lett., 310, 480-487, doi:10.1016/j.epsl.2011.09.009.

Koper, K. D., Hutko, A. R. & Lay, T. Along-dip variation of teleseismic short-period radiation from the 11 March 2011 Tohoku earthquake (Mw 9.0). .Geophys. Res. Lett. 38, L21309, doi:10.1029/2011GL049689 (2011).

Lay, T., C. J. Ammon, H. Kanamori, L. Xue, and M. J. Kim, Possible large near-trench slip during the 2011 Mw 9.0 off the Pacific coast of Tohoku Earthquake, Earth Planets Space, 63, 687–692, 2011.

Meng, L., Inbal, A. & Ampuero, J.-P. A window into the complexity of the dynamic rupture of the 2011 Mw 9 Tohoku-Oki earthquake. .Geophys. Res. Lett. 38, L00G07, doi:10.1029/2011GL048118 (2011).

Ohzono, M., Iinuma, T., Ohta, Y. & Miura, S. Coseismic slip distribution of the 2011 off the Pacific coast of Tohoku Earthquake (M9.0) estimated based on GPS data – Was the asperity in Miyagi-oki ruptured? .Earth, Planets and Space 63, 643–648, doi:10.5047/eps.2011.06.013 (2011)
Ozawa, S., T. Nishimura, H. Suito, T. Kobayashi, M. Tobita, and T. Imakiire (2011), Coseismic and postseismic slip of the 2011 magnitude-9 Tohoku- Oki earthquake, Nature, 475, 373–376, doi:10.1038/nature10227
Peyrat, S., Madariaga, R.,Buforn E., Campos, J., Asch, G. and Vilotte, J.P. Kinematic rupture process of the 2007 Tocopilla earthquake and its main aftershocks from teleseismic and strong-motion data. Geophys. J. Int. 182, 1411-1430, 2010
Pollitz, F., Bürgmann, R and Banerjee, P., 2011. Geodetic slip model of the 2011 M9.0 Tohoku earthquake. GRL,Vol. 38, L00G08, doi:10.1029/2011GL048632, 2011
Clues from joint inversion of tsunami and geodetic data of the 2011 Tohoku-oki earthquake Romano, F.; Piatanesi, A.; Lorito, S.; D'Agostino, N.; Hirata, K.; Atzori, S.; Yamazaki, Y.; Cocco, M. (2012). Clues from joint inversion of tsunami and geodetic data of the 2011 Tohoku-oki earthquake NPG Scientific Reports 2(385): 8 pp. dx.doi.org/10.1038/srep00385
Ruiz, S and Madariaga, R. (2011). Determination of the friction law parameters of the Mw 6.7 Michilla earthquake in northern Chile by dynamic inversion. Geophys. Res. Lett., 38, L09317, doi:10.1029/2011GL047147
Ruiz, **S.**, Madariaga, R., Astroza, M., Saragoni, G. R., Lancieri, M., Vigny, C and Campos, J., (2012). Short Period Rupture Process of the 2010 Mw 8.8 Maule Earthquake in Chile. In press Earthquake Spectra
Sambridge, M. (1999), Geophysical Inversion with a Neighbourhood Algorithm -I. Searching a parameter space, Geophys. J. Int., 138, 479-494.
Sato, M., T. Ishikawa, N. Ujihara, S. Yoshida, M. Fujita, M. Mochizuki, and A. Asada (2011), Displacement above the hypocenter of the 2011 Tohoku-Oki earthquake, Science, doi:10.1126/science.1207401.
Simons, M., et al. (2011), The 2011 magnitude 9.0 Tohoku-Oki earthquake: Mosaicking the megathrust from seconds to centuries, Science, doi:10.1126/science.1206731.
Vallée, M., and M. Bouchon (2004), Imaging coseismic rupture in far field by slip patches, Geophys. J. Int., 156, 615–630.
Suzuki, W., Aoi, S., Sekiguchi, H. & Kunugi, T. Rupture process of the 2011 Tohoku-Oki mega-thrust earthquake (M9.0) inverted from strong-motion data. .Geophys. Res. Lett. 38, L00G16, doi:10.1029/2011GL049136 (2011)
Yokota, Y., K. Koketsu, Y. Fujii, K. Satake, S. Sakai, M. Shinohara, and T. Kanazawa (2011), Joint inversion of strong motion, teleseismic, geodetic, and tsunami datasets for the rupture process of the 2011 Tohoku earthquake, Geophys. Res. Lett., 38, L00G21, doi:10.1029/2011GL050098.
Yue, H., and T. Lay (2011), Inversion of high-rate (1 sps) GPS data for rupture process of the 11 March 2011 Tohoku earthquake (M_w 9.1), Geophys. Res. Lett., 38, L00G09, doi:10.1029/2011GL048700.
Wang, D. and J. Mori (2011), Frequency-dependent energy radiation and fault coupling for the 2010 Mw8.8 Maule, Chile, and 2011 Mw9.0 Tohoku, Japan, earthquakes, Geophys. Res. Lett., 38, L22308, doi:10.1029/2011GL049652.

5. DETERMINATION OF THE FRICTION LAW PARAMETERS OF THE MW 6.7 MICHILLA EARTHQUAKE IN NORTHERN CHILE BY DYNAMIC INVERSION

Paper published in Geophysical Research Letters, Vol. 38, L09317,
doi:10.1029/2011GL047147, 2011

Authors: S. Ruiz and R. Madariaga

ABSTRACT

We perform a full dynamic inversion at low frequencies of the 16 December 2007 (Mw = 6.7) northern Chile earthquake that we model as a simple elliptical patch. We use two different stress-friction end-member models: asperities and barriers, finding similar results. The inversions are performed for strong motion data filtered between 0.02 and 0.5 Hz. Eleven geometrical and stress and friction parameters are inverted using the neighbourhood algorithm. The optimum solutions have relative errors lower than 0.21. The earthquake rupture has duration of less than 5 s and propagates at sub-shear speed. The rupture area is similar to that of the aftershock distribution and the seismic moment is 0.95 · 1019 Nm. We derive the friction law parameters from the models situated close to the optimum solution using a Monte Carlo technique. The results show a strong trade-off between applied stress and frictional resistance. We find that the distribution of friction models collapses into a finite zone of the space of moment and non-dimensional parameter κ. We conclude that it is possible to determine the friction law from near field seismograms, but there is a strong trade-off between friction and initial stress.

INTRODUCTION

Full dynamic inversions of seismic sources are scarce because of the limited number of well recorded earthquake and the large computational resources required. With few exceptions, dynamic inversion of earthquake rupture has been done in two steps. First a kinematic inversion is done and, then, stresses and strength are computed by dynamic

modelling [e.g., Fukuyama and Mikumo, 1993; Bouchon et al., 1998]. However, the approximations made in kinematic source models, affect the inferred dynamic parameters [Guatteri and Spudich, 2000; Piatanesi et al., 2004], propagating errors from the kinematic inversion to the dynamic simulation. In addition, dynamic inversion is intrinsically non unique as was discussed by Peyrat et al. [2001]. Two endmodels of the earthquake source heterogeneity can be used in the inversion: the barrier [Das and Aki, 1977] and asperity [Kanamori and Stewart, 1978] models. Although similar radiation is predicted for these two models [Madariaga, 1979], only in the partial dynamic inversion of the 1992 Landers earthquake has it been possible to test this hypothesis with strong motion data [Peyrat et al., 2001]. [3] Peyrat and Olsen [2004] did a full dynamic inversion of the 2000 Tottori earthquake using a classical discretisation of the fault into rectangles with constant stress and rupture resistance. Di Carli et al. [2010] improved these results using a stress distribution described by a few elliptical patches. Because of limited resolution and computer resources Di Carli et al. [2010] could not completely invert for the parameters of the friction law.

Here we do a full dynamic inversion of the Michilla, northern Chile, earthquake of 16 December 2007. This Mw 6.7 event was an intraplate intermediate depth earthquake recorded by strong motion, broad band and short period instruments. These high quality data allow us to invert for the parameters of stress, the friction law, and the geometry and location of the rupture area, in total 11 parameters. The search for the best solutions are made using the Neighbourhood algorithm (NA) [Sambridge, 1999], and once an optimum solution is found by NA, we use the Montecarlo method (MC) to explore the initial stress field and the friction law.

THE MICHILLA EARTHQUAKE

The 16 December 2007 Northern Chile earthquake occurred inside the subducted Nazca plate at 43 km depth with an epicenter at 22.98°S, 70.24°W near the town of Michilla in the southern part of the rupture area of the Mw 7.8 Tocopilla earthquake of 2007 [Delouis et al., 2009; Peyrat et al., 2010]. Peyrat et al. [2010] performed a kinematic inversion of this event finding that the earthquake could be modeled as a simple elliptical shear fault with

seismic moment of 2.14 × 1019 Nm (Mw = 6.8). The slab-push type rupture propagated along an almost vertical fault plane (strike 4°N, dip 85°, rake 90°) (Figure 5.1). The aftershocks of the Michilla earthquake were distributed along the fault plane covering an ellipsoidal zone less than 10 kilometres of radio centered on the hypocenter of the event (A. Fuenzalida et al., manuscript in preparation, 2012) (Figure 5.1).

This earthquake was very well recorded by short period, broad band and strong motion instruments [Sobiesiak et al., 2008; Schurr et al., 2009; R. Boroschek et al., Terremoto Norte Chile, 14 Noviembre de 2007 M = 7.7, available from http://www.terremotosuchile.cl]. For the inversion we used two types of strong motion data: Episensor FBA ES-T continuously recording accelerometers at 100 Hz with 24 bit digitizers; and triggered instruments, mostly Kinemetrics ETNA with 24 bit Episensor digitizers at 200 Hz (http://www.terremotosuchile.cl). The strongmotion data are baseline corrected and filtered using a band-pass causal Butterworth filter of order 4, and then integrated twice. The synthetic time series obtained from inversion are filtered in the same way. The corner frequency of the lowpass filter was chosen as 0.02 Hz because some records were triggered and had durations of only 100 seconds. We chose a highpass corner frequency of 0.5 Hz, because above this frequency site effects or reflections in shallow strata are not well reproduced by the 1D velocity model that we used [Husen et al., 1999]. Although, we tested all the strong motion records available, we worked with the 5 records shown in Figure 5.1 because they have the highest signal to noise ratio.

DYNAMIC INVERSION METHOD

In the forward dynamic problem we assumed that rupture occurred inside a flat elliptical patch. We assumed that stress and friction were uniform inside the fault because we are looking for the average properties of the rupture. Rupture propagation was controlled by the slip-weakening friction law proposed by Ida [1972]:

$$\begin{aligned} T_f(D) &= T_u\left(1-\frac{D}{Dc}\right) \qquad D < Dc \\ T_f(D) &= 0 \qquad\qquad\qquad\quad D > Dc \end{aligned} \tag{1}$$

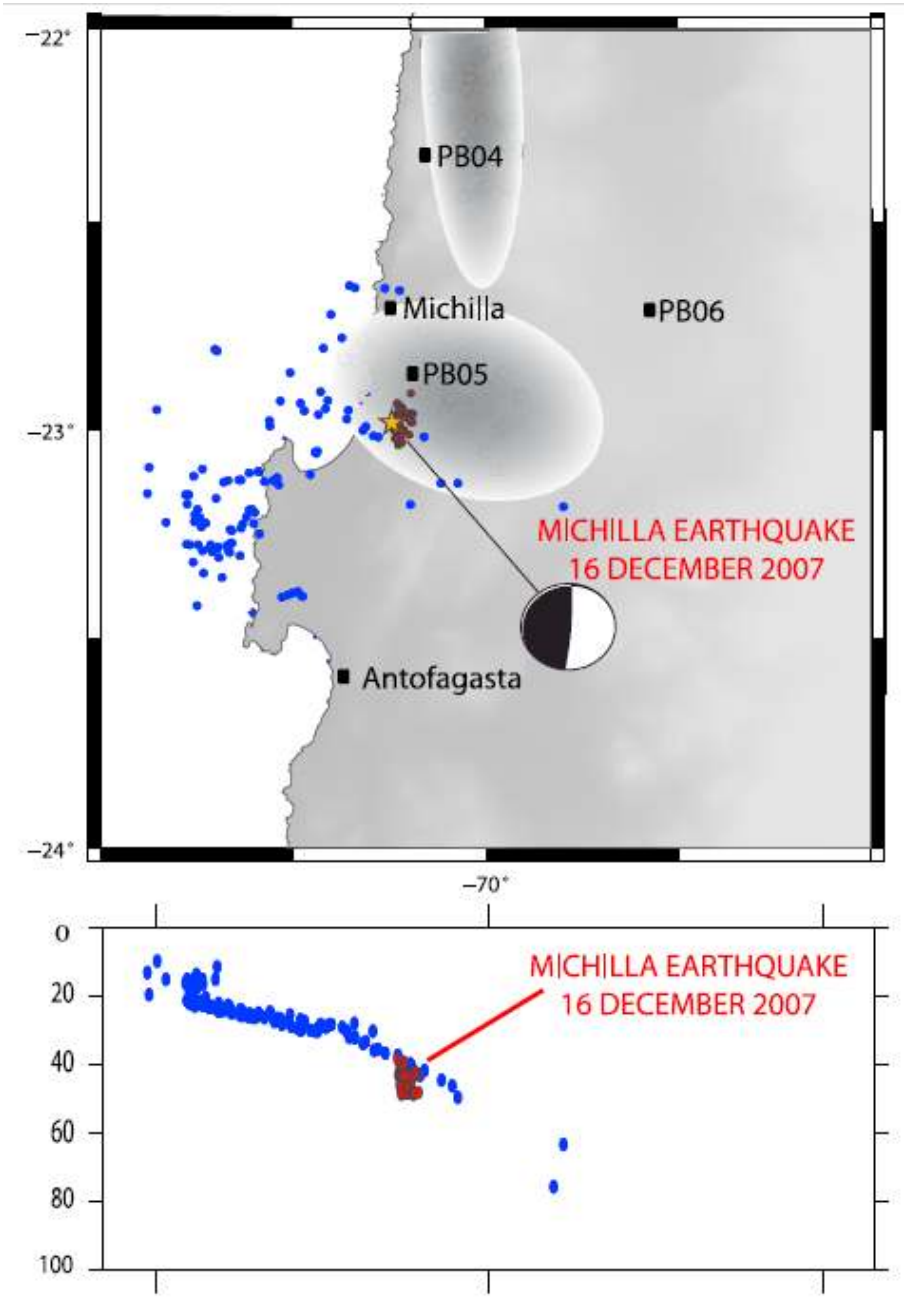

Figure 5.1. Location of the Michilla earthquake of 16 December 2007 in Northern Chile. This is a slab push event situated inside the subducted Nazca plate, immediately bellow the rupture zone of the Tocopilla earthquake of 14 November 2007. The grey ellipses show the slip areas determined by Peyrat et al. [2010] for the main event of 14 November 2007. Black squares are the locations of the strong motion instruments used in this work. The relocated events of 16 December 2007 are shown in red and the events from 13 to 16 December 2007 with blue colour (Fuenzalida et al., manuscript in preparation, 2012).

where Tf is friction as a function of slip D. Tu is the peak frictional stress or strength and Dc is the slip weakening distance. In (1) a constant kinematic friction should be added, for simplicity we assumed that it was equal to 0. Other versions of slip weakening friction [see, e.g., Bizzarri, 2009] can be used but we do not think that our observations can distinguish among them.

The elliptical patch is described by 5 parameters, two for the principal semi-axis (a and b), two for the position of the ellipse with respect to the hypocenter (X, Y) and the angle of the principal axis. As shown in Table 1 the range of variation of geometrical parameters was sufficiently broad so that a large set of potential elliptical ruptures were explored in the inversion. For rupture initiation we followed the methodology of Madariaga and Olsen [2000] assuming that rupture was triggered by a small circular asperity of radius R′ inside of the ellipse, with strength Te′ that is higher than the peak frictional stress Tu. We inverted both for R′ and Te′. Once rupture breaks the small asperity, it can grow or stop spontaneously depending on the values of the stress field (Te) and the friction law. In our model we assumed that stress and friction were constant inside the elliptical rupture zone. As shown in Table 5.1, we explored 4 stress parameters: the slip-weakening distance Dc and yield stress Tu of the friction law (1), and the external applied stress Te. Outside the ellipse, stress and friction depend on the rupture model. For the asperity model [Kanamori and Stewart, 1978], the region outside the ellipse was considered to have a negative initial stress load Tout so that rupture stopped when it reached this region of reduced initial stress. For the barrier model [Das and Aki, 1977] the yield stress outside the rupture zone was a very large positive Tout constant, so that rupture stops because friction becomes very large. The 11 parameters were inverted independently for the asperity and barrier models.

Table 5.1. Values of the 11 inverted parameters for the Asperity and Barrier models[a]

	Geometry					Nucleation		Stress			
Model	Semi Axis a [Km]	Semi Axis b [Km]	X [Km]	Y [Km]	Angle [rad]	R′ [Km]	T_e' [Mpa]	T_e [Mpa]	T_u [Mpa]	D_c [m]	T_{out} [Mpa]
Asperity	4.00	10.12	0.85	−2.00	1.50	0.98	23.65	14.97	19.18	0.65	−108.4
Barrier	4.23	12.42	0.28	−2.00	0.07	1.00	14.74	10.89	12.82	0.56	130.1
Range minimum	4	4	−2	−2	0	0.8	8	8	8	0.4	−8
Range maximum	14	14	2	2	1.57	2	120	50	100	2	8 −1800 1800

[a]The optimal values are on the first two lines and the ranges of variation of these parameters during the inversion are shown in the last two lines.

A 3D fourth-order staggered-grid finite differences method with absorbing boundaries and thin fault boundary conditions was used to solve the forward dynamic rupture simulation [Madariaga et al., 1998]. The spatial and temporal discretisations were 200 m and 0.005 s respectively. The grid had 160 × 160 × 160 elements and was centered at the hypocenter on the fault plane. The fault zone is 32 km wide and 32 km deep but only a small part broke during the earthquake. The AXITRA code [Coutant, 1990; Bouchon, 1981] was used to simulate wave propagation from the source to the receivers. Time and space steps in AXITRA were four times finer than those of the finite difference grid to insure accurate simulations. We used the crustal model proposed by Husen et al. [1999] for Northern Chile.

Synthetic records were compared with real records, using the L2 norm:

$$\chi^2 = \frac{\sum_i (obs - synth)^2}{\sum_i (obs)^2} \qquad (2)$$

where obs are the observed displacement and synth, the simulated displacement. The sum runs over all samples in every seismogram considered in the inversion. The inversion was made using NA in order to search for the rupture model with minimum misfit. During the inversion many models did not propagate at all, those models have $\chi^2 = 1$. Other models produced very fast ruptures that do not fit the data at all, they had $\chi^2 > 1$. Once the NA inversion converged, we explored solutions near the minimum using a Monte Carlo (MC) technique. Since we are particularly interested in the friction law, we fixed all the parameters except the applied stress and friction, Te, Tu and Dc.

For each model visited in the inversion we computed the seismic moment Mo and the non-dimensional parameter κ.

$$\kappa = \frac{T_e^2 L}{\mu T_u D_c} \qquad (3)$$

Where L, the characteristic size of the event, is taken as the shorter semiaxis of the source ellipse, m is the shear modulus, Te, Tu and Dc were already defined. κ is roughly the ratio

of available strain energy to energy release rate, it controls the overall characteristics of the rupture process as discussed by Madariaga and Olsen [2000].

DYNAMIC INVERSION RESULTS

The inversions of the asperity and barrier models converged to models that produce a relative residual χ^2 lower than 0.21. These models had slip and slip rate distributions that were in agreement with the seismic moment, duration and slip distribution expected for an intraplate intermediate depth earthquake of Mw 6.7. Figure 5.2 shows the slip distribution and rupture time as a function of position on the fault for the best barrier (Figure 5.2b) and asperity (Figure 5.2a) models. The ruptures are characterized by a slow initial rupture propagation and large slip in the final part of the rupture. The total duration of the rupture in both cases is less than 5 seconds. The fit between the real and synthetic records is shown in Figure 5.3 where only the results of the asperity model are shown; similar results were obtained for the barrier model.

Table 5.1 shows the values obtained for the 11 inverted parameters. Table 2 shows the χ^2 and κ values obtained for these models. We recall that the critical value for a circular rupture is $\kappa_c = 0.6$ [Madariaga and Olsen, 2000]. The geometrical parameters are practically the same for the best asperity and barrier models; this is reflected in Figure 5.2 where the slip distribution and rupture isochrones are very similar for the two models. However, the stress and friction parameters Te, Tu and Dc are quite variable. This difference does not affect the slip distribution and rupture time of the best models, because there is clearly a finite set of models that satisfies the observations.

Table 5.2. κ and χ values for the best asperity and barrier models

Model	χ^2	κ
Asperity	0.209	1.15
Barrier	0.206	1.11

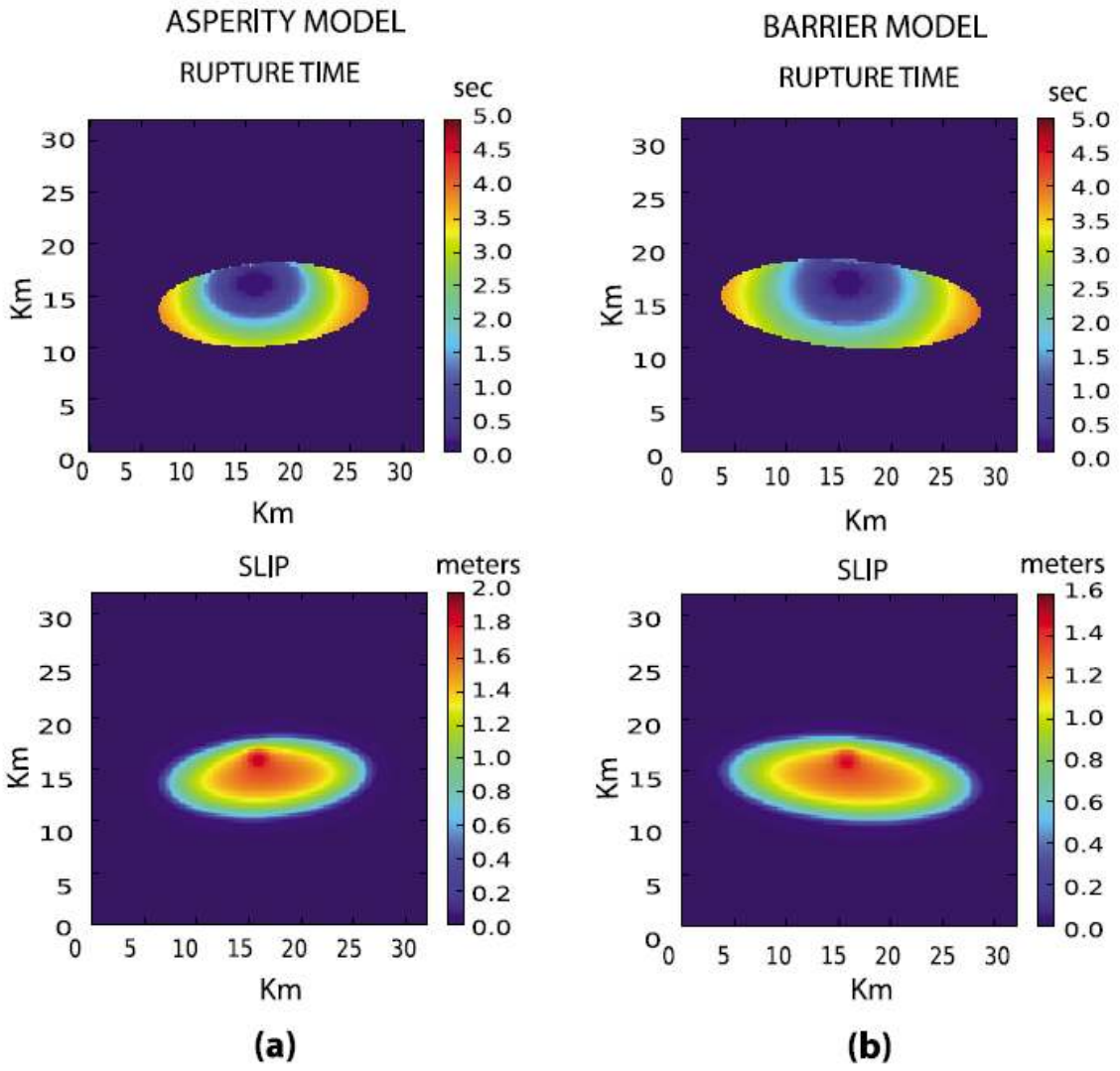

Figure 5.2. Slip and rupture isochrones for the 2007 Michilla earthquake of Northern Chile. The top figures show the rupture time and the lower figures the slip distribution of the best (a) asperity and (b) barrier model. The total moment for both models is 1. 1019 Nm and duration is 4.5 s for both models.

In order to explore the relation between stress and friction parameters we used the MC method, fixing all the parameters of the models with the exception of Te, Tu and Dc. The other parameters were fixed at those of the optimum model in Table 5.1. The MC inversions allow us to explore the solution space, showing the relations among the stress – friction parameters and how these are related to χ^2, Mo and κ. Figure 5.4 (top) shows the results for the MC inversion of the asperity model where more than 30,000 models were

simulated, similar results were obtained for the barrier model. In the same manner as for NA, many of the models explored correspond to combination of stress-friction parameters that do not fit the data well. Some have high χ^2 (small brown dots), others have χ^2 near to 1 (small green dots). In Figure 5.4 (top) the best MC models, with misfit c < 0.3 are drawn with larger blue dots. These models are located on a rather flat irregular surface of the space Te, Tu and Dc (Figure 5.4, top). As shown in Figure 5.4 (middle), these models could be collapsed into a single linear structure when the models were projected on the plane (Te^2, TuDc). In Figure 5.4 (middle) the models with $\chi^2 < 0.3$ appear as a narrow diagonal band of blue coloured dots. Similar results obtained for other values of χ^2 are shown in Figure 5.S1 of the auxiliary material.

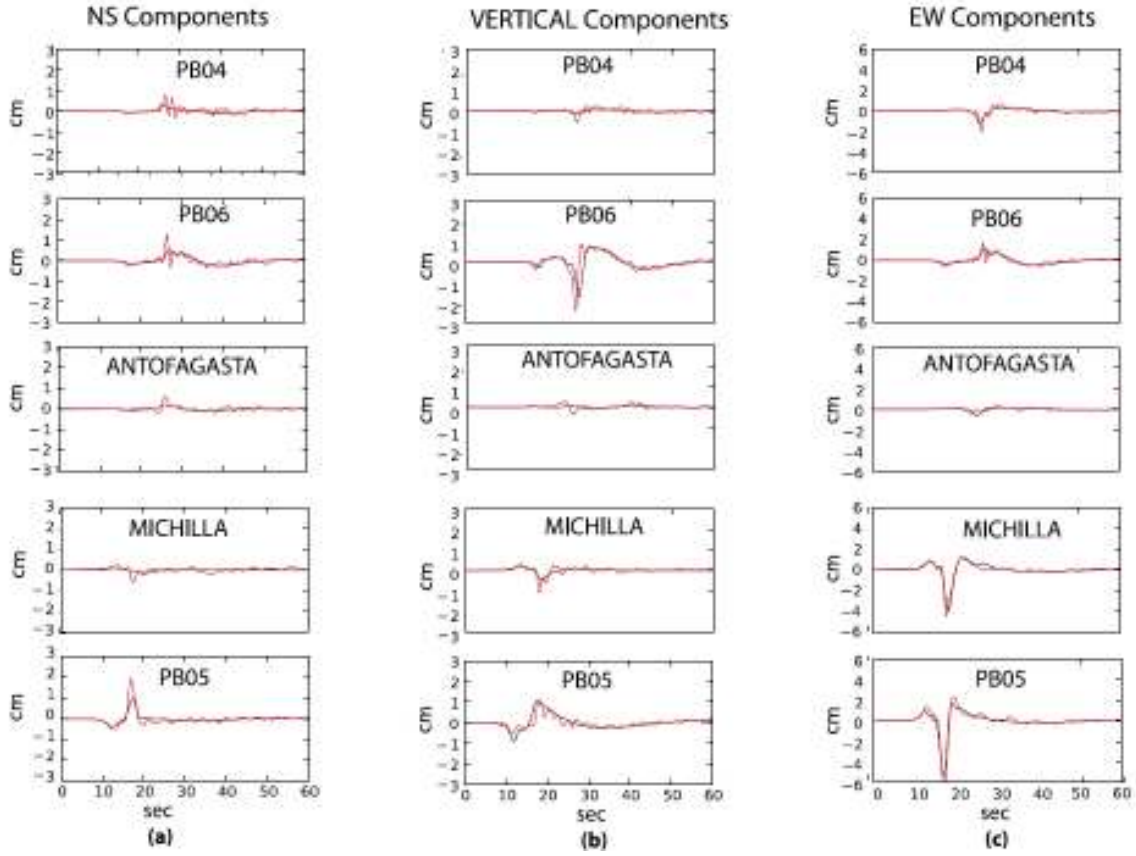

Figure 5.3. Comparison between real (red) and synthetic (black) displacements obtained with the NA inversion algorithm for the asperity model of the 2007 Michilla earthquake. The relative misfit between observed and synthetics was $\chi^2 = 0.2091$. (a) EW components, (b) vertical components and (c) NS components.

The alignment of the best models observed in Figure 5.4 (middle) has a simple interpretation. These models share similar values of κ, the non-dimensional control parameter defined in (3). In Figure 5.4 (bottom) we plot the models of Figure 5.4 (top), on the seismic moment vs κ plane. Figure 5.4 (bottom) shows that the models with $\chi^2 < 0.3$ can be grouped in an elongated volume where the seismic moment varies between 0.4 · 1019 and 1.4 · 1019 Nm and κ varies between κ = 0.7 and κ = 1.2. This zone is shown in a different way in Figure 5.S2 of the auxiliary material. The seismic moment associated with the best model inverted by NA was 0.95 · 1019 Nm which corresponds to Mw = 6.6. The models that fit the observations near the optimum form an extended surface that is controlled by the non-dimensional number κ and by the seismic moment that measures the overall slip at the source.

DISCUSSION AND CONCLUSIONS

We did a full dynamic inversion of the 16 December 2007 Michilla intermediate depth earthquake for both the asperity and barrier models of seismic rupture. The models were described by 11 parameters. The optimal models had normalized errors c2 lower than 0.21. The slip and slip rate distribution for the best asperity and barrier models are similar, confirming the earlier conjecture that seismic data cannot distinguish between barrier and asperity models [Madariaga, 1979]. The earthquake grew at low initial speed, accelerating near the boundaries of the elliptical rupture. The rupture area is similar to that of the aftershock distributions. The seismic moment was of 0.95 · 1019 Nm or Mw 6.6 slightly less than the Mw 6.8 found by Peyrat et al. [2010].

We explored the parameters of the friction law around the best solution using a MC technique fixing the geometrical parameters. We looked for the combination of stress and friction parameters that produced models that fit the data with relative errors of less than 30% We found that these solutions form a narrow irregular surface when the solutions were projected into the Te^2 vs TuDc plane. This is a clear indication that good solutions of the inverse problems are actually controlled by seismic moment and κ. Models with misfit $\chi^2 <$ 30% belong to a narrow range of κ values between 0.7 and 1.2. Our results clearly show that seismic observations are compatible with a certain range of frictional and stress

parameters determined by the seismic moment of the event and κ. We chose the Michilla earthquake because it had a simple rupture surface as determined from kinematic inversions by Peyrat et al. [2010]. For more complex events a single ellipse will not be sufficient to describe its geometry but we expect the main result to remain valid: it is possible to estimate the friction law from seismic observations but there are clear tradeoffs between stress and friction.

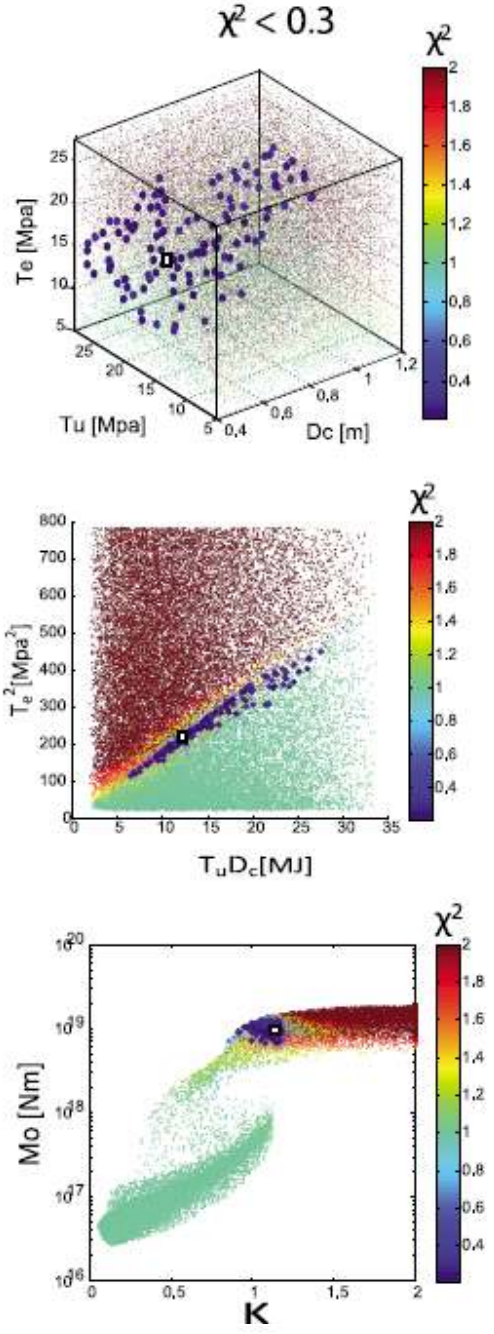

Figure 5.4. Study of the stress and friction parameters by Monte Carlo inversion. In all the plots, each dot corresponds to one simulated model. The larger points have a relative error $\chi^2 < 0.3$. The color scale is saturated for misfits $\chi^2 \geq 2$. The black square corresponds to the optimum solution determined by NA (lowest c2) (top) Plot of error for each model projected onto the Dc, Te, Tu, plane. Dots are coloured according to the value of χ^2 as indicated in the colour bar. Models with $\chi^2 < 0.3$ form a narrow irregular surface. (middle) The models are projected on the plane Te^2 versus TuDc. Models with $\chi^2 < 0.3$ are plotted with bigger blue dots; they form a narrow elongated structure that indicates that these models share a common non-dimensional number _. (bottom) Model relative error χ^2 plotted as a function of the global parameters seismic moment and κ. The better models form a narrow zone in the M0, κ plane (blue dots).

Acknowledgments. This work was supported by FONDECYT 1100429 in Chile and by ANR DEBATE in France. Sergio Ruiz was partially supported by the Nucleo Milenio IERC-MB. We thank B. Schurr and other colleagues at GFZ who deployed the plate boundary stations in Northern Chile (PBs); Frank Scherbaum of GFZ and R. Boroschek of Universidad de Chile for the accelerograms. We sincerely thank M. Lancieri, J. Campos, A. Fuenzalida, S. Peyrat and J. P. Vilotte for their help and advice. Finally, we thank Ruth Harris and two anonymous referees for their very useful and constructive reviews. The Editor thanks Andrea Bizzarri and an anonymous reviewer for their assistance in evaluating this paper.

REFERENCES

Bizzarri, A. (2009), What does control earthquake ruptures and dynamic faulting? A review of different competing mechanisms, Pure Appl. Geophys., 166(5–7), 741–776, doi:10.1007/s00024-009-0494-1.

Bouchon, M. (1981), A simple method to calculate Green's functions for elastic layered media, Bull. Seismol. Soc. Am., 71, 959–971.

Bouchon, M., M. Campillo, and F. Cotton (1998), Stress field associated with the rupture of the 1992 Landers, California, earthquake and its implication concerning the fault strength at the onset of the earthquake, J. Geophys. Res., 103, 21,091–21,097, doi:10.1029/98JB01982.

Coutant, O. (1990), Programme de simulation numerique AXITRA, Rapport LGIT, Univ. Joseph Fourier, Grenoble, France.

Das, S., and K. Aki (1977), Fault plane with barriers-versatile earthquake model, J. Geophys. Res., 82, 5658–5670, doi:10.1029/JB082i036p05658.

Delouis, B., M. Pardo, D. Legrand, and T. Monfret (2009), The Mw7.7 Tocopilla earthquake of 14 November 2007 at the southern edge of the Northern Chile seismic gap: Rupture in the deep part of the coupled plate interface, Bull. Seismol. Soc. Am., 99, 87–94, doi:10.1785/0120080192.

Di Carli, S., C. Francois-Holden, S. Peyrat, and R. Madariaga (2010), Dynamic inversion of the 2000 Tottori earthquake based on elliptical subfault approximations, J. Geophys. Res., 115, B12328, doi:10.1029/2009JB006358.

Fukuyama, E., and T. Mikumo (1993), Dynamic rupture analysis: Inversion for the source process of the 1990 Izu Oshima, Japan earthquake (M6.5), J. Geophys. Res., 98, 6529–6542, doi:10.1029/92JB02451.

Guatteri, M., and P. Spudich (2000), What can strong-motion data tell us about slip-weakening fault friction laws?, Bull. Seismol. Soc. Am., 90, 98–116, doi:10.1785/0119990053.

Husen, S., E. Kissling, and G. Asch (1999), Accurate hypocentre determination in the seismogenic zone of the subducting Nazca plate in northern Chile using a combined on-/off-shore network, Geophys. J. Int., 138, 687–701, doi:10.1046/j.1365-246x.1999.00893.x.

Ida, Y. (1972), Cohesive force across tip of a longitudinal-shear crack and Griffith specific surface-energy, J. Geophys. Res., 77, 3796–3805, doi:10.1029/JB077i020p03796.

Kanamori, H., and G. S. Stewart (1978), Seismological aspects of the Guatemala earthquake of February 4, 1976, J. Geophys. Res., 83, 3427–3434, doi:10.1029/JB083iB07p03427.

Madariaga, R. (1979), On the relation between seismic moment and stress drop in the presence of stress and strength heterogeneity, J. Geophys. Res., 84, 2243–2250, doi:10.1029/JB084iB05p02243.

Madariaga, R., and K. B. Olsen (2000), Criticality of rupture dynamics in 3-D, Pure Appl. Geophys., 157, 1981–2001, doi:10.1007/PL00001071.
Madariaga, R., K. B. Olsen, and R. Archuleta (1998), Modeling dynamic rupture in a 3D earthquake fault model, Bull. Seismol. Soc. Am., 88, 1182–1197.
Peyrat, S., and K. B. Olsen (2004), Nonlinear dynamic rupture inversion of the 2000 Western Tottori, Japan, earthquake, Geophys. Res. Lett., 31, L05604, doi:10.1029/2003GL019058.
Peyrat, S., K. Olsen, and R. Madariaga (2001), Dynamic modeling of the 1992 Landers earthquake, J. Geophys. Res., 106, 26,467–26,482, doi:10.1029/2001JB000205.
Peyrat, S., R. Madariaga, E. Buforn, J. Campos, G. Asch, and J. P. Vilotte (2010), Kinematic rupture process of the 2007 Tocopilla earthquake and its main aftershocks from teleseismic and strong-motion data, Geophys. J. Int., 182, 1411–1430, doi:10.1111/j.1365-246X.2010.04685.x.
Piatanesi, A., E. Tinti, M. Cocco, and E. Fukuyama (2004), The dependence of traction evolution on the earthquake source time function adopted in kinematic rupture models, Geophys. Res. Lett., 31, L04609, doi:10.1029/2003GL019225.
Sambridge, M. (1999), Geophysical inversion with a neighbourhood algorithm -I. Searching a parameter space, Geophys. J. Int., 138, 479–494, doi:10.1046/j.1365-246X.1999.00876.x.
Schurr, B., A. Asch, F. Sodoudi, A. Manzanares, O. Ritter, J. Klotz, G. Chong-Diaz, S. Barrientos, J.-P. Villotte, and O. Oncken (2009), The International Plate Boundary Observatory Chile (IPOC) in northern Chile seismic gap, Abstract EGU2009-11040 presented at General Assembly 2009, Eur. Geosci. Union, Vienna, 19–24 April.
Sobiesiak, M., S. Eggert, H. Grosser, T. Walter, B. Schurr, J. P. Vilotte, C. Arranda, H. Woith, H. U. Wetzel and G. Gonzales (2008), Post seismic task force operation after the Mw 7.7 Tocopilla earthquake in northern Chile, Abstract EGU2008-A-09928 presented at General Assembly 2008, Eur. Geosci. Union, Vienna, 13–18 April.

FIGURAS AUXILIARES

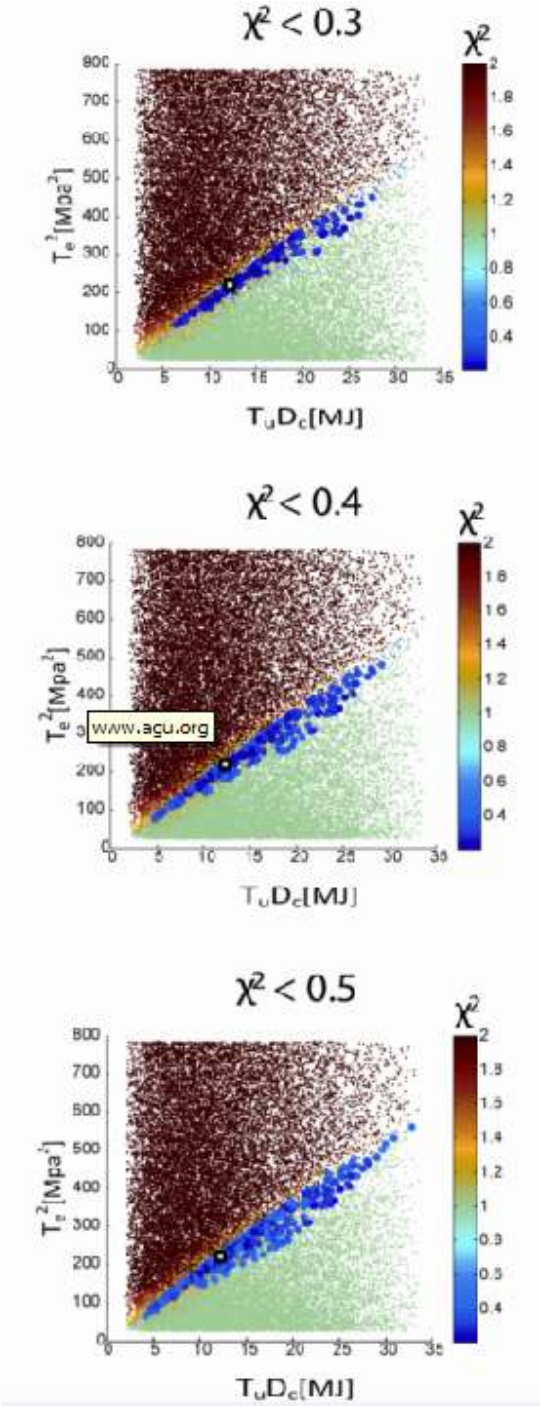

Figure 5.S1 Models sampled by the Monte Carlo method projected on the plane Te2 versus TuDc.

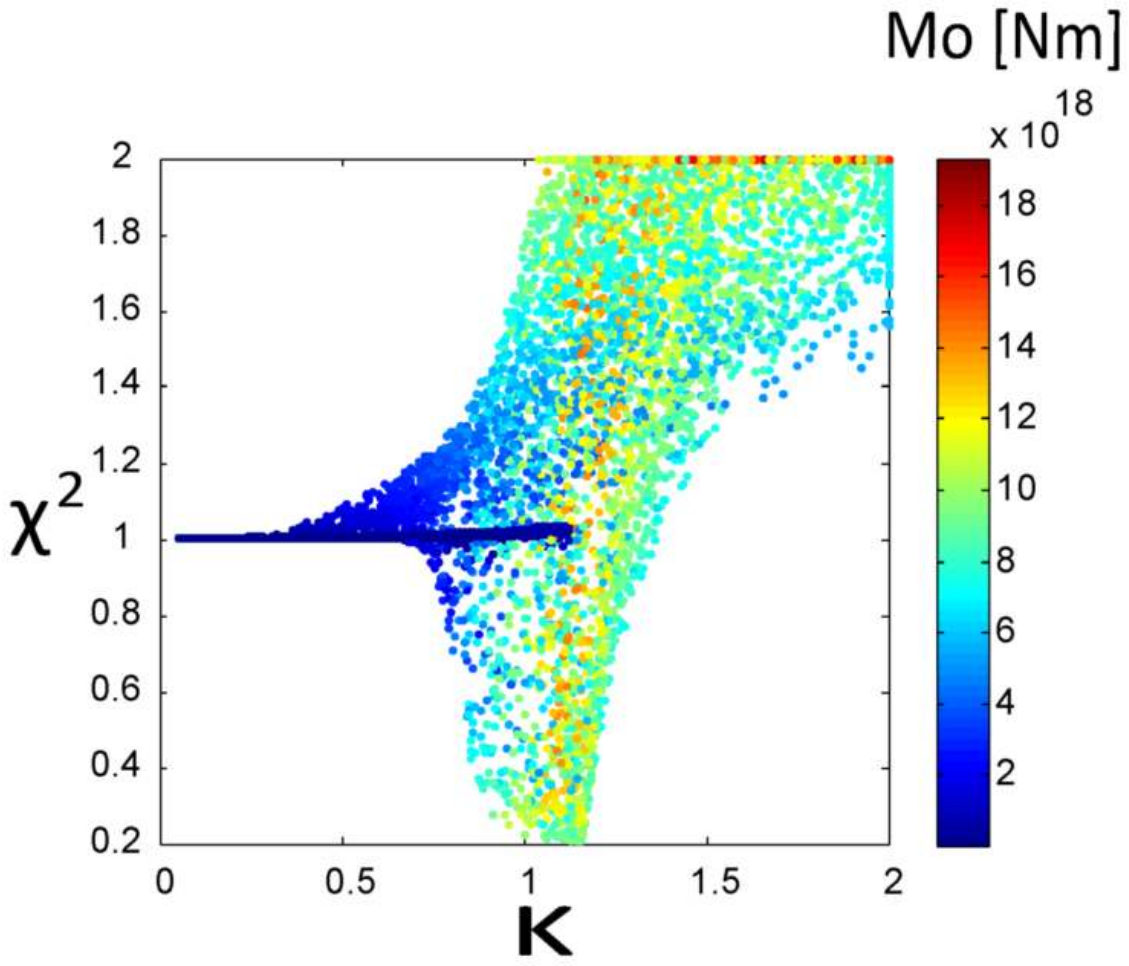

Figure 5.S2. Models sampled by the Monte Carlo method projected on the plane χ2 versus κ.

6. KINEMATIC AND DYNAMIC INVERSION OF THE 2008 NORTHERN IWATE EARTHQUAKE

Paper accepted in BSSA

Authors: S. Ruiz and R. Madariaga

ABSTRACT

We perform kinematic and dynamic inversion of the 24 July 2008 (Mw=6.8) Northern Iwate intermediate depth earthquake in Japan using strong motion records from the K-NET and Kik-Net networks. The rupture of this moderate magnitude earthquake is modeled as a simple elliptical patch. The optimal solutions are found comparing observed and synthetic records using an L^2 norm and the neighborhood algorithm to search for the best solution; followed by an exploration of solution space with a Monte Carlo technique. The geometry of the rupture, rupture velocity and slip distribution are estimated by kinematic inversion. The rupture geometry, stress and friction parameters are obtained by dynamic inversion. Both approaches converge to very similar source models with semi-minor axes of 4 km, maximum slip of about 4 m and large stress drops in the 30-45 MPa range. Rupture duration was less than 3 s because of very high sub Rayleigh rupture propagation speeds. Energy release rate for the best models was in the range 23-36 MJ/m^2, a rather large value for events of this size. For both kinematic and dynamic inversions we found families of solutions that fit the strong motions data within a certain error, confirming the strong trade-off among inverted parameters. Finally, we demonstrate that dynamic inversion solutions are controlled by the dynamic similarity parameter κ and by seismic moment M_0. These two parameters define a region of model space where dynamically similar models fit the observations with approximately the same misfit.

INTRODUCTION

The Iwate 2008 intra-slab intermediate depth (Mw 6.8) earthquake occurred inside the subducted Pacific plate in northern Japan (Suzuki et al., 2009). The epicenter of the

earthquake was located on land so that it had an excellent azimuthal coverage by strong motion instruments of the K-net and KIK-net networks. The maximum JMA seismic intensity was 6 and PGA values larger than 1 g were observed at a few sites. Strong intermediate earthquakes of this kind occur often in Japan, for instance the 1987 eastern Chiba event of M_{JMA} 6.7 (Fukuyama, 1991); the 1993 Kushiro-oki of Mw 7.6 (Ide and Takeo, 1996); the 2001 Geiyo earthquake of Mw 6.7 (Miyatake et al., 2004); the 2003 Miyagi-oki earthquake M 7.1 (Okada and Hasegawa, 2003) or the 1994 Hokkaido Toho-oki (Shikotan) earthquake Mw 8.2 (Kikuchi and Kanamori, 1995). Thanks to the dense seismic and strong motion networks of Japan it is possible to study these events in detail because local site effects are limited for the stations located closer to the epicenter.

The conventional approach to invert seismic ruptures in the near field is to do a kinematic inversion of the observed records in order to compute the distribution of slip or slip rate on the fault for simple models of the rupture process. From these kinematic models of the rupture process it is then possible to compute dynamic source parameters (Fukuyama and Mikumo, 1993; Ide and Takeo, 1996; Bouchon et al., 1998; among others). Many approximations used in the kinematic models affect the determination of the dynamic parameters (Guatteri and Spudich, 2000; Piatanesi et al., 2004), propagating errors from the kinematic inversion to the dynamic simulation. A better method would be to invert directly for stress and strength distribution using fully dynamic models. Dynamic inversion is difficult because we need exceptionally well-recorded events with limited site effects. Dynamic inversion is also expensive because at each step in the inversion process it is necessary to compute a full numerical simulation. The first full dynamic inversions were made by Peyrat and Olsen (2004), DiCarli et al. (2010) and Ruiz and Madariaga (2011). In the latter work a full dynamic inversion was made using an elliptical patch approach in which it is assumed that the geometry of the source can be modeled by a small number of elliptical patches. In the inversion of the 2007 Michilla northern Chile earthquake Ruiz and Madariaga (2011) used only 5 strong motion records for the determination of 11 source parameters, among them the stress, friction and geometrical parameters.

In the present paper we do dynamic inversion of the 2008 Northern Iwate intermediate depth earthquake of northern Japan. This earthquake was recorded by several

dozens strong motion instruments of the K-NET and KiK-net networks. Suzuki et al (2009) studied this earthquake using a classical kinematic inversion method based on rectangular slip patches. Here we model the earthquakes using simple elliptical slip o stress patches in the kinematic and dynamic inversion. We use a neighborhood algorithm (NA) to determine the best fitting models and a Monte Carlo approach (MC) to study the resolution of inversion and to explore the vicinity of the optimal model.

THE IWATE 2008 EARTHQUAKE AND AVAILABLE DATA

The 24 July 2008 Northern Iwate, Japan intraplate intermediate depth earthquake was located at 39.739°N, 141.671°E and 115 km depth (NIED). Its seismic moment was 1.93 10^{19} Nm and it had a normal-fault focal mechanism (strike 178°, Dip 73° and Rake -95°) with large non-double couple component according to the Global Moment Tensor project (GMT). For reasons of simplicity, however, in our inversions we used a single fault plane and did not consider possible non-double couple components, nor two different fault planes as was proposed by Suzuki et al. (2009). This earthquake was very well recorded by the K-NET (Kinoshita, 1998) and KiK-net strong motion networks (Aoi et al., 2000), deployed by the National Research Institute for Earth Science and Disaster Prevention (NIED) in Tsukuba and by the Japan Meteorological Agency (JMA), Figure 6.1. We used both networks in this work, but from the KiK-net network stations we chose only the strong motion instruments installed in boreholes. Figure 6.1 shows the location of the earthquake (star) and the location of the SM instruments that we used in kinematic and dynamic inversion.

Records from both networks were band pass filtered with a high-pass corner at 0.5 Hz and a variable low pass corner frequency; we used 0.02 Hz for borehole KIK-net stations and 0.04 Hz for surface K-NET stations. The low frequency cut-off was chosen to avoid the effects of rotation and noise on the integration of strong motion records. The high-pass limit is necessary to avoid deficiencies in the 1D velocity model available for the region and to reduce site effects. The strong motion records were filtered using a Butterworth filter of order 2, then they were resampled from 100 Hz to 5 Hz, and twice integrated removing the linear base line in each integration. Figure 6.2 shows the

processing of two records used in the inversion. In the upper panel (2a) we compare the Fourier Spectra at stations IWTH03 EW and IWT023 EW before and after the application of the band pass filter. The filter corners are indicated by the vertical lines. The gray trace shows the acceleration Fourier spectra of the original strong motion record with only a linear base line removed and the black trace shows the filtered acceleration Fourier spectrum. Figure 6.2b shows the filtered acceleration, velocity and displacement records at stations IWTH03 EW and IWT023 EW. Inversions were made using displacement because we were interested in determining the low frequency properties of the source like average slip, stress drop, etc. Several velocity records were affected by surface waves that we cannot reproduce with the 1D velocity model that we used. Modeling 2D or 3D wave propagation is currently beyond the computer resources that are available to us.

KINEMATIC INVERSION

We first did a kinematic inversion in order to determine the main features of the models based on the elliptical patch approximation that will be used in the dynamic inversion (see DiCarli et al., 2010; Ruiz and Madariaga, 2011). The shape of the rupture zone is assumed to be an elliptical patch, located inside a fault plane of 32 x 32 km. The geometry of the ellipse is defined by the following parameters: the location of the center of the ellipse with respect to the hypocenter of the earthquake, the principal semi-axes (noted *a* and *b*) and the angle of the principal axis with respect to the horizontal. We assumed also that the slip distribution had a Gaussian distribution

$$D(x,y) = D_m \exp\left[-\left(\frac{x^2}{a^2}+\frac{y^2}{b^2}\right)\right] \quad (1)$$

Where D_m is the maximum amplitude of slip inside the elliptical patch of semi-axes *a* and *b*. During the inversion a constant rupture velocity *Vr* was assumed. See Table 5.1 for a list of the parameters that we used. A total of 7 parameters were inverted of which 5 were geometrical: 2 axes (a, b) and 1 angle (α), and 2 for the position of the center of the ellipse. Two additional parameters define the kinematics: the maximum slip D_m and the rupture

velocity *Vr*. The source time function was the same for every point on the fault. By trial and error we chose a triangular function of duration 2 s around the rupture time.

The AXITRA code (Coutant, 1990; Bouchon, 1981) was used to simulate wave propagation from the source to the receivers. For the propagation of seismic waves we used the same model of the structure as Suzuki et al. (2009). Their model is a modification of that of Ukawa et al. (1984).

The inversion was made using the Neighborhood Algorithm (NA) to search for the rupture model with minimum misfit and the Monte Carlo technique to study the resolution in the vicinity of the best model. Synthetic records were compared with real records, using the normalized L^2 norm:

$$\chi^2 = \frac{\sum_i \left(obs_i - calc_i\right)^2}{\sum_i obs_i^2} \tag{2}$$

where obs are the observed displacement and calc, the simulated displacement. The sum runs over all samples in every seismogram considered in the inversion.

Because we disposed of a large number of records we used different combinations of them to create several datasets. For each dataset kinematic inversion converged in a few thousand iterations to very similar results. For this reason we show only the results for two datasets: Dataset 1 that consists of 17 KIK-net records filtered between 0.02 to 0.5 Hz,.and located within a radius of 65 km from the epicenter; These are denoted by grey circles in Figure 6.1. Dataset 2 consisted of all available K-net and KIK-net records within 40 km of the epicenter filtered between 0.04 to 0.5 Hz. Dataset 2 is shown by the black circles and squares in Figure 6.1. Both inversions converge to a well defined misfit minimum and stable seismic moment close to 1.5 10^{19} Nm in about 3000 iterations as shown in Figure 6.3. The best models found with the two data sets are listed in Table 5.1. Figure 6.4 shows the slip distribution and the rupture isochrones for these two models. In spite of their differences these models produce very similar records as shown in Figures 6.5 where we compare observed and synthetic EW and NS seismograms. The comparison between observed and synthetic records shows a good overall fit of the displacement records except

at stations IWTH23, IWTH22 and IWTH04 whose S wave arrival times appear to be shifted with respect to the other records in the dataset. This is probably due to problems with the 1D velocity model.

An important issue is how well the synthetics fit the records not just in time domain but also in the Fourier spectral domain. In Figure 6.6 we show two records for the best model obtained from Dataset 1. Full results for both datasets are shown in Auxiliary figures 6.1 and 6.2. All the synthetic Fourier Spectra present a strong negative hole at around 0.5 Hz (the cut-off frequency of the high pass cut-off filter). This occurs because of negative interference of stopping phases emitted by the edges of the ellipses.

Kinematic inversion is non-unique. During the study of NA inversions we found different solutions with low misfits. After close examination we found that there was a clear trade-off between maximum slip D_m, rupture velocity V_r and seismic moment Mo. To explore this trade-off, we did a Monte Carlo (MC) inversion of dataset 1 in which only V_r, D_m and the semi-axis a were allowed to change. In the MC inversion the semi-axis b and a were forced to have the same aspect ratio (b/a= 0.56). This is the aspect ratio for the best model that was found by the NA algorithm. All other parameters were fixed to the values listed in Table 5.1. In Figure 6.7 we plot the residuals of the models visited by the MC algorithm; those with misfits lower than 0.5 are plotted with larger dots (50 % of the variance is explained by the data). These models fill preferably a zone of the V_r space between 2 and 9 km/sec, D_m from 1 to 8 m and semi-axis a between 5 and 14 km. The seismic moment Mo of these models were in the range between $1 \cdot 10^{19}$ Nm and $2 \cdot 10^{19}$ Nm. The wide range of V_r values observed in Figure 6.7b to 6.7c, includes models with sub-shear and super-shear rupture.

This family of solutions provides the overall characteristics of the Iwate earthquake using double-couple mechanism and a single fault plane. These characteristics are in general agreement with the more detailed kinematic study made by Suzuki et al. (2009). In Figure 6.8 we compare the result of kinematic inversion by Suzuki et al (2009) with the best solution that we found. In our simulations there are small problems with the NS and

Vertical components of some records (See Figures 6.5 and 6.6 and auxiliar Figure 6.S1 and 6.S2), which could be due to non-double couple components in the mechanism (cGMT) or perhaps the need of a secondary rupture as suggested by Suzuki et al. (2009).

DYNAMIC INVERSION METHOD

We did a full dynamic inversion of the near field strong motion record starting from the previous kinematic results. We used a single elliptically-shaped fault instead of a grid of rectangles because the slip discontinuities at the edge of the rectangular patches produce strong stress singularities, and it is not clear how can rupture propagate from one patch to another. It is certainly possible to smooth the stress distribution of the rectangular patches using splines or other interpolation methods. For the moment such approach is still too expensive because of the large number of degrees of freedom involved. For this reason we adopted the same elliptical shaped fault model that we used for kinematics assuming that stress and friction were uniform inside the elliptical fault. This is a low frequency approach designed to look for the average properties of the rupture. We assumed that rupture propagation was controlled by the slip-weakening friction law proposed by Ida [1972]:

$$T_f(D) = (T_u - T_r)\left(1 - \frac{D}{Dc}\right) + T_r \qquad (3)$$

where T_f is friction as a function of slip D. T_u is the peak frictional stress or strength and D_c is the slip weakening distance. In (3) the constant kinematic or residual friction T_r on to the right hand side cannot be determined from seismic observations only (see Madariaga, 1979). For simplicity, in the following we assume that the residual friction $T_r = 0$. Other, more complex friction laws can be tested but we do not think that the present data can distinguish them. The only hope to obtain more detailed friction laws is to go to higher frequencies which are too expensive to model for the moment.

In our forward dynamic model, rupture starts at the hypocenter triggered by a small circular asperity following the methodology of Madariaga and Olsen (2000). Once rupture breaks the small asperity, it can grow or stop spontaneously depending on the values of the stress field (T_e) and the friction law. In our model we assumed that stress and friction were

constant inside the elliptical rupture zone. In the dynamic inversion we explored 3 friction and stress parameters: the yield stress T_u and the slip-weakening distance D_c of the friction law (3), the external applied stress T_e, and 2 parameters for the small circular asperity of Radius R' inside of ellipse and strength T_e' that is higher than the peak frictional stress T_u, in addition to the 5 geometrical parameters 2 axis and 1 angle and the position of the center of the ellipse. In total 10 parameters were inverted. As was proposed theoretically by Madariaga (1979) and observed by Ruiz and Madariaga (2011) the seismic data cannot distinguish between barrier (Das and Aki, 1977) or asperity models (Kanamori and Stewart, 1978). For this reason we only show the inversion made using the asperity model where the region outside the ellipse was considered to have a very large negative initial stress load that was enough to stop rupture when it reached the edge of the ellipse. The stress outside of ellipse was fixed *a priori* to a very large negative value, we checked that its exact value did not have much influence in the final results as long as it was able to stop rupture.

A 3D fourth-order staggered-grid finite differences method with absorbing boundaries and thin fault boundary conditions was used to solve the forward dynamic rupture simulation (Madariaga et al., 1998). The spatial and temporal discretization were 200 m and 0.005 s respectively. The CFL constant for this grid is everywhere less than 0.3 so that the finite difference method is stable. With this grid size it is possible to model rupture propagation and generate seismograms valid up to the cut off frequency as we will verify this at the end of the dynamic inversion. The grid had 160x160x160 elements and was centered at the hypocenter on the fault plane. The fault zone is 32 km wide and 32 km deep but only a small part broke during the earthquake. The AXITRA spectral code was used to simulate wave propagation from the source to the receivers, time and space steps were four times finer than those of the finite difference grid to insure accurate simulations. Once we found the best dynamic model using the Neighborhood Algorithm we explored a large region around the minimum with a Monte Carlo method in order to study the resolution of the inverse problem. As shown by Ruiz and Madariaga (2011) these solutions share the non-dimensional similarity parameter κ

$$\kappa = \frac{T_e^2}{\mu T_u} \frac{L}{D_c} \tag{4}$$

where L, the characteristic size of the event, is taken as the shorter semi axis of the source ellipse, μ is the shear modulus, T_e, T_u and D_c were already defined. κ is roughly the ratio of available strain energy to energy release rate, so that it controls the overall characteristics of the rupture process as discussed by Madariaga and Olsen, (2000).

DYNAMIC INVERSION RESULTS

We did non-linear dynamic inversion using the same two dataset that we used for kinematic inversion (Figure 6.1). Table 5.2 shows the optimal values for the inverted parameters of the two datasets and the range of values that were explored during the inversion. The best results using NA have a misfit $\chi^2 \approx 0.4$, meaning that our model explains 60% of the observed data. They also converge to a seismic moment Mo ≈ 1.5 10^{19} Nm, similar to that obtained from the kinematic inversion. The misfits for each step in the inversion are shown in Figure 6.9. In this figure we also show the value of κ for each model using a color scale, κ converges to a value of 1.34 and 1.45 for Dataset 1 and Dataset 2, respectively. The convergence to a well defined value of κ can be explained by the trade-off between the initial stress and the friction law parameters.

Figure 6.10 shows the slip distribution and slip rate for the best dynamic models obtained by the NA. The overall characteristics determined by kinematic inversion are confirmed: a very short rupture duration of less than 2.1 seconds, implying very high sub-shear rupture velocity. Rupture starts in the small asperity and then propagates to the rest of the fault mainly in a direction away from the surface. Figure 6.11 shows snapshots of slip rate on the fault plotted every 0.4 s. The largest values of slip rate are attained near the boundaries of ellipse where the large negative stress stopped the rupture. This happened at about 2.1 sec for both datasets.

Figure 6.12 shows synthetic and observed horizontal displacements at the different sites of dataset 1. We observe that synthetics reproduce very well the observed records with the exception of stations IWTH23, IWTH22 and IWTH04, the same stations that were not well modeled in the kinematic inversion. Duration is in the order of 4-5 sec for each record implying a very fast rupture and a massive stress drop. In Figure 6.12 we show the Fourier

spectra computed for a subset of the EW components of the seismograms shown in Figure 6.11. We observe that the dynamic models fit the spectra much better than the kinematic models shown in Figure 6.5. The most obvious difference is that the spectral hole near 0.5 Hz is only present in some of the most distant stations. We think that this is an effect of the variable rupture speed of dynamic models. In the auxiliary Figure 6.3 we show all the components of Dataset 1 and the results for Dataset 2 appear in the auxiliary Figure 6.4.

Dynamic inversion is non-unique. The previous results show that dynamic models converge to a zone where the misfit is of the order of 0.38-0.39 and the value of parameter κ approaches 1.34-1.45. There is a clear tradeoff between κ and the fit χ of the seismograms. This trade-off implies that there must be several models with similar κ that fit the data with a certain misfit. In order to explore the resolution of dynamic inversion we used the Monte Carlo method, fixing the geometric parameters to be those of best dynamic model found from the inversion of Dataset 1. The parameters for this model are listed in Table 5.2. Because the exploration of the model space is expensive and difficult to plot we decided to explore values of the dynamic parameters T_e, T_u and D_c. keeping all other parameters fixed to those of the best model. In Figure 6.14 at the top we plot the results of Monte Carlo exploration in the space of dynamic parameters *Te,* T_u, D_c. The fit of each model to the observed data is shown with the color scale. Models plotted in brown correspond to combination of stress-friction parameters that produce models that do not fit the data at all, many having misfits χ larger than 1. Models with misfits lower than 0.5 are drawn with large blue dots; these dots represent a family of models that fit the observations well. The results are similar to those observed for the Michilla 2007 inversion (Ruiz and Madariaga, 2011). The models that have lower misfits are located on a relatively flat irregular surface in the space of parameters T_e, T_u and D_c (Figure 6.14a). The zone is elongated in the T_u, D directions. We already observed in Figure 6.8 that convergence was closely related with the value of κ. In Figure 6.12 we projected the results onto the plane (T_e^2, T_uD_c). We observe (Figure 6.14b) that the blue models, those that have misfits less than 50 % are now located in a narrow wedge meaning that the good models are controlled by the ratio of T_e^2 to T_uD_c..

Finally we plotted the seismic moment Mo of the models against their κ. All the models that fit the data with error less than 50% are now grouped in an elongated area where the seismic moment varies around $1.5.10^{19}$ Nm and κ varies between 1 and 2.5. As was proposed by Madariaga and Olsen (2000) large values of κ correspond to models that tend to propagate at super-shear velocities. Considering that more than 30.000 models were visited during the MC inversion, the number of super-shear models that fit the data is small but not null. Among these models we chose one with low misfit ($\chi^2 = 0.45$) and high value of kappa ($\kappa = 2.06$). The parameters *Te, Tu* and *Dc* for this model are listed in Table 5.3. Although the synthetic records are very similar to those computed for sub-shear ruptures (see Auxiliar figure 6.5), the rupture process for the supershear model is very different from that of the model with best fit. In Figure 6.15 we show the slip and rupture isochrones for the supershear event. The rupture front shown in Figure 6.15a presents a clear super-shear instability in the *in-plane* direction which for the Iwate intermediate depth earthquake is in the almost vertical direction. The rupture front at 1 s has the characteristic "ears" in the supershear direction. The jump to supershear speed occurred around 0.7 s.

DISCUSSION

The kinematic and dynamic inversions of the 2008 Northern Iwate intermediate depth earthquake are non unique even if the sources are described by simple elliptical patches. In the kinematic inversion the solutions collapse to a limited set of values of rupture velocity, maximum slip and area of the ellipse, which converge to the similar values of the seismic moment of $1.5\ 10^{19}$ Nm and duration of the earthquake.

The admissible solutions from dynamic inversion form a region in parameter space that is controlled by the dynamic similarity parameter κ and the seismic moment. As shown by Olsen and Madariaga (2000) κ is a measure of the ratio between strain energy release per unit surface and the specific energy release rate, which in turn control rupture propagation. We can be more specific for the models shown in Figure 6.14c. These models share the same elliptical geometry described by the first line of Table 5.2, thus they all have the same ellipticity $\varepsilon = a/b = 2$. The slip on an elliptical fault under constant stress drop can

be computed using equation (10) from Madariaga (1979). The strain energy release for such a fault is simply

$$\Delta W = \frac{2}{3} C_f \frac{T_e^2}{\mu} \pi a^2 b \tag{5}$$

Where *a,b* are the length of the semi-axes and C_f is a form factor. For an ellipse of ellipticity 2, we find from Fig 6.1 of Madariaga (1979) that $C_f \approx 1.35$. We can also calculate the total fracture energy used to propagate the fault, $G_c\, S$, where the energy release rate for the friction model (3) is $G_c = 1/2\ T_u\ D_c$ times the surface of the fault. The ratio of energy release to fracture energy is thus

$$\frac{\Delta W}{G_c\, S} = 1.8\,\kappa \tag{6}$$

Looking at Figure 6.14c we observe that only solutions with $\kappa > 1$ fit the data so that the critical value of κ_c for the dynamic inversion of the Northern Iwate earthquake is of the order of 0.98. As κ increases beyond the critical value ruptures propagate at increasingly faster speeds and for values of $\kappa > 1.5\ \kappa_c$ super-shear solutions become possible. The model of Table 5.3 with $\kappa = 2.06$ is an example. (see Madariaga and Olsen, 2000 for further discussion).

The preferred models of Iwate 2008 earthquake are ellipses with semi-minor axes close to 4 km and have maximum slip of 4 m. Rupture duration for the two best models of Table 5.2 were less than 3 sec and propagated at high subshear velocities. The stress drop T_e obtained from dynamic inversion of the Northern Iwate earthquake are very high, of the order of 30 to 40 MPa. These T_e values are in agreement with those determined for other intra-slab intermediate depth events in Japan like the 1993 Kushiro-oki earthquake (Takeo et al., 1993; Ide and Takeo, 1996). In general, the results are also similar to those obtained for another intra-slab intermediate depth earthquake of similar magnitude: the Michilla 2007 Northern Chile earthquake (Ruiz and Madariaga, 2011). The energy release rate can be computed from $G_c = ½\ T_u\ D_c$. It is 23 MJ/m^2 for dataset 1 and 36 MJ/m^2 for dataset 2. These are large values compared with values of G_c estimated for similar magnitude events by Abercombrie and Rice (2005) and Lancieri et al (2012) for subduction events in

Northern Chile. These large values of G_c indicate that rupture propagation at intermediate depths requires much more energy than that of shallow events.

For these intermediate depth events, an elliptical rupture provides an efficient model of the event that can be inverted with present day computational resources. More complex source models, including variations of slip and stress on the fault plane are the next step in dynamic inversion. Larger magnitude earthquakes or more complex ruptures may also be modeled using more than one ellipse as was made for the Tottori 2000 Japan earthquake by DiCarli et al. (2010).

CONCLUSIONS

We used an elliptical patch approach to do kinematic and dynamic inversion of the intermediate depth 2008 Iwate earthquake. We explored the solution space in order to find the overall characteristics of the seismic rupture in the frequency band from 0.02 to 0.5 Hz. We used displacement wave forms obtained by integration of the strong motion records from the Kik-net and K-net networks. We obtain excellent fits of the displacement time series and Fourier spectra show that we fit the entire frequency band of the filtered records. Both dynamic and kinematic inversions are non-unique with large trade-offs between the control parameters. For the dynamic inversion we found that models that fit the data with similar errors can be described with similar values of moment Mo and dynamic similarity κ. These are two global parameters that describe the size of the earthquake (Mo) and the ratio of strain to fracture energy for the event (k). It would be tempting to reformulate the results in terms of the radiation efficiency, the ratio between radiated energy and available strain energy that can be derived from kappa, but our model does not include high frequencies. We conclude conservatively that dynamic inversion using the elliptical patch approximation gives results that are in excellent agreement with simpler dynamic models of seismic radiation like the Brune-Aki scaling laws. In the future we will try to evaluate radiated energy more accurately.

Data and Resources

The strong motion data used in this study were collected from the National Research Institute for Earth Science and Disaster Prevention (NIED) in Japan. Data can be obtained from the K-net, KiK-net and Hi-net websites at www.knet.bosai.go.jp and www.kik.bosai.go.jp

Acknowledgements

This work is part of the Millennium Nucleus Program ‘‘Montessus de Ballore—IERC’’, of Mideplan, Chile. Funding for this work was supported by contract FONDECIT No. 1100429 in Chile and by contract DEBATE of ANR Risk-08 in France.

REFERENCES

Abercrombie, R. E., and J. R. Rice (2005), Can observations of earthquake earthquake scaling constrain slip weakening?, Geophys. J. Int., **162**, 406-424.

Aoi, S., K. Obara., S. Hori, K. Kasahara, and Y. Okada, (2000). New strong-motion observation network : Kik-net, EOS Trans. AGU, 329.

Bouchon, M. (1981), A simple method to calculate Green’s functions for elastic layered media, *Bull. Seismol. Soc. Am*., **71**, 959–971.

Bouchon M., M. Campillo and F. Cotton (1998), Stress Field associated with the rupture of the 1992 Landers, California, earthquake and its implication concerning the fault strength at the onset of the earthquake, *J. Geophys. Res*., **103**, 21091-21097.

Coutant, O. (1990), Programme de simulation numerique AXITRA, Rapport LGIT, Univ Joseph Fourier, Grenoble, France

Das, S. and K. Aki (1977), Fault plane with barriers-versatile earthquake model, *J. Geophys. Res*., 82 (B36), 5658-5670.

Di Carli, S., C. Francois-Holden, S. Peyrat and R. Madariaga (2010). Dynamic inversion of the 2000 Tottori earthquake based on elliptical subfault approximations. *J. Geophys. Res*., **115**, B12328, doi:10.1029/20095B006358

Fukuyama, E., (1991), Inversion for the Rupture Details of the 1987 East Chiba Earthquake, Japan, Using a Fault Model Based on the Distribution of Relocated Aftershocks, *J. Geophys. Res*., **96**, B5, 8205-8217

Fukuyama, E. and T. Mikumo (1993), Dynamic rupture analysis: inversion for the source process of the 1990 Izu Oshima, Japan earthquake (M6.5), *J. Geophys. Res*., **88** , 6529-6542.

Guatteri, M. and P. Spudich (2000), What can strong-motion data tell us about slip-weakening fault friction laws?, *Bull. Seism. Soc. Am*., **90**, 98-116.

Ida, Y (1972), Cohesive force across tip of a longitudinal-shear crack and Griffith specific surface-energy, *J. Geophys. Res*., **77**, 3796-3805.

Ide, S., and M. Takeo (1996), The dynamic rupture process of the 1993 Kushiro-oki earthquake, *J. Geophys. Res*., **101**, 5561-5675.

Kanamori H. and G. S. Stewart (1978), Seismological aspects of the Guatemala earthquake of February 4, 1976. *J. Geophys. Res*., **83**, 3427-3434.
Kikuchi, M and H. Kanamori (1995), The Shikotan earthquake of Octubre 4, 1994: Lithospheric earthquake. *Geophys. Res. Lett.,* **22**, 1025-1028.
Kinoshita, S., Kyoshin net (K-NET), *Seism. Res. Lett.,* **69**, 209-332, 1998
Lancieri, M., R. Madariaga and F. Bonilla, (2012). Spectral scaling of the aftershocks of the Tocopilla 2007 earthquake in Northern Chile. In press *Geophys. J. Int.,* 2012.
Madariaga, R (1979), On the relation between seismic moment and stress drop in the presence of stress and strength heterogeneity. *J. Geophys. Res*., **84**, 2243-2250.
Madariaga, R., K. B. Olsen and R. Archuleta (1998), Modeling dynamic rupture in a 3D earthquake fault model, *Bull. Seismol. Soc. Am*., **88**, 1182-1197.
Madariaga, R. and K.B Olsen (2000), Criticality of Rupture Dynamics in 3-D, *Pageoph*, **157**, 1981-2001.
Miyatake, T., Yagi, Y. and T. Yasuda (2004), The dynamic rupture process of the 2001 Geiyo, Japan, earthquake, *Geophys. Res. Lett* **31**, L12612, doi:10.1029/2004GL019721
Okada, T. and A., Hasegawa (2003), The M7.1 May 26, 2003 off-shore Miyagi Prefecture Earthquake in northeast Japan: Source process and aftershock distribution of an intra-slab event. *Earth Planets Space*, **55**, 731–739.
Peyrat, S. and K. B. Olsen (2004), Nonlinear dynamic rupture inversion of the 2000 Western Tottori, Japan, earthquake, *Geophys. Res. Lett*., **31**, L05604, doi:10.1029/2003GL019058.
Piatanesi A., E. Tinti, M. Cocco and E. Fukuyama (2004), The dependence of traction evolution on the earthquake source time function adopted in kinematic rupture models, *Geophys. Res. Lett*., **31**, L04609, doi:10.1029/2003GL019225
Ruiz, S and Madariaga, R. (2011). Determination of the friction law parameters of the Mw 6.7 Michilla earthquake in northern Chile by dynamic inversion. *Geophys. Res. Lett*., **38**, L09317, doi:10.1029/2011GL047147
Sambridge, M. (1999), Geophysical Inversion with a Neighbourhood Algorithm -I. Searching a parameter space, Geophys. J. Int., **138**, 479-494.
Suzuki, W., Aoi, S., and Sekiguchi, H. (2009): Rupture Process of the 2008 Northern Iwate Intraslab Earthquake Derived from Strong-Motion Records, *Bull. Seismol. Soc. Am*.,, **99**, 2825–2835, doi:10.1785/0120080331.
Takeo, M., S. Ide, and Y. Yoshida (1993) The 1993 Kushiro-oki, Japan, earthquake: a high stress-drop event in a subducting slab, Geophysical Research Letters, 20, 2607-2610.
Ukawa, M., M. Ishida, S. Matsumura and K. Kasahara (1984). Hypocenter determination method of the Kanto-Tokai observational network for microearthquakes, Rep. Nat'l. Res. Disaster Prev. **53**, 1-88 (in Japanese with English abstract).

Table 5.1. Northern Iwate intermediate depth earthquake. Values of the 7 inverted parameters for the asperity models using NA. The optimal values for the two dataset are on the first two lines and the range of variation of these parameters during the inversion is shown in the last two lines.

Model	**Semi-Axis *a* [km]**	**Semi-Axis *b* [km]**	***α*** **[rad]**	***X*** **[km]**	***Y*** **[km]**	V_r **[km/s]**	D_m **[m]**
Dataset1	9.02	5.08	0.80	-0.62	0.47	4.31	2.48
Dataset2	5.34	5.91	0.08	0.68	0.058	3.24	3.22
Range minimum	4	4	0	-4	-4	0.1	0.1
Range maximum	14	14	3.14	4	4	8	10

Table 5.2. Dynamic inversion of the 2008 Northern Iwate earthquake. Values of the parameters inverted for the two Dataset. The optimal values are on the first two lines and the range of variation of these parameters during the inversion are shown in the last two lines.

Model	**Geometry**					**Nucleation**		**Stress**		
	Semi-Axis a [km]	**Semi-Axis b [km]**	**Alfa [rad]**	**X [km]**	**Y [km]**	**R' [km]**	**Te' [MPa]**	**Te [MPa]**	**Tu [MPa]**	**Dc [m]**
Dataset1	4.02	8.06	1.01	0.01	0.06	1.32	61.45	34.25	55.96	1.01
Dataset2	6.77	4.00	0.38	-4.00	-0.90	0.86	83.28	41.15	71.54	1.05
Range minimum	4	4	0	-4	-4	0.8	8	8	8	0.4
Range maximum	14	14	1.57	4	4	2	150	50	100	2

Table 5.3. Parameters for a possible super-shear model of the 2008 Northern Iwate intermediate depth earthquake

χ^2	κ	Mo [Nm]	Te [MPa]	Tu [MPa]	Dc [m]
0.45	2.06	1.59E19	34.83	59.78	0.63

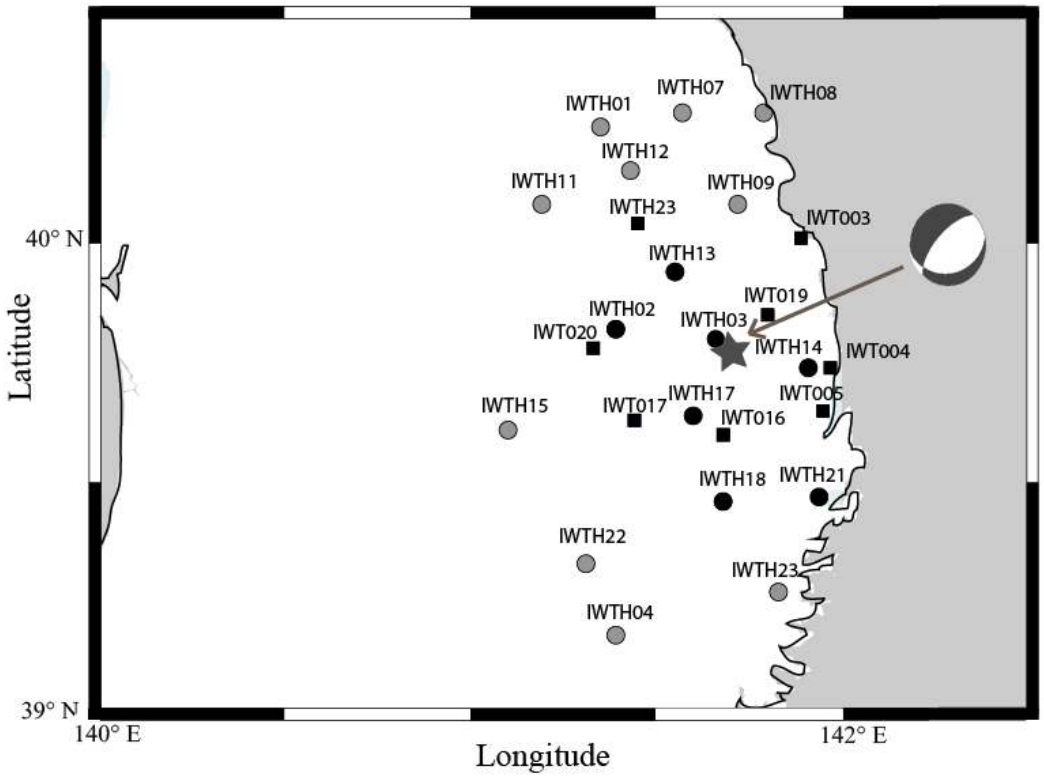

Figure 6.1. Location and instruments available for the study of the Northern Iwate intermediate depth earthquake of 2008. The star is the epicenter, circles denote KiK-net and squares, K-NET stations. The black circles and squares are strong motion sites located less than 40 km from the epicenter, gray circles and squares are the sites at epicentral distances less than 65 km.

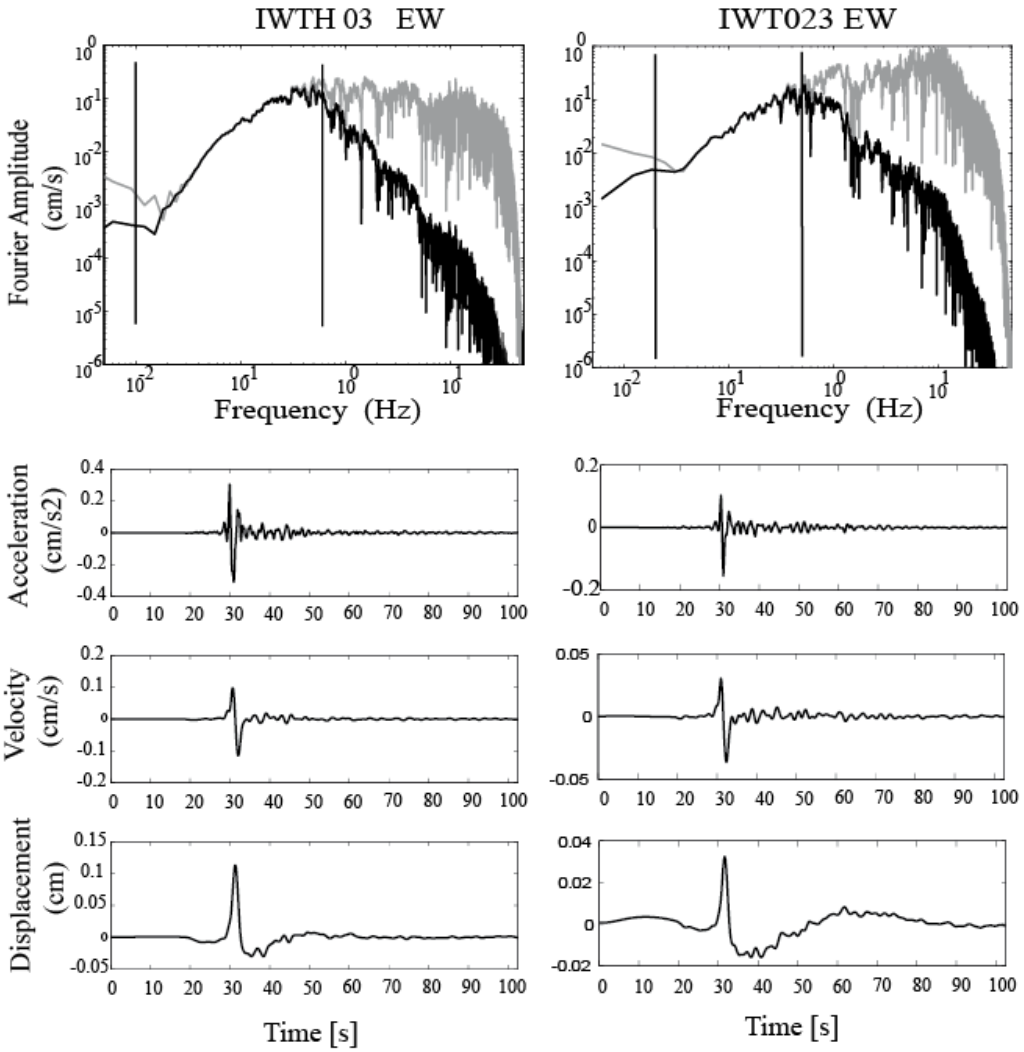

Figure 6.2. Northern Iwate intermediate depth earthquake of 2008. Fourier spectra of the EW accelerograms recorded at stations IWTH03 (a) and IWT023 (b). The unfiltered spectra are shown in gray; the filtered spectra in black. The band-pass filter had corners of 0.02 – 0.5 Hz and 0.04 – 0.5 Hz, respectively. (c) and (d) filtered acceleration, velocity and displacement EW records at IWTH03 and IWT023.

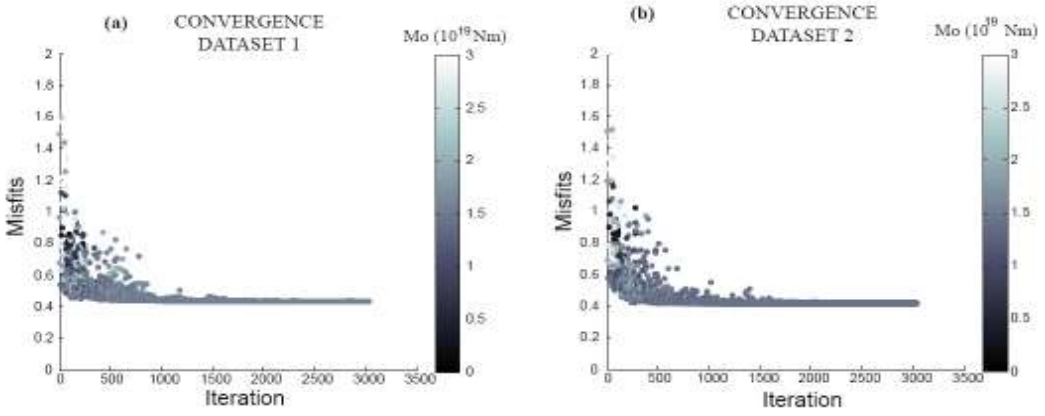

Figure 6.3. Kinematic inversion of the 2008 Northern Iwate intermediate depth earthquake. The figure shows the misfit between synthetics and observed displacement records as a function of iteration number for the kinematic inversion using NA. Dataset 1 and 2 are shown on (a) and (b), respectively. Each dot is one inversion solution colored by the corresponding seismic moment. The color scale is saturated for Mo > 3 10^{19} Nm. The solutions converge to a misfit value of 0.436 for Dataset 1 and 0.417 for Dataset 2 and both converge to a moment of Mo ≈ 1.5 10^{19} Nm.

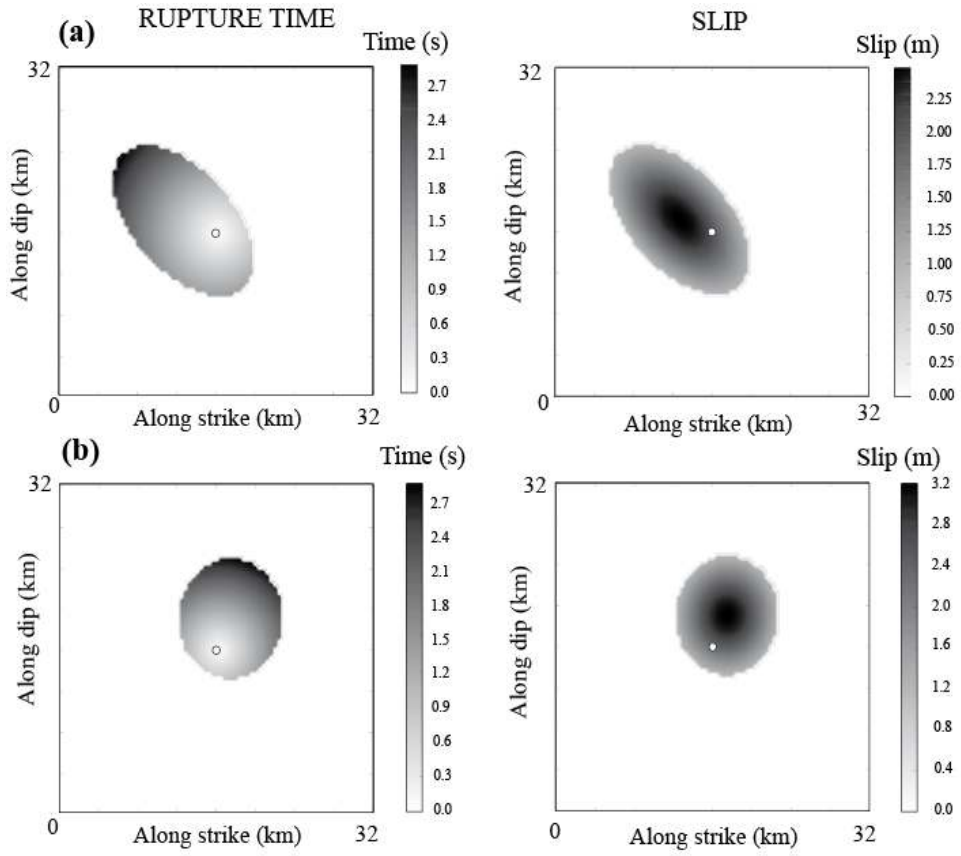

Figure 6.4. Kinematic inversion of the Northern Iwate intermediate depth earthquake. Left: slip distribution; and Right: rupture time isochrones for the best kinematic models of Dataset 1 (upper figures) and Dataset 2 (lower figures).

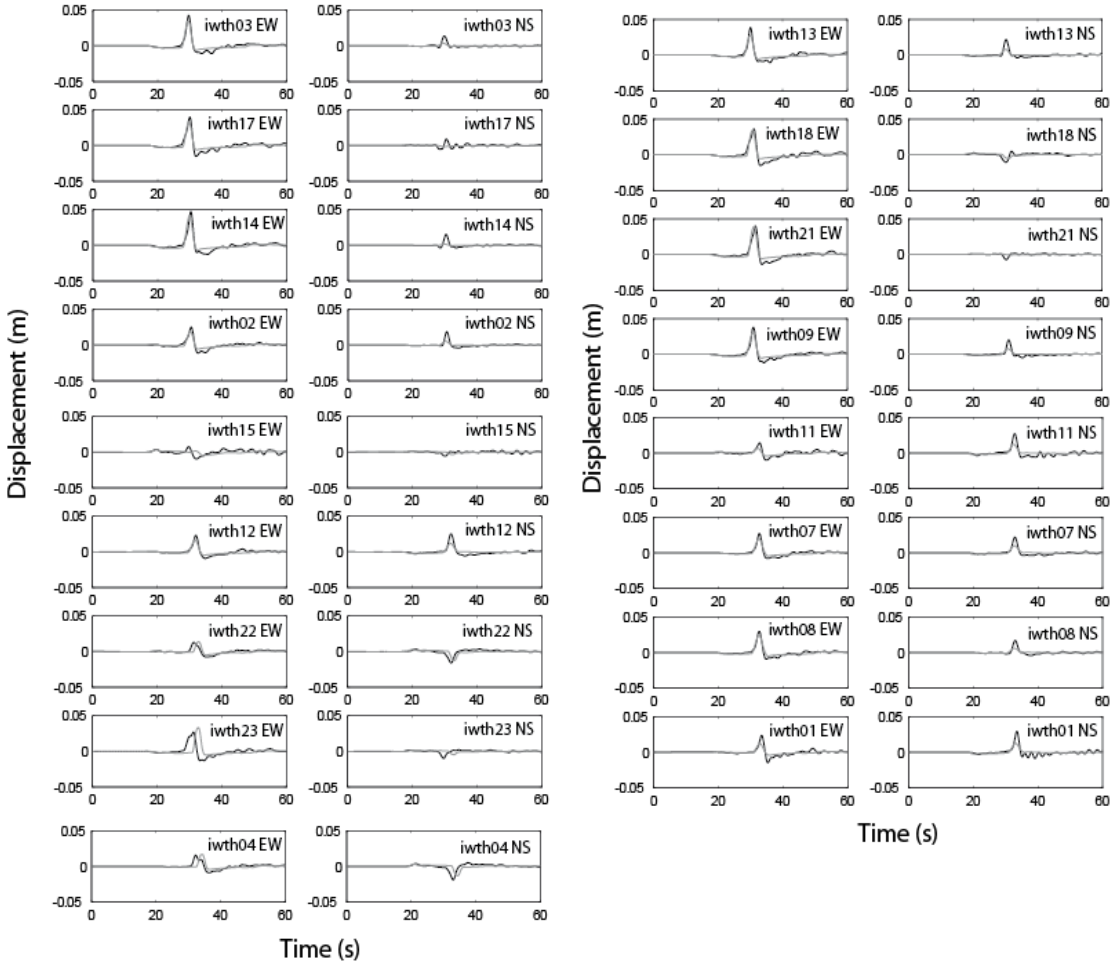

Figure 6.5. Kinematic inversion of the Northern Iwate intermediate depth earthquake. Comparison of observed (black traces) and synthetic (gray traces) EW and NS displacement records of Dataset 1 for the best kinematic model using NA.

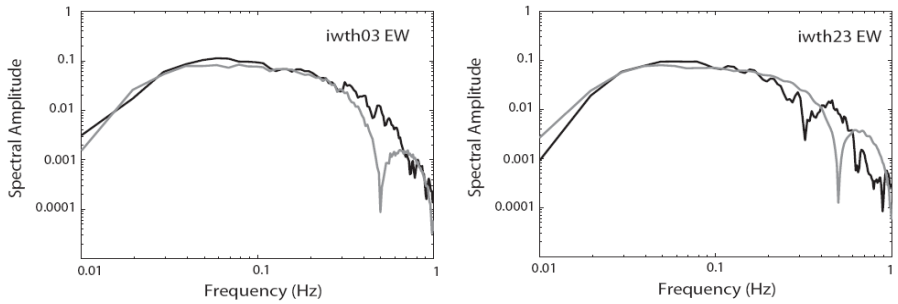

Figure 6.6. Kinematic inversion of the Northern Iwate intermediate depth earthquake. Comparison of observed and synthetic EW component of Fourier spectra of Dataset 1 for the best model of kinematic inversion using NA. Black is real data and gray is synthetic record.

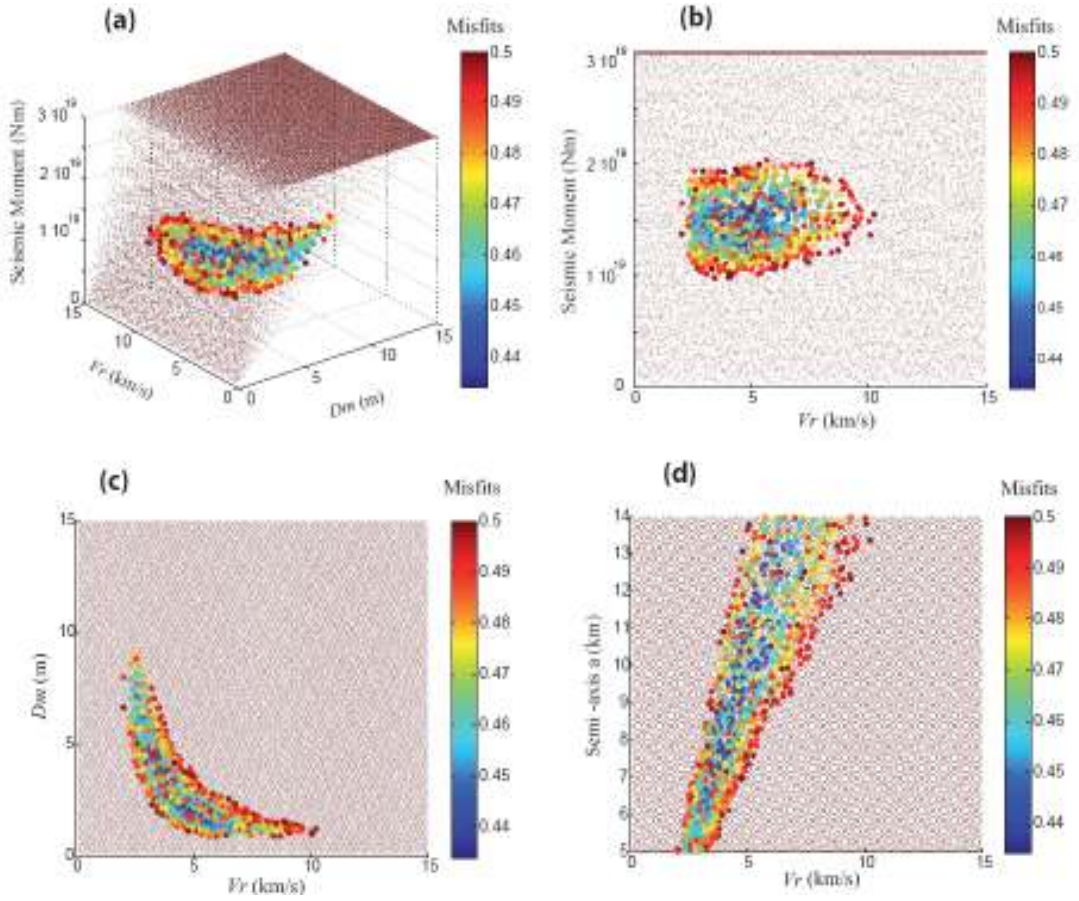

Figure 6.7. Kinematic inversion of the Northern Iwate intermediate depth earthquake. Study of resolution of kinematic inversion by the Monte Carlo method. In each figure, dots plot the result of one simulation. The larger dots have misfits $\chi^2 < 0.5$ and their color is given by the misfit. The color scale is saturated for misfits $\chi^2 \geq 0.5$. **(a)** Three dimensional figure showing Seismic Moment Mo, velocity rupture V_r and Maximum slip D_m, Mo is saturated for Mo > $3 \cdot 10^{19}$ Nm. **(b)** and **(c)** are projections from this figure. **(b)** Misfits projected on Mo v/s V_r. **(c)** Misfits projected on the (D_m , V_r) $_{plane}$. Figure (d) shows the tradeoff between semi-axis a and rupture velocity V_r.

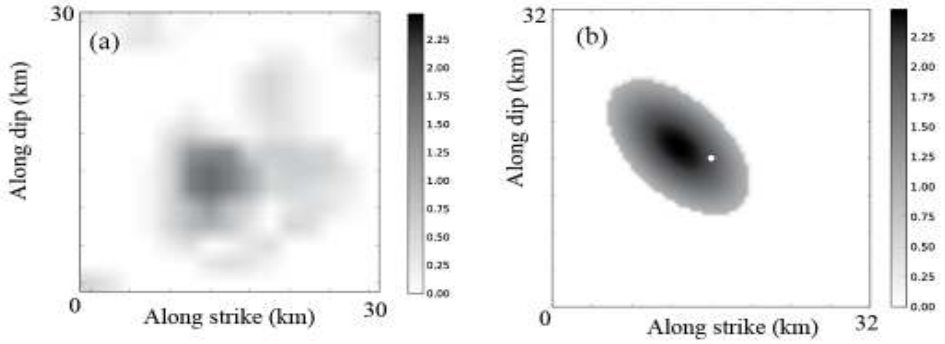

Figure 6.8. Kinematic inversion of the Northern Iwate intermediate depth earthquake. (a) Slip distribution inverted by Suzuki et al. (2009) (b) slip distribution obtained by kinematic inversion of Dataset 1.

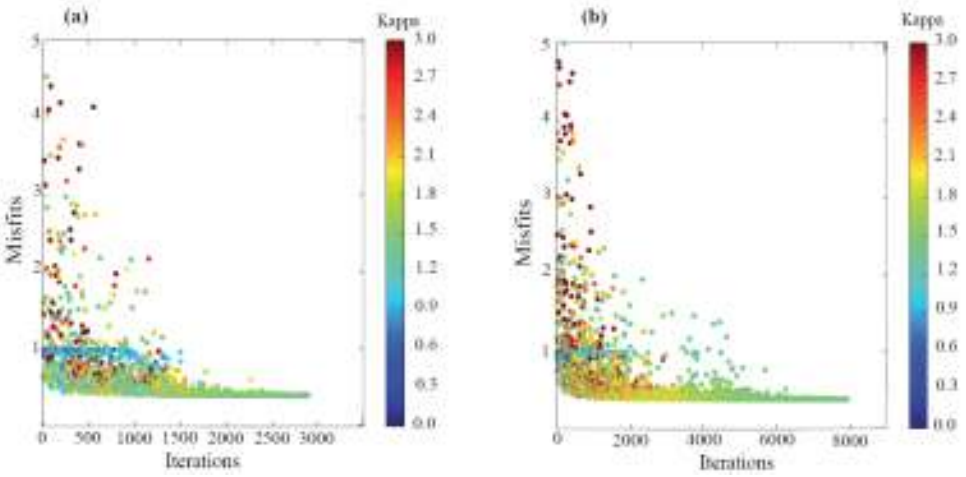

Figure 6.9. Dynamic inversion of the Northern Iwate intermediate depth earthquake. Misfit between synthetics and observed displacement records as a function of iteration number for datasets 1 (left) and 2 (right). The solutions converge to misfits values of 0.39 for Dataset 1 and 0.38 for Dataset 2. The color corresponds to the value of □computed for each model. The color scale is saturated for □ > 3, □converges to 1.34 for Dataset 1 and 1.44 for Dataset 2.

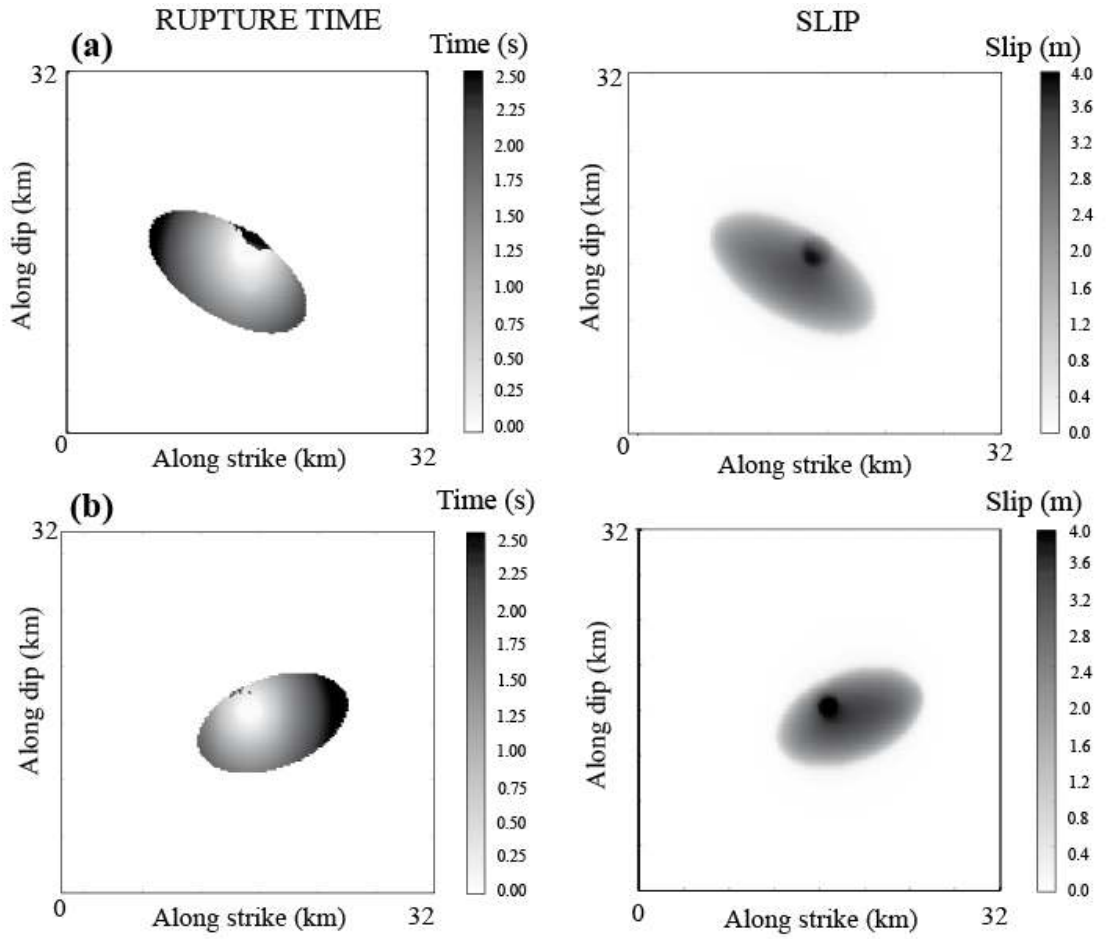

Figure 6.10. Dynamic inversion of the Northern Iwate intermediate depth earthquake. Slip distribution and rupture isochrones for. (a) Dataset 1 and (b) Dataset 2.

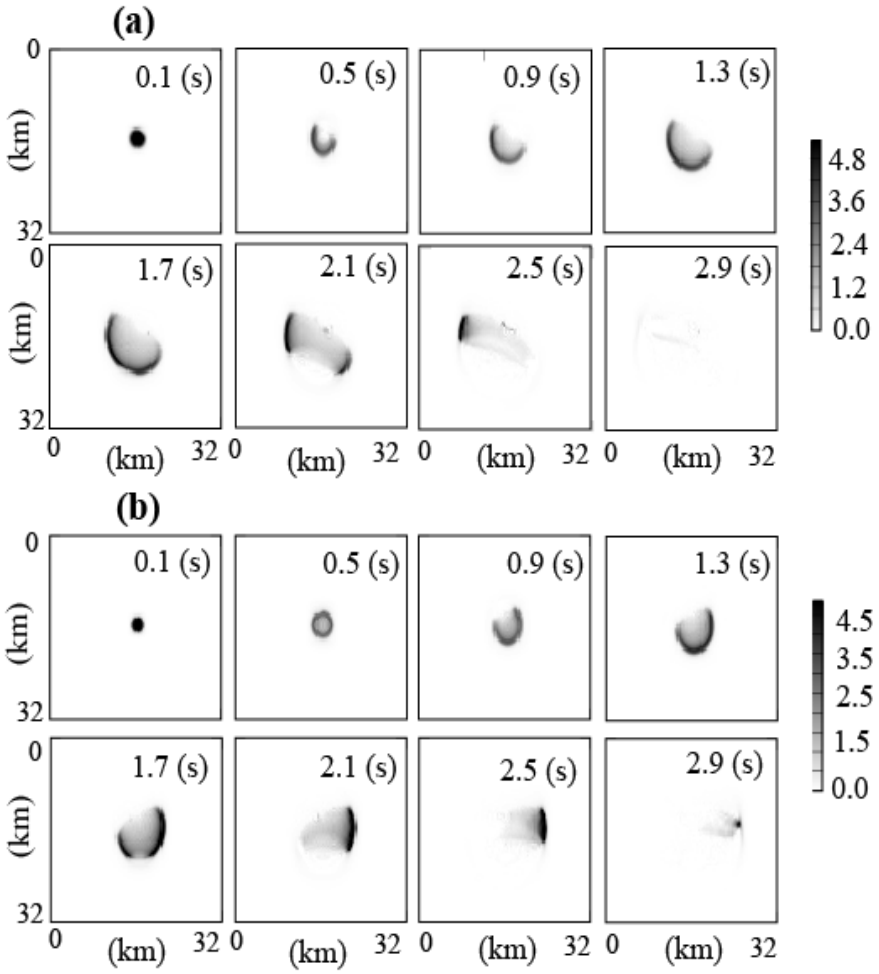

Figure 6.11. Dynamic inversion of the Northern Iwate intermediate depth earthquake. Snapshots of slip rate for the best model obtained by dynamic inversion (a) Dataset 1 and (b) Dataset 2.

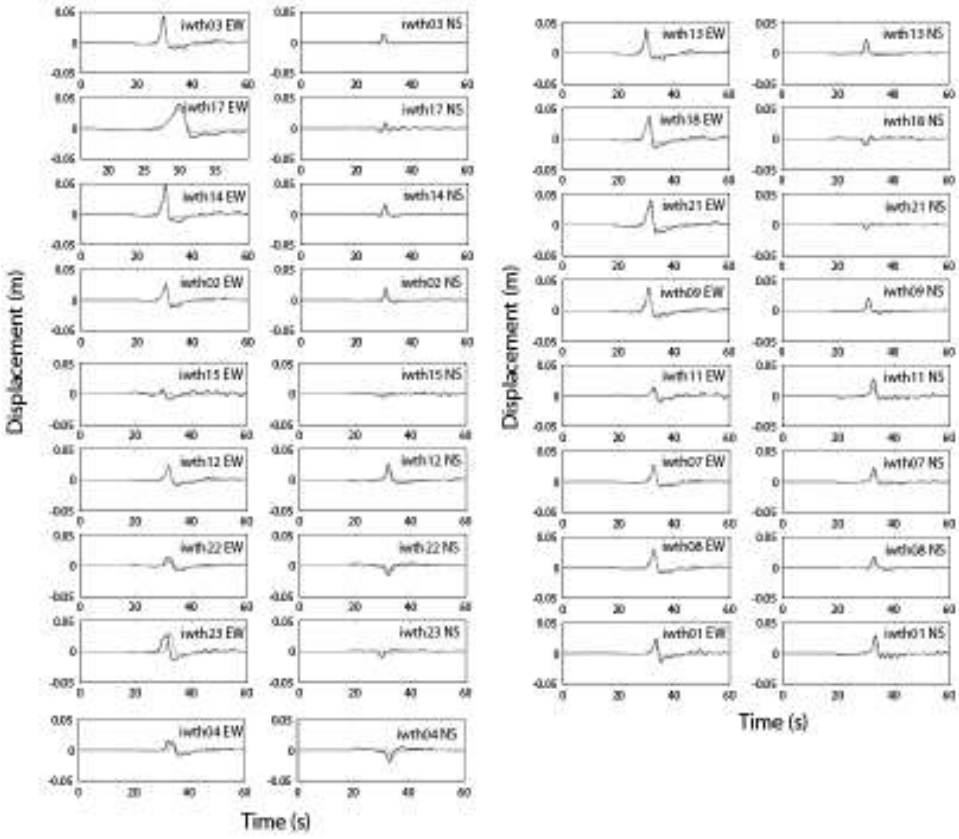

Figure 6.12. Dynamic inversion of the Northern Iwate intermediate depth earthquake. Comparison of the EW component of the observed displacements (black) with the synthetics (grey) computed for the best dynamic model obtained by dynamic inversion.

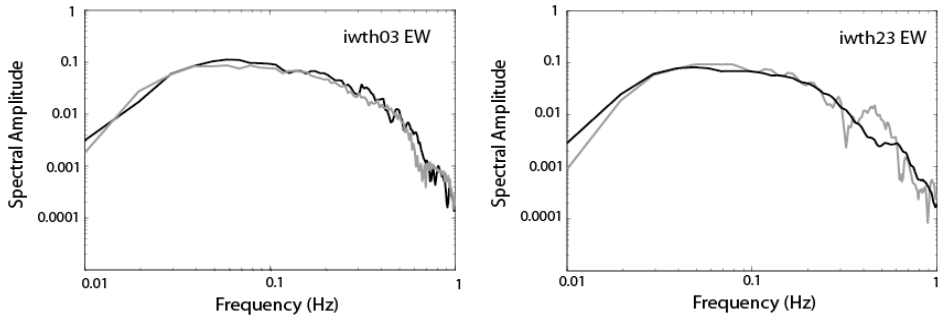

Figure 6.13. Dynamic inversion of the Northern Iwate intermediate depth earthquake Comparison of observed and synthetic Fourier spectra of the displacement records computed for the best model found by dynamic inversion of Dataset 1. Black is the observed spectra and gray shows the synthetic records.

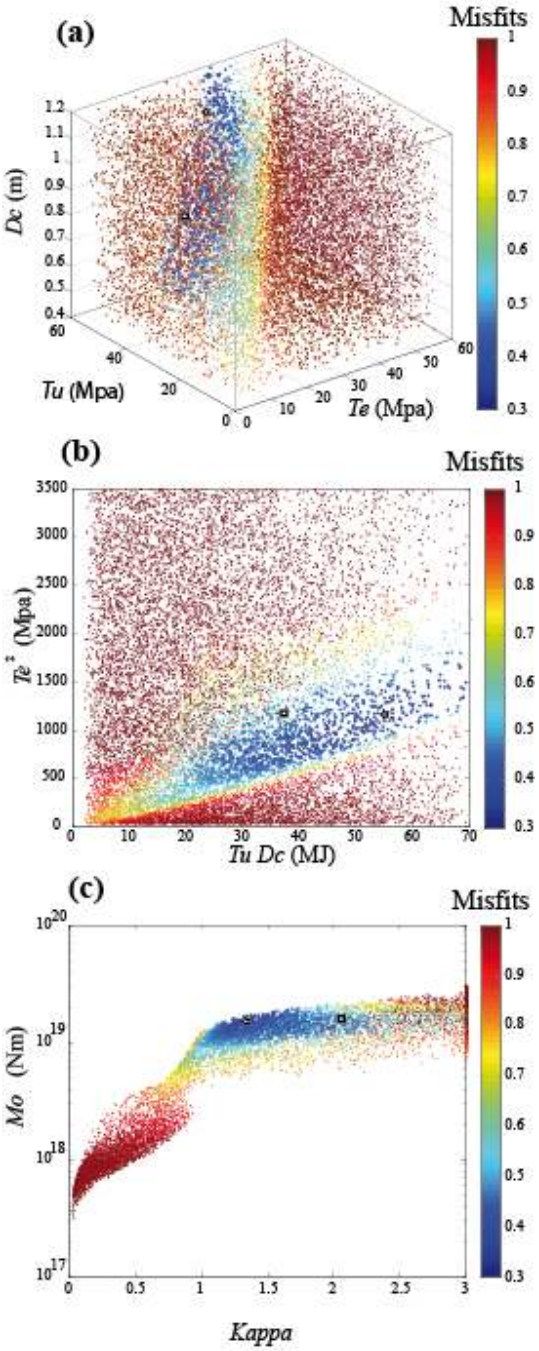

Figure 6.14. Dynamic inversion of the 2008 Northern Iwate intermediate depth earthquake. Each dot represents a model, the dots are colored by the misfit value following the color scale shown on the right. The scale is saturated for misfits ≥ 0.5. **(a)** Plot of misfits for each model projected onto the space of dynamic parameters T_e, T_u and D_c **(b)** Projection of model space onto the plane T_e^2 and T_uD_c The misfits lower than 0.5 converge to narrow band which ratio tends to k value. **(c)** Projection of model space onto the plane Mo and Kappa. The misfits lower than 0.5 are controlled by the seismic moment (~Mw 6.7) and a narrow band of k value ($1 \leq k \leq 1.6$). The black star corresponds to the optimal solution determinate by NA, and the black square is the supershear solution shows in Figure 6.15.

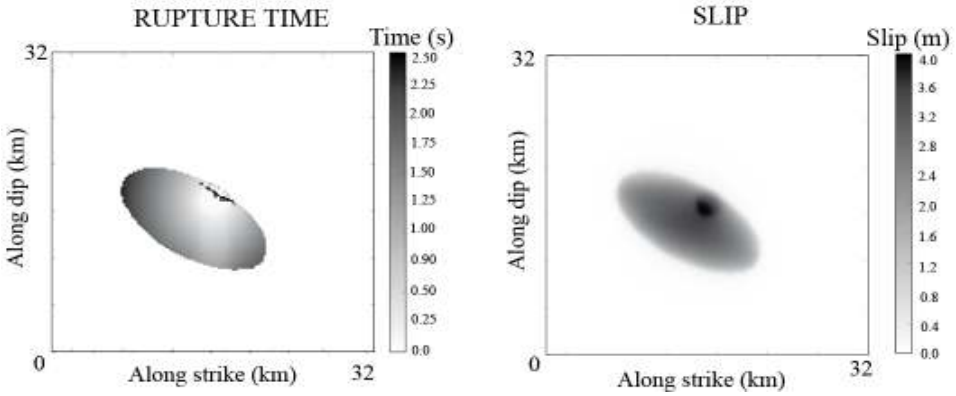

Figure 6.15. (a) Rupture isochrones and (b) slip of model with super-shear rupture for the 2008 Iwate earthquake of Northern Japan.

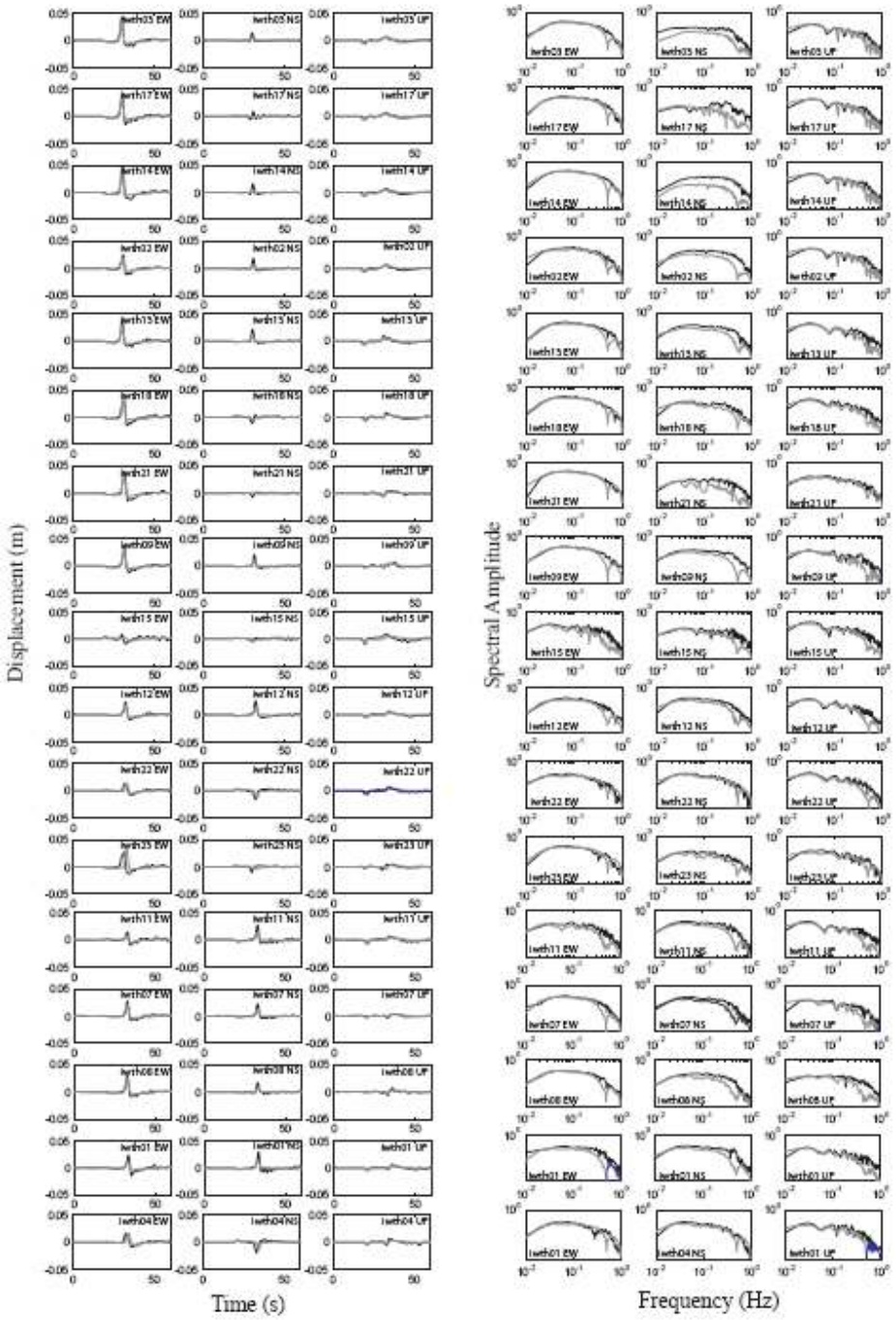

Figure 6.S1. Kinematic inversion of Northern Iwate intermediate depth earthquake. Left: Comparison of observed (black traces) and synthetic (gray traces) displacements records of Dataset 1. Right: Comparison of observed (black traces) and synthetic (gray traces) Fourier spectrum of Dataset 1

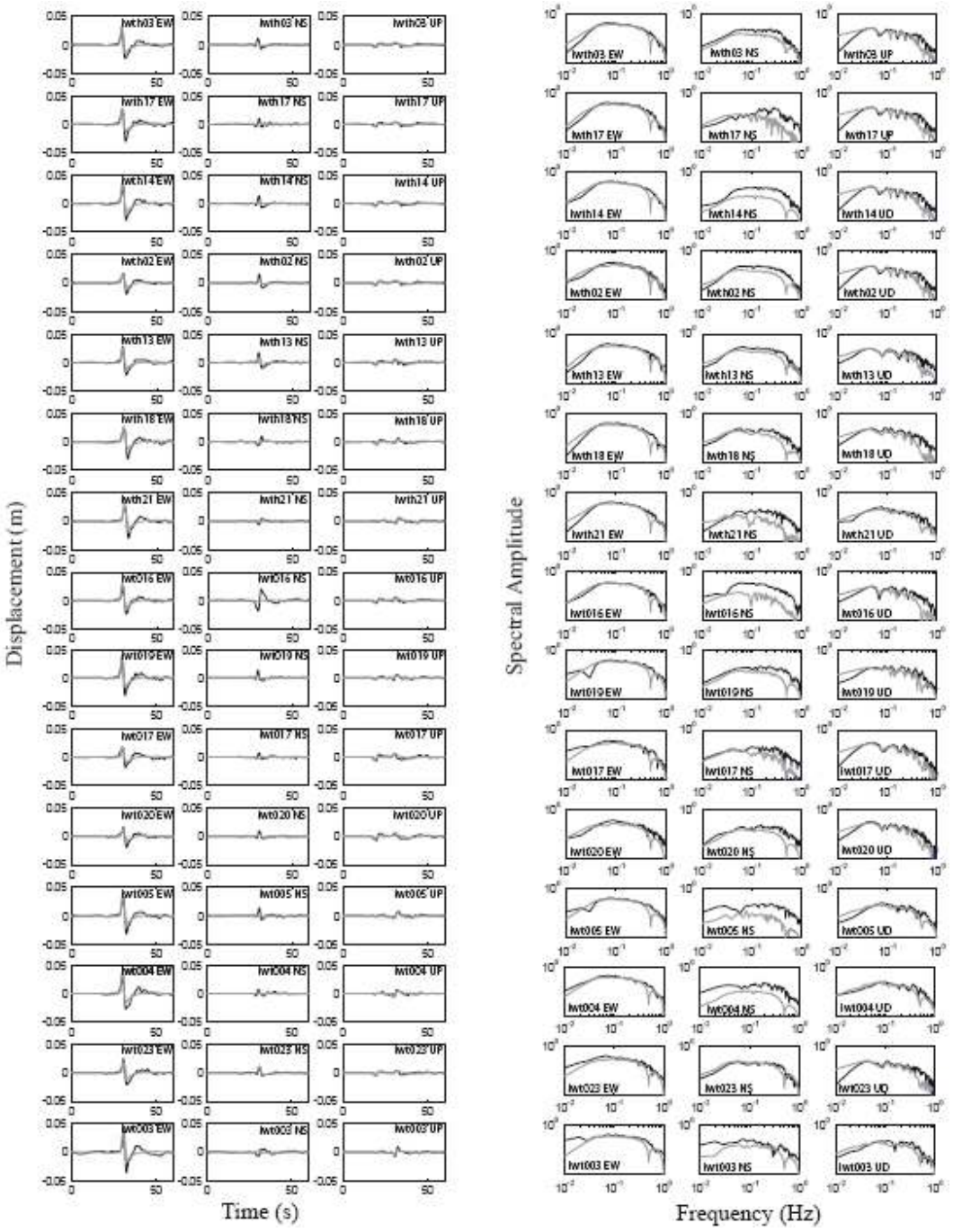

Figure 6.S2. Kinematic inversion of Northern Iwate intermediate depth earthquake. Left: Comparison of observed (black traces) and synthetic (gray traces) displacements records of Dataset 2. Right: Comparison of observed (black traces) and synthetic (gray traces) Fourier spectrum of Dataset 2.

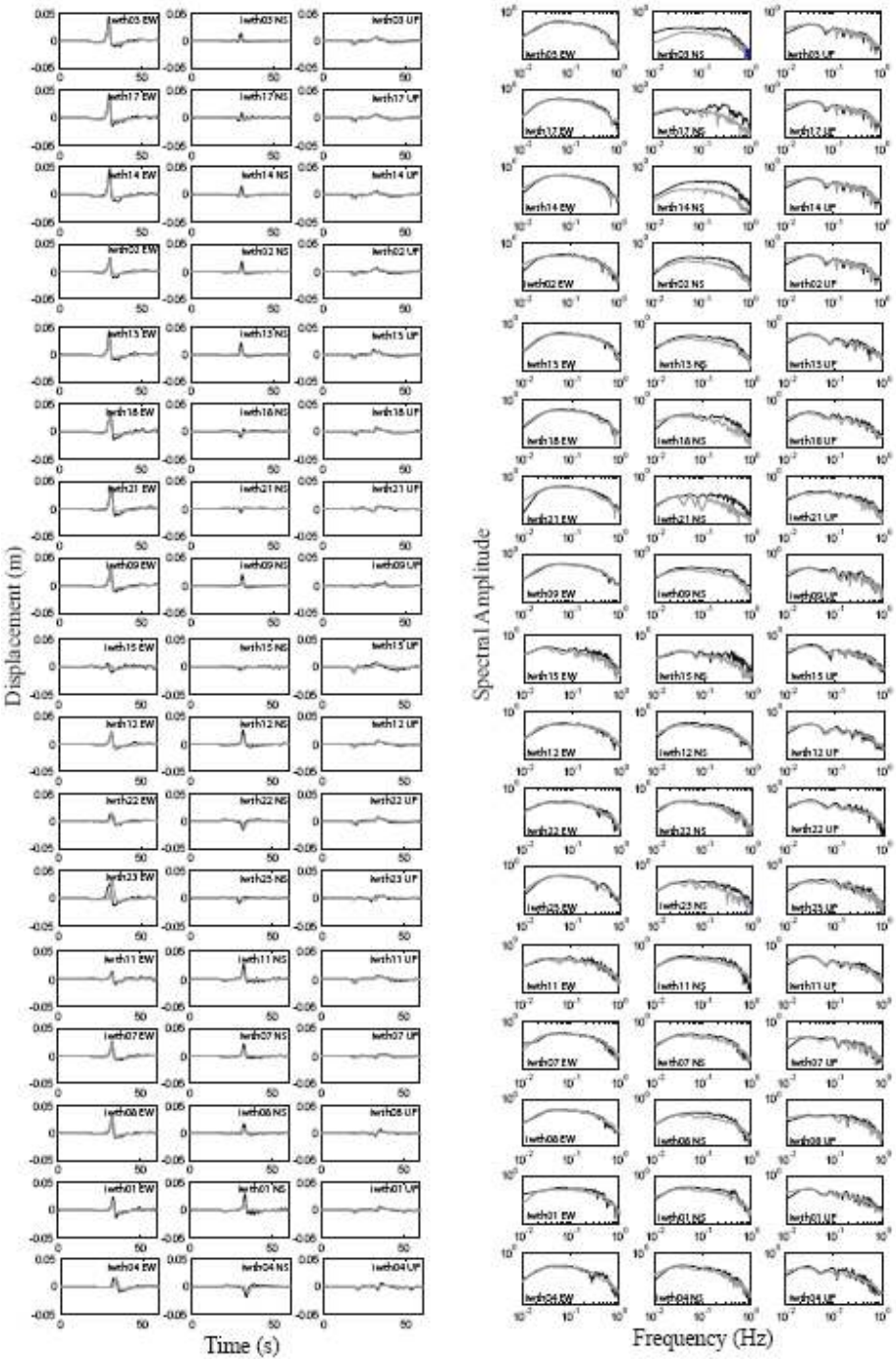

Figure 6.3. Dynamic inversion of Northern Iwate intermediate depth earthquake. Left: Comparison of observed (black traces) and synthetic (gray traces) displacements records of Dataset 1. Right: Comparison of observed (black traces) and synthetic (gray traces) Fourier spectrum of Dataset 1.

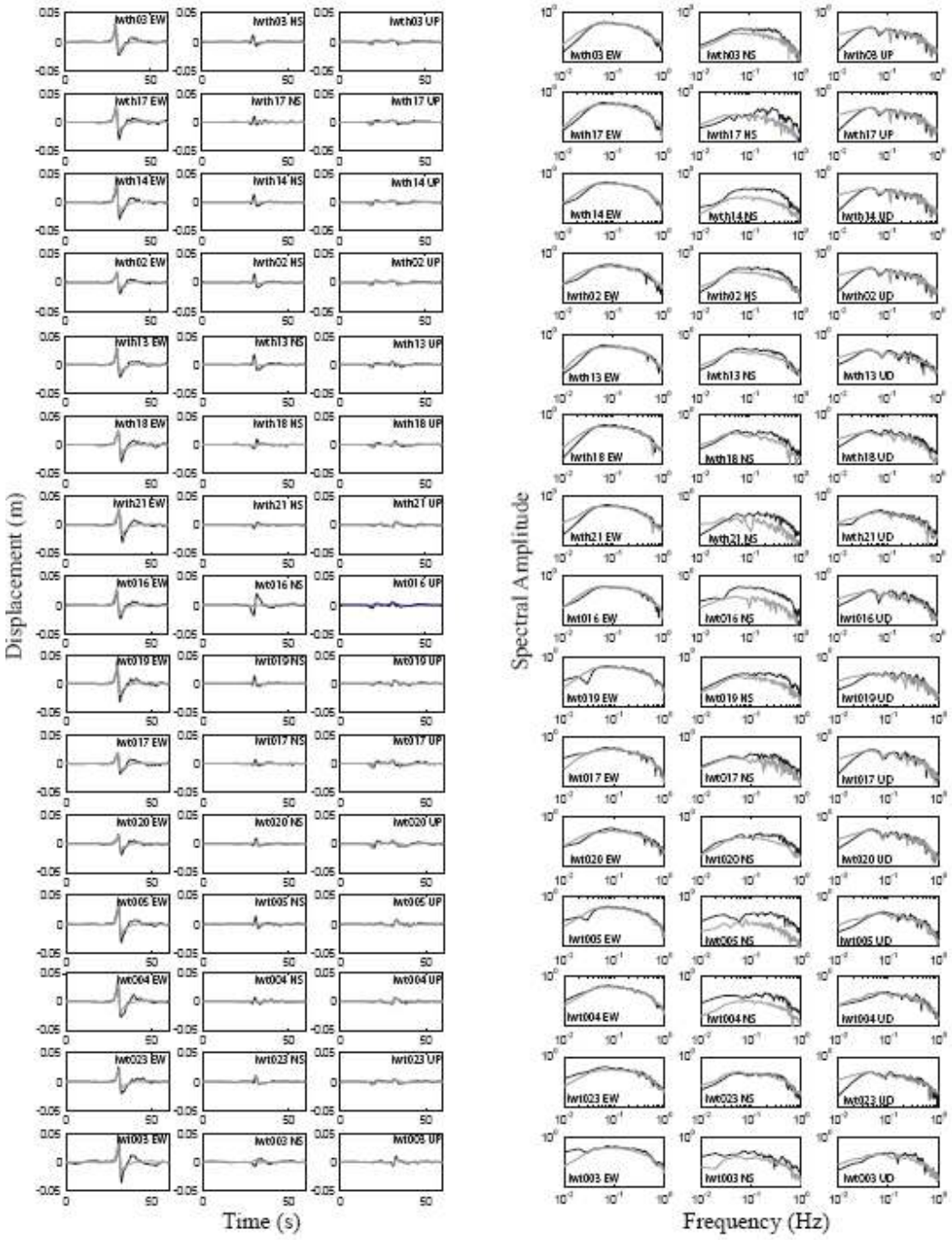

Figure 6.S4. Dynamic inversion of Northern Iwate intermediate depth earthquake. Left: Comparison of observed (black traces) and synthetic (gray traces) displacements records of Dataset 2. Right: Comparison of observed (black traces) and synthetic (gray traces) Fourier spectrum of Dataset 2.

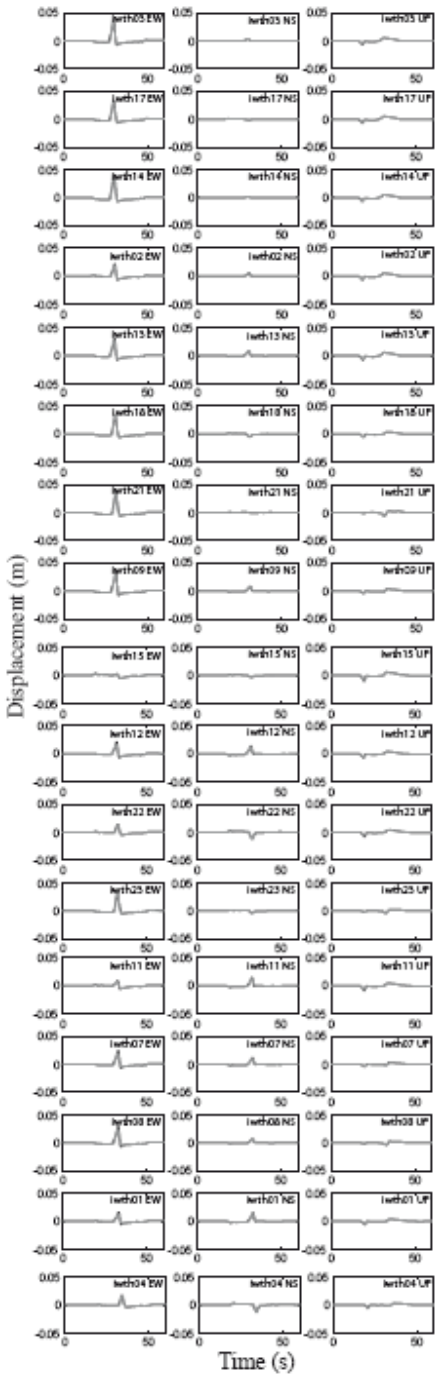

Supplementary Figure 6.5. Dynamic inversion of Northern Iwate intermediate depth earthquake. Comparison of synthetic sub-shear rupture of Dataset 1 (black traces) and synthetic super-shear rupture of Dataset 1 (gray traces).

7. CONCLUSIONS AND PERSEPECTIVES

CONCLUSIONS

The well recorded Tocopilla Chile 2007, Mw 7.8; Maule Chile 2010, Mw 8.8; Tohoku Japan 2011, Mw 9.0; Michilla Chile 2007, Mw 6.7 and Iwate Japan 2008, Mw 6.8, have allowed us to do kinematic and dynamic inversions. For the inversions we used elliptical patch approach and the neighborhood algorithm for the search for best solution, in some cases we compared our results with classic rectangular grid inversions and also we made Monte Carlo inversions.

The use of cGPS to do seismic source inversions was validated during the Tocopilla 2007 earthquake. This type records were used also in the Maule 2010 and Tohoku 2011 inversions. The elliptical approach in the kinematic inversions is a good solution to study large earthquakes with sparse records such as Tocopilla 2007 and Maule 2010. We show that the elliptical approach and the classic rectangular grid give similar results for the Tohoku 2011 earthquake. The inversions for slip distribution are not unique, but they are controlled by the seismic moment. The dynamic inversions, which allow introducing physical aspects of the rupture process, show that the rupture is controlled by the seismic moment and also by κ (the ratio of strain to fracture energy for the event). The conclusions of each studied earthquake are the following:

For the Tocopilla 2007 earthquake a joint inversion of strong motion and cGPS data was made. The kinematic inversion confirms that this earthquake is characterized by a sub-shear rupture with two main zone of large slip confined to 35 to 50 km of depth, at the bottom of the subduction interface.

For the Maule 2010 earthquake we studied the intermediate and high frequency radiation using cGPS and strong motion records. Unfortunately these data are only available for the Northern part of the rupture of the event, from Concepcion (37.5 ° S) the North. We

inverted the ground velocities obtained by band limited differentiation of the cGPS records in central Chile. Although the data are strongly dominated by the propagation of the rupture front, we could determine that a local asperity located roughly westward of the city of Constitucion produced a significant part of the high frequency waves observed in local accelerograms. In all the stations located North of Constitucion two big strong motion pulses are observed that we associated with the two asperities situated north of the city of Constitucion. Finally a comparison of records from the 1985 Valparaiso earthquake shows that high frequency emission from that earthquake and from Maule were very similar in the Northern stations. This similarity is striking in the envelopes of strong motion data and in the acceleration response spectra of accelerograms. Thus it seems that the 2010 mega-earthquake was huge at low frequencies but the strong motion was very similar to that of a smaller event of magnitude 8. Similar observations have been reported for the recent 2011 Tohoku earthquake.

For the Tohoku 2011 earthquake we preliminary compared our elliptical patch approach results with the fixed rectangles approach, the results shows that both inversions are similar. Also we tested the inversion assuming a crack type rupture. The preliminary solutions show that at higher frequencies Tohoku 2011 strong motion is controlled by a strong nucleation and stopping phase waves.

For the Michilla 2007 earthquake, we did a full dynamic inversion of the 16 December 2007 Michilla intermediate depth earthquake for both the asperity and barrier models of seismic rupture. The models were described by 11 parameters. The optimal models had normalized errors lower than 0.21. The slip and slip rate distribution for the best asperity and barrier models are similar, confirming the earlier conjecture that seismic data cannot distinguish between barrier and asperity models. The earthquake grew at low initial speed, accelerating near the boundaries of the elliptical rupture. The rupture area is similar to that of the aftershock distributions. We explored the parameters of the friction law around the best solution using a MC technique fixing the geometrical parameters. We looked for the combination of stress and friction parameters that produced models that fit the data with relative errors of less than 30% We found that these solutions form a narrow irregular surface when the solutions were projected into the Te^2 vs TuDc plane. This is a clear

indication that good solutions of the inverse problems are actually controlled by seismic moment and κ (the ratio of strain to fracture energy for the event). Models with misfit χ^2 < 30% belong to a narrow range of κ values between 0.7 and 1.2. Our results show that seismic observations are compatible with a certain range of frictional and stress parameters determined by the seismic moment of the event and κ.

For the Iwate 2008 earthquake, we used an elliptical patch approach to do kinematic and dynamic inversion of the intermediate depth 2008 Iwate earthquake. We explored the solution space in order to find the overall characteristics of the seismic rupture in the frequency band from 0.02 to 0.5 Hz. We used displacement wave forms obtained by integration of the strong motion records from the Kik-net and K-net networks. We obtain excellent fits of the displacement time series and Fourier spectra show that we fit the entire frequency band of the filtered records. Both dynamic and kinematic inversions are non-unique with large trade-offs between the control parameters. For the dynamic inversion we found that models that fit the data with similar errors can be described with similar values of moment Mo and dynamic similarity κ. These are two global parameters that describe the size of the earthquake (Mo) and κ. It would be tempting to reformulate the results in terms of the radiation efficiency, the ratio between radiated energy and available strain energy that can be derived from kappa, but our model does not include high frequencies. We conclude conservatively that dynamic inversion using the elliptical patch approximation gives results that are in excellent agreement with simpler dynamic models of seismic radiation like the Brune-Aki scaling laws.

PERSPECTIVES

The Tocopilla 2007, Maule 2010 and Tohoku 2011 earthquakes show the advantage of using cGPS records during the inversions. In spite of this our inversions have a very low high pass frequency (~0.02 Hz). At this moment due to large signal to noise ratio of cGPS data it is not possible to make inversion at frequencies higher than 0.1 Hz. This could change in the future, but is also necessary to install accelerographs and antennas of GPS together to obtain the complete frequency range of earthquakes, as is show in Figure 1.13.

For the future of inversion the use of higher corner frequencies could be associated to use of 2D or 3D soil structure models. In this thesis only 1D models where used, and this approximation is adequate to model long period waves, but shorter period waves are controlled by the detailed soil structure, for this reason it is necessary introduce new soil structural models if we want to model propagation higher than 0.3 Hz.

For subduction zones the implementation of OBS or GPS/accustic instruments installed at ocean bottom should improve the azimuthal coverage of interplate thrust earthquakes. For Japan where more than 500 cGPS recorded the Tohoku 2011 earthquake, nowadays it is necessary to improve the azimuthal coverage more than using denser inland cGPS networks.

In contrast to kinematic inversion, dynamic inversions introduce physical aspects of the seismic rupture. However, limitations of near field strong motion and computational resources have limited its use so far to earthquake of rupture area smaller than 40 km x 40 km. Both limitations are changing with more recent earthquakes. Nowadays there are some theoretical and numerical limitations to make dynamic inversions to adequately define the stress distribution in kink zones or the use of different fault planes. In spite of these limitations simple earthquake can be full inverted using dynamic inversion as is shown in this thesis.

The preliminary crack inversion for Tohoku 2011 mega-earthquake shows that the nucleation and stopping phases controlled most of the seismic rupture. The simplicity of this model opens important perspectives to make a dynamic inversion for an important mega-earthquake using the elliptical patch approach.

8. RÉSUMÉ ÉTENDU EN FRANÇAIS

Le principal objectif de cette thèses a été d'effectuer des inversions des données sismologiques et géodésiques afin d'obtenir la distribution de glissement de cinq tremblements de terre qui ont eu lieu dans des zones de subduction. Ils s'agit des séismes de : Tocopilla 2007 (Mw 7.8) ; Michilla 2007 (Mw 6.7) et Maule 2010 (Mw 8.8) lesquelles ont frappé le Chili ; et ceux de Iwate 2008 (Mw 6.8) et Tohoku 2011 (Mw9.0) qui se sont produit au Japon. Nous avons calculé des inversions cinématiques pour tous ces événements et avons fait des inversions dynamiques pour Michilla 2007 et Iwate 2008. Ces inversions ont été réalisées en proposant une géométrie à priori de forme elliptique pour la zone de rupture avec une distribution gaussienne de glissement. La recherche de la meilleure solution est réalisée en utilisant l'algorithme de voisinage. Accélérogrammes et GPS en continu (cGPS) ont été utilisés dans l'inversion.

L'utilisation de données de GPS continu (cGPS) dans ces inversions a été validée avec l'étude du séisme de Tocopilla de Novembre 2007. Des enregistrements cGPS ont été ensuite utilisés dans les inversions des méga séismes de Maule 2010 et Tohoku 2011. L'approche elliptique dans les inversions cinématiques est une bonne solution pour étudier les grands séismes avec des enregistrements limités comme Tocopilla 2007 et Maule 2010. Des résultats préliminaires obtenus dans l'étude de tremblement de terre de Tohoku-oki de 2011 nous montrent que l'approche elliptique et la classique grille rectangulaire donnent des résultats très similaires pour la distribution du glissement sur la faille. Il est bien connu que les inversions de la distribution de glissement ne sont pas uniques. Dans les inversions cinématiques le glissement est contrôlé par le moment sismique. Les inversions dynamiques montrent que le processus de rupture est contrôlé par le moment sismique et aussi pour le κ (le rapport entre l'énérgie disponible pour la rupture et l'énergie de fracture consommé par l'événement).

Les conclusions obtenues dans l'étude de différents tremblement de terre étudiés sont les suivantes :

Pour l'inversion du séisme de Tocopilla 2007 nous avons utilisé accélérogrammes and cGPS, la solution converge vers une distribution de glissement modélisée par deux ellipses, Figure 8.1. Les enregistrements d'accélération sont intégrés une fois et les données cGPS

sont dérivés pour obtenir la vitesse du sol. Ces enregistrements de vitesse sont ensuite filtrés pour retenir la bande de fréquences entre 0.02 et 0.1 Hz. La distribution de glissement proposé en Figure 8.1 explique bien les données observées comme on peut le voir en Figure 8.2.

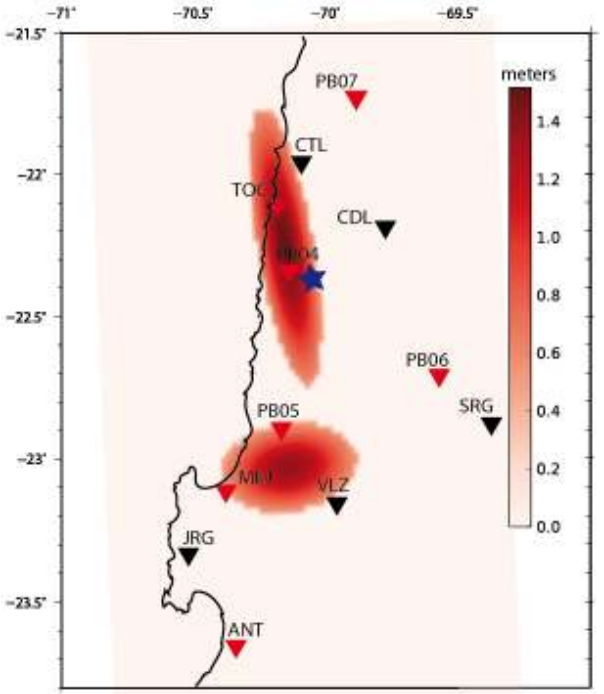

Figure 8.1. Distribution de glissement du tremblement de terre de Tocopilla 2007. Deux ellipses avec glissement maximal d'environ 1 mètre expliquent les enregistrements d'accélération ainsi que le donnes cGPS, voir Figure 8.2

Pour le méga séisme de Tohoku 2011, nous avons comparé nos résultats préliminaires entre l'approche elliptique et l'approche classique utilisant une grille de rectangles fixes. Les résultats présentés dans la Figure 8.4 montrent que la distribution de glissement obtenue par deux sont similaires. Récemment, nous avons testé l'inversion en supposant que le séisme été dû a la propagation d'une fissure de cisaillement. Les solutions préliminaires montrent que les fréquences plus élevées du mouvement fort provoqué par le séisme de Tohoku de 2011 sont contrôlées par une nucléation forte et par des fortes phases d'arrêt.

Enfin nous avons fait l'inversion de deux tremblements de terre intraplaques de profondeur intermédiaire (Mw 6.8), l'un au Chili, l'autre au Japon. Ces séismes ont été très bien enregistrés par un réseau de accélérographes. Il est important de signaler que la plus petite

surface de la rupture de ces séismes de profondeur intermédiaire, par rapport aux grands séismes de subduction étudiées auparavant, permet de faire des inversions avec des capacités de calcul de inversion dynamique disponibles aujourd'hui. Nous confirmons ici que les inversions dynamiques ne sont pas uniques et que la rupture des tremblements de terre est contrôlée par les paramètres de la loi de frottement et la géométrie de la rupture. Ces coefficients peuvent être regroupées dans un coefficient kappa spécifiques (kappa est un paramètre proportionnel au rapport entre l'énergie disponible pour la rupture sismique et celle dépensé pour propager la rupture). Figure 8.5 (Ruiz et Madariaga, 2011; Ruiz et Madariaga, 2012).

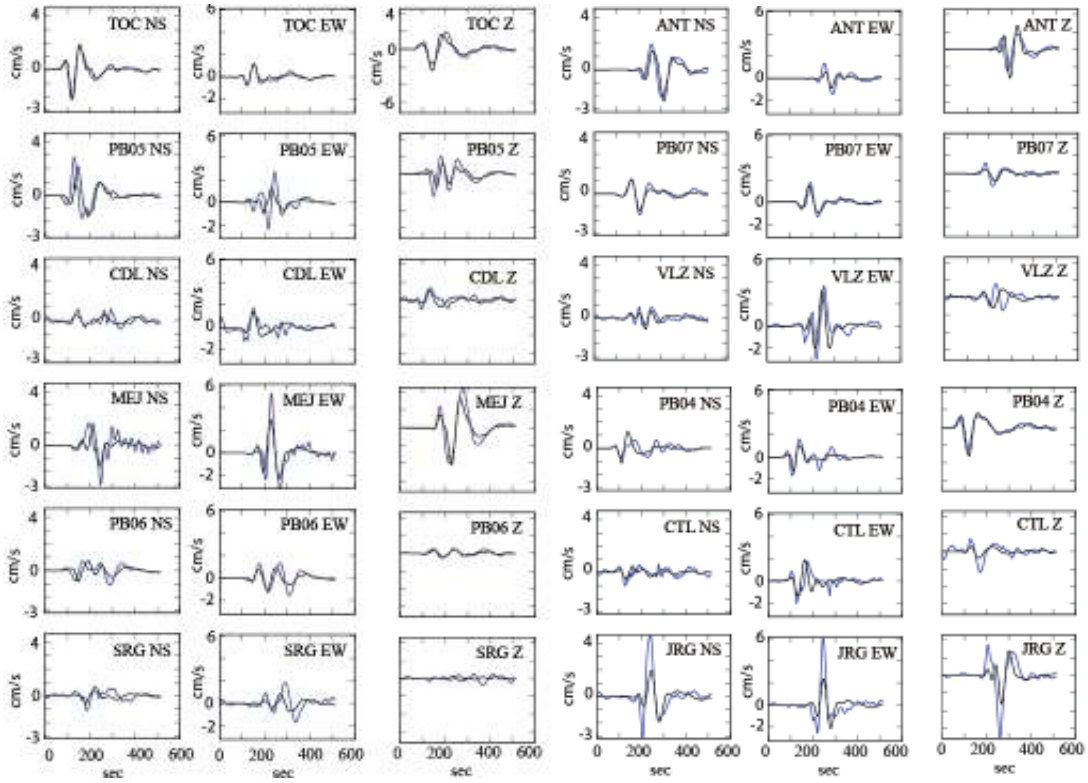

Figure 8.2**.** En bleu les enregistrements observées et en noire les enregistrements simulés avec le modèle de la figure 8.1, les données sont filtrées entre 0,02 et 0,1 Hz

Pour le tremblement de terre de Maule 2010 nous avons utilisé des données cGPS. Dans ce cas la solution converge aussi vers une distribution de glissement modélisée par deux ellipses, le glissement maximal étant situé sur la partie nord de la rupture sismique Les deux aspérités inversées expliquent bien le rayonnement sismique dans le de fréquences intermédiaires (0,02 Hz à 0,1 Hz) dans le nord de la rupture.

La Figure 8.3 montre le processus de rupture proposé, nous observons que la zone de glissement maximale coïncide avec la zone de plus forte intensité sismique (Ruiz et al., 2012).

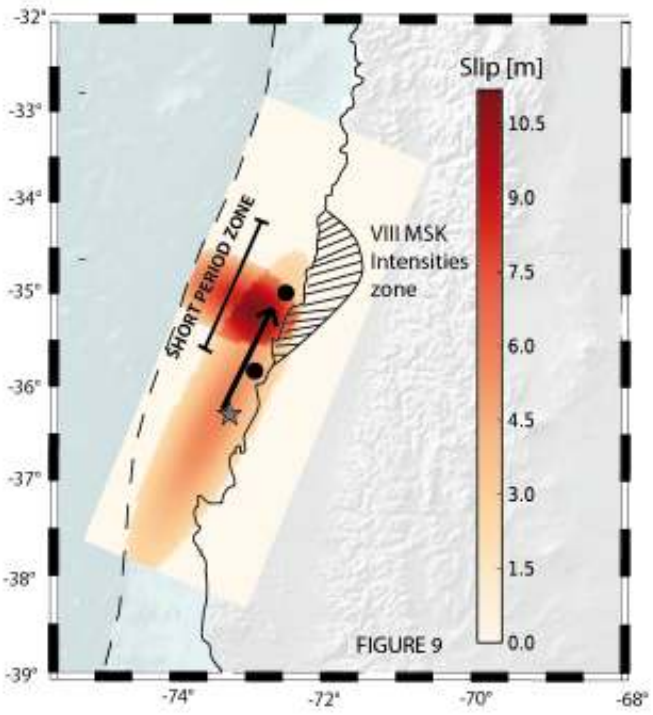

Figure 8.3. Distribution de glissement, la zone de glissement maximale coïncide avec la zone de maximum des intensités sismiques. L'étoile désigne l'épicentre et les points noirs de l'emplacement des 2 aspérités qui contrôlent l'énergie des fréquences intermédiaires.

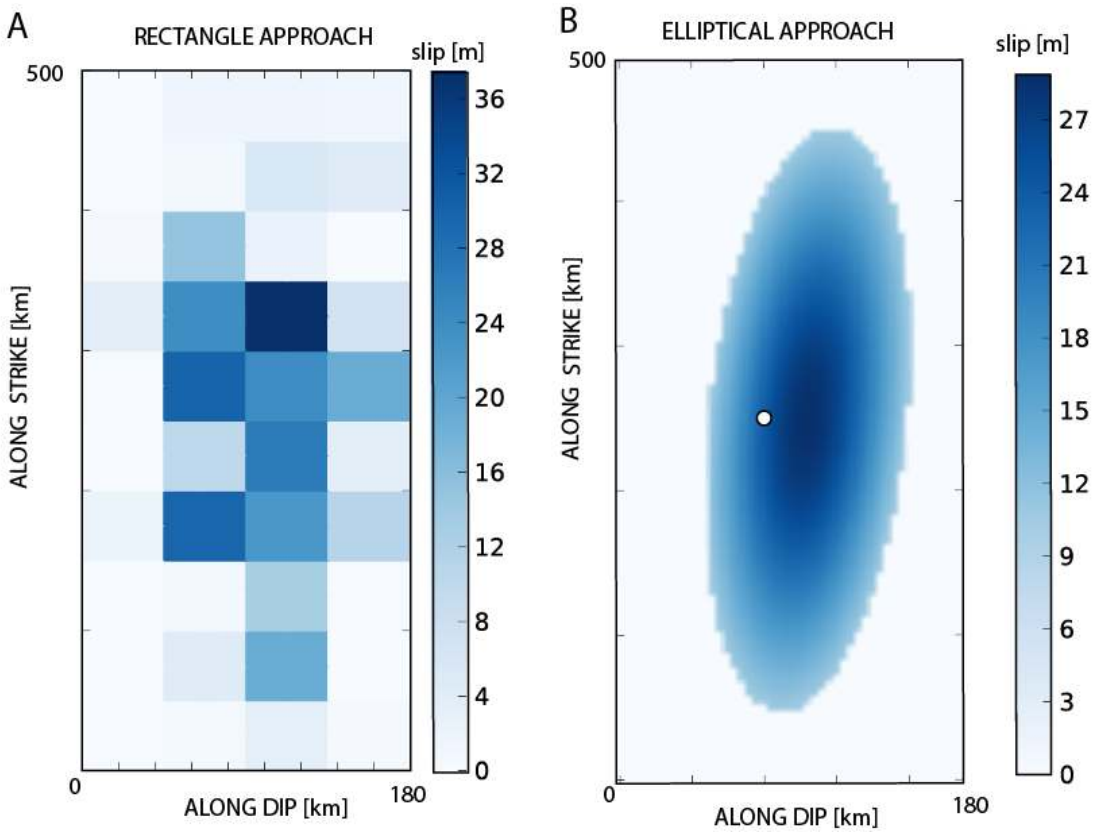

Figure F.4. Distribution de glissement obtenu en utilisant l'approximation elliptique, à droite, et une grille classique de rectangles, à gauche. On observe que les deux approches convergent vers des solutions similaires.

RÉFÉRENCES

Ruiz, S., Madariaga, R., Astroza, M., Saragoni, G. R., Lancieri, M., Vigny, C and Campos, J., (2012). Short Period Rupture Process of the 2010 Mw 8.8 Maule Earthquake in Chile. *Accepted Earthquake Spectra*

Ruiz, S and Madariaga, R. (2011). Determination of the friction law parameters of the Mw 6.7 Michilla earthquake in northern Chile by dynamic inversion. *Geophys. Res. Lett., 38, L09317, doi:10.1029/2011GL047147*

Ruiz, S and Madariaga, R. (2012) Kinematic and Dynamic Inversion of the 2008 Northern Iwate Earthquake *Submitted to BSSA*

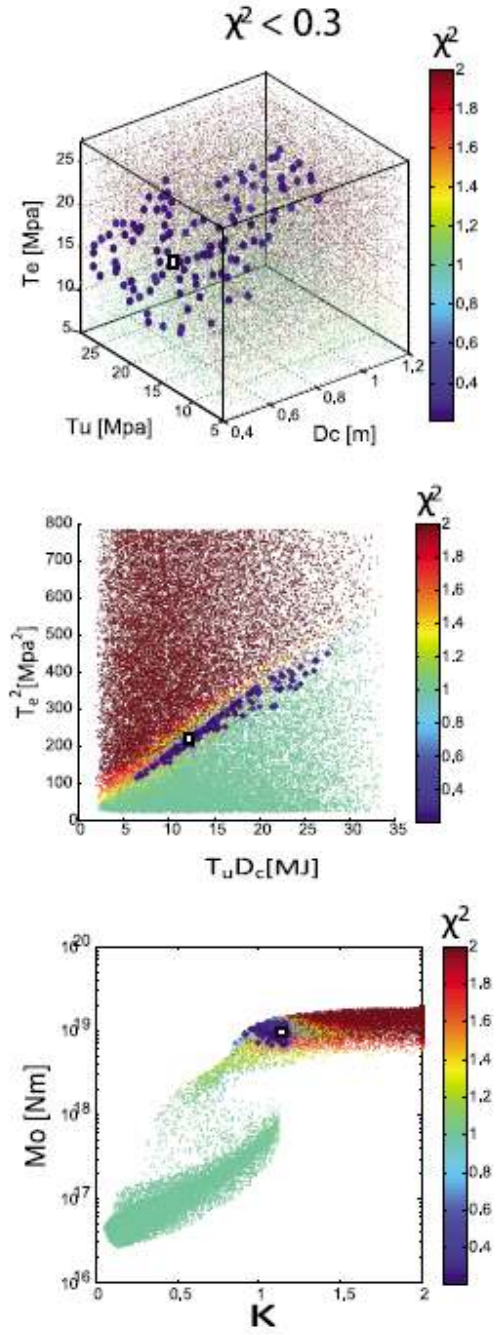

Figure 8.5**.** Etude des paramètres de la loi de frottement à avec une inversion de type Monte Carlo. Chaque point représente un modèle inverse. Les points les plus grands désignent des modèles qui ont une erreur inférieure à 0,3 ($\chi 2$ <0,3). L'échelle de couleur est saturée pour les modèles avec erreur supérieure à 0,3 ($\chi 2 \geq 2$). Le carré noir / blanc correspond à la meilleure solution trouvée en utilisant l'algorithme de voisinage. En haut l'erreur associée à chaque modèle est dessiné dans une projection à trois dimensions, sur les axes Dc, Te et Tu. Chaque point est coloré en fonction de leur erreur qui est indiqué dans la barre de couleur. Modèles avec une erreur inférieure à 0,3 ($\chi 2$ <0,3) sont regroupés dans une surface irrégulière. Centre: Projection sur le plan Te^2 , TuDc, les modèles avec une erreur inférieure à 0,3 ($\chi 2$ <0,3) sont tracées avec points plus gros, qui sont regroupées dans une structure étroite et allongée indiquant que ces modèles dépendent d'un seul nombre sans dimension κ. En bas : L'erreur ($\chi 2$) tracée en fonction du moment sismique et du paramètre κ. Les meilleurs modèles sont regroupés dans une petite zone formée par le moment sismique et κ (points bleus).

9. RESUMEN EXTENDIDO EN ESPAÑOL

Se invierte la distribución de deslizamiento de cinco terremotos, 3 ocurridos en Chile (Tocopilla 2007, Mw 7.8; Michilla 2007, Mw 6.7; Maule 2010; Mw 8.8) y dos de Japón (Iwate 2008, Mw 6.8 y Tohoku 2011, Mw 9.0). Se realizan inversiones cinemáticas para ellos con la excepción de Michilla 2007 e inversiones dinámicas para Michilla 2007 e Iwate 2008. Las inversiones son hechas proponiendo a priori una distribución geométrica del área de ruptura formada por una o dos elipses y distribución gaussiana de deslizamiento. La búsqueda de la mejor solución se realiza utilizando el algoritmo de vecindad. Acelerogramas y GPS continuos (cGPS) fueron invertidos.

El uso de CGPS durante inversiones sísmica fue validado para el terremoto de Tocopilla 2007. Este tipo de registros se utilizo también durante las inversiones de los terremotos de El Maule, 2010 y de Tohoku 2011. El enfoque elíptico en las inversiones cinemáticas es una buena solución para estudiar los terremotos de gran tamaño con escasos registros como Tocopilla, 2007 y Maule 2010. Para el 2011 Tohoku terremoto, preliminarmente se ha comparado la aproximación elíptica y la clásica grilla rectangular, las cuales entregan resultados similares. Las inversiones de la ruptura sísmica no son únicas, siendo controladas por el momento sísmico. Las inversiones dinámicas, las cuales permiten introducir aspectos físicos del proceso de ruptura, son controlados por el momento sísmico y también para el parámetro κ (la razón entre la deformación de la fractura y la energía del evento). Las conclusiones de cada terremoto de estudio son los compañeros:

Para el terremoto de Tohoku 2011 se han comparado nuestros resultados preliminares de aproximación elípticas con la aproximación de rectángulos fijo, los resultados muestran que ambos resultados son similares. También hemos probado la inversión suponiendo una ruptura tipo de grieta. Las soluciones preliminares muestran que en la frecuencia más alta de Tohoku 2011 movimiento fuerte son controlados por una nucleación fuerte y parada ondas de fase.

Para Tocopilla 2007 se utilizaron acelerogramas y cGPS en forma conjunta obteniéndose una distribución de slip caracterizado por 2 elipses, Figura G.1. Los registros de aceleración son integrados una vez y los cGPS derivados, para transformar los datos a velocidad, luego

son filtrados entre 0.02 y 0.1 Hz. La distribución propuesta de slip ajusta bien los datos, Figura G.2.

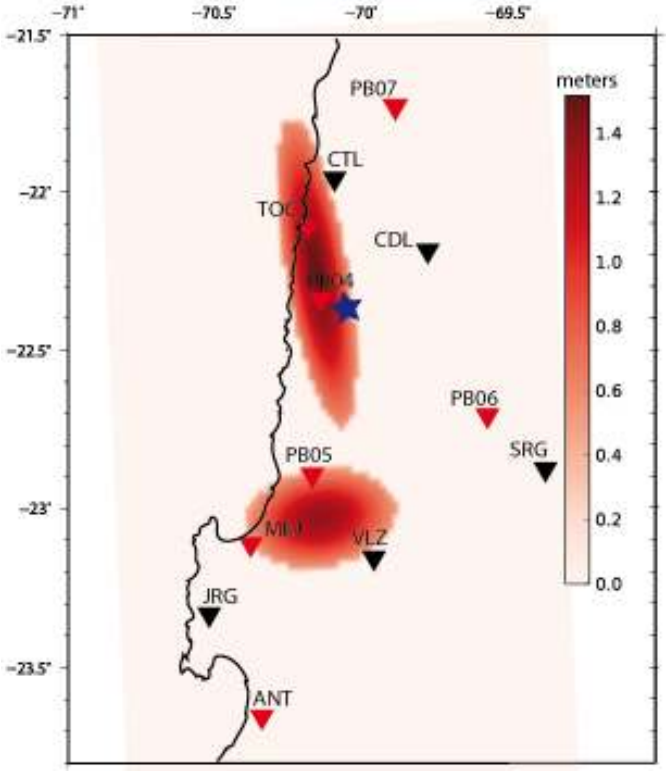

Figura G.1. Distribución de deslizamiento del terremoto de Tocopilla 2007. Dos elipses con deslizamientos máximos del orden de 1 metro explican bien los registros de aceleración y cGPS que registraron este terremoto, ver Figura G.2

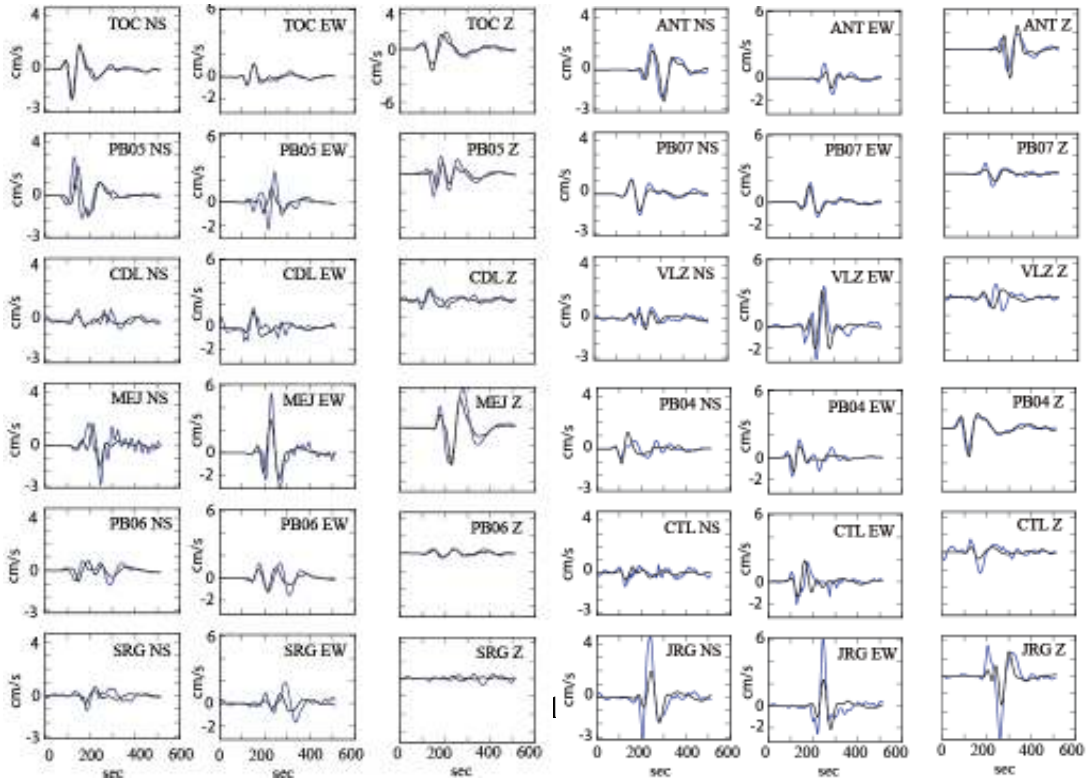

Figura G.2. En azul registros artificiales y en negro registros de acelerogramas y cGPS, ambos filtrados entre 0.02 y 0.1 Hz.

Para el terremoto del Maule 2010 se utilizaron dos elipsess, invirtiéndose los datos de cGPS y encontrando que el máximo deslizamiento se ubica en la zona norte de una ruptura de casi 500 km; para este terremoto además se identificaron las asperezas que controlaron el movimiento en el rango de frecuencias intermedias (0.02 Hz a 0.1 Hz) en la zona norte de la ruptura. La Figura G.3 muestra el proceso de ruptura propuesto para este terremoto, donde se observa que la zona de máximo deslizamiento coincide con la zona de mayor intensidad sísmica (Ruiz et al., 2012).

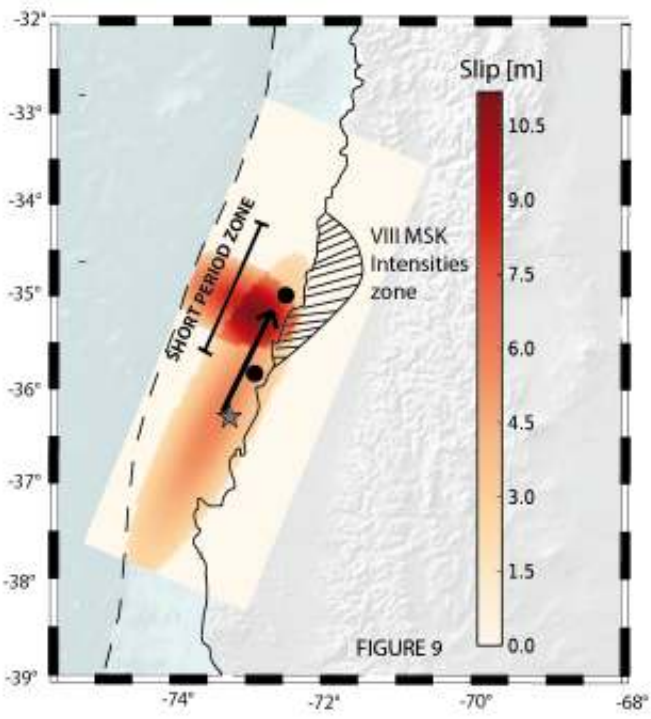

Figura G.3. Distribución de slip, la zona de máximos slip coincide con la zona de máximas intensidades sísmicas. La estrella es el epicentro y los puntos negros la ubicación de las 2 asperezas que controlan la energía de frecuencias intermedias.

El terremoto de Tohoku 2011 pudo ser caracterizado por la ruptura de una elipses y luego se realizó una búsqueda de la mejor solución utilizando un método de Monte Carlo fijando algunos parámetros y liberando solo 3 de ellos: velocidad de ruptura, deslizamiento máximo y el tamaño de la elipse (manteniendo fija la razón de aspecto entre sus ejes), encontrando que entre estos tres parámetros existen fuertes acoplamientos, confirmando que la solución no es única, Figura G.4. También para este terremoto se realiza desarrolla una preliminar inversión utilizando una discretización clásica de rectángulos, encontrándose resultados similares a la inversión por elipse, Figura 5.

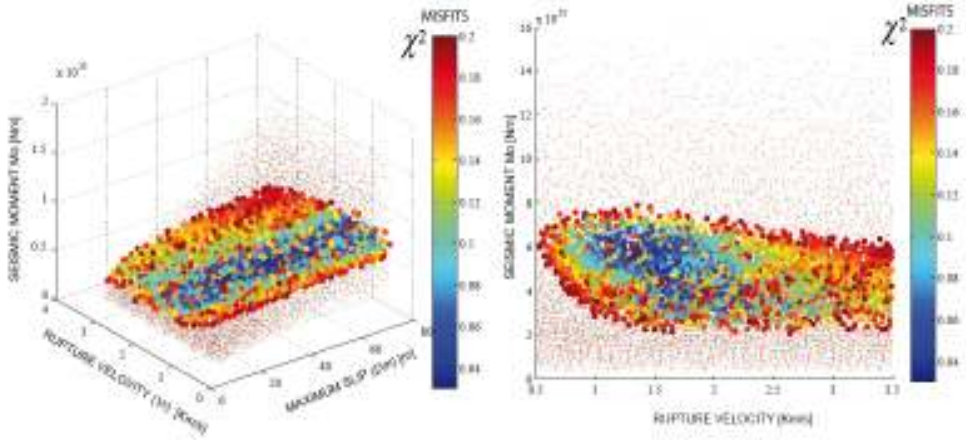

Figure G.4. Estudio en detalle de los parámetros cinemáticos que controlan la ruptura sísmica, realizando una inversión del tipo Monte Carlo. Cada punto es una inversión. Los puntos más grandes tienen un error menor a 0.2 (χ^2<0.2), la escala de colores se encuentra saturada para inversión con error mayor a 0.2. Izquierda: Figura en tres dimensiones mostrando el momento sísmico, la velocidad de ruptura y el desplazamiento máximo. Derecha. Projección del momento sísmico con la velocidad de ruptura.

Finalmente realizamos la inversión de dos terremotos intraplaca de profundidad intermedia de magnitud cercana a Mw 6.8, dado que estos eventos fueron extraordinariamente bien registrados por una red de acelerógrafos. Por otro lado, su menor área de ruptura, en comparación con los grandes terremotos de subducción estudiados antes, permite que con las capacidades computacionales de hoy se puedan realizar inversiones dinámicas. Aquí nosotros confirmamos que las inversiones no son únicas y que la ruptura de los terremotos queda controlada por los parámetros de la ley de fricción, pudiendo tomar diferentes valores pero agrupándose en un valores de kappa específicos (kappa es un parámetro que relaciona la energía liberada con la energía disponible para que el terremoto se propague), Figura G.6 (Ruiz and Madariaga, 2011; Ruiz and Madariaga, 2012).

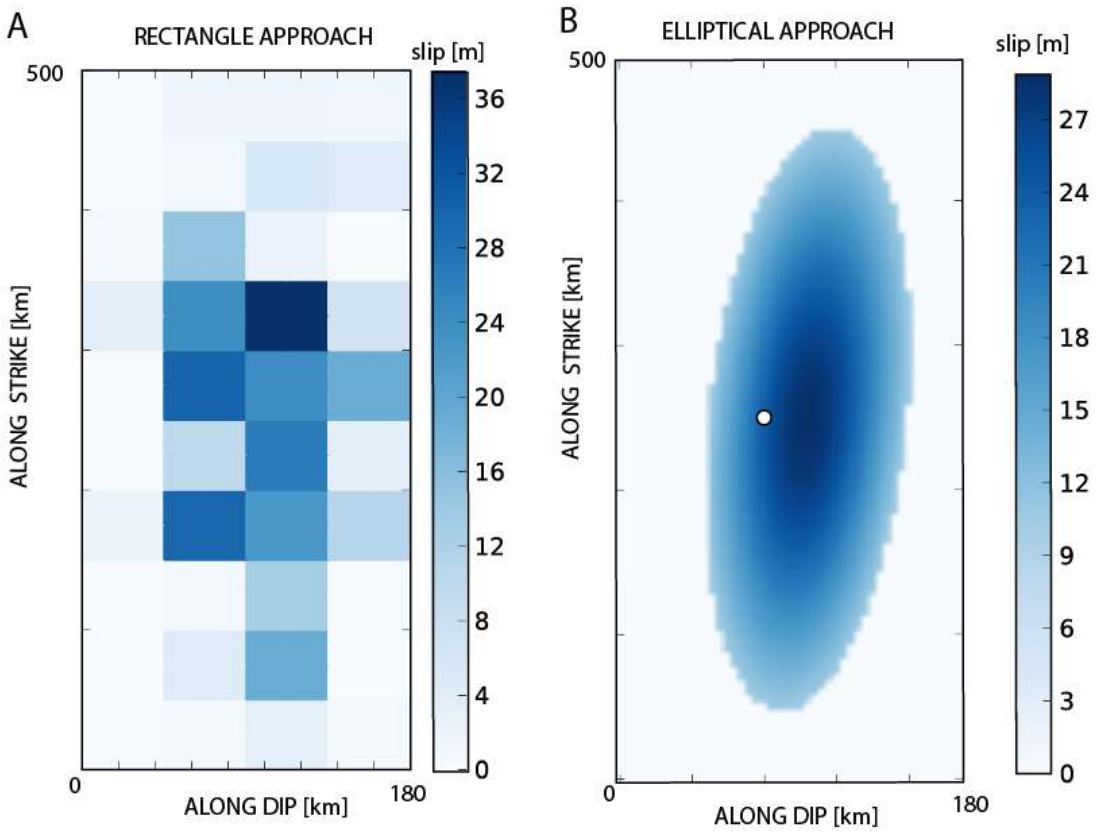

Figura G.5. Distribución de desplazamiento utilizando la aproximación elíptica y de rectángulos, se observa que ambas convergen a soluciones similares.

REFERENCIAS

Ruiz, S.**,** Madariaga, R., Astroza, M., Saragoni, G. R., Lancieri, M., Vigny, C and Campos, J., (2012). Short Period Rupture Process of the 2010 Mw 8.8 Maule Earthquake in Chile. *Accepted Earthquake Spectra*

Ruiz, S and Madariaga, R. (2011). Determination of the friction law parameters of the Mw 6.7 Michilla earthquake in northern Chile by dynamic inversion. *Geophys. Res. Lett., 38, L09317, doi:10.1029/2011GL047147*

Ruiz, S and Madariaga, R. (2012) Kinematic and Dynamic Inversion of the 2008 Northern Iwate Earthquake *Submitted to BSSA*

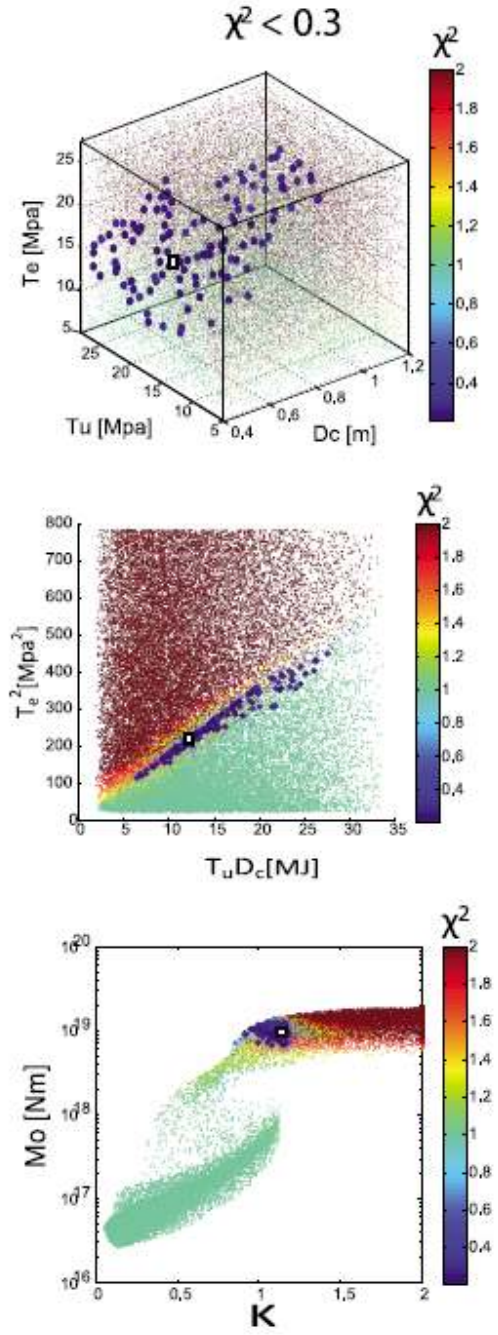

Figura G.6. Estudio de los parámetros de la ley de fricción usando una inversión del tipo Monte Carlo. Cada punto representa un modelo invertido. Los puntos que tienen un tamaño mayor presentan un error menor a 0.3 ($\chi^2 < 0.3$). La escala de colores se encuentra saturada para modelos con error mayor a 0.3 ($\chi^2 \geq 2$). El cuadrado negro/blanco corresponde a la mejor solución encontrada utilizando el algoritmo de vecindad. Arriba: El error asociado a cada modelo es dibujado en una proyección en tres dimensiones de Dc, Te y Tu. Cada punto es coloreado de acuerdo a su error el cual es indicado en la barra de colores. Los modelos con un error menor a 0.3 ($\chi^2 < 0.3$) se agrupan en una superficie irregular. Medio: Proyección en los planos de Te^2 y TuDc, modelos con error menor a 0.3 ($\chi^2 < 0.3$) son dibujados con puntos más grandes, los cuales se agrupan en una angosta y alargada estructura que indican que estos modelos están agrupando en un adimensional numero κ. Abajo: error relativos (χ^2) dibujados como función del momento sísmico y κ. Los mejores modelos se agrupan en una pequeña zona formada por el momento sísmico y κ (puntos azules).

ANNEX A

Lancieri, M., Fuenzalida, A., Ruiz, S. and Madariaga, R (2011) Magnitude Scaling of early-warning parameters for the Mw 7.8 Tocopilla, Chile, earthquake and its aftershocks. Bulletin of the Seismological Society of America (BSSA); 101 (2); 447-463.

ANNEX B

Contreras-Reyes, E., Jara, J., Grevemeyer, I., Ruiz, S. and Carrizo, D., (2012) Abrupt subducting plate dip change governs megathurst and upper plate seismicity in North Chile. Submitted to Nature Geoscience.

ANNEX C

Ruiz, S.**,** Kausel, E., Campos, J., Saragoni, G. R. y Madariaga, R. (2011). Identification of High Frequency Pulses from Earthquake Asperities Along Chilean Subduction Zone Using Strong Motion. Pure and Applied Geophysics, 168, (1-2), 125-139

ANNEX D

Astroza, M., Ruiz, S. and Astroza, R. (2012). Damage assessment and seismic intensity analysis of the 2010 (Mw 8.8) Maule Earthquake. Accepted in Earthquake Spectra

ANNEX E

Ruiz, S**.** and Madariaga R. (2012). Sismogénesis, proceso de ruptura y réplicas del mega terremoto del Maule 2010, Chile. Chapter XX in press "Mw= 8.8, Terremoto en Chile, 27 de Febrero 2010" Departamento de Ingeniería Civil, Universidad de Chile. (In Spanish)

ANNEX F

Saragoni, G. R. and Ruiz, S. (2012). Implicaciones y nuevos desafíos de diseño sísmico de los acelerogramas del terremoto del 2010. Chapter XX in press. "Mw= 8.8, Terremoto en Chile, 27 de Febrero 2010" Departamento de Ingeniería Civil, Universidad de Chile. (In Spanish)

ANNEX G

Astroza, M., Ruiz, S., Astroza, R. and Molina, J. (2012). Intensidades Sísmicas del Terremoto del 27F. Chapter XX in press. "Mw= 8.8, Terremoto en Chile, 27 de Febrero 2010" Departamento de Ingeniería Civil, Universidad de Chile. (In Spanish)